MLBP

AFWAL-TR-80-4176

ADA100523

RELATIONSHIP OF INTERFACIAL COMPATIBILITY TO DURABILITY OF ADHESIVE-BONDED JOINTS

E.E. PETERSON
D.B. ARNOLD

Boeing Military Airplane Company
Boeing Company
Seattle, Washington 98124

March 1981
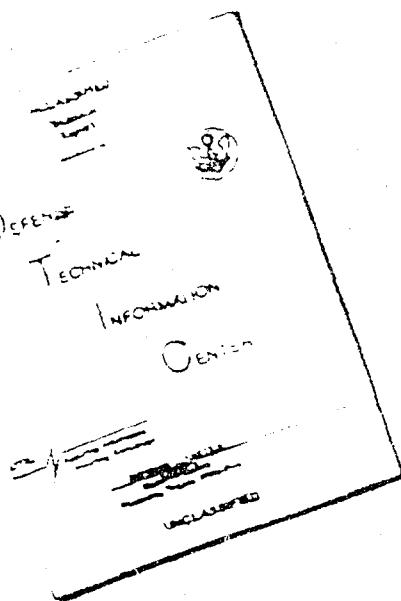
TECHNICAL REPORT AFWAL-TR-80-4176
FINAL REPORT FOR PERIOD
SEPTEMBER 1978 TO SEPTEMBER 1980

80040226192

DISCLAIMER NOTICE

THIS DOCUMENT IS BEST QUALITY AVAILABLE. THE COPY FURNISHED TO DTIC CONTAINED A SIGNIFICANT NUMBER OF PAGES WHICH DO NOT REPRODUCE LEGIBLY.

NOTICE

When Government drawings, specifications, or other data are used for any purpose other than in connection with a definitely related Government procurement operation, the United States Government thereby incurs no responsibility nor any obligation whatsoever; and the fact that the government may have formulated, furnished, or in any way supplied the said drawings, specifications, or other data, is not to be regarded by implication or otherwise as in any manner licensing the holder or any other person or corporation, or conveying any rights or permission to manufacture, use, or sell any patented invention that may in any way be related thereto.

This technical report has been reviewed and is approved for publication.

S. Schwartz Matls Rsch. Eng.
Composites Adhesives & Fibrous Matls Br.
Nonmetallic Materials Division

J. Reinhart, Jr., Chief
Composites Adhesives & Fibrous Matls Br.
Nonmetallic Materials Division

FOR THE COMMANDER:

J. M. Kelble, Chief
Nonmetallic Materials Division

REPORT DOCUMENTATION PAGE		READ INSTRUCTIONS BEFORE COMPLETING FORM
1. REPORT NUMBER AFWAL-TR-80-4176	2. GOVT ACCESSION NO.	3. RECIPIENT'S CATALOG NUMBER
4. TITLE *(and Subtitle)* Relationship of Interfacial Compatibility to Durability of Adhesive - Bonded Joints		5. TYPE OF REPORT & PERIOD COVERED Final Technical Report 9/1/78 to 9/1/80
		6. PERFORMING ORG. REPORT NUMBER
7. AUTHOR(s) Erick E. Peterson Daniel B. Arnold		8. CONTRACT OR GRANT NUMBER(s) F33615-78-C-5133
9. PERFORMING ORGANIZATION NAME AND ADDRESS Boeing Military Airplane Company Boeing Materials Technology P. O. Box 3707, Seattle, Washington 98124		10. PROGRAM ELEMENT, PROJECT, TASK AREA & WORK UNIT NUMBERS 1457
11. CONTROLLING OFFICE NAME AND ADDRESS		12. REPORT DATE March, 1981
		13. NUMBER OF PAGES 221
14. MONITORING AGENCY NAME & ADDRESS(If different from Controlling Office)		15. SECURITY CLASS. (of this report) Unclassified
		15a. DECLASSIFICATION/DOWNGRADING SCHEDULE

16. DISTRIBUTION STATEMENT *(of this Report)*

Approved for Public Release; Distribution Unlimited

17. DISTRIBUTION STATEMENT *(of the abstract entered in Block 20, if different from Report)*

18. SUPPLEMENTARY NOTES

19. KEY WORDS *(Continue on reverse side if necessary and identify by block number)*

Phosphoric Acid Anodize	Oxide Structure and Chemistry
Forest Products Laboratory Etch	Interfacial Compatibility
350°F Curing Adhesive Systems	Bonded Joint Fracture Toughness
Bonded Joint Durability	Bonded Joint Mechanical Strength

20. ABSTRACT *(Continue on reverse side if necessary and identify by block number)*

Previous investigations reported reduced lap-shear strength or stress durability of some 350°F curing adhesive systems on phosphoric acid anodize (PAA) compared to Forest Products Laboratory (FPL) etch. When certain elastomer-modified primers were utilized, the reported reductions in mechanical properties were more severe. These investigations employed 0.0625 in. thick adherend machined lap-shear specimens. Various mechanisms were hypothesized to explain an apparent primer/PAA compatibility problem.

DD _{1 JAN 73} FORM 1473   EDITION OF 1 NOV 65 IS OBSOLETE

(Continuation of Block 20)

This investigation determined the structure and chemistry of the PAA and FPL oxides; and investigated the mechanical properties and component interactions of bonded joints containing 350°F curing adhesive systems combined with PAA and FPL. On .0625 in. thick adherend machined lap-shear specimens, FPL had greater strength. However the significant reduction in strength, reported earlier, were not substantiated. Because of the significant normal stress gradients present in this specimen other investigators have recommended that it not be employed to measure shear strength. On .125 in. thick adherend machined lap-shear specimens, PAA had greater shear strength. Stress durability on PAA was superior to or equal to that of FPL.

Analysis determined that the failure modes were independent of the surface preparation, and depended on the intrinsic properties of the adhesive or primer. Three different mechanisms for toughening epoxy primers were detected. Addition of an "incoherent" elastomeric additive to the primer, which formed phase separated rubber particles having poor mechanical linkage with the matrix resin, resulted in significant loss in shear strength and negligible increase in toughness. Addition of a "coherent" elastomeric additive to the primer, which formed phase separated rubber particles having good mechanical linkage with the matrix resin, resulted in good shear strength retention and significantly increased toughness. An adhesive primer possessing good matrix resin ductility has high shear strength and toughness.

FOREWORD

TABLE OF CONTENTS

LIST OF ILLUSTRATIONS

LIST OF TABLES

LIST OF TABLES (Concluded)

SECTION I

INTRODUCTION

1. HISTORICAL BACKGROUND OF INVESTIGATION

The state of the art of adhesively bonded aluminum has been significantly improved in recent years. Adhesives and primers have been developed to optimize strength, toughness, and environmental durability. Prebond surface preparations have been developed to yield stable oxide substrates. Specifically, Forest Products Laboratory (FPL) etch has been replaced by phosphoric acid anodize (PAA), noncuring epoxy primers have been replaced with corrosion-inhibiting adhesive primers (CIAP), and moisture-sensitive adhesives have been replaced with moisture-resistant adhesives. These improvements have provided the technology base for expanded usage of adhesive bonding and commitment of bonding to primary aircraft structure (fig. 1). The Primary Adhesively Bonded Structure Technology (PABST) program at McDonnell-Douglas and the bonded honeycomb structure on the Boeing YC-14 AMST are examples of the aircraft industry's commitment to adhesive bonding.

The greatest improvement has been obtained with 250°F-curing, 180°F-service, modified epoxy adhesives, CIAP primers, and PAA substrates. An apparent "incompatibility" was reported for one 350°F-curing adhesive/primer system—BR-227A/FM-61 on PAA oxide. The characteristics of the incompatibility were reduced lap-shear strength and a slick-appearing, potentially interfacial failure mode. The failure mode appeared to be interfacial between the primer and oxide surfaces when examined visually and with optical microscopes. A subsequent investigation demonstrated that this incompatibility occurred with anodically produced oxides, but not with FPL-etched surfaces (table 1). Also, an analysis of the failure modes using the scanning electron microscope (SEM) showed the failure modes on all the anodically produced oxides to be cohesive within the primer, with a very thin layer of primer over the oxide surfaces (ref 1, 2). Figure 2, an SEM photomicrograph, shows a typical failure that has a very thin layer of primer over the oxide surface and bridging across islands of oxide. Use of BR-227A, containing an elastomeric additive, resulted in some reduction in lap-shear strength in comparison to BR-227 on all surface preparations tested.

*Phosphoric acid anodize
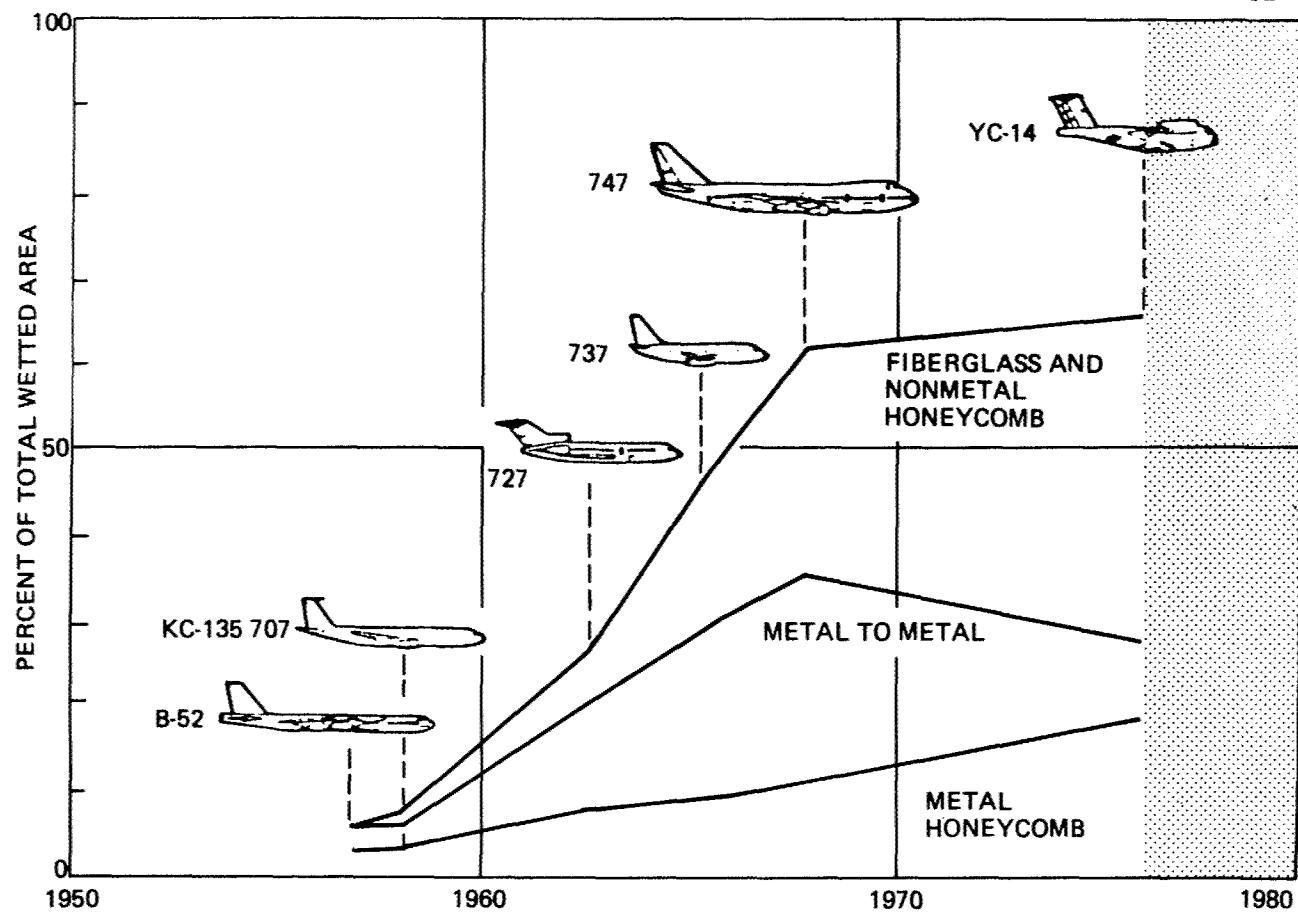
Figure 1. Boeing Bonded Applications
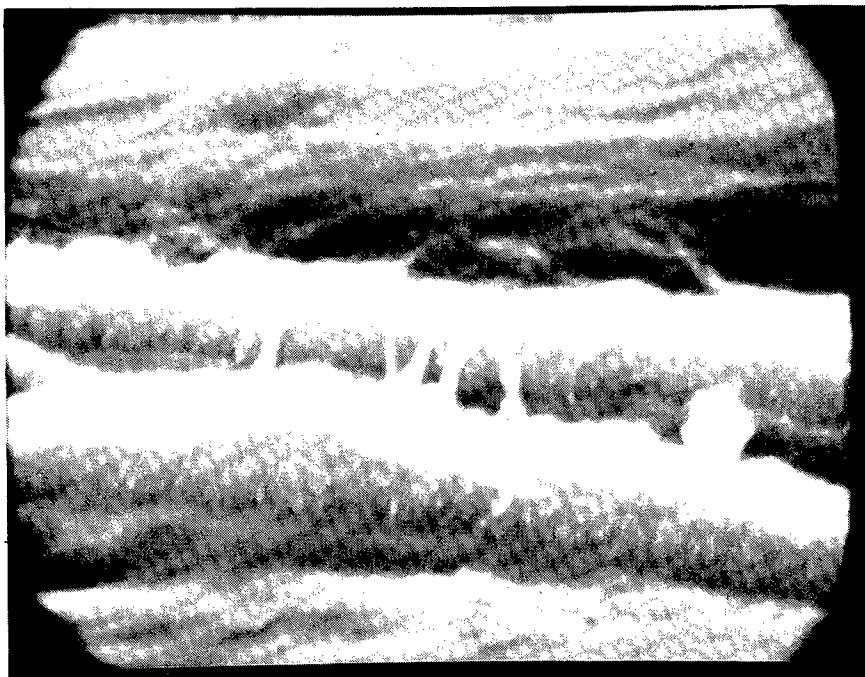
*Table 1. Lap-Shear Strengths for Different
Aluminum Surface Treatments
vs BR-227A and BR-227 Primers*

Primer	(Solids (%)	Average (5) lap shear strengths (lb/in^2)			
		Surface treatments			
		FPL	PO$_4$ 20V	PO$_4$ 5V	CrO$_3$ 22V
BR-227A	15* 30**	3,293 2,664	2,317 2,535	2,263 2,198	2,565 2,348
BR-227	15 30	3,577 3,312	3,290 3,402	3,306 3,450	3,279 3,202

*Primers at 15% solids were sprayed on aluminum
**Primers at 30% solids were dipped on aluminum

FM-61 Adhesive was employed

2

Oxide cross section of surface of failed lap shear specimen
that has been anodized in phosphoric acid at 20V and
primed with BR-227A. An elastomeric polymer is evident
on surface of oxide and stretched across the oxide islands

Figure 2. Oxide Cross Section

More recent studies at Boeing have shown that the method of primer application influences the behavior of BR-227A on anodized surfaces. Spray application of the primer produces reduced lap-shear values, whereas "curtain coating" application produces greater lap-shear values.

BR-227A primer is obtained by modifying BR-227 with a nitrile rubber elastomer. Historically, the modification was made to obtain a primer with higher viscosity during the final cure.

The reduction in lap-shear strength of the non-rubber-modified primer (BR-227) on PAA in comparison to FPL was not as pronounced as for BR-227A.

During the course of Air Force Contract F33615-74-C-5056 (ref 3), a similar "incompatibility" was reported for another 350°F-curing adhesive/primer system, PL-728/PL-729-3. This incompatibility was a reduction in the measured lap-shear strength of the adhesive system on PAA in comparsion to FPL when clad adherends were used (2024-T3 and 7075-T6 clad). For the same alloys bare, the measured lap-shear

3

strengths of this adhesive system on both surface preparations are equal. The mean lap-shear strength of this adhesive system on 7075-T6 bare/PAA exceeds that of 7075- T6 bare/FPL. However, the difference is not statistically significant. The statistical significance of the data was determined using the statistical test for the difference between two means employing Student's t-distribution and a 1% critical value (ref 4, 5). This test was used throughout this investigation to analyze the statistical significance of differences in mechanical test data.

Neither of the two investigations cited report reduced stress durability of the two adhesive systems on PAA in comparison to FPL. Quite to the contrary, the durability on PAA is as good as or better than that on FPL.

An independent investigation conducted by Schwartz (ref 6) showed that lap-shear specimens bonded with PL-728/PL-729-3 on PAA surfaces failed prematurely when exposed to 95°F salt spray while under a sustained stress at 50% of their room-temperature ultimate strengths. The same adhesive/primer system bonded to FPL-etched surfaces showed much better stressed-durability performance. When the PL-728 primer was omitted from the bondline of the PAA specimens, the stressed-durability performance was equal to or better than that of PL-728 on FPL-etched surfaces. The differences in lap-shear strength of PL-728/PL-729-3 on PAA in comparison to FPL using two alloys are not statistically significant. The alloys used were 2024-T3 and 7075-T6 bare.

Failure mode analyses were not conducted during either of the studies that investigated PL-728/PL-729-3.

The results of the three investigations are summarized as follows:
1. Marceau (ref 1) reported significantly reduced room-temperature lap-shear strengths on anodically produced oxides when BR-227A was used.
2. Marceau (ref 1) reported good stress durability for systems using BR-227A and BR-227.
3. Marceau et al. (ref 3) reported reduced room-temperature ultimate lap-shear strength on 2024-T3 clad and 7075-T6 clad PAA in comparison to 2024-T3 clad and 7075-T6 clad FPL when PL-728/PL-729-3 was used.
4. Marceau et al. (ref 3) reported good stress durability on PAA and optimized FPL for PL-728/PL-729-3. The residual strength of PL-728/PL-729-3 on PAA was

4

greater than that on FPL for 2024-T3 (clad or bare) and 7075-T6 (clad or bare). Some of the differences may be statistically significant.

5. Marceau (ref 1) reported that the failure mode of test specimens containing BR-227A was cohesive within the primer.

6. Schwartz (ref 6) reported inferior stress durability for the PL-728/PL-729-3 adhesive system on PAA in comparison to FPL.

7. Schwartz (ref 6) reported room-temperature lap-shear strengths for PL-728/ PL-729-3 on PAA and FPL that did not differ statistically. On 2024-T3 bare adherends, he reported greater mean shear strength for PAA than for FPL.

These differences in reported results are summarized in Table 2. The stress-durability test results reported for PL-728/PL-729-3 are not consistent.

Table 2. Comparison of Investigation Results for PL-728/PL-729-3 System

	Marceau investigation	Schwartz investigation
Lap-shear test	Equivalent strength on bare aluminum FPL superior on Clad aluminum	Equivalent strength on bare aluminum No tests on Clad aluminum
Stress durability test	PAA superior	FPL superior

2. HYPOTHESIZED MECHANISMS OF BONDED JOINT FAILURE

The differences in test results discussed above raise the following questions:

1. Do high-temperature adhesive systems (i.e., those that cure at 350°F) have reduced room-temperature ultimate lap-shear strength on PAA in comparison to FPL?

2. Do these adhesive systems have reduced stress durability on PAA in comparison to FPL?

3. Why does BR-227A have a greater reduction in shear strength on anodically produced oxides than does BR-227?

4. Are rubber-modified primers incompatible with PAA?

Marceau and Schwartz proposed some mechanisms they believed might explain the phenomena they observed.

Schwartz proposed that some primers—particularly those that contain elastomers—do not totally penetrate the thick, porous columnar PAA oxide, resulting in a zone of unimpregnated oxide that is weak in shear. When the joint is loaded in shear, the unsupported oxide fails (ref 6) (see fig. 3).

(A) BONDED SYSTEM UNSTRESSED

(B) BONDED SYSTEM UNDER SHEAR STRESS

Hypothesis of oxide failure in a bonded system with a thick duplex oxide when exposed to shear stresses
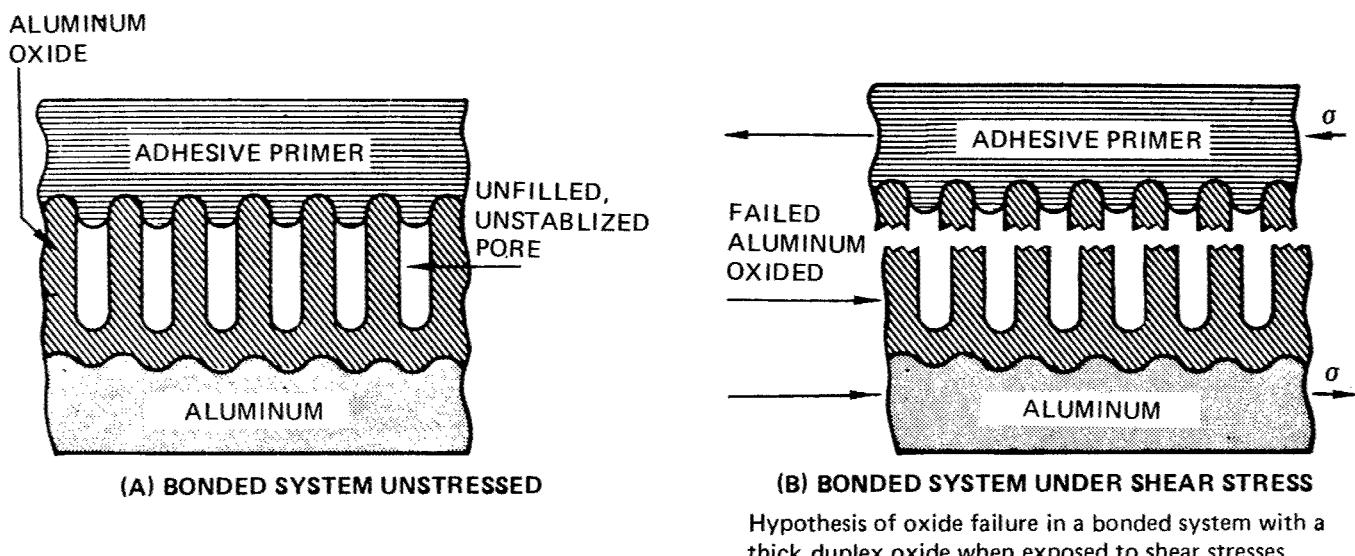
Figure 3. Proposed Oxide Failure Model (First Mechanism)

Marceau proposed that the high-molecular-weight rubbers in rubber-modified adhesive primers could not penetrate the porous PAA oxide, whereas the lower molecular weight components could. This would result in an elastomer-rich zone above the thick PAA oxide. The elastomer-rich zone can function as a weak boundary layer (ref 1) (see fig. 4).

Marceau proposed a second mechanism, illustrated schematically in Figure 5, that would probably operate in conjunction with his first mechanism. This mechanism postulates that premature failures do not occur until the oxide fractures, thus creating stress risers in the primer at these points. Thick oxides produced by anodizing break into larger pieces than do thin oxides, such as produced by FPL etch, thereby creating zones of higher stresses at these points of oxide fracture. These stresses, coupled with a thin, weak boundary layer of polymer just at the oxide surface, can cause premature failure (ref 1).

3. REQUEST FOR INVESTIGATION RECEIVED BY BOEING
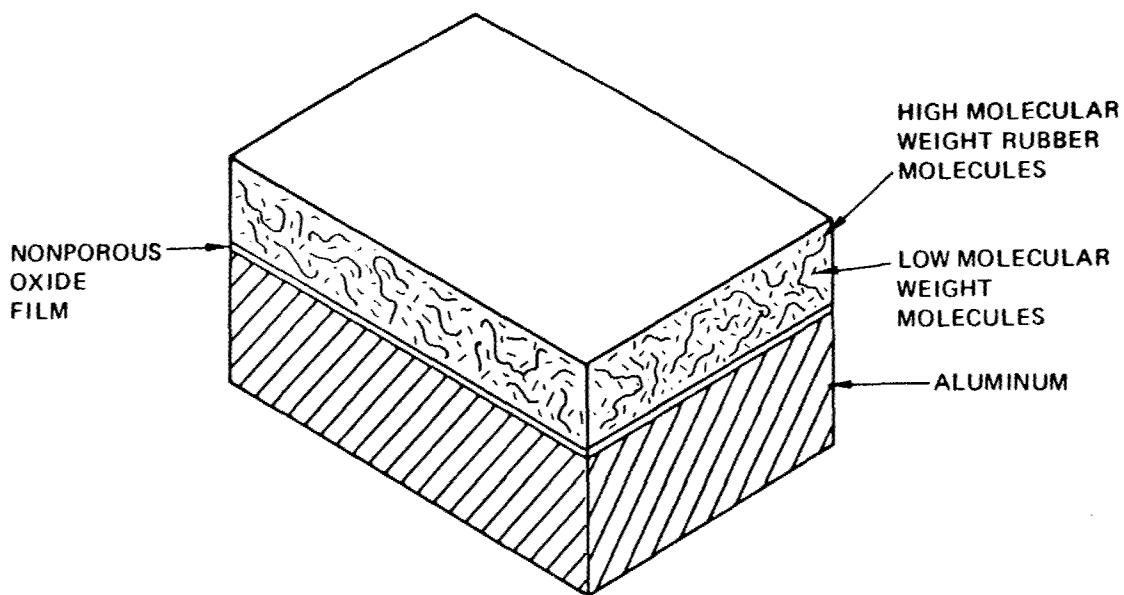
To investigate the failure mechanisms and further determine the mechanical properties of higher temperature adhesive primers on porous anodic oxides, Boeing was awarded this contract.

Boeing's technical proposal (ref 7) postulated one more failure mechanism. According to this hypothesis, primers that contain elastomeric additives may undergo excessive deformation during long-term loading. This loading might fracture an unstabilized, anodic, porous oxide.
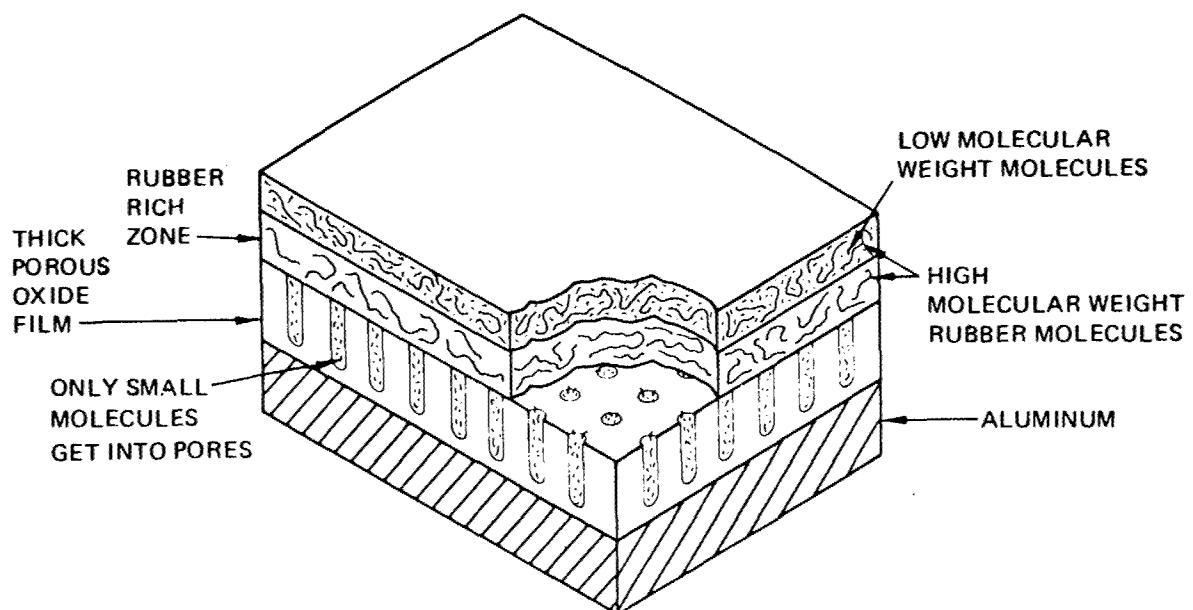
4. DESCRIPTION OF INVESTIGATION

The investigation to be reported later herein consisted of the following five tasks:
o   Task I—Selection of Materials for Investigation
o   Task II—Postulation of Candidate Mechanisms of Behavior
o   Task III—Experimental Investigations to Define Mechanisms of Behavior and Relevant Materials Parameters
o   Task IV—Engineering Characterization and Evaluation to Validate Mechanisms of Behavior Defined in Task III
o   Task V—Range of Materials and Environmental Parameters for Acceptable Bonded Joint Performance

7

(A) MOLECULAR DISTRIBUTION—NONPOROUS OXIDE

Labels on figure A: HIGH MOLECULAR WEIGHT RUBBER MOLECULES; NONPOROUS OXIDE FILM; LOW MOLECULAR WEIGHT MOLECULES; ALUMINUM

(B) MOLECULAR DISTRIBUTION—POROUS DUPLEX OXIDE

Labels on figure B: RUBBER RICH ZONE; THICK POROUS OXIDE FILM; ONLY SMALL MOLECULES GET INTO PORES; LOW MOLECULAR WEIGHT MOLECULES; HIGH MOLECULAR WEIGHT RUBBER MOLECULES; ALUMINUM

Influence of oxide surface characteristics on molecular distribution at the oxide/polymer interface: (A) nonporous surface with low tendency to influence molecular separation; (B) porous oxide with strong tendency to influence separation of small molecules from large rubber molecules.

Figure 4. Molecular Distribution on Porous and Nonporous Oxide Surfaces (Second Mechanism)
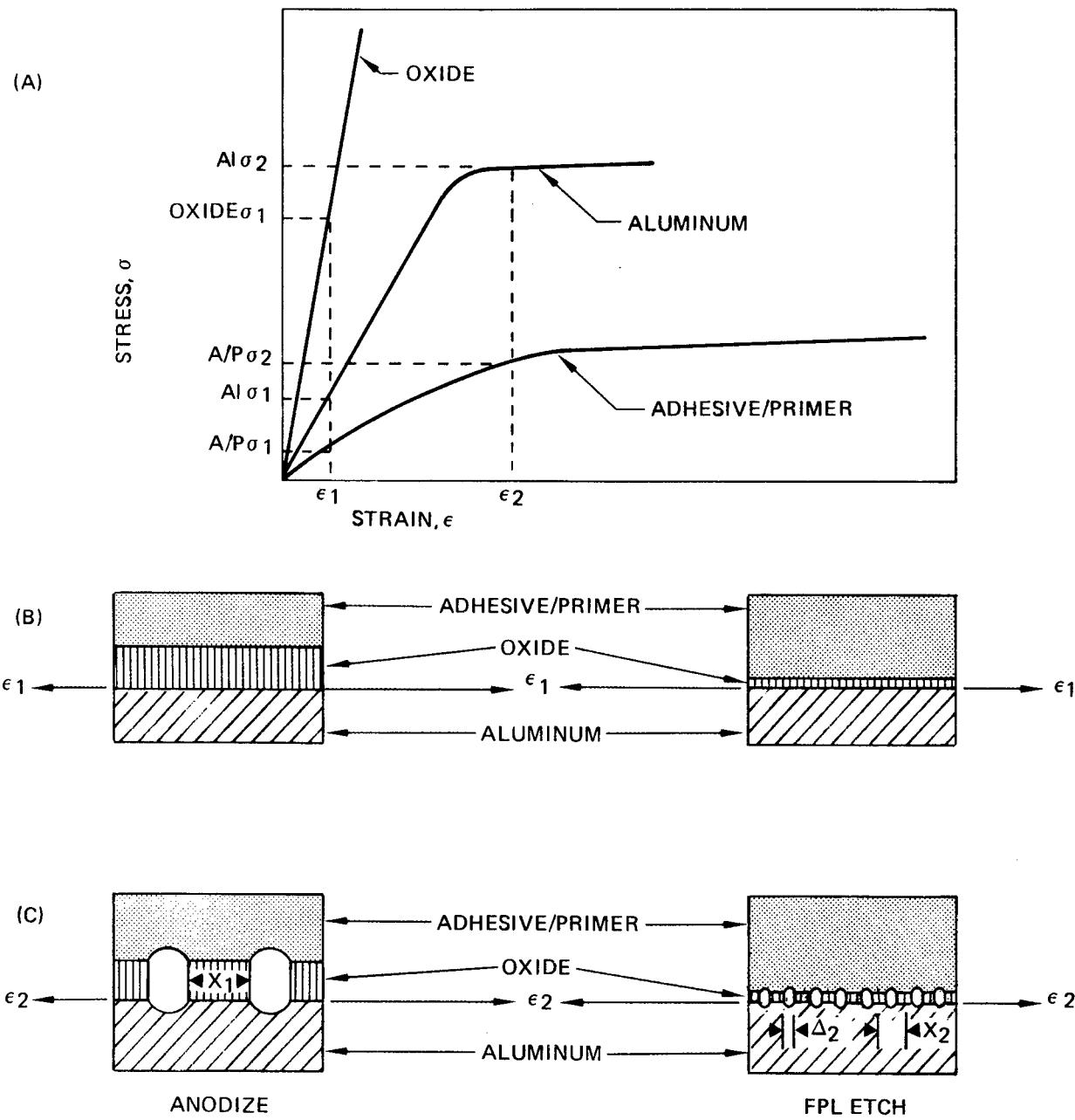
Illustration of how the stress-strain characteristics of the different components in a bonded system influence failure: (A) relative stress-strain characteristics of the three components; (B) system at strain, ϵ; and (C) system at strain ϵ_2 where oxide has failed.

Figure 5. Stress/Strain Characteristics of Bond System Components (Third Mechanism)

9

To further characterize anodic oxides of aluminum, a subcontract was let to the Physics Department of Washington State University. For a discussion of this investigation, see Appendix D.

Each task will be described briefly (see fig. 6).

Task I defines the materials and processes used in the investigation. Test materials were selected that exhibited the apparent incompatibility, and these materials were compared with systems displaying no incompatibility. Three pairs of adhesive primers were investigated. One member of each pair did not contain rubber additives. The second member of each pair had a composition identical to the first, except that it did contain rubber additives. Anodization processes were selected that produce oxides of varying morphology and chemistry.

Task II defines the four original candidate failure mechanisms proposed to explain the interaction of various primers and porous anodic oxides. These mechanisms have been described in detail. Two more mechanisms were added during the investigation to explain the mechanical properties of the adhesive systems. One mechanism is an explanation of the reduction in shear strength of an epoxy resin when it is modified with a nonreactive rubber additive (the rubber-modified epoxy is a true composite, because it is a mixture of heterogeneous phases) (ref 8). Admittedly, the theory is semiquantitative at best. However, the knowledge that the shear strength is reduced and that this reduction can be estimated is very important.

The second mechanism hypothesized is that the overall shear strength of an adhesive-bonded joint also is dependent on the primer/adhesive interaction. This hypothesis is important because the different primers were evaluated initially with different adhesives on the same surface preparations. Consequently, experimental results that could be interpreted as resulting from interactions between the oxide and primer actually might result from primer/adhesive interactions. This possibility greatly influenced the design of the mechanical tests during Task IV.

Most of the experimental investigation occurred during Task III. The main activities of Task III are as follows:
1. Oxide/primer/adhesive interactions
2. Stress-durability testing
3. Failure analysis
4. Discussion of failure mechanisms
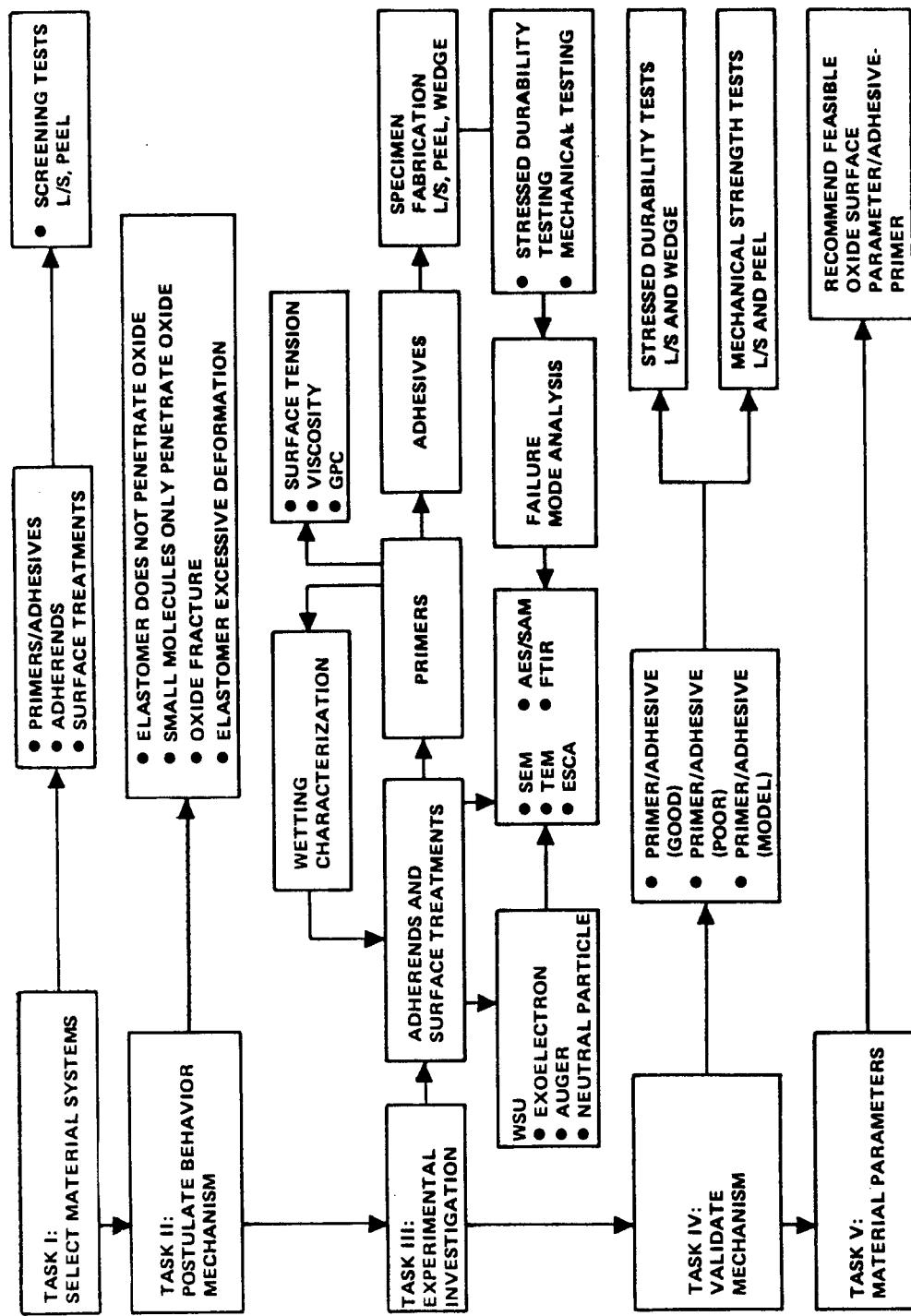
Figure 6. Program Task Flow

11

The main purpose of these activities was to determine the mechanical properties and failure mode of specific adhesive systems on specific surface preparations for bonding. Various types of mechanical tests were used. It was particularly important to determine if the mechanical properties and/or failure mode of a specific system depend on the type of loading mode. If this is true, then the important loading mode is the one for which bonded joints are designed. Many bonded assemblies are designed to transfer the load in shear. Ideally, one strives to minimize, if not eliminate, peeling stresses in bonded assemblies.

Equally important are the relative mechanical test values for those primer/adhesive systems that can be compared. For example, the mechanical properties of two different adhesive primers on the same surface preparation cannot be compared if they were bonded with different adhesives. Relevant relative comparisons of mechanical values are necessary because of the requirement to establish the materials parameters for acceptable bonded joint performance.

The purpose of Task IV was to further verify the mechanisms of behavior identified in Task III. This was accomplished by performing the test plan shown in Figure 7. The significant aspects of this plan are as follows:

1. Two different alloys were used because they create different oxide morphologies.

2. Specimens were bonded with an adhesive primer and its elastomer-modified counterpart. Intermediate- and high-modulus adhesives were used.

3. The Bell peel test and the unsymmetrical wedge test also were used to test the integrity of the bonded joints.

4. The shear strength of both adhesive systems on PAA and FPL was tested with thick- and thin-adherend machined lap-shear specimens (fig. 8) to measure the effect of different ratios of normal stresses to shear stresses on the measured shear strength.

5. Sustained stress and unsymmetrical wedge specimens were exposed to 160°F, 100% relative humidity (RH) to determine the environmental durability of the adhesive systems under investigation. These two tests were performed on PAA only for the following reasons:

   a. Tests were performed to determine if primer and/or adhesive can cause interfacial incompatibility during environmental testing. No potential interfacial compatibility has been identified during environmental testing on FPL-processed adherends. Consequently, it was not tested.

12

b. Results of Task III indicated that failure mode was independent of surface preparation. Consequently, it was not necessary to test these primer/adhesive combinations on both surface preparations.

c. Bonded specimens using FPL-processed adherends were not fabricated, to reduce costs toward the end of the contract.

The wedge test evaluates the fracture toughness of the adhesive joint. The sustained-stress test evaluates the load-carrying capacity of the joint during environmental exposure.

ADHERENDS

● 2024-T3-clad
● 2024-T3-bare

OXIDES
● Clad oxide - thick and regular
● Bare oxide - thin, less regular

PRIMER
● BR-227
● BR-227A

ADHESIVE
● FM-300(Low G)
● PL-729-3(High G)

SUBSTRATE → ANODIZE → SPRAY AND CURE → BOND

BONDED PANELS

SPECIMENS

● Lap shear (0.063, 0.125)
● Bell peel
● Wedge, asymmetric

TESTING

● Static, ambient LS
● Static, ambient peel
● Stressed LS, 1500 PSI 100% RH, 160°F
● Fracture (100% RH. 160°F)

ANALYSIS

● Ultramicrotomy plus EELS and TEM
● Oxide cross section SEM, STEM
● Failure loads and times
● Surface analysis ESCA or ATIR

MACHINE COUPONS → TEST AND EXPOSURE →

PROPERTIES   CONCLUSIONS

Figure 7. Task IV Test Plan
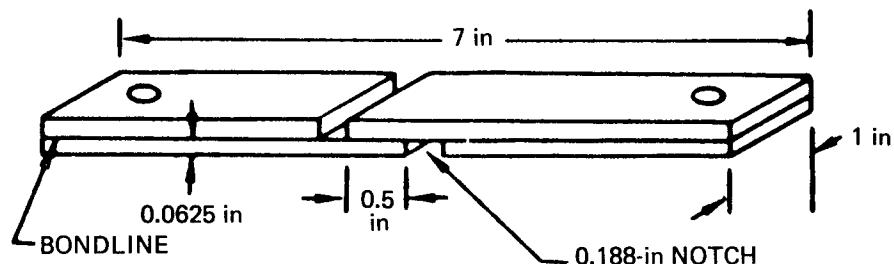
Figure 8. Machined Lap-Shear Specimen

13

Task V established the materials and processes necessary to improve the performance of elevated-service-temperature bonded joints.

5. OVERVIEW OF INVESTIGATION

a. Task I—Selection of Materials for Investigation

The screening test in Task I did not confirm the previous ambient ultimate lap-shear test trends. Also, the values were generally low. A portion of the test was rerun. The latter lap-shear values were higher, but the inferior performance on PAA was not evident. The decision was made to investigate this phenomenon in Task III.

b. Task II—Postulation of Candidate Mechanisms of Failure

See Task III for new mechanisms developed during that task.

c. Task III—Experimental Investigation to Define Mechanisms of Behavior and Relevant Materials Parameters

The principal activities of this task were to investigate the interaction between the components in the bonded joint and to determine the failure mechanism of those systems still under investigation. The information resulting from the other activities of this task is presented in four appendices, as follows:

o   Appendix A, Methods for Characterizing Oxide Topography and Chemistry—This is a discussion of the analytical techniques used during Task III.

o   Appendix B, Oxide Structures and Chemistries—This is a discussion of the structure and chemistry of the oxides.

o   Appendix C, Chemical Characterization of Primers—The purpose of this analysis was to chemically characterize the primers. Next, pairs of primers (with and without rubber modifiers) were compared to see if there were differences other than rubber content.

o   Appendix D, Emission Phenomena During Deformation of Materials and During Anodization—This is the final report of the subcontractor.

d. Task IV—Engineering Characterization and Evaluation to Validate Mechanisms of Behavior Defined in Task III

Mechanical testing and failure analysis in this task confirmed the mechanisms defined in Task III. Specifically, the failure mechanism depends on primer or adhesive properties only. Mechanical properties depend on type of test used.

e. Task V—Range of Materials and Environmental Parameters for Acceptable Bonded Joint Performance

This task developed a series of conclusions that will result in improved elevated-service-temperature bonded joints.

6. CONCLUSIONS

Conclusions of the program are:

1. The shear strength of 350°F-curing adhesive systems on PAA is greater than that on FPL. This finding is significant because initial lap-shear testing during this program with thin-adherend lap-shear specimens implied that the converse was true. Because of the high normal stress gradients in thin-adherend lap-shear specimens, the adhesive bond fails in peel and not in shear. Failure analysis of the tested specimens determined that loading of the fracture surface was mode 1. Because of the high normal stress gradients, recommendations have been presented that thin-adherend lap-shear specimens not be used to measure shear strength (ref 19, 21). Our experimental data support this recommendation.

2. It was determined that high-temperature adhesive primers must have good tough-ness and strength if environmental durability is desired. Rubber additives can improve the toughness of epoxy primers. Unfortunately, this addition often results in a loss in shear strength. An example of this is BR-227A. Analysis determined that the rubber additive in BR-227A is incoherent (i.e., the rubber particle functions like a void). On the other hand, the rubber particles in PL-728 are coherent (i.e., there is good mechanical linkage between the rubber particle and the matrix resin). Furthermore, we determined that the matrix resin of PL-728 is ductile. The adhesive primer PL-728 has good durability and shear strength because of the matrix ductility and coherent rubber additive. Conse-quently, a ductile matrix and coherent rubber additive are two good ways to obtain good toughness and high shear strength.

3. The PL-728/PL-729-3 system has greater strength and durability than either the BR-227/FM-61 or BR-227A/FM-61 systems.

15

4. The failure mechanism of BR-227/FM-61 is an interfacial failure between the primer and the phenolic side of FM-61 or a cohesive failure in the phenolic side of FM-61. This is a duplex adhesive, one side of which is an epoxy and the other a nitrile/phenolic. Teamed with other adhesives, BR-227 primed, bonded specimens demonstrated markedly improved shear strength and environmental durability.

5. The model primers, formulated for this investigation, and FM-300 demonstrated excellent shear strength and environmental durability.

7. RECOMMENDATIONS

Recommendations of the program are:

1. There must be industry-wide agreement as to what constitutes the compatibility criterion between 350°F-curing adhesive primers and surface preparations for bonding. Currently, this agreement does not exist. The position taken in this report is that the shear strength, as measured by the thick-adherend lap-shear specimen, is the appropriate criterion. Many bonded assemblies are designed to transfer their load in shear. Other people contend that the shear strength, as measured by the thin-adherend lap-shear specimen, is appropriate. This specimen has a significant normal stress gradient.

2. The controversy concerning testing bonded joints with thin-adherend lap-shear specimens must be resolved. The position taken in this report is that the thin-adherend lap-shear specimen is not a suitable measure of bonded joint shear strength. It is a mixed-mode test that is difficult to interpret.

3. More information is needed to describe how the surface preparation affects the mechanical strength of bonded joints. The shear strength of the 350°F-curing adhesive systems that were tested is greater on PAA than on FPL. When the normal stress gradients present are increased, 350°F-curing adhesive systems have greater strength on FPL than on PAA.

4. This investigation has determined that if 350°F-curing adhesive primers are to possess good environmental durability, they must be tough. However, toughening the system should not result in significant loss of shear strength. Using coherent rubber additives (i.e., those that provide good mechanical linkage between the phase-separated rubber particles and the matrix resin) and/or using ductile matrix resins appear to be two good approaches to obtaining good strength and toughness. It is recommended that these approaches be further developed for 350°F-curing adhesive primers.

16

5. The PL-728/PL-729-3 system is recommended over the BR-227A/FM-61 or BR-227/FM-61 systems. Primer PL-728 has good matrix ductility.

6. Teaming BR-227 with a different adhesive would result in higher strength bonds. This may be productive for some applications. The toughness of the bonded joint would be limited by the low ductility of this primer.

7. The two model primers should be evaluated further as potential new "production" primers. These primers have good strength and durability.

SECTION II
EXPERIMENTAL INVESTIGATION

1. TASK I—SELECTION OF MATERIAL SYSTEMS FOR INVESTIGATION

The material systems evaluated are listed in Tables 3 and 4. These systems represent primers, adhesives, alloys, and surface treatment processes that are commonly used throughout the aerospace industry. Included are both old and new technology systems, and those bonded systems that have exhibited bond-joint performance anomalies when anodic oxide surfaces were present. The use of all these systems in this program was necessary for the successful identification of oxide/primer behavior mechanisms. A more detailed description plus the rationale for selecting each system is given in the following sections.

Table 3. Adhesives and Primers

Item	Primer	Description	Adhesive	Description
1	BR-227	350°F cure modified epoxy primer	FM-61*	350°F cure duplex film adhesive
2	BR-227A*	Same as BR-227 only contains an elastomer		
3	PL-728**	350°F cure modified epoxy with elastomer	PL-729-3**	350°F cure modified epoxy film adhesive
4	BR-238*	350°F cure nitrile/ phenolic primer	BR-238*	350°F cure nitrile/ phenolic film adhesive
5	Modified BR-238*	Same as BR-238, only with the nitrile rubber removed		
6	Model synthetic— 350*	350°F cure epoxy containing no elastomer	FM-300*	350°F cure modified epoxy film adhesive
7	Model synthetic— 350R*	350°F cure epoxy containing elastomer		

*American Cyanamid Company

**B.F. Goodrich Company

Table 4. Aluminum Alloys and Surface Treatment Processes

Alloys	Surface treatment processes
2024-T3-bare	Phosphoric acid anodize per Boeing Specification BAC 5555 (including in-specification and out-of-specification variables)
2024-T3-clad	Optimized FPL etch per Boeing Specification BAC 5514
7075-T6-bare	Chromic acid anodize following two commercially used processes: 1 Fokker process (Netherlands) 2 Bell process per BPS FW 4352, Rev G.

a. Adhesives and Adhesive Primers

(1) Systems 1 and 2—BR-227/FM-61 and BR-227A/FM-61

These primer/adhesive systems, 350°F-curing modified epoxies, had been tested extensively by Boeing on PAA, chromic acid anodized (CAA), and FPL-etched aluminum surfaces (ref 1). FM-61 is the adhesive system designed for use with the two primers BR-227 and BR-227A. FM-61 is a duplex film adhesive supported by a nylon carrier. One side of it is an epoxy film and the other is a nitrile-phenolic film. BR-227 and BR-227A are identical in composition, with the exception that BR-227A contains a nitrile rubber elastomer. Boeing tests had shown a difference in behavior between the two primers on anodized surfaces, with the BR-227A yielding inferior results.

(2) System 3—PL-728/PL-729-3

This system is a 350°F-curing modified epoxy system, but of a different composition than Systems 1 and 2. PL-728 is an elastomer-containing primer that had been tested at Boeing on FPL-etched and PAA surfaces with reduced mechanical test properties when tested on the anodized clad surfaces (ref 3). Independent studies by Schwartz (ref 6) showed premature failures of highly stressed lap-shear specimens in stressed-durability tests.

(3) Systems 4 and 5—BR-238/FM-238 and Modified BR-238/FM-238

BR-238/FM-238 is a nitrile-phenolic system that cures at 350°F. BR-238 is a phenolic-based primer containing a nitrile rubber that is highly soluble in the phenolic matrix.

In contrast, nitrile rubber is less soluble in the BR-227A primer epoxy matrix. The modified BR-238 primer is the same as BR-238, but with the nitrile rubber removed. Because the phenolic matrix resin has different binding properties to the elastomer than do the epoxy resins, the effects of the matrix resin type on behavior can be studied.

(4) Systems 6 and 7—Model Synthetic 350°F-Curing Epoxy Primers/FM-300

Two model synthetic 350°F-curing primers were obtained, with a partial chemical analysis of each supplied by the manufacturer. These primers have a simpler composition than the more complex commercial systems.

b. Aluminum Alloys

Three aluminum alloys—2024-T3 bare, 2024-T3 clad, and 7075-T6 bare—were chosen because of their wide use in structural bonding applications throughout the aerospace industry. Boeing uses 2024-T3 clad and 2024-T3 bare extensively for primary structural bonding, with less emphasis on bonding to 7075-T6 bare. Clad and bare aluminum alloys have different PAA oxide structures. On clad aluminum, the oxide has a regular structure and an open-cell geometry, and is thick. On bare aluminum, the oxide has a less regular structure and an open-cell geometry, and is thin. The PABST program chose 7075-T6 bare for all the bonded YC-15 fuselage test structure (ref 9). Later, 2024-T81 bare was added to the current program at AFWAL's request.

c. Surface Treatment Processes

Because of the many variables involved, the choice of surface treatments and the specific processing parameters were most critical to this program. The structure of the oxides produced by aluminum surface treatment processes varies considerably, depending on the type of process, the conditions within the allowed range of conditions in any given process, and the alloys being processed. As an example, for a specific anodizing condition in PAA, the oxides produced on 2024-T3 clad, 2024-T3 bare, and 7075-T6 bare will all be different in thickness, porosity, and chemistry (ref 10, 11). For a specific alloy, a change in solution temperature will create significant changes in the oxide structure (ref 11). Therefore, for this program, the surface treatment processes and the variations within a given process were chosen with these factors in

mind, since they all affect the interaction with the oxide. The variations were used to synthesize oxides of varying structure.

(1) Phosphoric Acid Anodize (PAA)

This process was developed by Boeing specifically to provide a more durable bond between the oxide and adhesive primer and is described in Boeing process specification BAC 5555 (ref 12). The range of operating parameters determined for BAC 5555 (e.g., voltage, solution temperature, solution concentration, and anodizing time) were established to anodize all the aluminum alloys for Boeing assemblies. Since there are numerous variables in the process that significantly affect the resulting oxide structure, those anodizing parameters selected for this program did include some of the extreme conditions within the operating envelope and some conditions outside of the envelope. Table 5 lists the conditions that were studied.

Table 5. Surface Treatment Process Conditions

Process	Anodize potential (V)	Solution concentration	Solution temperature ($^\circ$F)	Process time (min)
Phosphoric acit anodize (BAC 5555)	5 10 15	H_3PO_4 11% (wt)	67 72 77	20
Bell chromic acit anodize	40	Chromic acid 6% (wt)	95	30
Fokker chromic acit anodize	40 with 50 at finish	Chromic acid 6% (wt)	95	40
Optimized FPL etch (BAC 5514)	—	30 parts H_2o 10 parts H_2SO_4 2 parts $Na_2Cr_2O_7$ + 2024 aluminum	155	15

All preanodizing conditions remained constant and consisted of an alkaline clean rinse, a 10-minute etch at room temperature in deoxidizer (Amchem 6-16), rinse, and anodize. All postanodizing conditions also were constant. Delay time simulated typical production conditions of about 1.5 minutes, rinsing was spray, and drying was at 140°F.

22

(2) Chromic Acid Anodize (CAA)

Two CAA processes were used, each representing years of service on aircraft and helicopters (table 5). The Bell process has been used for many years in the manufacture of bonded helicopter blades. This process also was evaluated, along with PAA, under Air Force Contract F33615-74-C-5065 (ref 3). The process was conducted in accordance with Bell process specification BPS FW 43-52, Revision G, Method 1A (ref 13). The process consists of a typical 40V CAA, but includes post-treatment sealing consisting of a hot, dilute chromic acid solution (approximately 100 ppm CrO_3).

The Fokker process has been used for many years for primary structural bonding of the Fokker F-27 and F-28 (Fokker-VFW Company, the Netherlands) (ref 14). The critical ingredients of this process are an FPL-type pre-etch, followed by a 40V anodize in chromic acid that is completed by increasing the voltage to 50V over a period of 5 minutes and by a subsequent hold at 50V for another 5 minutes. There is no post-treatment sealing.

Each of these CAA processes produce oxides with distinctly different characteristics, which in turn are different than those produced by PAA (ref 11).

(3) Optimized FPL Etch

The optimized FPL etch is a slight modification of the FPL etch used industry-wide for over 20 years. In 1972-73, Boeing optimized the process by changing some of the critical chemical species in the etch solution. These changes, coupled with a durability test (process control wedge test), made the process more consistent and reliable (ref 15). This process was used as a baseline process.

d. Screening Tests

The initial screening tests evaluated the alloys, surface preparations, and adhesive systems listed in Table 6. Group A represents the two adhesive/primer systems that have shown abnormal behavior either in ultimate lap-shear strengths or in stressed-durability tests (ref 1, 6). Therefore, we felt that a screening test, including four surface treatment processes and two methods of primer application, was necessary to establish the relative behavior of these two adhesive systems. Boeing studies of BR-227A have shown that the method of primer application (e.g., spray versus flow

23

coating) can influence the behavior of adhesive-bonded joints. Therefore, both application techniques were included. Group B provided comparative information to determine similarities or dissimilarities between Systems 2 and 3 and the other five systems.

Table 6. Matrix for Screening Tests

Group	Aluminum alloy	Surface preparation *	Adhesive/primers	Primer application
A	2024-T3 bare 2024-T3 clad 7075-T6 bare	FPL etch (reference) PAA 50-volt chromic acid anodize (Fokker)	FM-61/BR-227A (system 2) PL-729-3/PL-728 (system 3)	Spray Curtain coating
B	2024-T3 bare 2024-Te clad 7075-T6 clad	PAA	FM-61/BR-277 (system 1) FM-238/BR-238 (system 4) FM-238/BR-238 modified (system 5) FM-300/model primer (system 6) FM-300/model primer (system 7)	Spray

*Processing parameters will follow nominal specification parameters.

Based on the previous testing, it was decided to use the thin-adherend lap-shear specimen. The specimen configuration is illustrated in Figure 8.

The lap-shear tests were run; results are listed in Table 7. These data are significantly lower than those reported by Schwartz (ref 6). The shear strength data for BR-227/ FM-61 and BR-227A/FM-61 on optimized FPL etch and PAA reported herein are generally somewhat lower than the data reported by Marceau (ref 1).

With the exception of those specimens incorporating the two model primers, BXR-MSR and BXR-MSNR, almost all specimens exhibited a slick, potentially interfacial failure mode, with only a few specimens exhibiting mixed failure modes. This failure phenomenon seems to be independent of alloy, surface treatment, and method of primer application. The failure modes of those specimens containing the two model primers appeared to be primer/adhesive oriented and independent of alloy and primer rubber content. A look at the lap-shear ultimate shear strengths suggests some

24

Table 7. Room-Temperature Lap-Shear Ultimate Strengths

	Surface treatment	Adhesive/primer system	Primer application method	Shear lb/in² (average of 5)					
				7075-T6 bare	Apparent* failure mode	2024-T3 bare	Apparent* failure mode	2024-T3 clad	Apparent* failure mode
A	Optimized FPL etch	FM-61/BR-227A	Spray	2274	A	2092	A	2341	A
		FM-61/BR-227A	Roll coat	2886	A/C 90%	**	**	2312	A
		PL-729-3/PL-728	Spray	3666	A	3357	A	3374	A
		PL-729-3/PL-728	Roll coat	3911	A	3749	A	3566	A
	Phosporic acid anodize (PAA)	FM-61/BR-277A	Spray	2416	A	2286	A	2220	A
		FM-61/BR-227A	Roll coat	2301	A	2642	A/C 80%	2344	A/C 85%
		PL-729-3/PL-728	Spray	3594	A	3408	A	2513	A
		PL-729-3/PL-728	Roll coat	3594	A	3316	A	2430	A
	Chromic acid anodize (Bell)	FM-61/BR-227A	Spray	2560	A/C 80%	2660	A	2802	A/C 80%
		FM-61/BR-227	Roll coat	2660	A	2464	A/C 95%	2656	A/C 95%
		PL-729/PL-728	Spray	3568	A	3355	A	3038	A
		PL-729/PL-728	Roll coat	3126	A	3326	A	2676	A
	Chromic acid anodize (Fokker)	FM-61/BR-227A	Spray	1936	A	2668	A	2364	A
		FM-61/BR-227A	Roll coat	2704	A/C 95%	2956	A/C 90%	2737	A
		PL-729-3/PL-728	Spray	2048	A	2632	A	2300	A
		PL-729-3/PL-728	Roll coat	2918	A	2810	A	2352	A
B	Phosporic acid anodize	FM-61/BR-227	Spray	2669	A/C 50%	2838	A/C 20%	2714	A
		FM-238/BR-238	Spray	2836	A/C 90%	3102	A/C 90%	2278	C
		FM-238/BR-238 NR	Spray	1492	A	868	A	4267	C
		FM-300/BXR-MSR	Spray	4440	C	3808	A/C 40%	3718	A/C 70%
		FM-300/BXR-MSNR	Spray	4054	A	3375	A	3492	A

* A: slick, adhesive-appearing failure
  C: obvious cohesive failure within the adhesive or primer
  A/C: mixed A and C, (%) indicates amount of A

** Voids in bondline—data invalid

25

interaction with alloy and surface treatment. Comparison of data representing the two methods of primer application (i.e., spray and roll coat) shows variable results. In most cases, the trend seems to be higher shear strengths with roll coating of the primers for FPL etch, PAA, and Fokker CAA, whereas the trend is for lower shear strengths with Bell CAA. However, the visual appearance of the failure modes does not suggest any such trend.

e. Series B Tests

Because of the generally low ultimate lap-shear strengths of these specimens and the possibility of an interfacial failure, Boeing and the Air Force technical monitor agreed to rerun a portion of the Task I screening test. The experimental matrix for the partial retest of the screening test is listed in Table 8. The retest of the Task I screening test is identified as the Series B lap-shear test.

Table 8. Matrix for Lap-Shear Test—Series B

Alloy	Surface preparation	Primer/adhesive	Primer application
7075-T6 Bare	PAA FPL	BR-227A/FM-61 PL-728/PL-729-3	Spray Flow
2024-T3 Bare	PAA FPL	BR-227A/FM-61 BR-227/FM-61 PL-728/R-729-3 BXR-MSR/FM-300 BXR-MSNR/FM-300	Spray Flow
2024-T3 Clad	PAA FPL	BR-227A/FM-61 PL-728/PL-729-3	Spray Flow
2024-T81 Bare	PAA FPL	BR-227A/FM-61 BR-227/FM-61 PL-728/PL-729-3 BXR-MSR/FM-300 BXR-MSNR/FM-300	Spray Flow

Note: Stress lap-shear testing was performed on 2024-T3 and -T81 bare only

26

Application of the primer was accomplished by two methods: (1) using the standard spray method with pressurized air, and (2) flowing the primers over the cleaned aluminum surfaces from a container. The flow application was accomplished by pouring the primers from a suitable container (e.g., a small can or cup) onto the inclined surface of the aluminum panels. Excess BR-227A primer was removed using a doctor blade with a large enough gap to leave a dry film thickness of approximately 2 mils. This procedure was necessary because of the high viscosity of the primer. It was not necessary to use the doctor blade for those panels with the PL-728 primer, since excess primer was not a problem due to its low viscosity. Efforts were made during the refabrication of specimens to reduce the bondline thickness when using FM-61 adhesive. One layer of positioning fabric was used during the fabrication of panels for the Series B tests in an effort to increase the bondlines of the other adhesives by a few mils.

Lap-shear data from the Series B tests are shown in Table 9. Again, the failure modes visually appeared to be mostly slick, potentially interfacial failures, but for the most part had respectable shear strengths. This is a puzzling situation, particularly since the failure modes of the optimized FPL etch specimens are as bad as, if not worse than, those of the PAA specimens. In the Series B tests, an attempt was made to increase the bondline thicknesses of the PL-728/PL-729-3 bonded specimens. These bondline thicknesses were 3 to 6 mils in the initial tests. As shown in Table 9, the bondline thicknesses were increased (in two cases, excessively—up to 22 mils) for those specimens bonded to 2024-T81 bare alloy. However, the failure modes appeared the same whether the bondline was thin or thick.

The following observation was made of the failure modes related to the BR-227/FM-61 and BR-227A/FM-61 systems. In the Series B tests, the epoxy and phenolic sides of FM-61 adhesive film were noted on the lap-shear specimens. When the bond was made using BR-227A primer (rubber containing), the failure modes were predominately slick, potentially interfacial failures. The adhesive-appearing failure was always to the epoxy side and, if any cohesive failure was evident, it was always to the phenolic side. Likewise, when BR-227 primer was used, the same pattern existed except that cohesive failures were more predominant. More cohesive failure was apparent in specimens prepared with PAA.

The "anomalies" associated with lap-shear failure modes from Task I were discussed with the Air Force project monitor. Points in question were: surface treatments out

Table 9. Room-Temperature Lap-Shear Ultimate Strengths—Series B Test

Surface treatment	Adhesive or primer system	Primer application method	7075-T6-bare (5 spec) (1)	(2)	(3)	2024-T3-bare (5 spec) (1)	(2)	(3)	2024-T3-clad (5 spec) (1)	(2)	(3)	2024-T81-bare (5 spec) (1)	(2)	(3)
Optimized FPL etch	FM-61/BR-227A	Spray	2,952	A	21–25	2,832	A	14–18	2,748	A	12–17	2,352	A/C 95%	13–17
	FM-61/BR-227A	Flow	2,228	A/C 60%	14–15	2,612	A	18–24	2,652	A	15–22	2,776	A	15–18
	FM-61/BR-227	Spray				2,744	A/C 60%	10–15				2,940	A/C 25%	10–13
	FM-61/BR-227	Flow				2,868	A/C 40%	15–17				2,864	A/C 40%	12–14
	PL-729-3/PL-728	Spray	2,560	A	5–9	2,590	A	6–12	2,740	A	6–10	2,224	A	15–21
	PL-729-3/PL-728	Flow	3,612	A/C 95%	6–10	3,280	A/C 60%	7–11	3,032	A/C 85%	6–10	2,360	A	11–21
	FM-300/BXR-MSNR	Spray				4,200	A/C 20%	7–8				4,812	A/C 95%	6–7
	FM-300/BXR-MSNR	Flow				3,752	A/C 80%	7–9				4,404	A/C 95%	5–7
	FM-300/BXR-MSR	Spray				764	A	5–6				1,130	A	4–7
	FM-300/BXR-MSR	Flow				2,224	A	6–7				4,440	A/C 95%	4–7
PAA	FM-61/BR-227A	Spray	2,980	A	11–15	2,820	A/C 90%	14–18	2,640	A	14–16	2,820	A	14–15
	FM-61/BR-227A	Flow	2,124	A	18–22	2,456	A	18–22	2,508	A	19–22	2,720	A	16–18
	FM-61/BR-227	Spray				2,900	A/C 20%	10–14				2,780	A/C 10%	10–18
	FM-61/BR-227	Flow				2,684	A/C 10%	15				2,700	C	16
	PL-729-3/PL-728	Spray	2,720	A	8–11	2,868	A	6–10	2,592	A	11–12	2,100	A	20–22
	PL-729-3/PL-728	Flow	3,440	A/C 85%	11–12	3,304	A/C 95%	6–10	2,980	A	11–12	2,716	A	13–22
	FM-300/BXR-MSNR	Spray				4,376	A/C 5%	6–7				4,672	C	4–8
	FM-300/BXR-MSNR	Flow				3,988	A/C 45%	6–7				4,408	A/C 10%	5–9
	FM-300/BXR-MSR	Spray				4,340	A/C 20%	5–7				4,900	A/C 25%	5–7
	FM-300/BXR-MSR	Flow				4,084	A/C 25%	6–7				4,620	A/C 15%	4–7

(1) Shear (lb/in²)

(2) Apparent failure mode
  A: Slick adhesive-appearing failure
  C: Obvious cohesive failure within the adhesive or primer
  A/C: Mixed A and C; (%) indicates amount of A

(3) Bondline thickness (mil)

28

of specification, alloys, deficient primer properties, primer thickness, bondline thickness, test method, environment (humidity), primer application, out-of-specification adhesive film and contamination. Most of these items were ruled out with the following rationales:

1. **Surface Treatment Out of Specification**—Chemistry and procedure were checked, but nothing out of specification was apparent. Day-to-day variations should not have been a factor, since many different processing days were represented and several months separated the initial tests from the Series B tests. In addition, the optimized FPL etch had demonstrated normal performance with 250°F-curing adhesive/primer systems.

2. **Alloys**—There were four alloys involved—2024-T3, 2024-T81 bare, 2024-T3 clad (1230 alloy), and 7075-T6 bare—which made it unlikely that each alloy would respond in the same way, particularly when several distinctly different surface treatments were used.

3. **Deficient Primer Properties**—Six of the seven primers were made up by American Cyanamid on a special order. The seventh primer was purchased from B.F. Goodrich as an off-the-shelf item. It does not seem likely that primers from two different manufacturers would have similar deficiencies. The two best performing primers were the model primers, BXR-MSR and BXR-MSNR, supplied by American Cyanamid.

4. **Primer Thickness**—Primer thicknesses (as measured by Isometer and Permascope) varied from a few tenths of a mil for PL-728, BXR-MSR, and BXR-MSNR to several mils for BR-227 and BR-227A. All primers exhibited a slick, adhesive-appearing failure mode even within thickness variations of each primer.

5. **Bondline Thicknesses**—Although some bondlines were thicker than optimum (some as thick as 22 mils), this does not seem to have had much influence on the slick, adhesive-appearing failure mode. This was illustrated by the PL-728/PL-729-3 system when increased bondline thicknesses were attempted in the Series B tests. Most bondlines were increased from 3-5 mils to 6-10 mils with some 20+ mils; however, failure modes were the same in all cases.

6. **Test Method**—During the initial test, specimens were found to be tested slightly off center (i.e., loaded nonaxially), thus causing a slight torque or twist on the bondline. This was corrected in the Series B test, but the failure mode situation did not change.

7. **Environment**—The environmental conditions during surface treatment and priming were considered and subsequently monitored for the Series B tests.

Humidity was always less than 40% RH and temperature was always between 72 and 74°F.

8. **Primer Application**—Three methods of primer application were used: spray, roll coating, and manually flowing the primers over the surfaces. All three techniques exhibited the same slick-type failure modes.

9. **Out-of-Specification Adhesive Film**—Whenever failure modes were cohesive or predominantly cohesive, lap-shear strengths were always as expected. Even many of the slick failures had respectable strengths. All slick-type failures were either primer-oriented or oxide-oriented, which is not a function of the film adhesive.

10. **Contamination**—This could have been a possibility. However, much bonding work not associated with this program goes through the same laboratory, but using different adhesive/primer systems, and these systems have not exhibited similar problems. Therefore, contamination did not seem to be a likely cause.

Since an explanation was not readily apparent, the approach was to concentrate on Task III to help get a better understanding of the primer/oxide relationship. This approach, coupled with failure mode analyses, provided a basis for the design of subsequent tests.

2. TASK II—POSTULATION OF CANDIDATE MECHANISMS OF BEHAVIOR

Although redundant, the candidate failure mechanisms will be restated here for purposes of continuity. The entire content of Task II is a statement of these mechanisms.

Schwartz proposed that some primers—particularly those that contain elastomers—do not totally penetrate the thick, porous columnar PAA oxide, resulting in a zone of unimpregnated oxide that is weak in shear. When the joint is loaded in shear, the unsupported oxide fails (ref 6) (see fig. 3).

Marceau proposed that the high-molecular-weight rubbers in rubber-modified adhesive primers could not penetrate the porous PAA oxide, whereas the lower molecular weight components could. This would result in an elastomer-rich zone above the thick PAA oxide. The elastomer-rich zone can function as a weak boundary layer (ref 1) (see fig. 4).

Marceau proposed a second mechanism, illustrated schematically in Figure 5, that would probably operate in conjunction with his first mechanism. This mechanism postulates that premature failures do not occur until the oxide fractures, thus creating stress risers in the primer at these points. Thick oxides produced by anodizing break into larger pieces than do thin oxides, such as produced by FPL etch, thereby creating zones of higher stresses at these points of oxide fracture. These stresses, coupled with a thin, weak boundary layer of polymer just at the oxide surface, can cause premature failure (ref 1).

A fourth mechanism was proposed in Boeing technical proposal for this investigation. According to this hypothesis, primers that contain elastomeric additives may undergo excessive deformation during long-term loading. This loading might fracture an unstabilized, anodic, porous oxide.

During Task III, two other failure mechanisms were proposed to explain the mechanical properties of these adhesive systems. These mechanisms will be discussed in Section II.3.

3. TASK III—EXPERIMENTAL INVESTIGATION TO DEFINE MECHANISMS OF BEHAVIOR

The discussion of the Task III investigation has been organized functionally. This investigation has been divided into the following facets:

1. Oxide/primer/adhesive interactions
2. Stress-durability testing
3. Failure analysis
4. Discussion of failure mechanisms

The information resulting from the other activities of this task is presented in four appendices, as follows:

o   Appendix A, Methods for Characterizing Oxide Topography and Chemistry—This is a discussion of the analytical techniques used during Task III.

o   Appendix B, Oxide Structures and Chemistries—This is a discussion of the structure and chemistry of the oxides.

o   Appendix C, Chemical Characterization of Primers—The purpose of this analysis was to chemically characterize the primers. Next, pairs of primers (with and

31

without rubber modifiers) were compared to see if there were differences other than rubber content.

o   Appendix D, Emission Phenomena During Deformation of Materials and During Anodization—This is the final report of the subcontractor.

a. Oxide/Primer/Adhesive Interactions

The main purpose of this study was to obtain a fundamental understanding of the structural characteristics of bonded joint components and their interactions. The primary impetus behind this study was the possible interfacial failures of PL-728 or BR-227A primers on PAA oxides. Prior to these analyses, both poor primer penetration into the oxide and elastomeric segregation had been hypothesized to account for these failures.

The subsequent analyses proved to be very successful; both oxide/primer penetration and ultrastructural behavior were illustrated. These results showed oxide/primer penetration in every case. Additionally, these analyses showed that elastomeric modification can be structurally recognized and that, as yet, no unusual elastomeric segregation has been recognized at the oxide/primer interface. However, the duplex film adhesive FM-61 was shown to exhibit some interfacial adhesive/adhesive and primer/adhesive segregations.

(1) Primer/Oxide Interactions

The oxide/primer zone interactions and structural characteristics were analyzed using a wide variety of techniques and analysis methods. The primer/oxide zone was studied by: (1) polished/etched specimens analyzed by SEM/STEM instrumentation, (2) fractured specimens analyzed by SEM/STEM instrumentation, and (3) thin, microtomed sections analyzed by SEM/TEM instrumentation. Table 10 summarizes the various oxide/primer combinations, as well as the various techniques used in each case. FPL oxide interactions were not examined owing to their small size and apparent system compatibility.

The general advantages and relative disadvantages of each technique are shown in Table 11, as reported in reference 20. Each technique can be seen to provide a unique, yet complementary, view of the primer/oxide interface. In each case, the oxide, the primer, and, upon closer inspection, the relative wetting and penetration of the primer

Table 10. Oxide/Primer Combinations Analyzed by Various Analytical Techniques

Oxide/Alloy		Primer				
		BR-227	BR-227A	PL-728	BXR-MSR	BXR-MSNR
PAA	2024-T3 clad	TEM/ section	SEM/ fracture TEM/ section	SEM/ fracture	SEM/ fracture	SEM/ fracture
PAA	2024-T3 bare		SEM/ polish	SEM/ fracture		
PAA	2024-T81 bare			SEM/ fracture		
PAA	7075-T6 bare			SEM/ fracture		

Table 11. Summary of Analytical Methods and Procedures

Specimen preparation	Analytical instrument	Regions analyzed	Max plate magnification	Comments
Polish/ etch	Optical micro	Oxide/ primer	1500X	Weak in this area, SEM/STEM preferred
Polish/ etch	Optical micro	Primer/ adhesive	1500X	Good within mag range
Polish/ etch	SEM/STEM	Oxide/ primer	50,000X	Polishing artifacts possible. Preferential attack by etchant
Polish/ etch	SEM/STEM	Primer/ adhesive	50,000X	Generally quite good with restriction of polishing artifacts
Fractured	SEM/STEM	Metal/ oxide	200,000X	Excellent provided coating procedure acceptable
Fractured	SEM/STEM	Oxide/ primer	200,000X	Lacks good detail. Intrinsic to analysis
Fractured	SEM/STEM	Primer/ adhesive	200,000X	Not usually informative
Thin section	TEM/STEM	Metal/ oxide	200,000X	Can be excellent. Artifacts due to sectioning of unsupported oxide
Thin section	TEM/STEM	Oxide/ primer	200,000X	Excellent method
Thin section	TEM/STEM	Primer/ adhesive	200,000X	Excellent method

33

into the oxide are recognizable. However, the primer ultrastructure, and any subsequent segregations, can only be seen by TEM/microtomy or, in certain instances, by SEM polishing and etching techniques. Although in each case artifacts were produced, these are recognizable, particularly within the multianalytical approaches used.
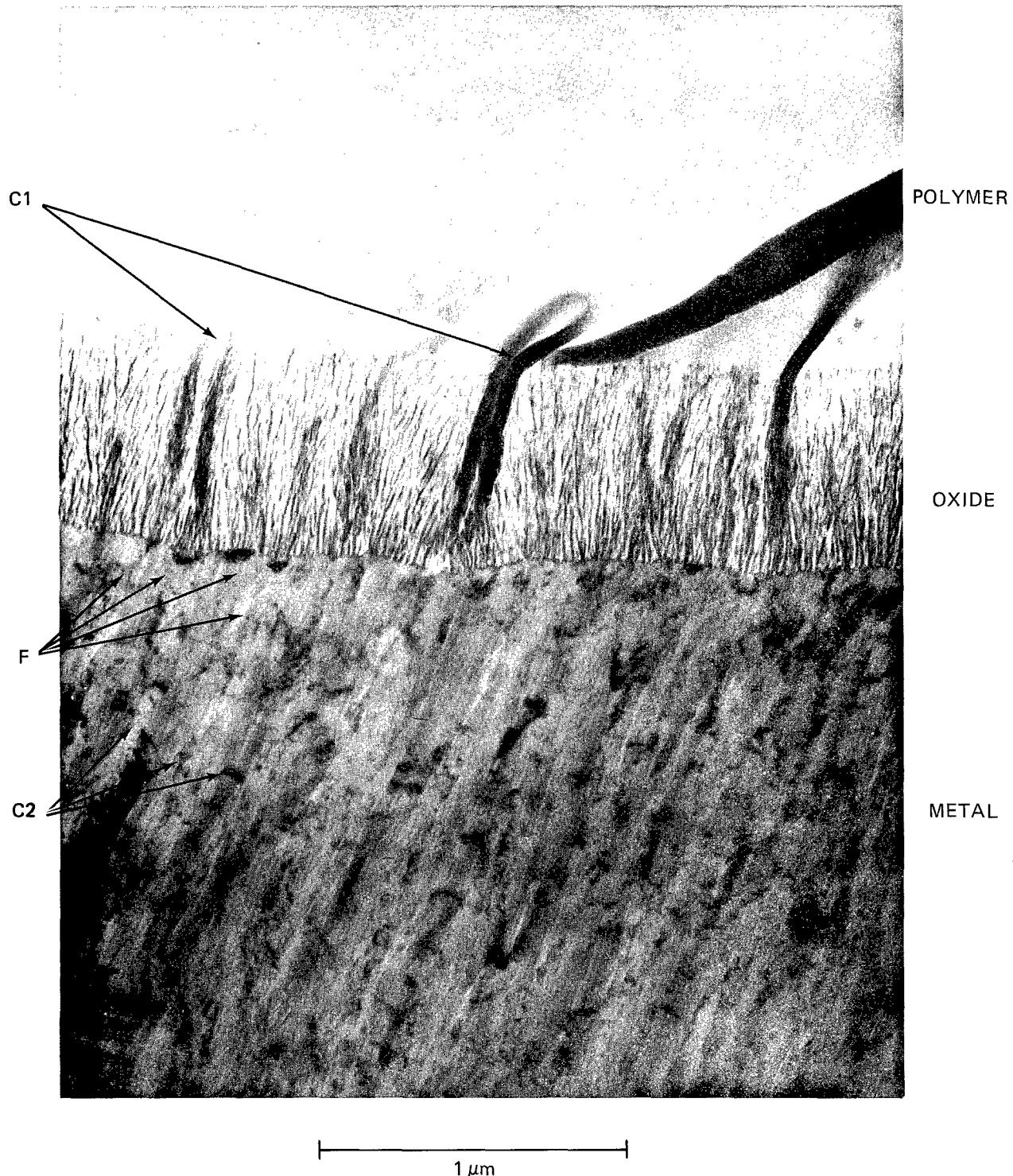
(2) PAA 2024-T3 Clad/BR-227 Interactions

The oxide/primer component interactions as revealed by TEM/microtomy are illustrated in Figures 9 and 10. The primer itself appears homogeneous and continuous. Although actual primer penetration cannot be seen in these TEM/ microtomy sections, penetration is suggested by the overall continuity of the oxide/ primer interface, as well as the apparent oxide stabilization during sectioning.

Further complementary results were provided by SEM/fracture analysis (fig. 11). Oxide/primer pentration is suggested by the filled-in appearance of the oxide structure when compared to oxide characterizations (fig. B-1). Additionally, both primer continuity and oxide wetting are evidenced.

Electron energy loss spectroscopy (EELS) gives information on the light elements present in a thin specimen of material. The sample is penetrated by an electron beam in a transmission electron microscope. The primary beam energy is reduced by interaction with the atoms of the specimen. For a single reaction event, the loss in energy is characteristic of the target atom, and the ΔE (incident minus transmitted energy) can be used to determine the composition of the specimen. The method is particularly useful for determination of the light elements. The results appear in the form of a spectrum displaying the number of counts per ΔE interval versus ΔE. Although the method can be semiquantitative, only qualitative analyses were performed on these samples.

The EELS technique was used on samples of 2024-T3 clad PAA with BR-227 primer and with BR-227A primer. The analysis was performed in a scanning transmission electron microscope with EELS attachment. Transmission specimens were prepared of the samples on a supporting mesh of formvar/carbon. EELS analysis was performed on a region of the specimen over a hole so that no signal was contributed by the supporting film. Analysis was performed at the regions shown in Figure 10. Position 1 is on polymer alone, and a carbon peak only was obtained on the EELS spectrum. Oxygen is believed to be in the primer also, but at concentrations too low for detection under the

34

- C1 represents compression artifacts in the polymer.
- C2 represents compression artifacts in the metal.
- F represents brittle metal fracture artifacts.

Figure 9. Transverse View of 2024-T3-Clad PAA with BR-227 Primer

35

PRIMER

OXIDE

MET...

1	C
2	C + O
3	C + O
4	C + O
5	C + O
6	O
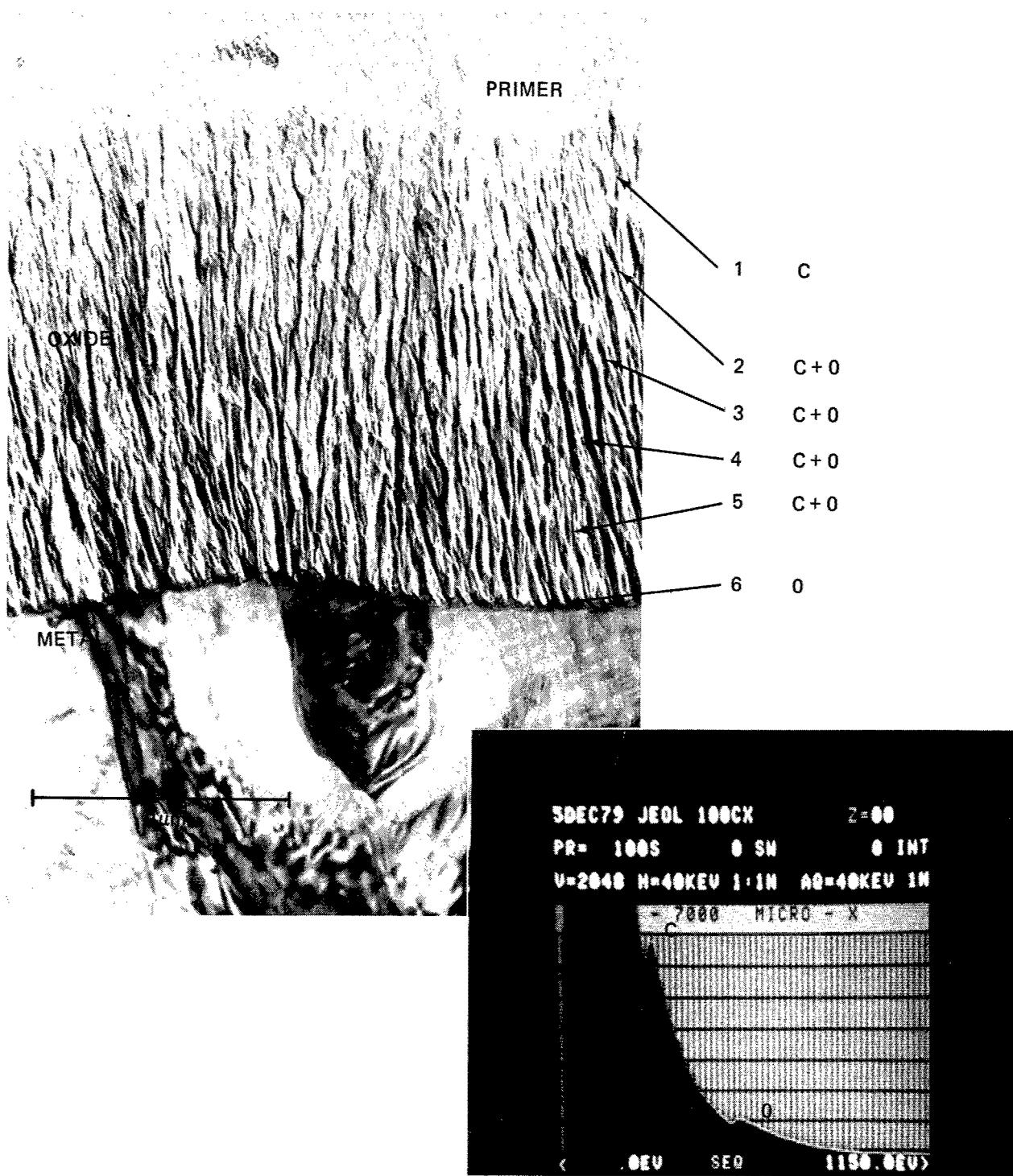
Figure 10. TEM Photomicrograph of a Thin Section of 2024-T3-Clad PAA with BR-227 Primer, Inset is an EELS Spectrum from Region 3

36
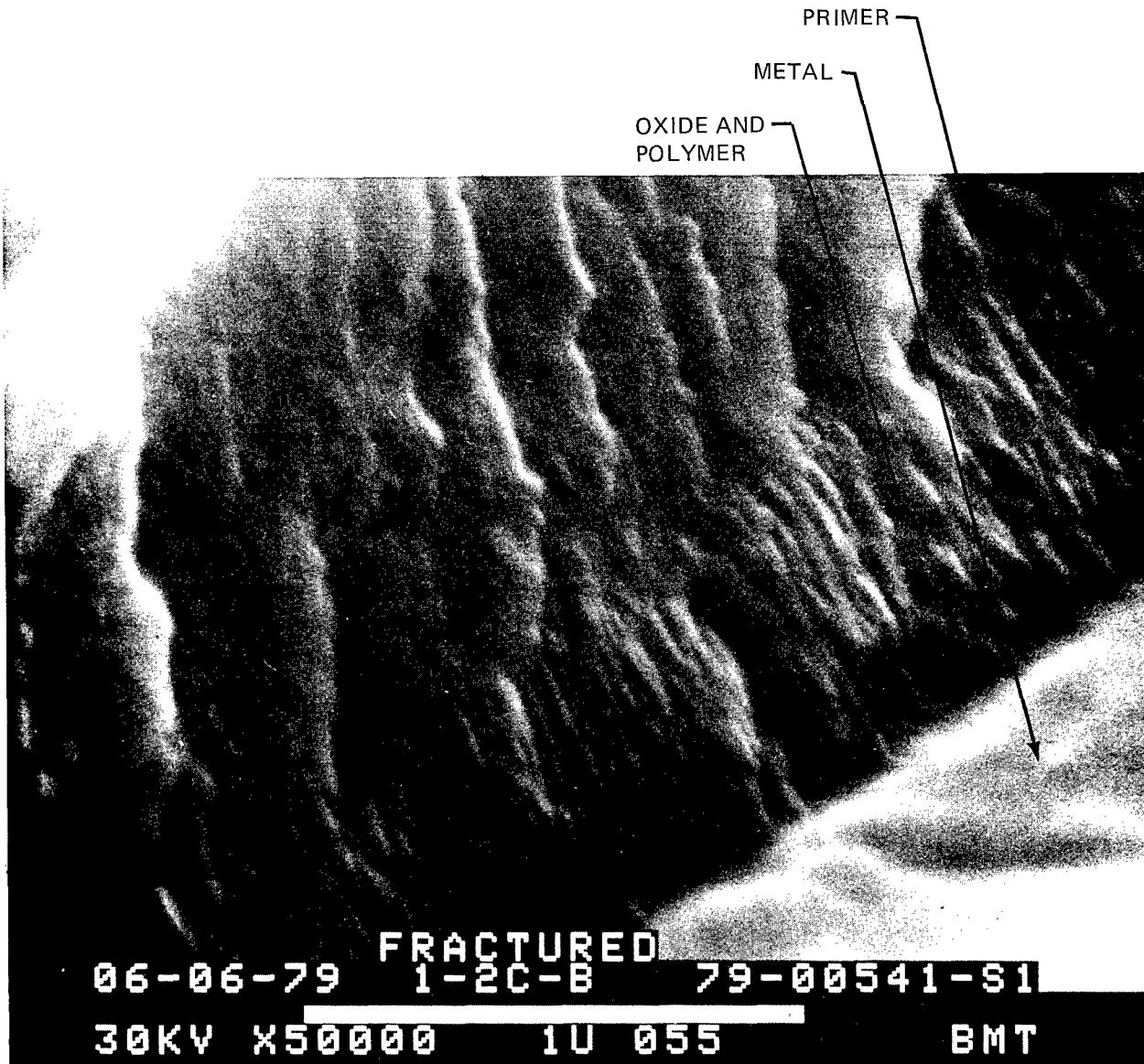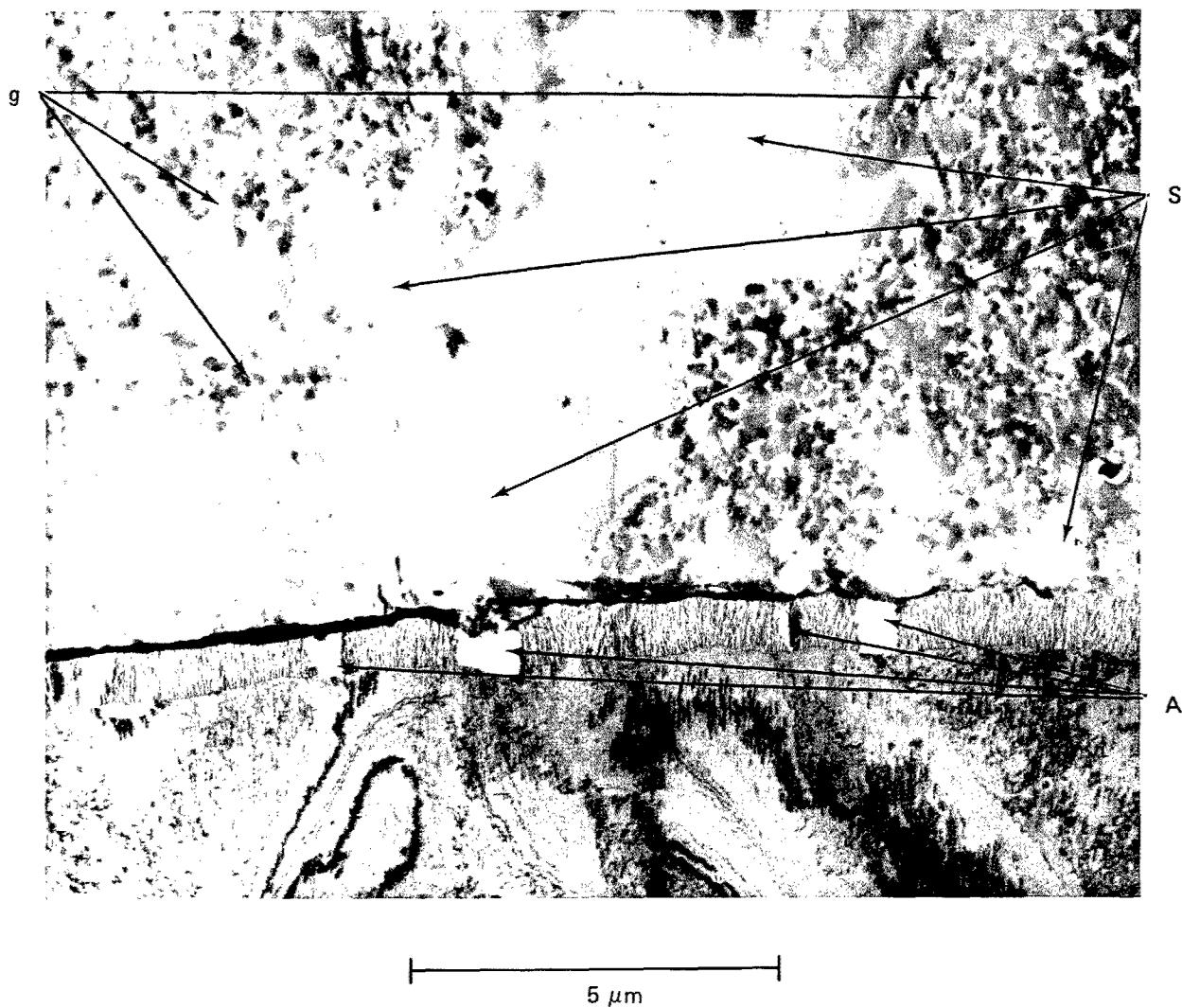
Figure 11. Transverse View of 2024-T3-Clad PAA with BR-227 Primer

experimental conditions employed. Positions 2 through 5 are at increasing depths into the oxide cell layer. At all of these positions, carbon and oxygen peaks were found. The oxygen peak is due to the oxide. Position 6 is on the oxide base plate region and showed oxygen alone. It can be concluded that the carbon peaks occurring in positions 2 through 5 are due to polymer, since the oxide alone gives only an oxygen peak. The polymer, therefore, has been shown to penetrate to the base of the oxide cell layer. No aluminum peak is shown because it is off the scale of the spectrometer display under the experimental conditions employed.

(3) PAA 2024-T3 Clad/BR-227A Interactions

The oxide/primer component interactions as revealed by TEM/microtomy are illustrated in Figure 12. Clear inhomogeneities can be seen in the primer, particularly in comparison to BR-227. The primer has inclusions (S) lacking the appearance of the surrounding matrix (M). The granular structures seen are primarily of two types: (1) larger, smooth granules up to $1\,\mu m$ in diameter, and (2) smaller, darker granules about $0.1\,\mu m$ in diameter. This particular ultrastructure would appear to be characteristic of the elastomeric modification in BR-227A. The primer is thought to contain more than one elastomer, which may be responsible for the various finer microstructures.

5 μm

- S represents smooth regions in primer.
- g represents granular regions in primer.
- A represents sectioning artifacts.

Figure 12. Transverse View of 2024-T3-Clad PAA with BR-227A Primer

38

Additional photomicrographs taken at higher magnifications reveal evidence of polymer penetration into the oxide cell layer in the regions of sectioning artifacts. In Figure 13, the oxide has torn during sectioning and at least two examples of necked polymer can be seen clearly. Additional supportive evidence can be seen in Figure 14, where entrapped bubbles within the oxide are highly suggestive of polymer penetration.

Figure 15 shows SEM photomicrographs of 2024-T3 clad PAA with BR-227A primer. Again, continuity is shown between the primer and the oxide layer, indicating primer penetration of the oxide. Ths process is shown in more detail in Figure 16. This photomicrograph also shows elastomeric stretching of the primer coat during the fracturing process for SEM specimen preparation.
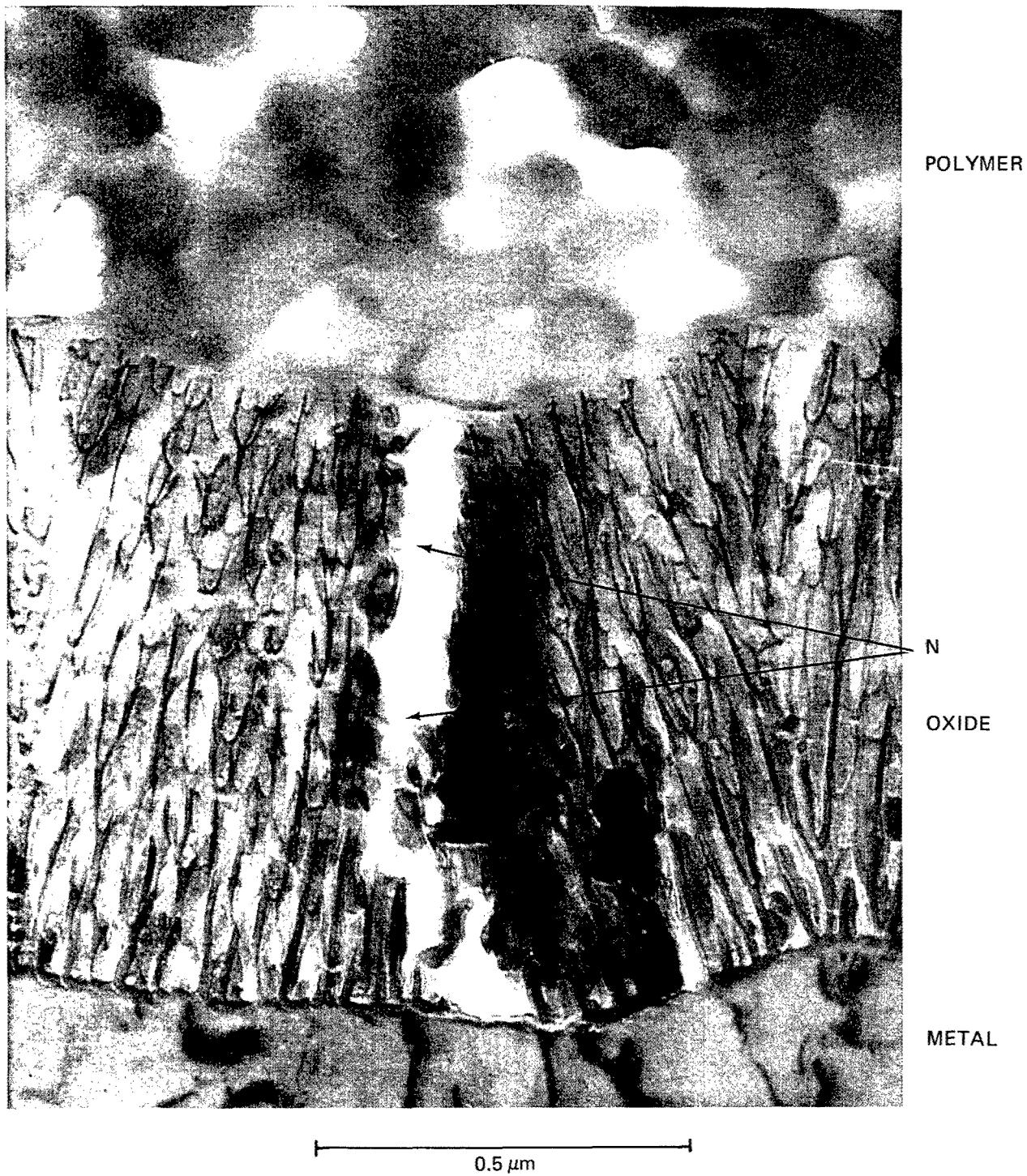
An EELS analysis also was performed on microtomed transverse sections of PAA 2024-T3 clad/BR-227A in an attempt to verify oxide/primer pentration. Regions for analysis were chosen in a manner similar to that for Figure 10. Again, the primer was shown to have a carbon peak only, while the oxide base plate exhibited an oxygen peak only. Positions within the oxide, however, exhibited both carbon and oxygen peaks. It can be concluded, therefore, that oxide/primer penetration also has occurred for BR-227A.

(4) PAA 2024-T3 Clad/PL-728

The primer/oxide interactions as revealed by SEM/fracture techniques are shown in Figures 17 and 18. Primer penetration is evidenced by the filled-in appearance of the oxide structure under both thin and thick primer application coats. Although PL-728 contains elastomeric additives, no topographical electron microscopy data were found by SEM/fracture techniques that would indicate any preferential segregation. One of the most likely topographical features for preferential segregation of the elastomeric components with this technique would be a "stretching-out" of the elastomer between islands of fractured oxides as reported previously for a BR-227A elastomer-containing primer (fig. 16). The fact that the oxide was fractured in LN_2 may account for this lack of elastomer stretching-out between oxide islands.
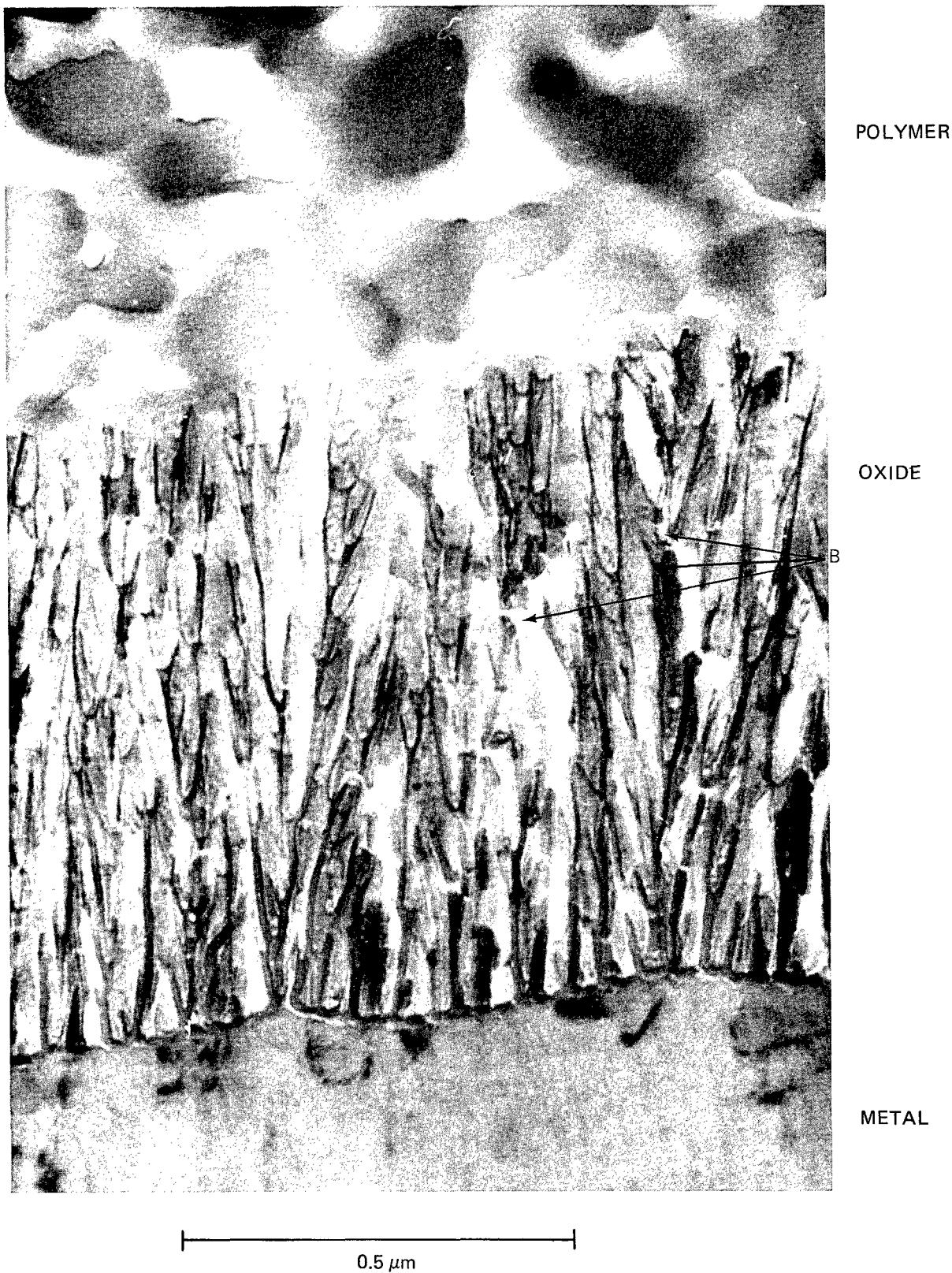
(5) PAA 2024-T3 Clad/BXR-MSR and BXR-MSNR

The primer/oxide interactions for the BXR-MSR elastomer-containing primer and the

POLYMER

N

OXIDE

METAL

0.5 μm
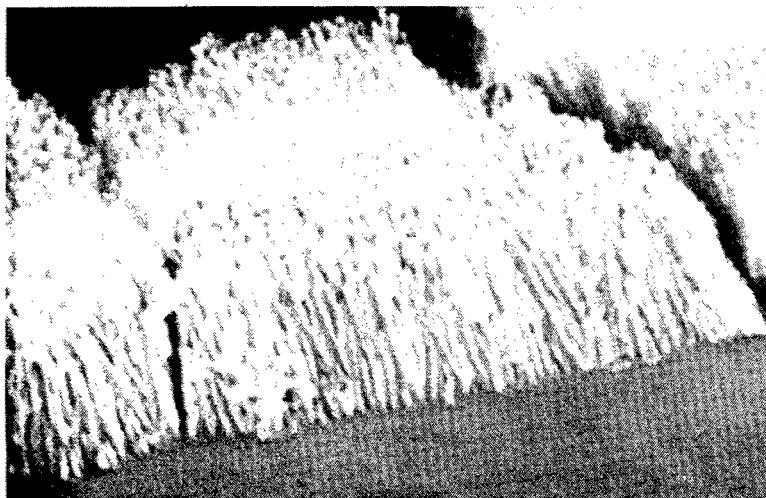
● Polymer necking (N) occurs at position of rear in oxide layer caused by sectioning.

Figure 13. Transverse View of 2024-T3-Clad PAA with BR-227A Primer

POLYMER

OXIDE

B

METAL

0.5 μm
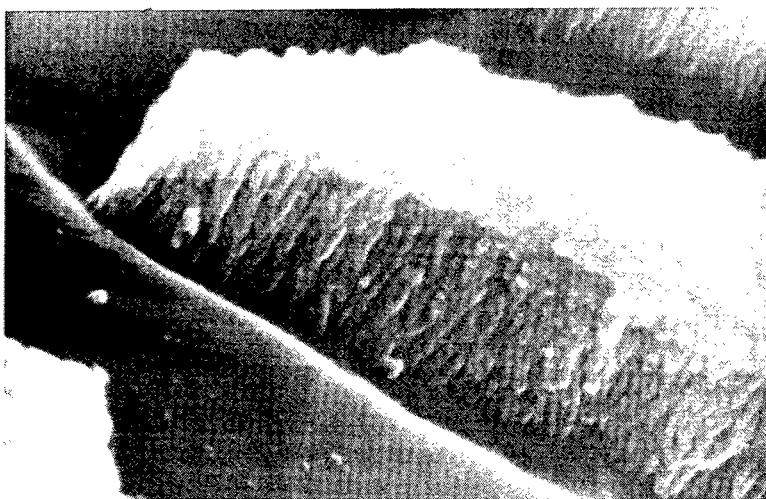
● Air bubbles (B) occur in oxide layer where penetrating primer has not completely wetted oxide cell walls.
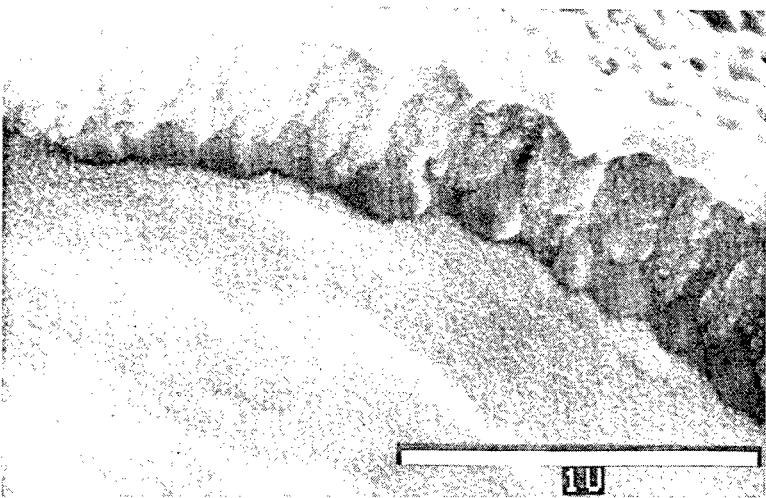
Figure 14. Transverse View of 2024-T3-Clad PAA with BR-227A Primer

41

OXIDE WITHOUT PRIMER

THIN PRIMER

THICK PRIMER

Figure 15. SEM Photomicrographs of PAA on 2024-T3-Clad Coated with
BR-227A Primer

42
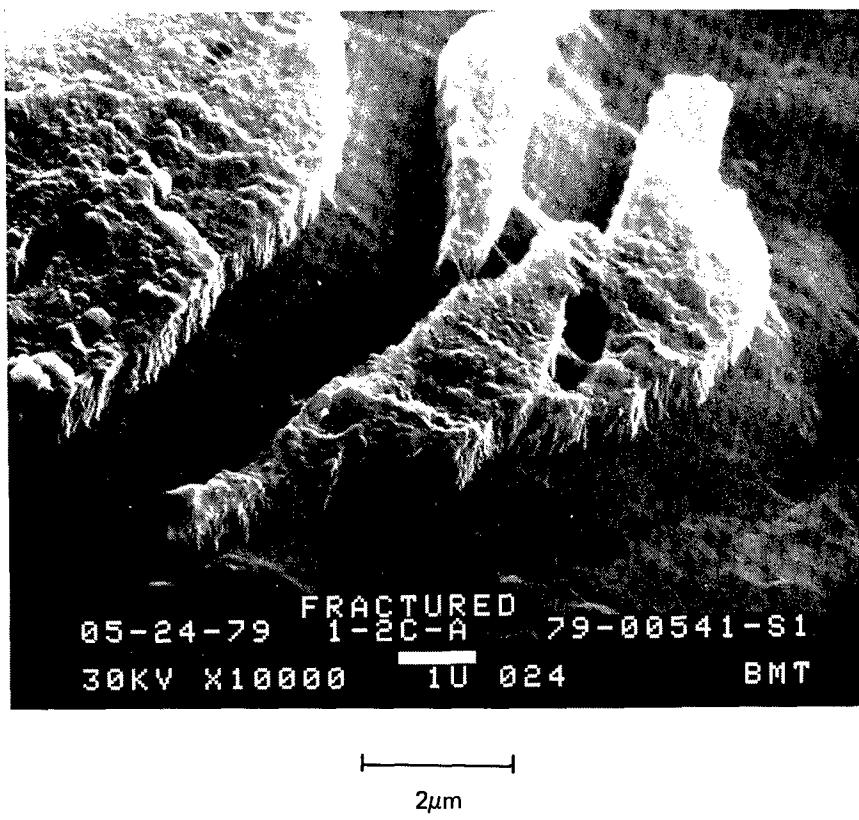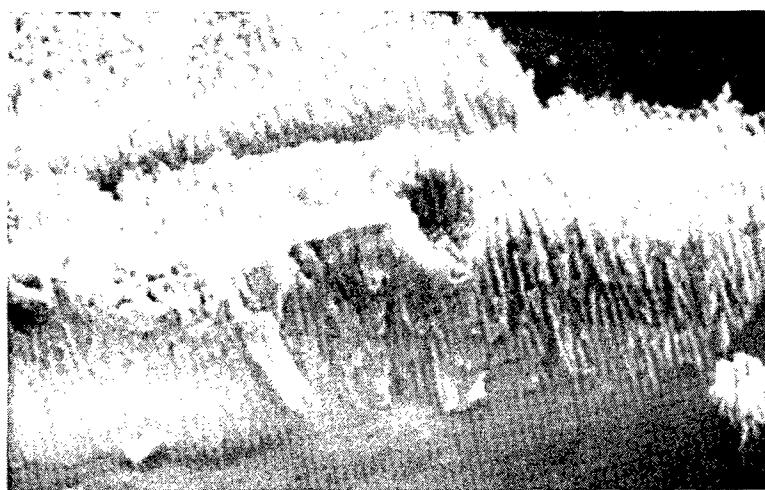
Figure 16. SEM Photomicrograph of PAA on 2024-T3-Clad Coated with BR-227A Primer
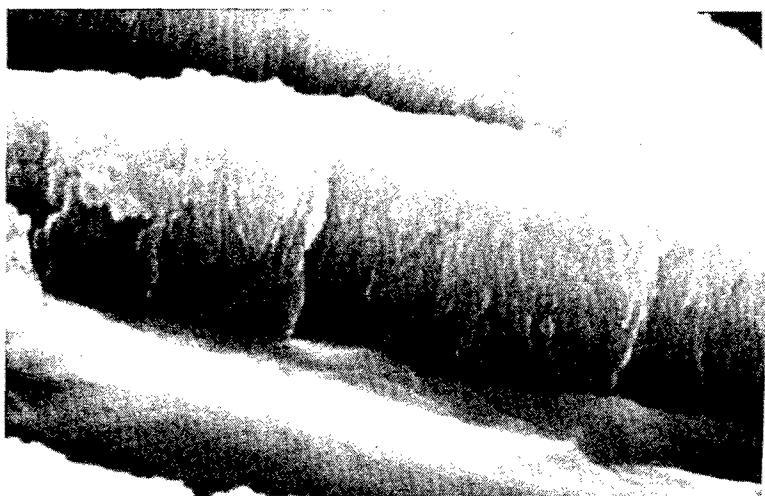
BXR-MSNR non-elastomer-containing primer on 2024-T3 clad are shown in Figures 19 and 20. These primers appear to have partially infiltrated the porous oxide. No significant difference was observed between the elastomer- and non-elastomer-containing primers. However, as discussed previously, this may be only a consequence of the preparation and analysis technique used.

(6) PAA 2024-T3 Bare/BR-227A
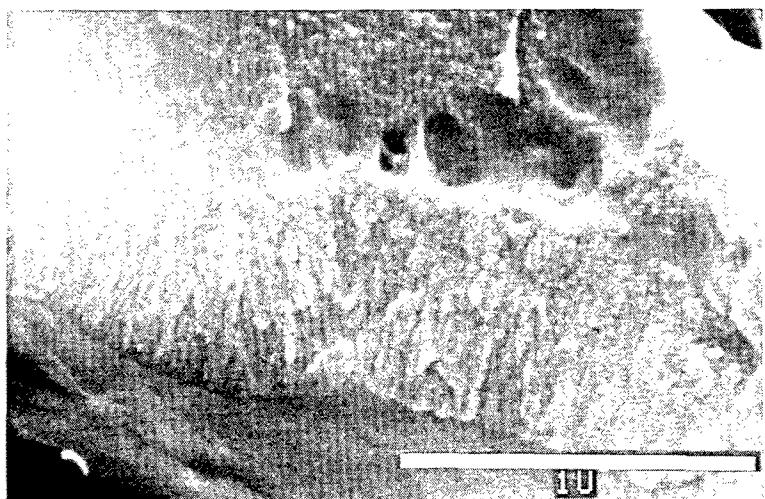
The BR-227A oxide/primer interactions with PAA 2024-T3 bare as viewed by SEM/polish and etch techniques are illustrated in Figure 21. The photomicrograph is supportive of the previous TEM/microtomy work performed on 2024-T3 clad aluminum. Here, too, the heterogeneous nature of the primer layer can be seen, although no evidence of segregation is visible. Additionally, oxide/primer penetration can be seen, as evidenced by the thin polymer link remaining where the oxide has been pulled away from the base alloy.

OXIDE WITHOUT PRIMER
(PRIMER IN THE LEFT HAND
SIDE PHOTOGRAPH)
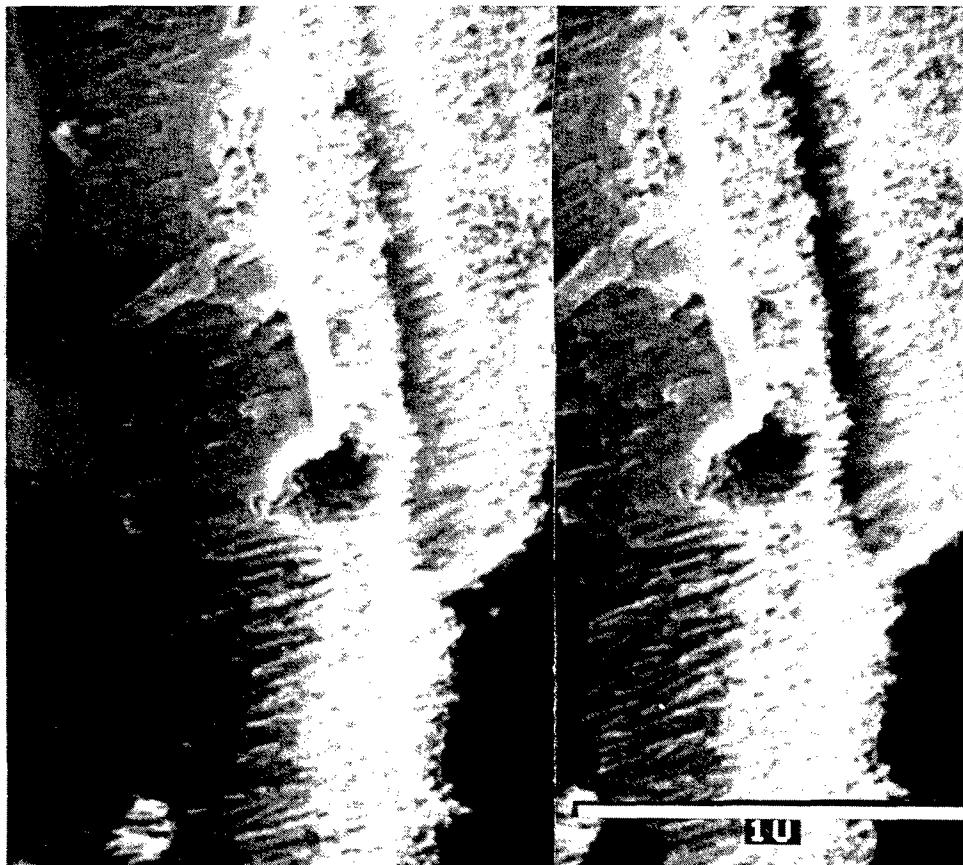
THIN PRIMER

THICK PRIMER

Figure 17. SEM Photomicrographs of PAA on 2024-T3-Clad Coated with PL-728 Primer

STEREO PAIR OF FRACTURED OXIDE. (PRIMER IN TOP
LEFTHAND CORNER OF PHOTOGRAPH)
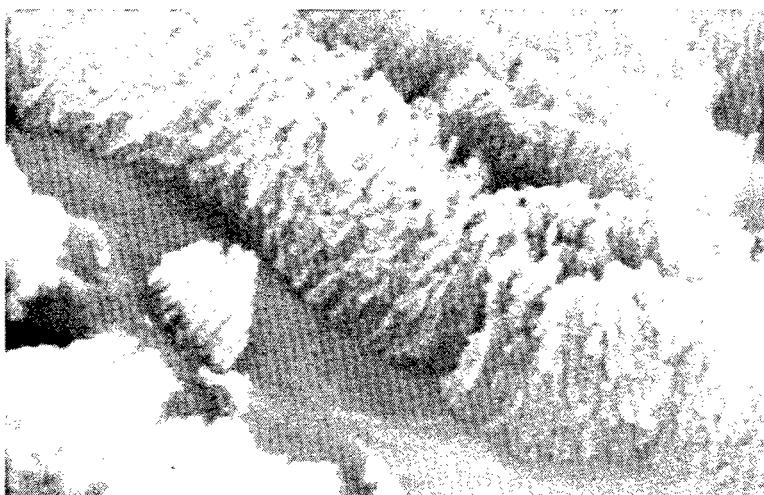
*Figure 18. SEM Photomicrograph of PAA on 2024-T3-Clad
Partially Coated with PL-728 Primer*

(7) PAA 2024-T3 Bare/PL-728
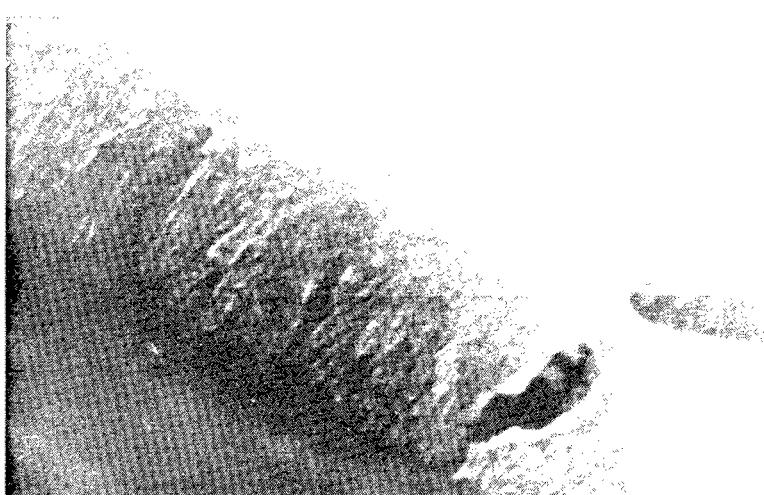
The primer/oxide interactions as revealed by SEM/fracture techniques are shown in
Figure 22. Primer penetration is evidenced by the filled appearance of the oxide
structure. Although PL-728 contains elastomeric additives, no morphologies that
would suggest any such modification were found. However, the fact that the oxide
was fractured in LN_2 may account for the lack of any visible elastomeric modifi-
cation.

(8) PAA 2024-T81 Bare/PL-728
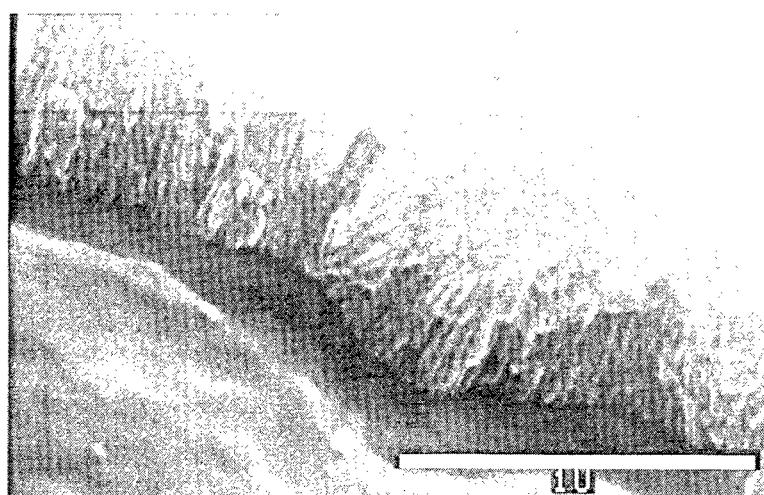
Figure 23 illustrates the primer penetration of oxide as viewed by SEM/fracture
techniques. Primer penetration again is clearly evidenced by the apparently filled
appearance of the oxide structure. No evidence of elastomeric modification was

45

OXIDE WITHOUT PRIMER
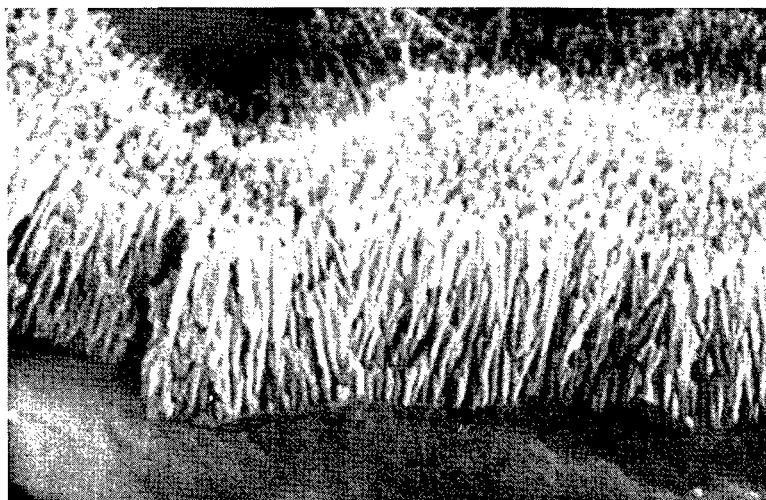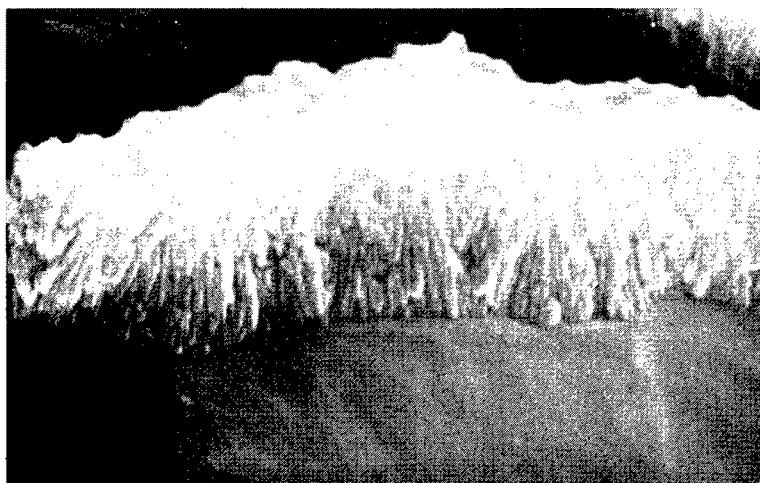
THIN PRIMER
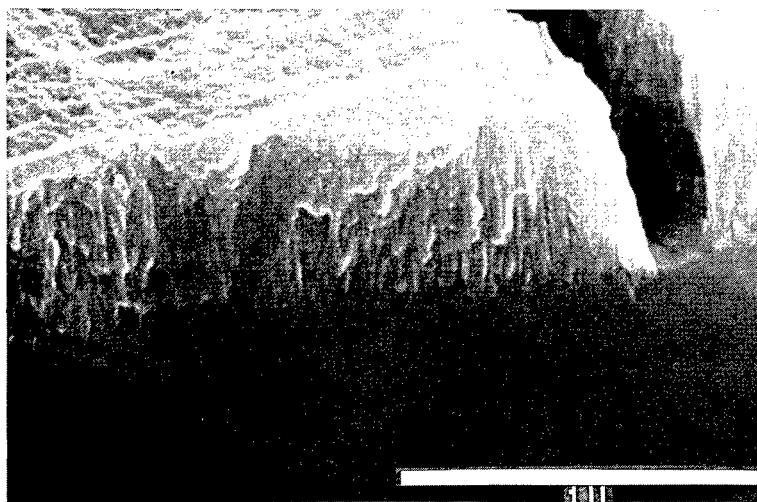
THICK PRIMER

Figure 19. SEM Photomicrographs of PAA on 2024-T3-Clad Coated with BXR-MSR Primer

46

OXIDE WITHOUT PRIMER

THIN PRIMER

THICK PRIMER

Figure 20. SEM Photomicrographs of PAA on 2024-T3-Clad Coated with BXR-MSNR Primer

30KV X27000   1U 000   BMT

├────────────┤

1 μm
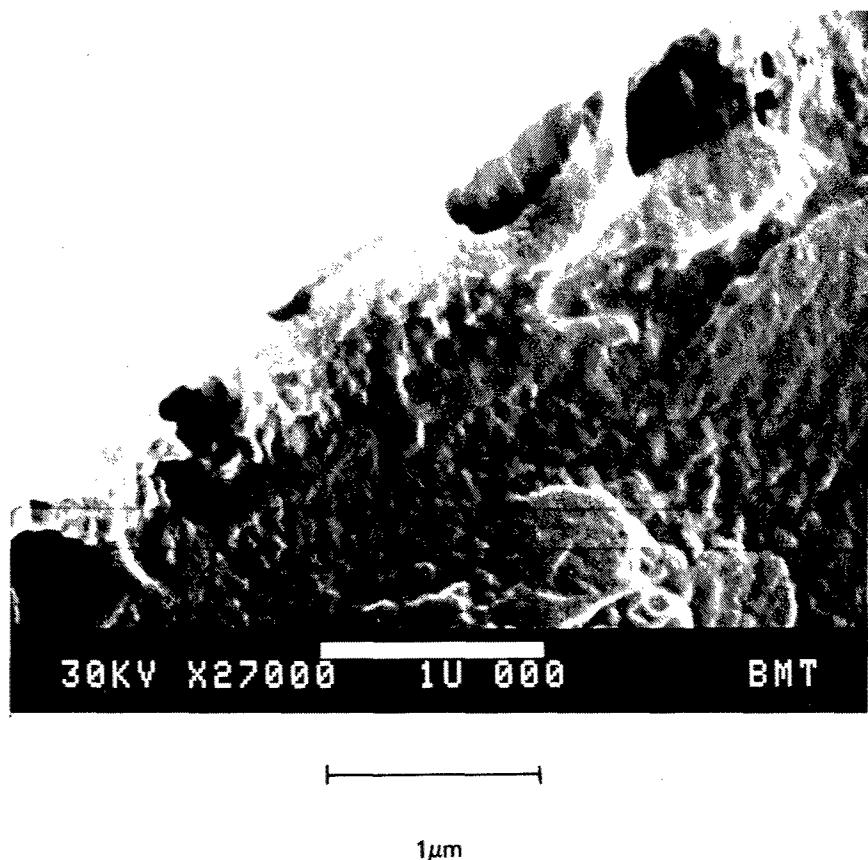
*Figure 21. SEM Photomicrograph of 2024-T3-Bare PAA Coated with BR-227A,
Polished/Etched*
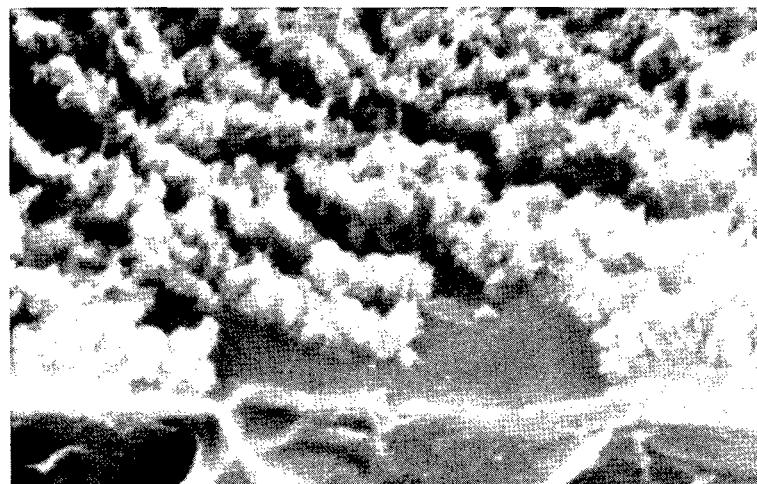
observed. However, as pointed out earlier, fracturing in LN_2 may prevent elastomeric stretching.

(9) PAA 7075-T6/PL-728
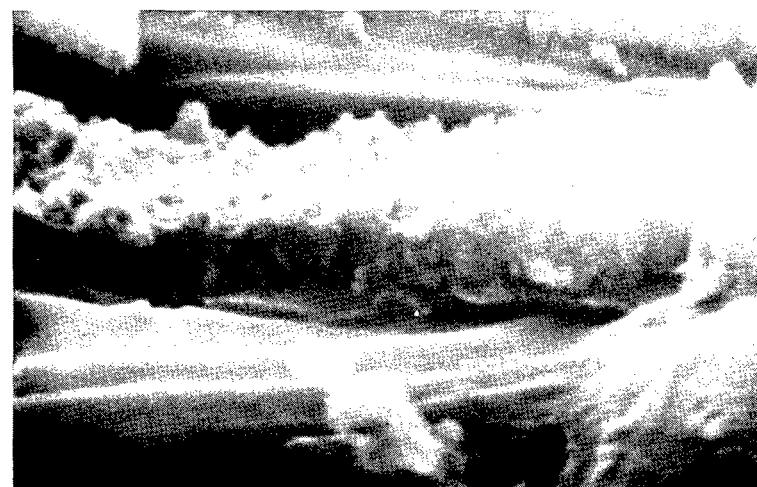
Figure 24 illustrates the oxide penetration as viewed by SEM/fracture techniques. Despite the differing alloy, primer penetration again is evidenced by the apparently filled oxide structure. Again, no evidence of elastomeric modification and/or segregation is observable.

(10) BR-227 and BR-227A/FM-61 Interactions

BR-227 and BR-227A primer interactions with FM-61, as well as FM-61's duplex nature, have been studied using both TEM/microtomy and SEM/polish and etch techniques. No segregated features were observed by either technique for BR-227

48

OXIDE WITHOUT PRIMER
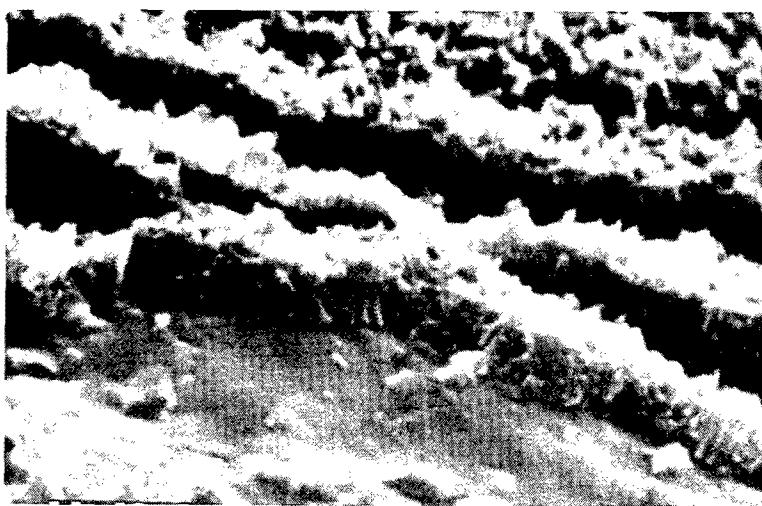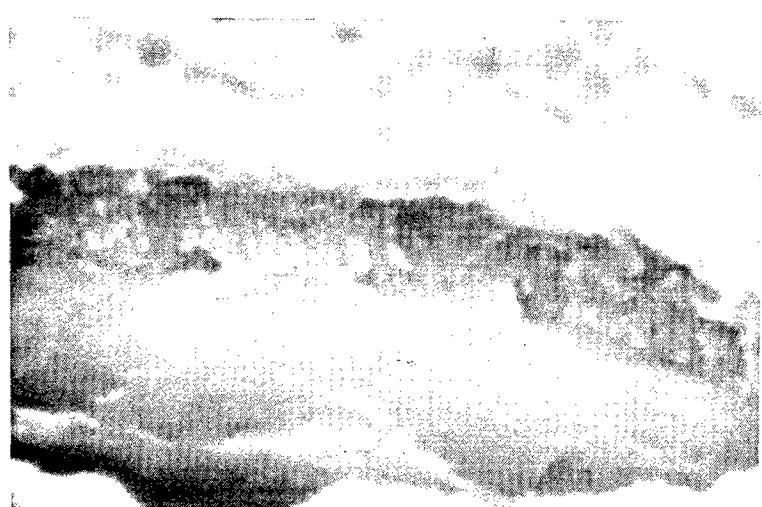
THIN PRIMER
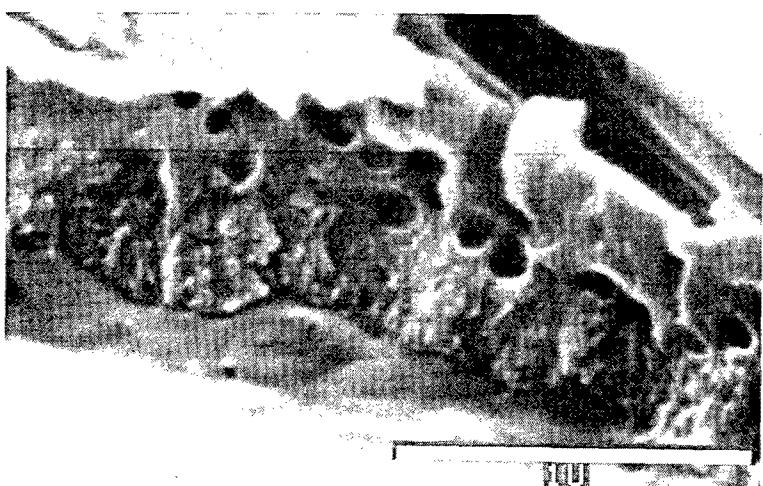
THICK PRIMER

Figure 22. SEM Photomicrographs of PAA on 2024-T3-Bare Coated with PL-728 Primer

49

OXIDE WITHOUT PRIMER
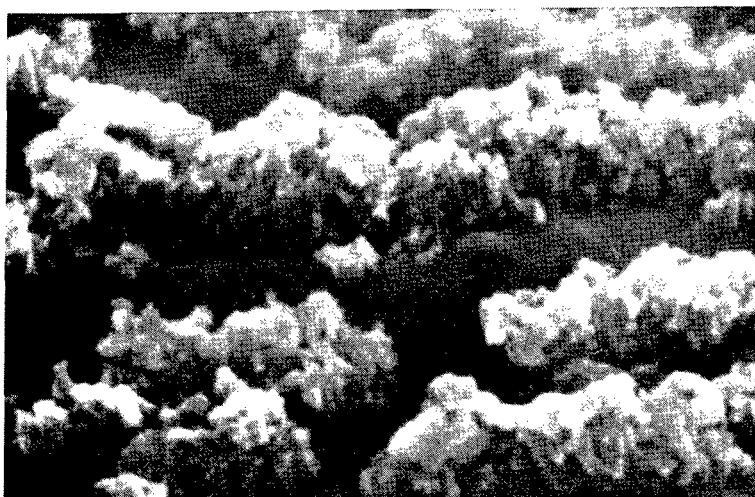
THIN PRIMER ON
RIGHTHAND SIDE
(NO PRIMER ON
LEFT)

THICK PRIMER
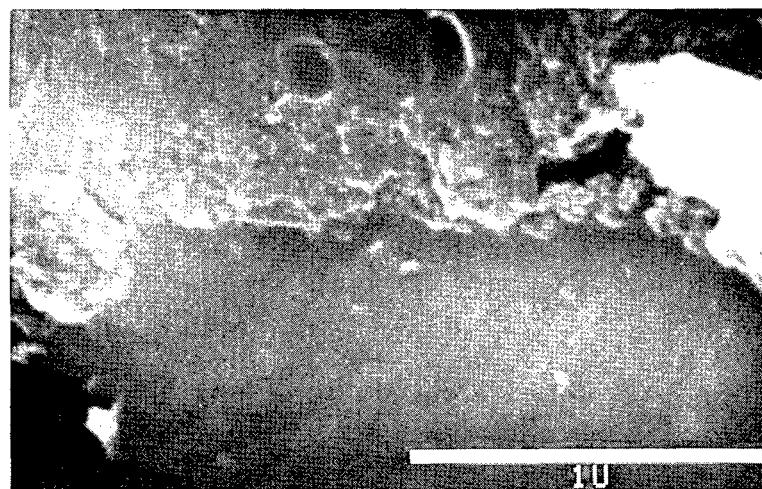
Figure 23. SEM Photomicrographs of PAA on 2024-T81-Bare Coated with
PL-728 Primer

50

OXIDE WITHOUT PRIMER

THIN PRIMER

THICK PRIMER

*Figure 24. SEM Photomicrographs of PAA on 7075-T6-Bare Coated with
PL-728 Primer*

primer/adhesive interfaces. However, both BR-227A and the epoxy and phenolic sides of FM-61 exhibit discrete second-phase reinforcement and segregated layers.

The SEM/polish and etch photomicrograph in Figure 25 and the TEM/microtomy photomicrograph in Figure 26 both illustrate the existence of a segregated layer between the BR-227A primer and the epoxy side of FM-61. SEM/polish and etch and TEM/microtomy photomicrographs, Figures 27 and 28, illustrate an apparently similar layer between the FM-61 nitrile-phenolic and epoxy layers. No segregating layers were found between BR-227A and the nitrile-phenolic side of the FM-61, or with any of the BR-227/FM-61 interfaces. At this point, it is unclear which layer is forming these segregating layers.

10μm
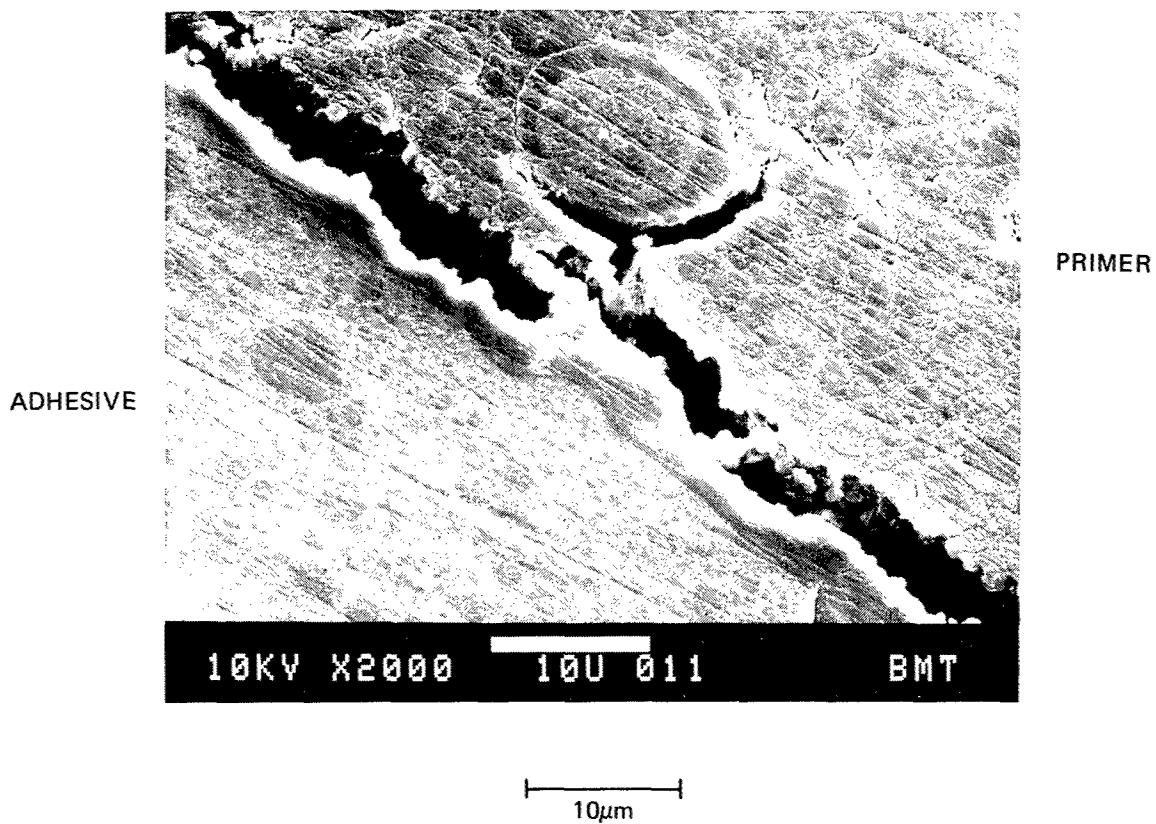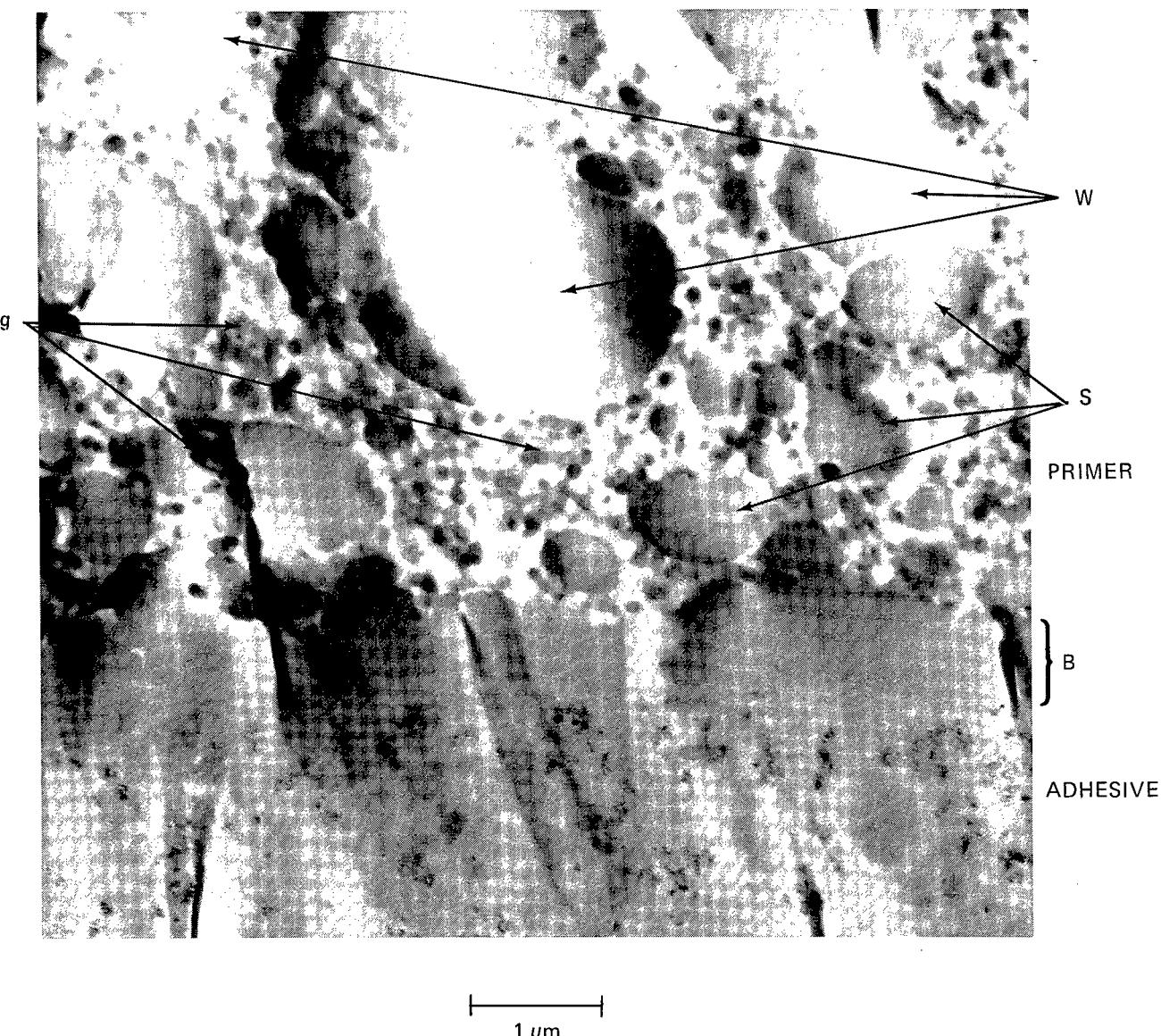
Figure 25. SEM Polish/Etch Photomicrograph of the Boundary Between BR-227A Primer and the Epoxy Side of FM-61 Adhesive

52

W .... W

S .... S

PRIMER

B

ADHESIVE

|← 1 μm →|

- W represents areas of artifact where the polymer has torn during sectioning.
- S represents smooth regions in the primer.
- g represents granular regions in the primer.
- B is the boundary regions between primer and adhesive.

Figure 26. Interface Region Between BR-227A Primer and Epoxy Side of FM-61 Adhesive

PHENOLIC

EPOXY

10KV X5000 10U 010 BMT

|← 5 μm →|
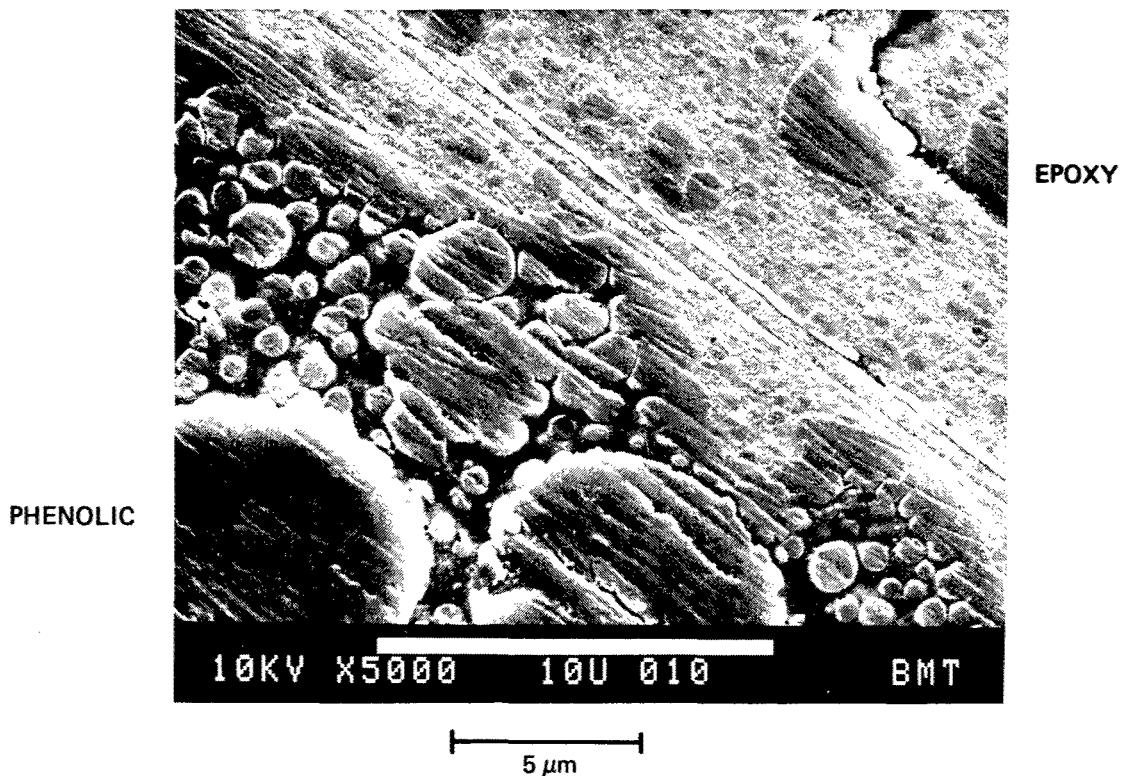
Figure 27. Boundary Between Nitrile-Phenolic and Epoxy Layers of FM-61

(11) Summary

Use of SEM/fracture, TEM/microtomy, and SEM/polish and etch techniques has greatly enhanced our understanding of both the oxide and the primer structures, as well as their interactions. These techniques have demonstrated that:

1. Every primer studied exhibits relatively good wetting and continuity on PAA oxide structures.

2. The more closely studied BR-227A and BR-227 primers exhibit excellent oxide penetration.

3. The elastomer-modified BR-227A has a recognizable ultrastructure suggestive of discrete elastomeric modification; however, no significant evidence has yet been discovered that suggests the existence of any segregating layers at the oxide surface, other than possible preclusion of large, elastomeric constituents with BR-227A primers.

4. Boundary segregated layers have been observed at both the BR-227A/FM-61 epoxy interface and the FM-61 phenolic/FM-61 epoxy interface.

54
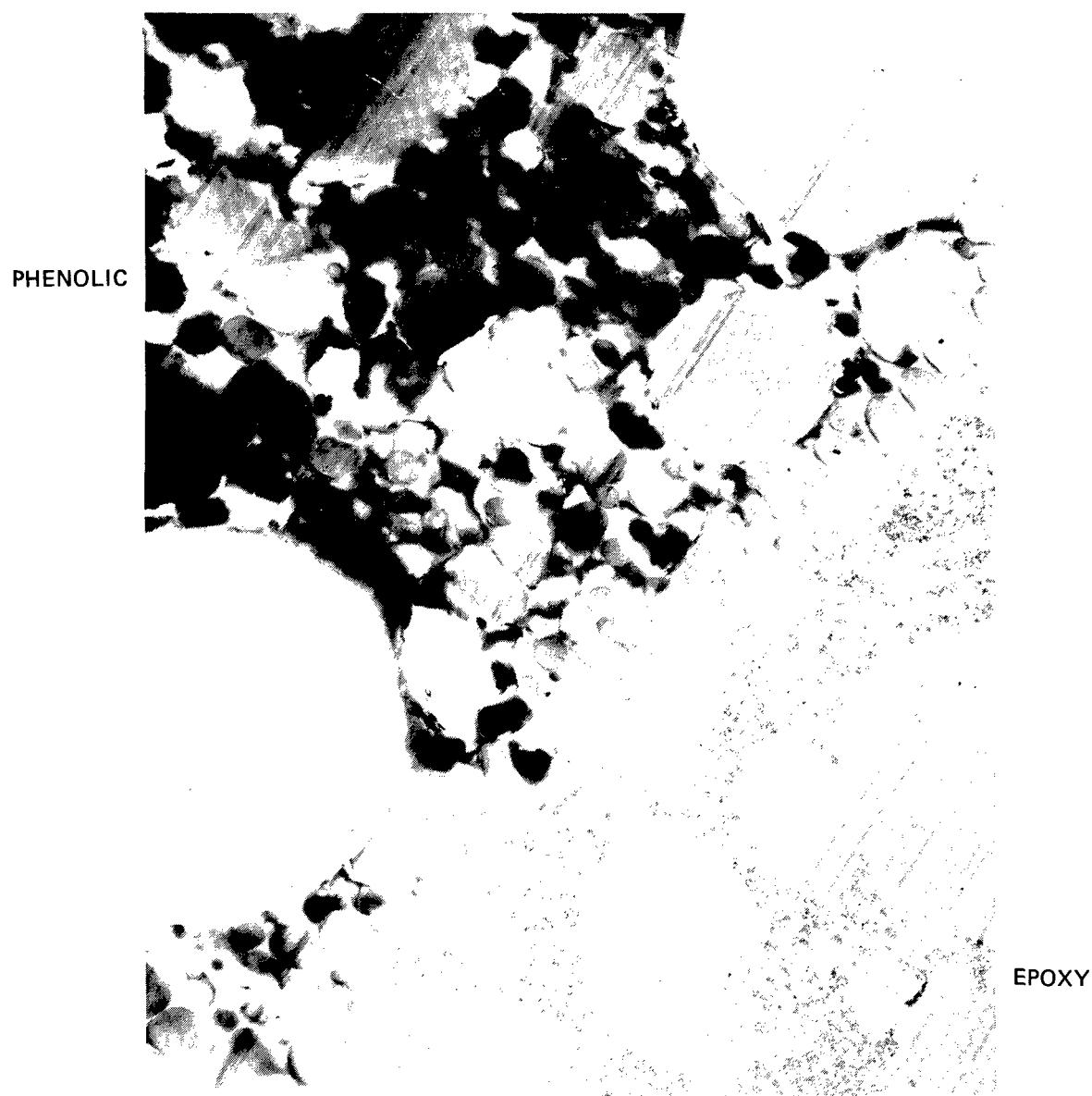
PHENOLIC

EPOXY

Figure 28. TEM Photomicrograph of a Microtomed Section of the
Boundary Between FM-61 Nitrile-Phenolic and Epoxy Layers

b. Stress-Durability Testing

Stress-durability testing was conducted at fixed load (1500 psi), elevated temperature (140°F), and 100% RH for 4400 hours. The test configuration was a machined lap-shear specimen with 0.0625-inch-thick metal adherends. Five primer/adhesive combinations, two primer application processes, and two surface preparations were used (see table 8).

Table 12 lists the test results for all specimens prepared using PAA. The alloy was 2024 bare. The heat treatment was as indicated. Primer application by conventional spraying is indicated by "S." Primer application by flow coating is indicated by "F." Specimens with less than 4400 hours failed during the test at the times indicated. At the test conclusion, the residual strengths of all remaining specimens were determined as soon as possible. Timely evaluation of the specimens guaranteed that their moisture content was relatively constant and was similar to what it was in the environmental chamber.

Table 12. Sustained Stress Durability Test Data—PAA

Heat treatment [A]	Primer	Adhesive	Primer application	Exposure (hr)	Residual stress (lb/in^2)
T3	BR-227	FM-61	F	592	—
T3	BR-227	FM-61	S	996	—
T81	BR-227	FM-61	F	1,184	—
T81	BR-227	FM-61	S	858	—
T3	BR-227A	FM-61	F	888	—
T3	BR-227A	FM-61	S	1,134	—
T81	BR-227A	FM-61	F	1,410	—
T81	BR-227A	FM-61	S	1,212	—
T3	PL-728	PL-729-3	F	4,400	3,670
T3	PL-728	PL-729-3	S	4,400	3,131
T81	PL-728	PL-729-3	F	4,400	3,461
T81	PL-728	PL-729-3	S	4,400	3,980
T3	BXR-MSNR	FM-300	F	4,400	3,407
T3	BXR-MSNR	FM-300	S	4,400	3,737
T81	BXR-MSNR	FM-300	F	4,400	3,751
T81	BXR-MSNR	FM-300	S	4,400	4,122
T3	BXR-MSR	FM-300	F	4,400	3,292
T3	BXR-MSR	FM-300	S	4,400	3,368
T81	BXR-MSR	FM-300	F	4,400	3,639
T81	BXR-MSR	FM-300	S	4,400	3,655

Surface preparation: phosophoric acid anodize   [A] Alloy is 2024 bare

.0625" thick adherend machined lap-shear specimen employed

56

The two systems that failed in test were bonded with an unmodified adhesive primer (BR-227) and its rubber-modified version (BR-227A). According to the manufacturer, the only difference between the two formulations is the presence or absence of a nitrile rubber elastomer. Both systems were bonded with the same duplex adhesive (FM-61).

The specimens primed with BR-227A had more hours of exposure on the average than did specimens primed with BR-227. However, the difference in hours of exposure between the two groups of specimens is not statistically significant in all cases. The experimental data (minimum of three samples) were analyzed using the test for the difference between two means employing Student's t distribution and a 1% critical value.

The next three adhesive systems did not fail during the test. The two model adhesive primers had identical formulations, except that one (BXR-MSR) was modified by the addition of a reactive carboxy-terminated butadiene-acrylonitrile copolymer (CTBN). The residual strengths of the two model primers (BXR-MSNR and BXR-MSR) were statistically analyzed to determine if they differed. There is a statistically significant difference between the residual strength of the two primers when both primers were applied by conventional spraying. One might expect the unmodified primer to have a higher shear modulus than the modified primer because of the potential effect of CTBN on the modified primer's shear modulus. Such a reduction in shear modulus would explain the difference between the two primers when applied by conventional spraying. What requires explanation is why the two primers have essentially equal residual shear strength when applied by flow coating. At present, no theory exists to explain these later data.

The residual strength of the specimens bonded with the model primers was less than their room-temperature ultimate lap-shear strength. The residual lap-shear strength of specimens primed with PL-728 was greater than the room-temperature ultimate lap-shear strength of Series B specimens.

Table 13 lists the test results for all specimens prepared using optimized FPL etch. The environmental durability of BR-227 and BR-227A on optimized FPL etch is inferior to their performance on PAA.

Table 13. Sustained Stress Durability Test Data—FPL

Heat [A] treatment	Primer	Adhesive	Primer application	Exposure (hr)	Residual strength (lb/in^2)
T3	BR-227	FM-61	F	330	—
T3	BR-227	FM-61	S	384	—
T81	BR-227	FM-61	F	2,234	—
T81	BR-227	FM-61	S	732	—
T3	BR-227A	FM-61	F	204	—
T3	BR-227A	FM-61	S	177	—
T81	BR-227A	FM-61	F	1,476	—
T81	BR-227A	FM-61	S	496	—
T3	PL-728	PL-729-3	F	2,960	—
T3	PL-728	PL-729-3	S	1,877	—
T81	PL-728	PL-729-3	F	4,188	2,580
T81	PL-728	PL-729-3	S	4,400	2,460
T3	BXR-MSNR	FM-300	F	4,400	2,582
T3	BXR-MSNR	FM-300	S	4,400	2,699
T81	BXR-MSNR	FM-300	F	4,400	3,819
T81	BXR-MSNR	FM-300	S	4,400	3,691
T3	BXR-MSR	FM-300	F	1,361	—
T3	BXR-MSR	FM-300	S	0	—
T81	BXR-MSR	FM-300	F	4,400	2,772
T81	BXR-MSR	FM-300	S	0	—

Surface preparation: optimized Forest Products Laboratory (FPL) etch

[A] Alloy is 2024 bare

.0625" thick adherend machined lap-shear specimen employed

The experimental values are sufficiently close and the scatter sufficiently great that it is impossible to tell which of the two combinations (BR-227/FM-61 FPL or BR-227A/FM-61 FPL) has the greatest stress durability—if, in fact, there is any difference.

The next primer (PL-728) had inferior durability on 2024-T3 bare FPL compared to 2024-T3 bare PAA. On 2024-T81 bare FPL and 2024-T81 bare PAA, the specimens primed with PL-728 did not fail during the test. However, the residual lap-shear strength on PAA was significantly superior to that on FPL.

On FPL, the stress durability of BXR-MSNR was superior to that of BXR-MSR (the rubber-modified version). The residual lap-shear strength of BXR-MSNR on PAA was equal or superior to the equivalent values on FPL. Except for specimens that were flow coated and used 2024-T81 adherends, the greater durability of this primer on PAA

58

is statistically significant. There were no failures in either case during the test. The rubber-modified BXR-MSR primer exhibited the least durability when sprayed on FPL. However, this primer demonstrated superior durability on PAA.

The experimental data indicate the general superiority of these adhesive systems on PAA in comparison to FPL. Furthermore, there is no significant difference between the stress durability within pairs of modified and unmodified adhesive primers.

c. Failure Analysis

Failure analyses were performed on both lap-shear and stress-durability specimens. The primary objective of this investigation was the determination of the overall failure locus, whether it be oxide, primer, adhesive, or interfacial, and the actual fracture mechanism involved.

The overall result of this failure analysis investigation has led to the following fundamental conclusions:
1. Each adhesive/primer system fails in a characteristic way.
2. In no case were any oxide or interfacial failures observed.
3. The two modified primer systems each fail in a different way, with each exhibiting a different toughening mechanism.

(1) Methods of Analysis

Failed specimen surfaces were analyzed using a variety of techniques. The overall fracture surface topographies were studied by macroscopic, visual, and SEM techniques. More detailed analyses were performed by SEM/STEM analyses, as well as by TEM analysis of fractured and microtomed specimens, respectively. Table 14 summarizes the various oxide/primer/adhesive combinations analyzed, as well as the techniques used in each case.

(2) Visual Failure Analysis

Visual examination of two Task I ultimate lap-shear specimens, as well as stress-durability lap-shear specimens, was carried out for the majority of the available specimens. Where appropriate, wide-field, 10 to 40X magnifications were used in an attempt to accurately determine the apparent failure locus. However, it should be

Table 14. Specimen Configuration, Failure Mode for Mechanical Tests, and Analysis Technique

Primer/Adhesive	Alloy/Oxide	Test type	Test series	Failure types		
				Characteristic primer/adhesive	Analyzed by SEM	Analyzed by TEM
BR-227/ FM-61	2024-T3-clad PAA	Lap shear	A	B	A	—
	2024-T3-bare PAA	Lap shear	A	B	B	B
	2024-T3-bare FPL	Stress durability	—	B	A	—
BR-227A/ FM-61	2024-T3-clad PAA	Lap shear	A	A	A	—
	2024-T3-clad FPL	Lap shear	A	A	A	—
	2024-T3-bare PAA	Stress durability	—	A	A	—
	2024-T3-bare FPL	Lap shear	A	A	A	—
PL-728/ PL-729-3	2024-T3-clad PAA	Lap shear	A	C	C	—
	2024-T3-clad FPL	Lap shear	A	C	C	—
	2024-T3-bare PAA	Lap shear	A	C	C	—
	2024-T3-bare FPL	Lap shear	A	C	C	—

noted that the results presented below are descriptive of the major failure trend within any one group only. As such, there may be some discrete samples that do not obey the observed trends within any one group.

As a result of macroscopic visual failure analyses, three basic failure types were recognized. These three types, subsequently referred to as Type A, B, or C, are illustrated in Figures 29, 30, and 31, respectively. The adjacent schematic drawings more definitively characterize the failure types.

This program determined the following three failure mode types. Type A failures traditionally have been referred to as "slick" or adhesive-type failures. Type B failures traditionally have been referred to as "nonslick" or cohesive-type failures. Type C failures represent a mixed failure mode, with the aluminum on either side of the transition zone often appearing "slick" and in some cases "nonslick." However, for the purposes of the following discussion, all samples have been evaluated in terms of their major characteristic, whichever type exceeded 70% of the fracture area. As such, with Type C no distinction has been made between samples exhibiting both slick- and nonslick-appearing adherends.

Table 15 summarizes the observed trends for the inspected oxide/primer/adhesive groups. With the exception of the first ultimate lap-shear test (called Series A test), the major trends are as follows:

1. Type A failures always occur with BR-227A regardless of oxide used. When

ALLOY
OXIDE
PRIMER

PHENOLIC
SIDE

ADHESIVE

EPOXY
SIDE

FAILURE
PLANE {

PRIMER

OXIDE
ALLOY
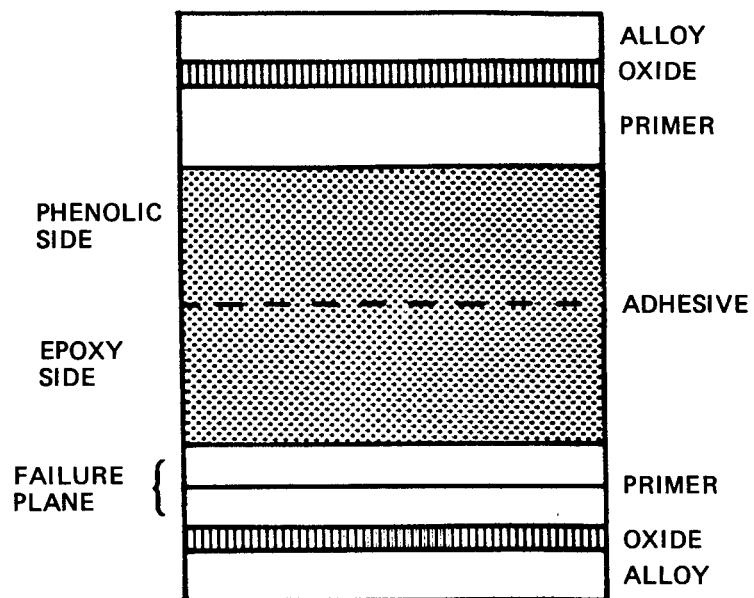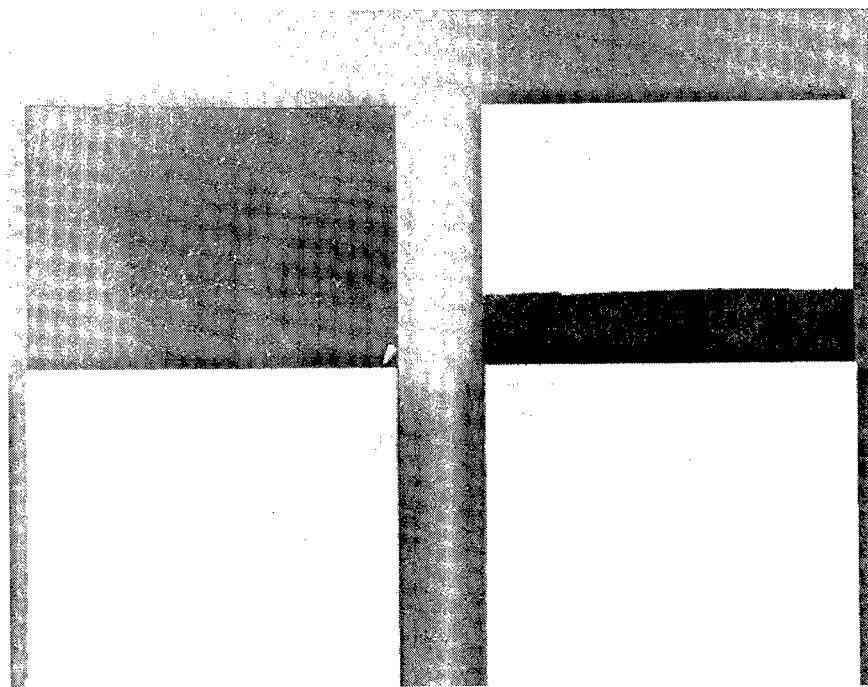
Figure 29. Type A Failure for all BR-227A/FM-61 Bonded Specimens

61
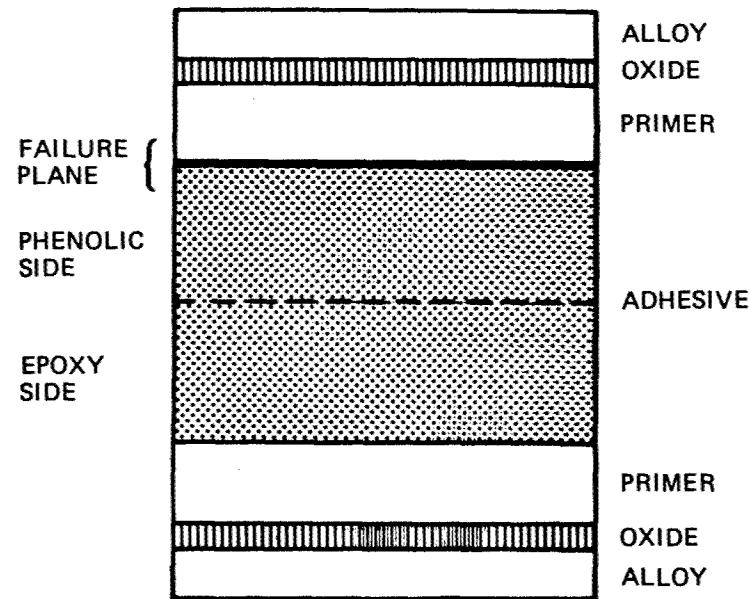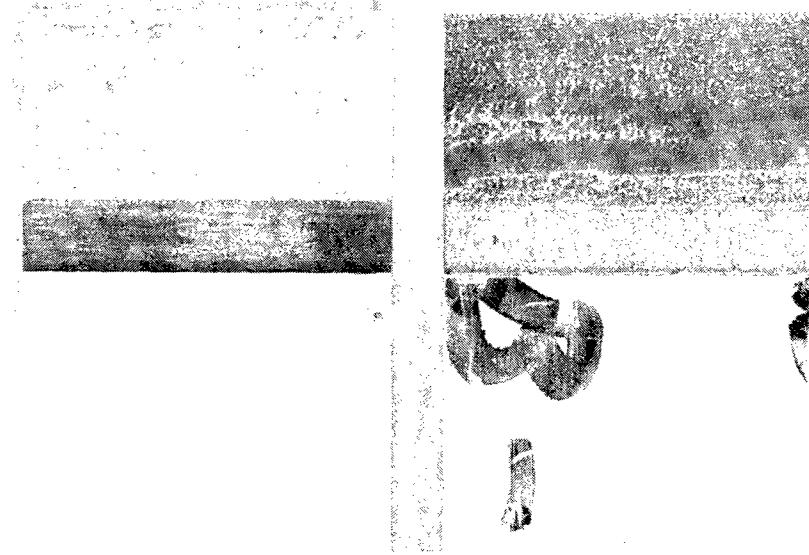
Figure 30. *Type B Failure for all BR-227/FM-61 Bonded Specimens*
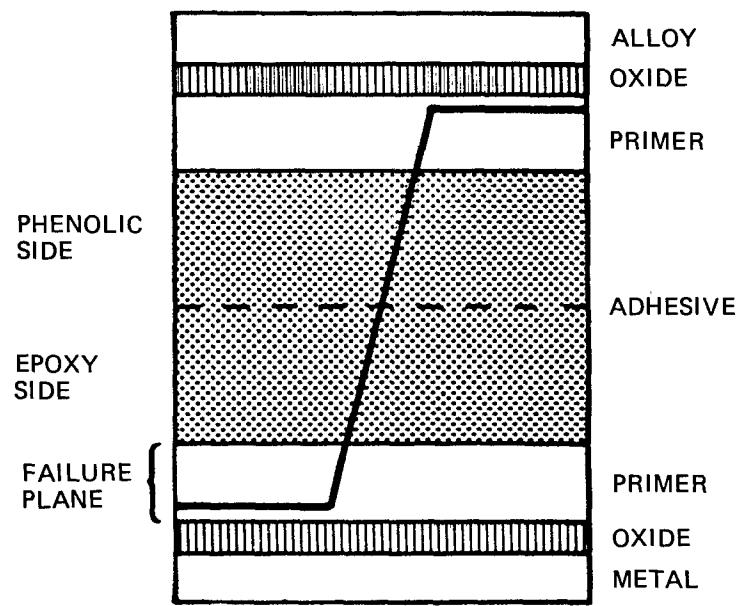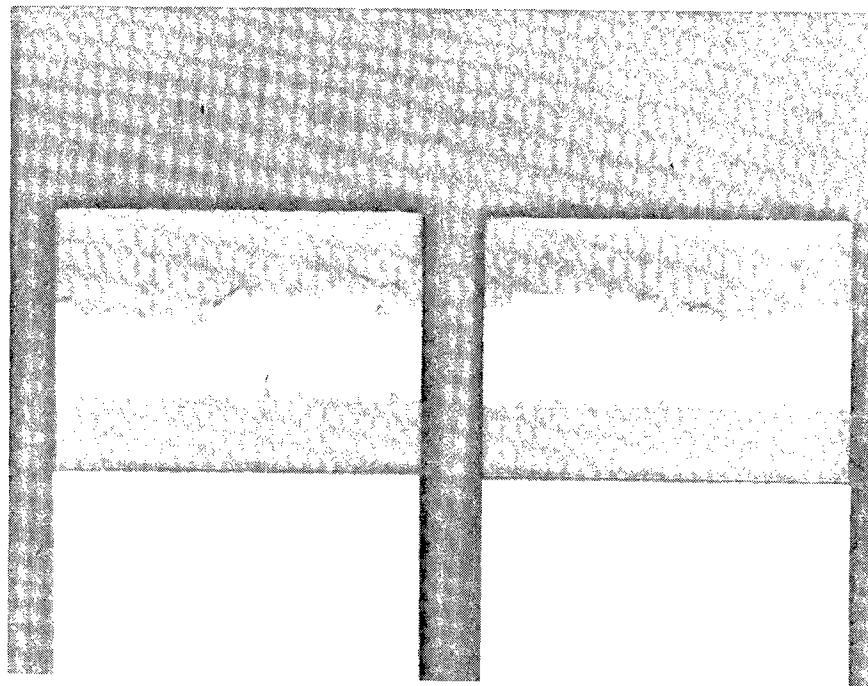
Figure 31. Type C Failure for all Other Adhesive Bonded Specimens

63

Table 15. Primer/Adhesive Failure Trends

Primer/Adhesive	Series A	Series B	Stress durability
BR-227/FM-61	A	B	B
BR-227A/FM-61	A	A	A
BXR-MSNR/FM-300	C	C	C

FM-61 adhesives were used, Type A failures occurred predominantly on the epoxy side of the duplex adhesive.

2. Type B failures were found to always occur with BR-227 when used with FM-61, regardless of the oxide used. These failures occurred predominantly on the nitrile-phenolic side of the duplex adhesive.

3. Type C failures were found to occur in all other situations; that is, wherever BR-227A or FM-61 were not used.

Numerous BR-227/FM-61 lap-shear specimens from the first Task I test exhibited failures anomalous to the overall group trends. These lap-shears exhibited Type A failures. No reason was determined for these anomalous failures, although improper primer application has been suspected.

Table 14 indicates which specimens were analyzed, as well as the technique used. In addition, this table summarizes the test type, the test series, and the individual failure type analyzed in each case and compares this to the overall primer/adhesive group trends listed previously.

(3) BR-227/FM-61 Failures

As Table 14 indicates, the failures were predominantly Type B, with the exception of the first Task I lap-shear tests, which exhibited Type A failures. As indicated in Table 14, the BR-227/FM-61 samples analyzed by SEM discussed below were from the Series A lap-shear tests exhibiting Type A failures. Thus, the specimens analyzed by SEM represent somewhat anomalous BR-227/FM-61 failures, as opposed to the more typical Type B failures analyzed by TEM/microtomy.

Figures 32 and 11 are transverse SEM views of the failure surface generated on 2024-T3 clad PAA with BR-227 and FM-61 at 10,000 and 50,000 magnifications, respective-

64

FRACTURED
06-06-79   1-2C-B   79-00541-S1
30KV X10000   1U 056   BMT

Figure 32. Transverse View of Failed Specimen—2024-T3-Clad, PAA Oxide, BR-227 Primer, FM-61 Adhesive

ly. Figure 33 shows a similar section only on a 2024-T3 bare FPL oxide substrate. The failure can be seen to have occurred primarily by crack propagation within the primer. Although the residual primer thickness does show some variation, in no instance was there any evidence of oxide failure. In general, the fracture surface morphology was relatively smooth, with little observable plastic deformation of the specimens. This tends to verify the brittle nature of the BR-227 primer component (i.e., its low ductility), as well as its limited strain deformation ability.

Figure 34 shows a TEM view of a transversely microtomed section representative of BR-227/FM-61 Type B failures on FPL 2024-T3 bare. In this microtomed section, the fracture plane is delineated by a thin line of Au-Pd deposited prior to sectioning. This Au-Pd layer, as indicated, reveals that the failure occurred primarily by crack propagation within the nitrile-phenolic side of the FM-61 adhesive. Higher magnification
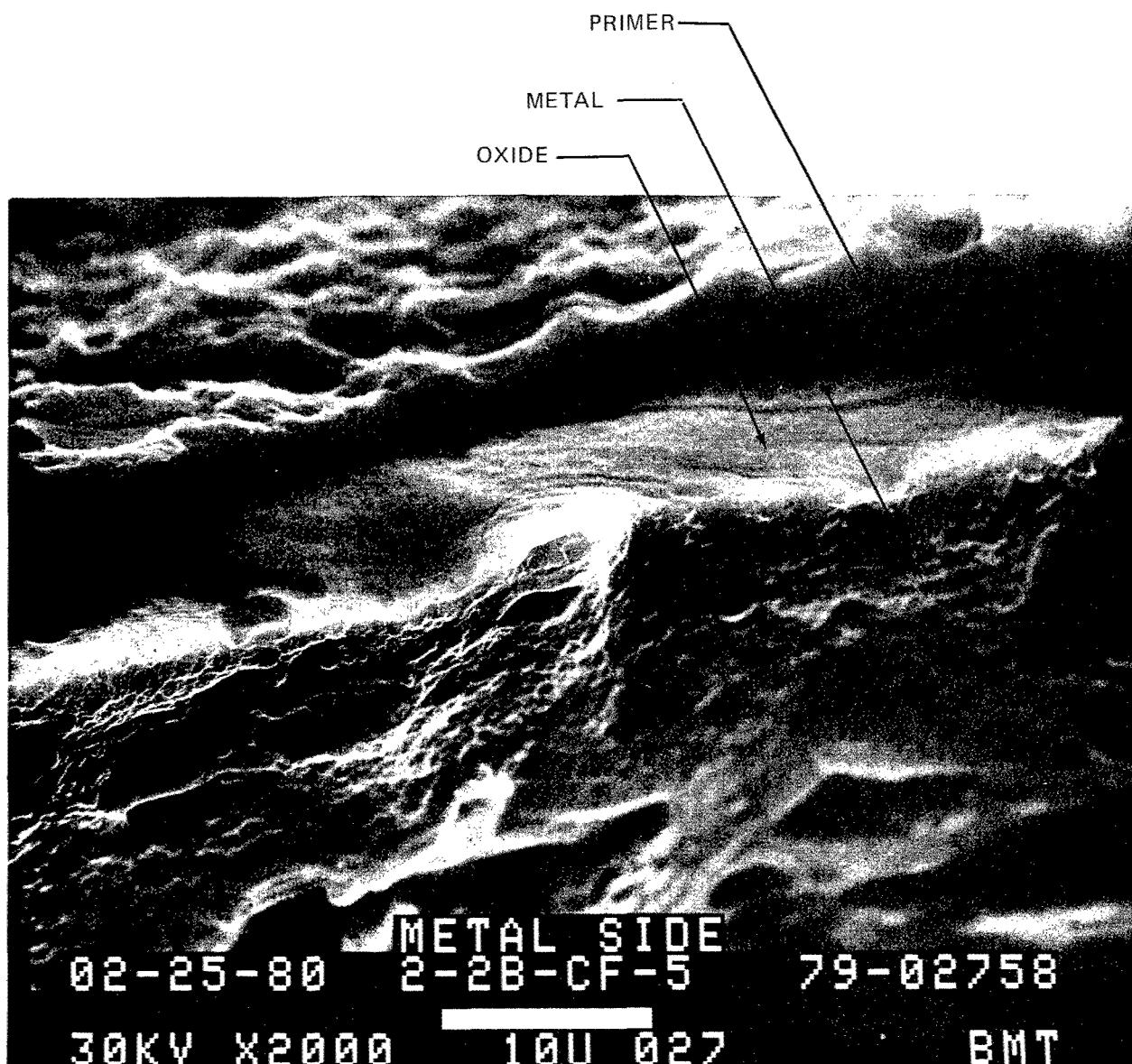
Figure 33. Transverse View of Failed Specimen—2024-T3-Bare, FPL Oxide, BR-227 Primer, FM-61 Adhesive

examinations failed to reveal the existence of any chemical segregation adjacent to the fracture plane.

(4) BR-227A/FM-61 Failures

BR-227A failures were noted in the previous visual failure analyses to always yield predominantly Type A failure surfaces. This was found to be true regardless of the oxide used. Thus, the specimens analyzed both by SEM and TEM represent typical failure surfaces for BR-227A/FM-61.

66
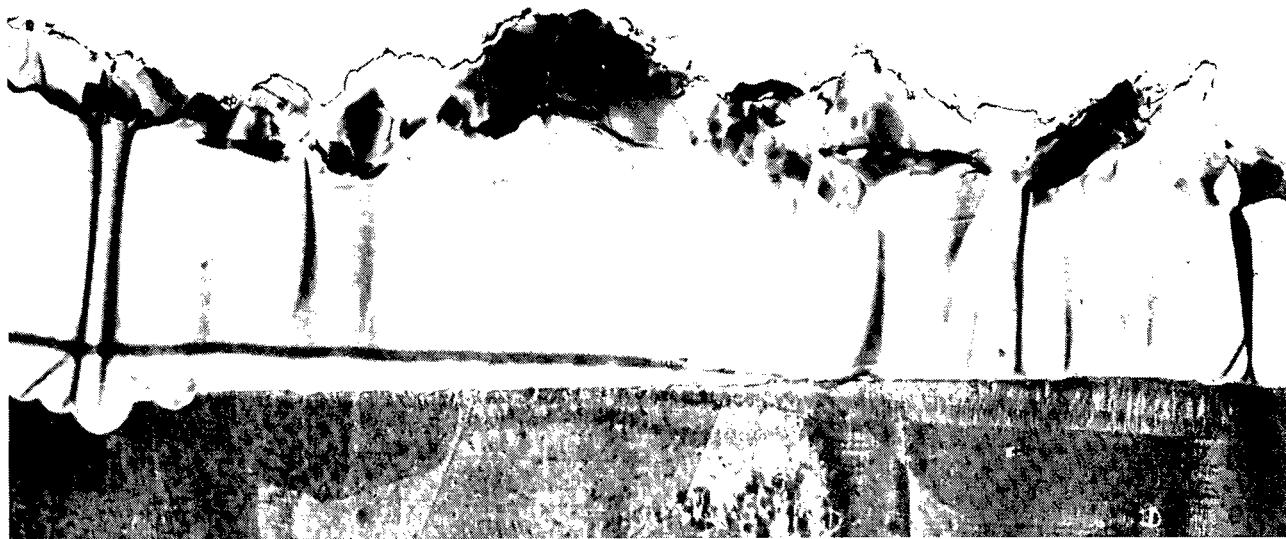
Figure 34. Transversely Microtomed Section of BR-227/FM-61
on 2024-T3-Bare FPL

Figures 16, 35, 36, and 37 represent transverse SEM/STEM views of the failure surfaces generated with BR-227A/FM-61 on 2024-T3 clad PAA, 2024-T3 clad FPL, 2024-T3 bare PAA, and 2024-T3 bare FPL surfaces, respectively. Although these specimens encompass several oxide and alloy conditions, the basic failure locus remains essentially the same. In almost all cases, the failure occurred by crack propagation within the primer adjacent to the oxide layer. The distance, however, was generally much closer than observed in any BR-227/FM-61 Type A failures. The residual primer thickness on the oxides examined shows a generalized trend toward thicker residual primer layers on FPL oxides.

In general, the actual fracture surface morphology of the BR-227A/FM-61 Type A failures starkly contrasts with that of BR-227/FM-61 Type B failures. The exhibited BR-227A morphologies are generally very lumpy and exhibit significant amounts of plastic deformation and elastomeric stretching. These observations tend to verify the elastomeric modification of the BR-227A primer, as well as indicate its ductile, high strain behavior during fracture.

Complementary TEM/microtomy analyses were performed on 2024-T3 bare FPL with BR-227 and FM-61, Figure 38. The magnification of this figure does not allow the oxide to be resolved. However, subsequent higher magnification examinations have

67
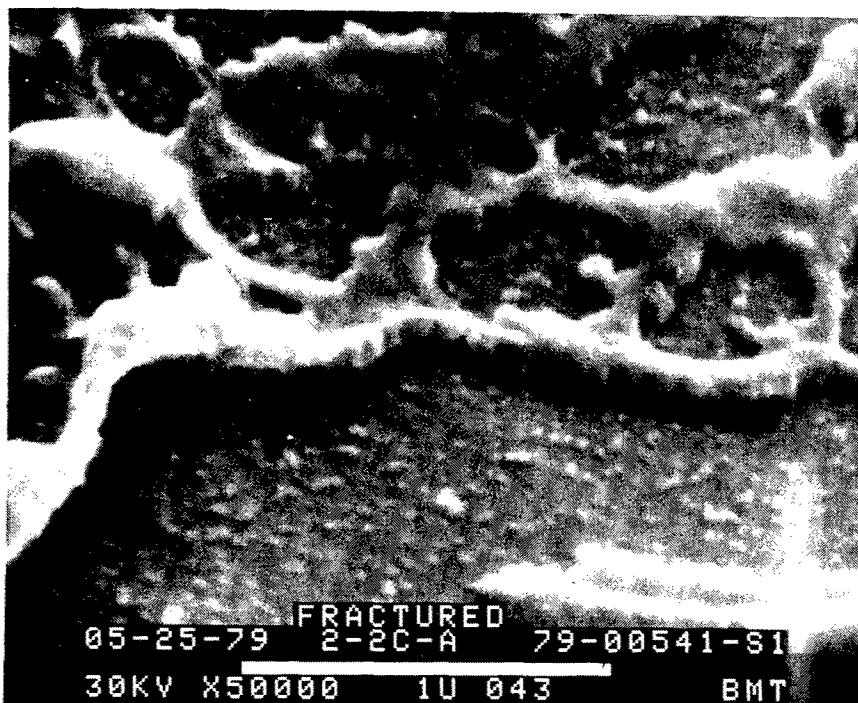
Figure 35. Transverse View of BR-227A/FM-61 Failure Surface on 2024-T3-Clad FPL

confirmed the existence of a thin layer of BR-227A primer on top of the oxide structure, a result in good agreement with the prior SEM/STEM analyses.

(5) PL-728/PL-729-3 Failures

As indicated in Table 15, PL-728/PL-729-3 failures have occurred primarily in a Type C fashion, regardless of the oxide system used. Subsequently, the SEM/STEM analyses performed on specimens indicated in Table 14 represent typical failure surfaces.

Figures 39, 40, 41, and 42 are transverse views of PL-728/PL-729-3 with 2024-T3 clad PAA, 2024-T3 clad FPL, 2024-T3 bare PAA, and 2024-T3 bare FPL oxide substrates, respectively. These analyses indicate that the failures occurred primarily by crack propagation through the primer. However, no single, well-constrained plane of failure within the primer exists. Rather, a wide range of residual primer thicknesses are seen, both optically and by SEM/STEM analyses. The general pattern of the residual primer is somewhat suggestive of the adhesive scrim.

The fracture surface morphology of PL-728/PL-729-3 appears scalloped and shows significant matrix ductility. Figure 43 shows the presence of small cavities or holes

68

LIGAMENT
STRETCHING
FROM LUMPY
PARTICLES
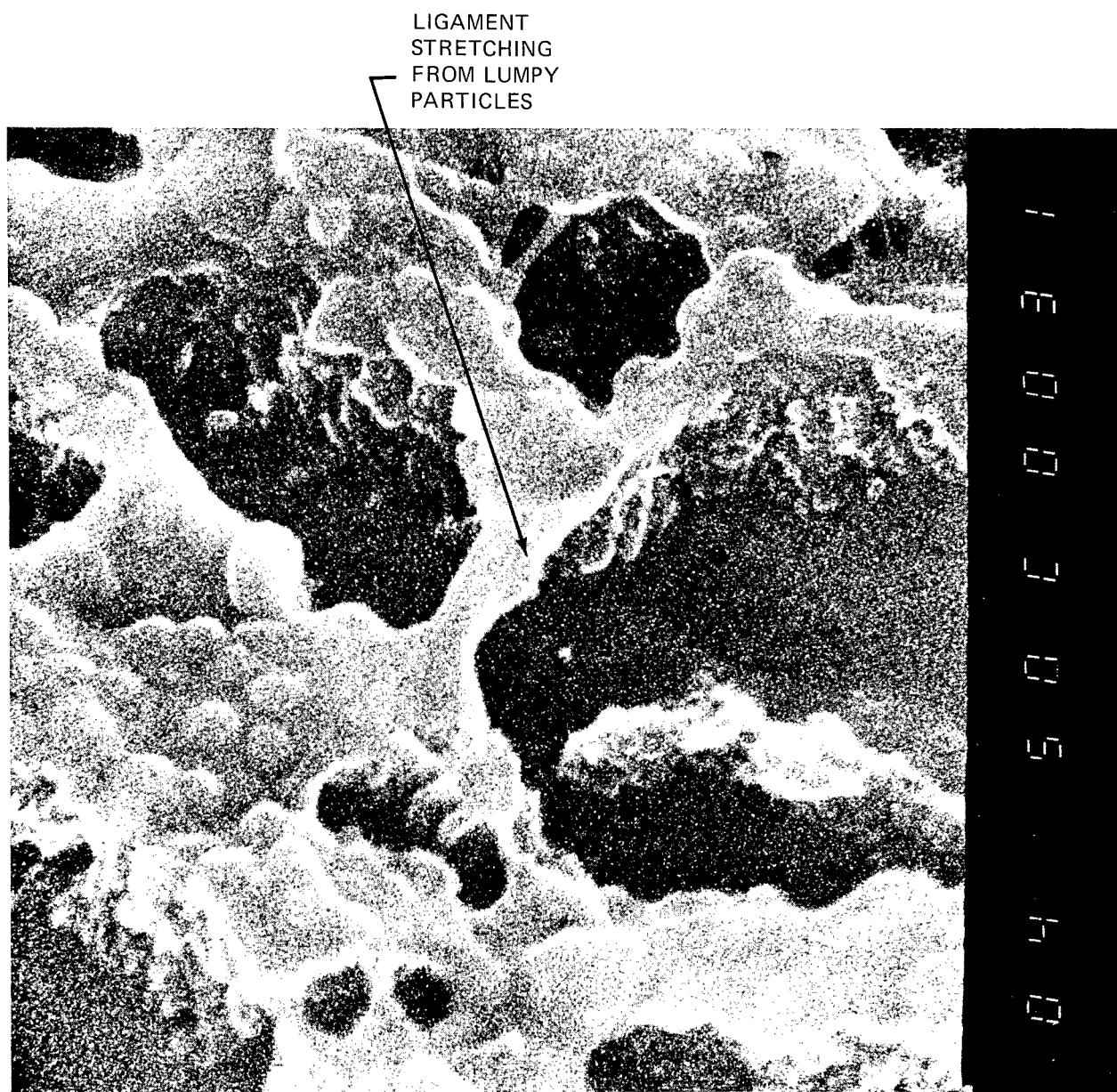
*Figure 36. Transverse View of Failed Specimen—2024-T3-Bare, PAA Oxide,
BR-227A Primer, FM-61 Adhesive*

69
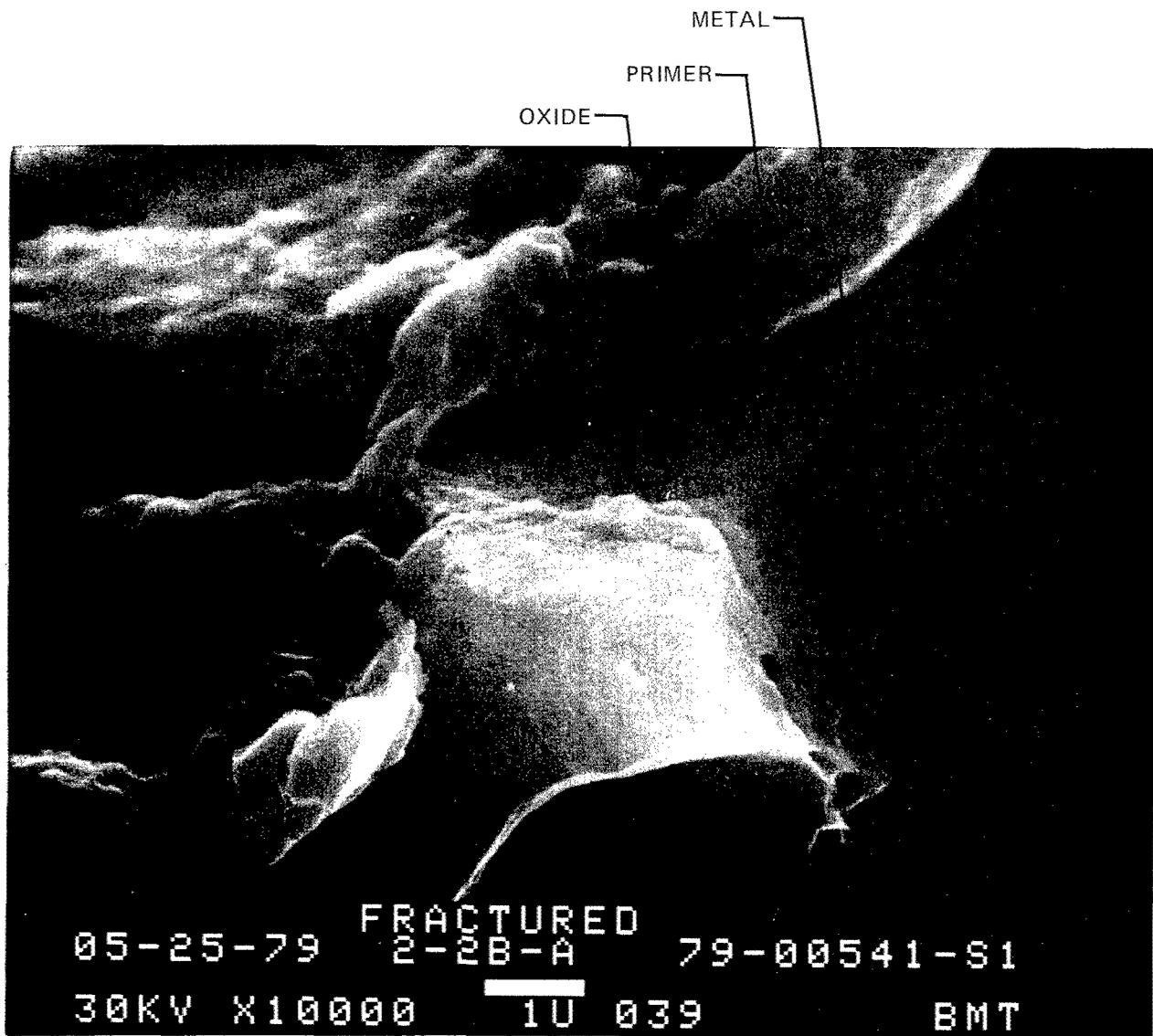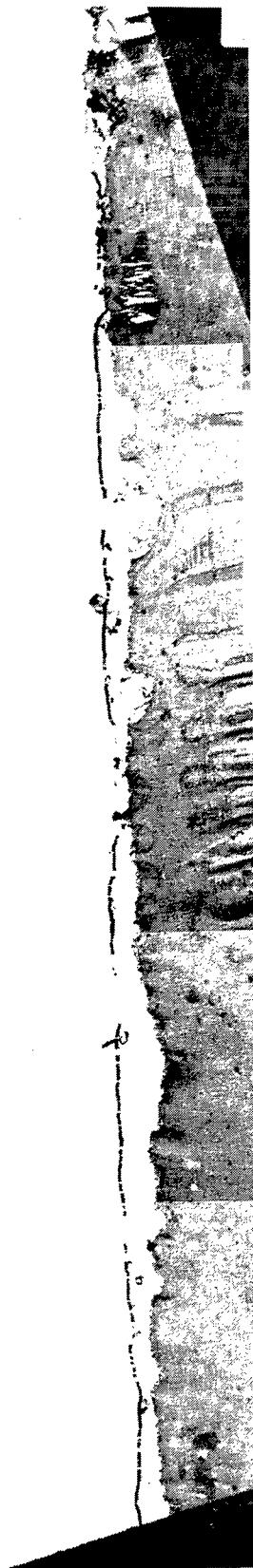
Figure 37. Transverse View of Failed Specimen—2024-T3-Bare, FPL Oxide, BR-227A Primer, FM-61 Adhesive

Figure 38. Montage of Microtomed Sections of
BR-227/FM-61 on 2024-T3-Bare FPL

MATRIX DUCTILITY

FRACTURED
06-21-79   1-2C-C   79-00541-S1
30KV X50000   1U 069   BMT
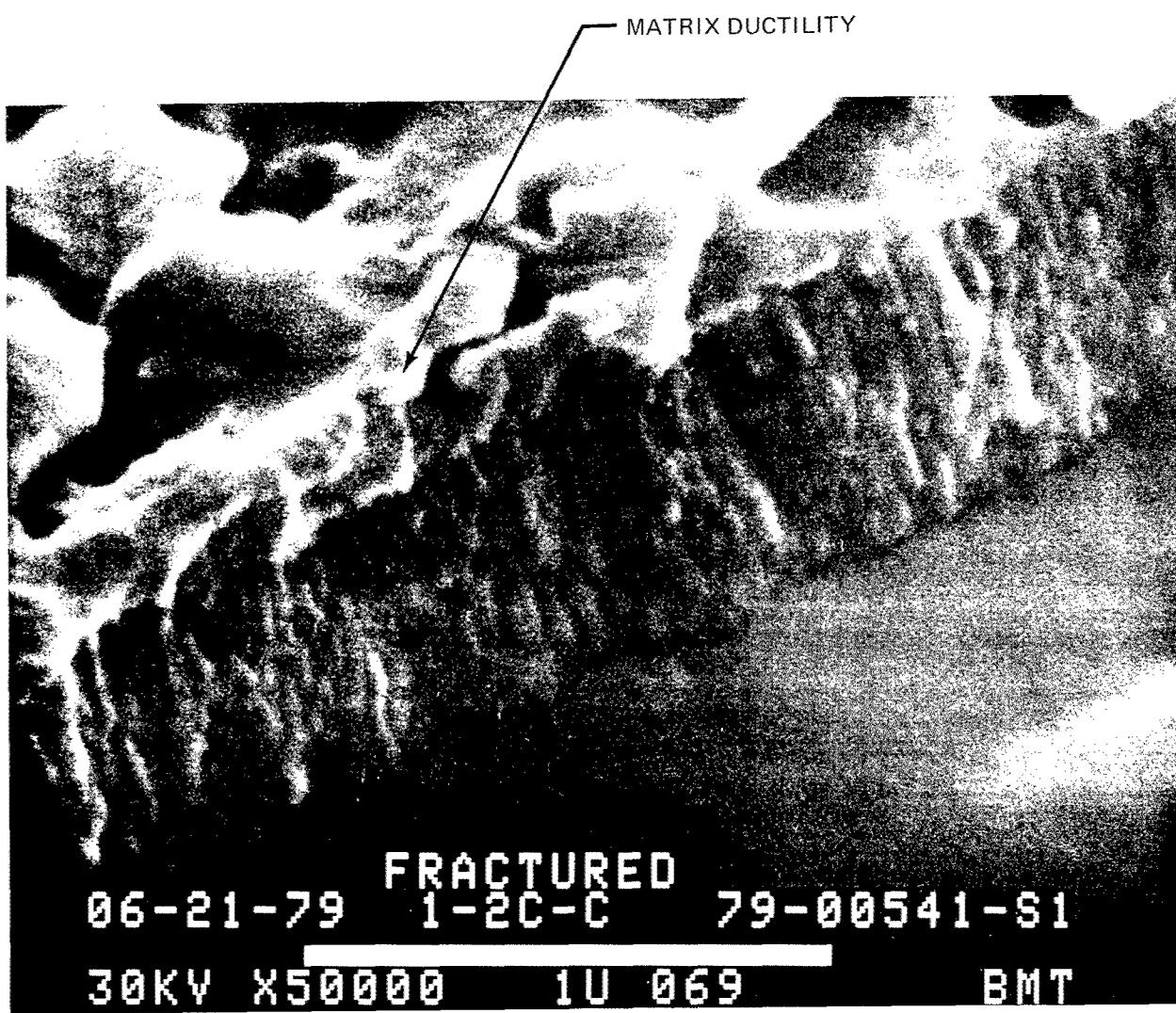
Figure 39. *Transverse View of Failed Specimen—2024-T3-Clad, PAA Oxide, PL-728 Primer, PL-729-3 Adhesive*

PRIMER   CRACKING DUE TO SPECIMEN PREPARATION
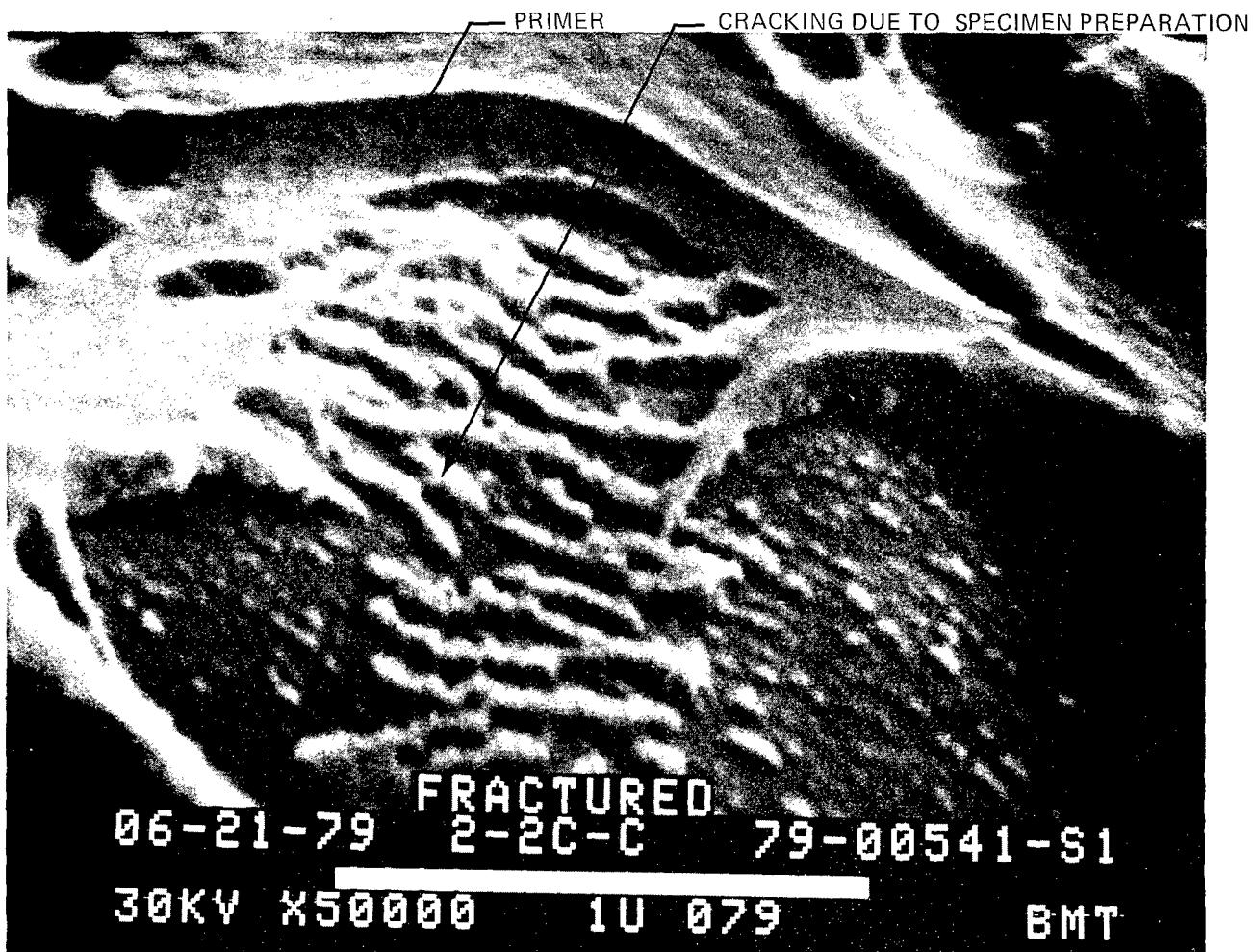
Figure 40. *Transverse View of Failed Specimen—2024-T3-Clad, FPL Oxide,
PL-728 Primer, PL-729-3 Adhesive*
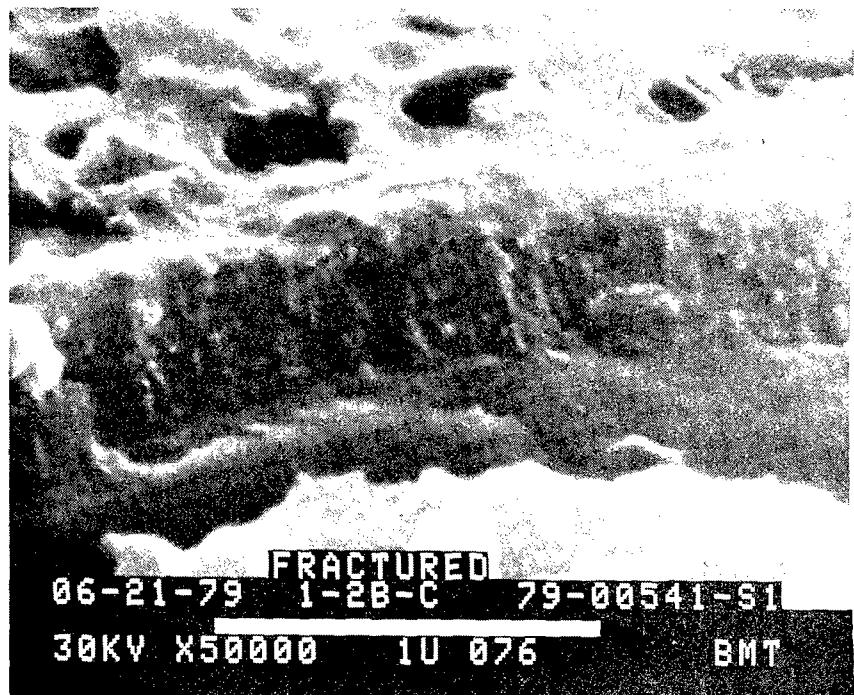
Figure 41. Transverse View of PL-728/PL-729-3 Failure Surface on 2024-T3-Bare PAA

73

Figure 42. Transverse View of PL-728/PL-729-3 Failure Surface on 2024-T3-Bare FPL
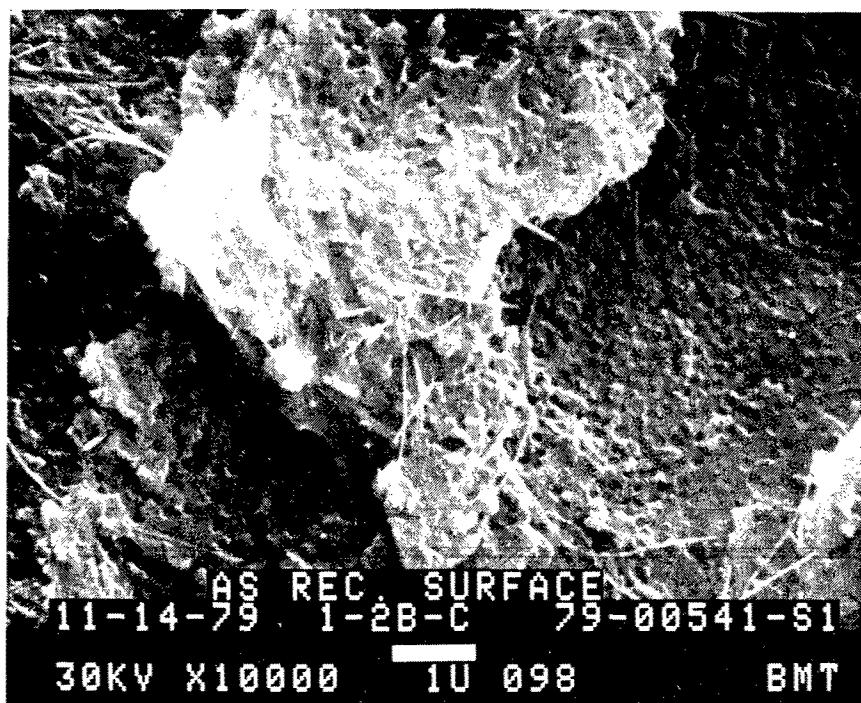
Figure 43. Failure Surface Showing Matrix Ductility of PL-728/PL-729-3 (on 2024-T3-Bare PAA)

and filamentary stretching of elastomeric modifiers similarly reported by NASA, presumably caused by the fracture process. These photomicrographs support the existence of a crack propagation mechanism different from that shown in Figure 44 for the BR-227A elastomer-modified system. A schematic diagram of how the crack might propagate is illustrated in Figure 45. Here, the stresses built up at the crack tip cause flow of the matrix around the elastomer phases. Matrix flow and elongation of the elastomeric particles inhibit crack extension, thereby toughening the system. This process requires more coherent matrix ductility than is apparently observed in BR-227A.
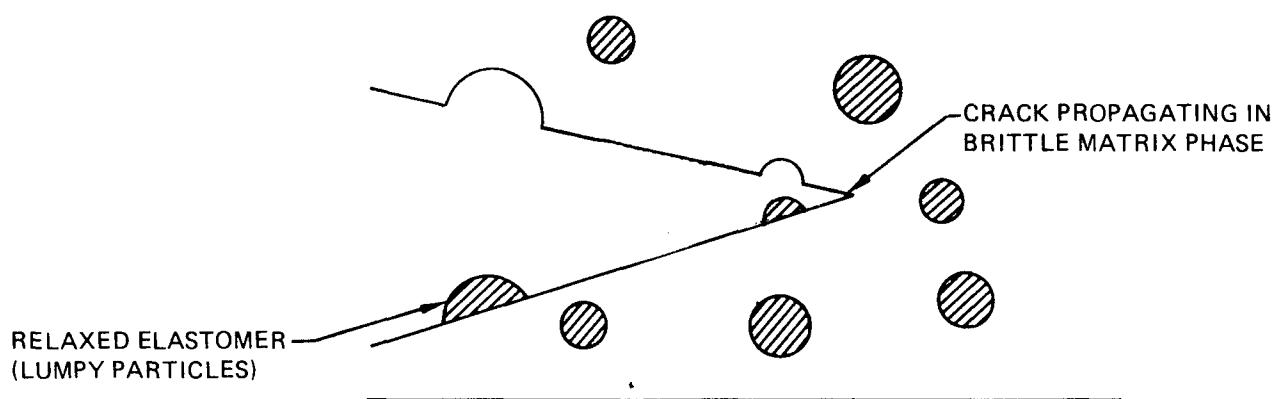
Figure 44. Hypothesized Crack Growth Mechanism in BR-227A Primer
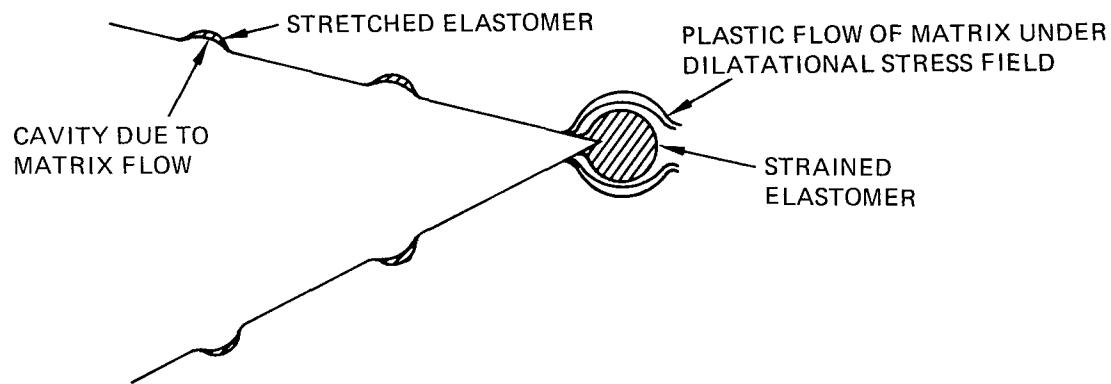
Figure 45. Hypothesized Crack Growth Mechanism in PL-728 Primer

The PL-728 failed surface on the FPL oxide, Figure 46, shows a fracture surface with fewer of the small cavities observed for the PAA oxide case, Figure 43. The matrix shows plastic flow, but to a lesser degree than the PL-728 on the PAA oxide. These differences could be due partly to compositional gradients in the PL-728 primer.
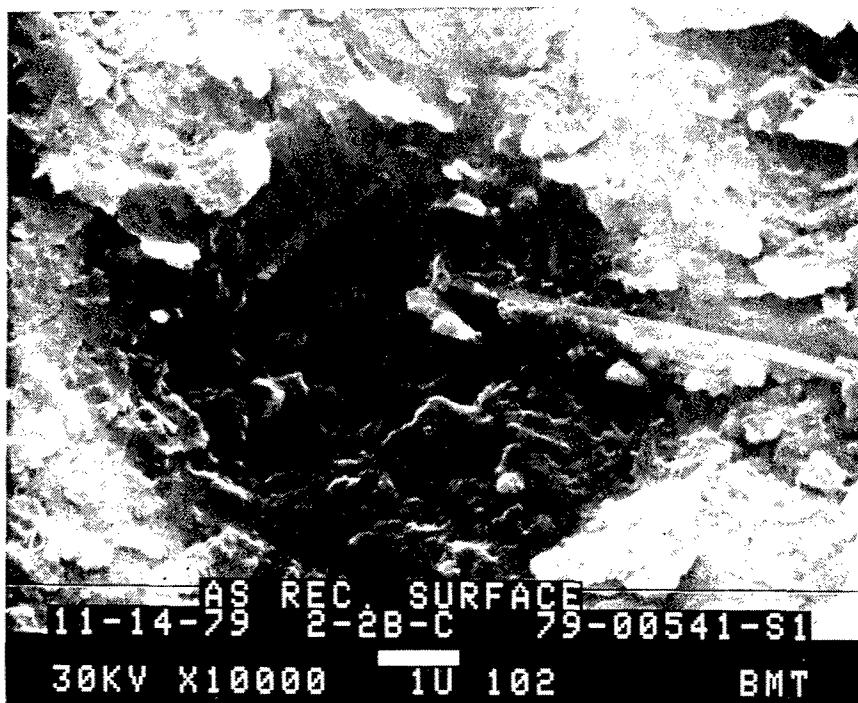
Figure 46. Failure Surface of PL-728/PL-729-3 on 2024-T3-Bare FPL

Alternately, the thinner FPL oxide may not be allowing chemical segregation, as would the PAA oxide. Lastly, the much thinner FPL oxide/polymer composite may be expected to have much different load-transfer characteristics to the aluminum alloy.

d. Failure Mechanism Discussion

The primary objective of this program was to define the relationships between interfacial characteristics of adhesive/primer systems and surface oxides of aluminum that govern both the long-term stress durability and the ultimate performance of adhesively bonded joints. Mechanical testing, baseline analysis, and failure analysis were performed to understand apparently interfacial failures as well as overall oxide/primer/adhesive incompatibilities. The following discussion reviews these incompatibilities and analyzes and proposes a model failure mechanism to explain the data.

76

(1) Mechanical Testing

Apparent interfacial incompatibilities exclusive to BR-227A/FM-61 on PAA 2024-T3 clad formed the primary impetus for this program. This primer/adhesive combination on PAA, when subjected to ultimate lap-shear tests, exhibited lower ultimate strengths than on optimized FPL. However, lap-shear and stress-durability tests carried out within this program did not strongly support earlier observations.

Lap-shear testing within this program has indicated that, in comparison to other adhesive systems, BR-227 and BR-227A combined with FM-61 have poor strength and stress durability on both PAA and FPL. Stress-durability testing indicates that BR-227A with FM-61 is, in general, equivalent on PAA to BR-227/FM-61 under the same conditions and, in some cases, is superior.

(2) Failure Analyses

Failure analyses and baseline primer oxide studies have been performed in depth on numerous samples. These analyses have consistently demonstrated that there are several distinct, recognizable failure types, each specific to a particular primer/adhesive combination. These may be reviewed as follows:

1. Each oxide/primer/adhesive system exhibits its own visually consistent failure mode. This failure mode for each system is the same for both ultimate and stress-durability lap shears.
2. These failure modes have been found to fall into three basic categories:
    a. Type A (fig. 29)
    b. Type B (fig. 30)
    c. Type C (fig. 31)
3. a. All BR-227A primed systems exhibit Type A failures, specific to the epoxy side of the FM-61.
    b. BR-227 with FM-61 exhibits Type B failures, specific to the nitrile-phenolic side of the FM-61.
    c. All of the other primers, when combined with either FM-300 or PL-729-3, exhibit Type C failures.
4. Each failure mode occurs predominantly in the primer, and no evidence of an oxide failure has been identified.
5. Primer oxide wetting occurs in all cases.

77

(3) Review of Failure Mechanisms

Apparent incompatibilities observed with BR-227A/FM-61 on PAA 2024-T3 clad surfaces in studies prior to this were evidenced by low lap-shear ultimate strengths and "slick"-appearing failures. At that point, four failure mechanisms were proposed to account for apparent incompatibilities between the BR-227A primer when used with FM-61 on PAA oxides.

1. Shear failure of unstabilized porous oxides occurs due to poor penetration of polymers into pores.

2. Excessive primer deformation occurs during long-term loading, thereby transmitting deformation into the unstabilized porous oxide.

3. Premature failures occur only when the thick surface oxide ruptures, thereby creating stress risers at the oxide/polymer interface. Because the PAA oxide is thicker, stress risers in it are more detrimental.

4. Selective absorption of low-molecular-weight polymer species into small pores of porous oxides occurs, leaving large molecules on top of oxide. Concentration of high-molecular-weight rubber additives near the oxide surface creates a weak boundary layer.

The first mechanism requires incomplete penetration of the primer into the oxide. The TEM data do not support this hypothesis, nor do any of the SEM data. All of our work to date indicates that some polymer phase of the primer is wetting and flowing into the porous oxide down to the base plate. In addition, no failure surfaces have been found in this program that indicate that the crack propagation plane extends into the oxide. Our conclusion at this time is that mechanism 1 does not operate for the BR-227, BR-227A, and PL-728 primers when they are used on properly prepared PAA and FPL oxide surfaces.

The second mechanism was proposed primarily on the basis of reportedly reduced stress durabilities of BR-227A primed PAA oxides. However, the mechanical behaviors noted in this report have not borne out this anomaly. In addition, the second mechanism also requires incomplete polymer penetration into the oxide. Thus, for the same reasons as cited for mechanism 1, the second mechanism does not appear to be relevant to the systems studied.

Mechanism 3 requires fracture of the oxide, leading to stress risers. These stress risers were hypothesized to be more destructive in thicker oxides than in thinner

78

oxides. However, the majority of the mechanical results obtained demonstrate no distinct difference between PAA and FPL oxides that can be discriminated. In addition, all of our data indicate that failure occurs due to polymer fracture at a discrete distance away from the oxide. As yet, no evidence of fractured oxides has been obtained. Consequently, this mechanism also is not relevant.

Mechanism 4 requires size separation of the primer molecular species by the oxide structures. For the thicker, more organized oxides such as PAA, this hypothetically may create a weak boundary layer just above the oxides. While some segregation effects have been observed in BR-227A, these do not appear to define a fracture plane near the oxide surface. Because of the interstitial dimensions of the PAA oxide, selective absorption of primer components in the oxide is highly likely. Consequently, this failure mechanism also is not relevant.

(4) Discussion

Investigations of failures within this program have revealed the existence of several discrete and recognizable cohesive failure types. These failure types—A, B, and C— are illustrated in Figures 29 through 31. Both failure analysis and mechanical testing have revealed that these failure types are predominantly related to the primer or primer/adhesive combination used. In no specific cases were any oxide-controlled failure mechanisms observed, although some mechanical strengths and stress durabilities may have been affected.

These results suggest that there are several fundamental controlling factors inherent in determining the observed failure type. These factors are believed to be: (1) the lap-shear test geometry, (2) modulus of the primer/adhesive combination, and (3) the mode I and mode II toughness of each component.

These factors are postulated to determine both the polymer layer within which the fracture occurs and where and how the fracture will propagate. However, this by no means implies any prediction of ultimate tensile or stress-durability strength behaviors.

(a)   Factor 1—The Lap-Shear Test

The lap-shear test affects the failure mode in that it determines the fundamental loading of the overall joint. The overall joint, thus loaded, is postulated to fail by crack propagation in the least-tough component for the given loading geometry.

In this program, single machined lap-shear specimens were used to measure the ultimate and long-term durabilities of the adhesively bonded joints. The lap joint is illustrated in Figure 47. Due to the bending moment in the metal, both normal peel (or mode I) and shearing (mode II) stress gradients are induced along each of the adherend surfaces. Figure 48 presents the numerically predicted increases in mode I and mode II loading at both lap-shear zones normalized to the average overall shear stress (ref 19). As can be seen in this figure, the result is a mixed mode (mode I and mode II) loading along the lap joint length. The resulting mode I stress gradients are typically more severe than the mode II stress gradients.
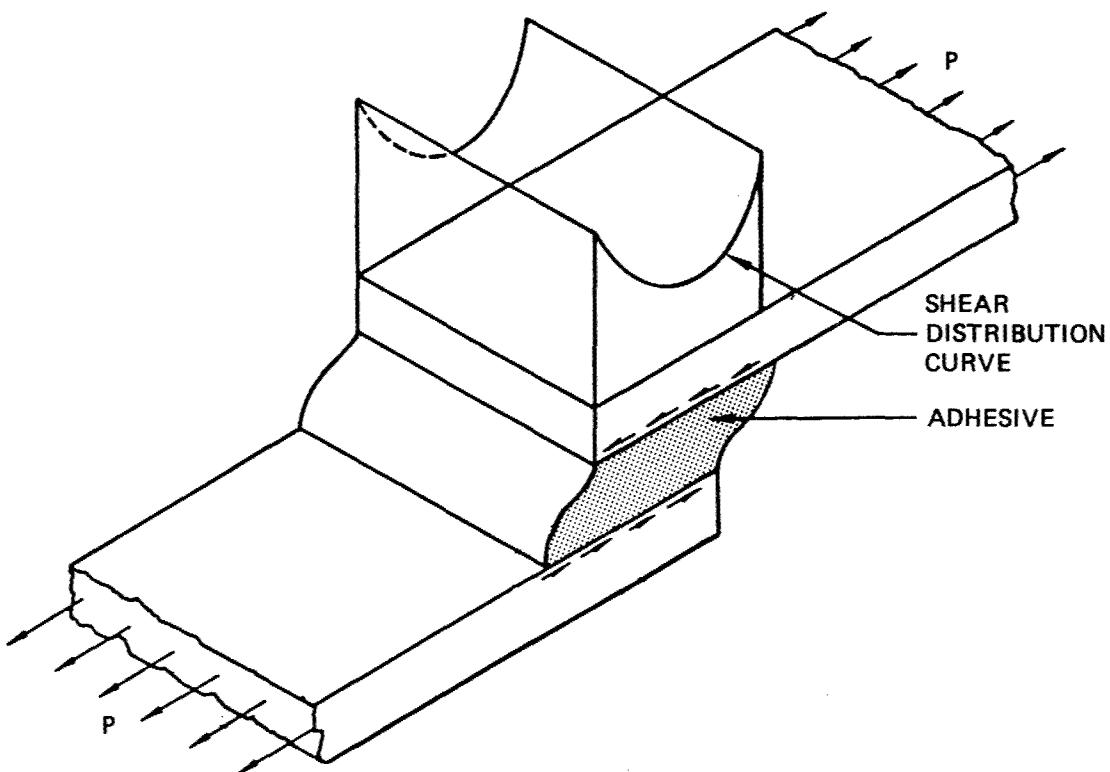
Figure 47. Lap Joint
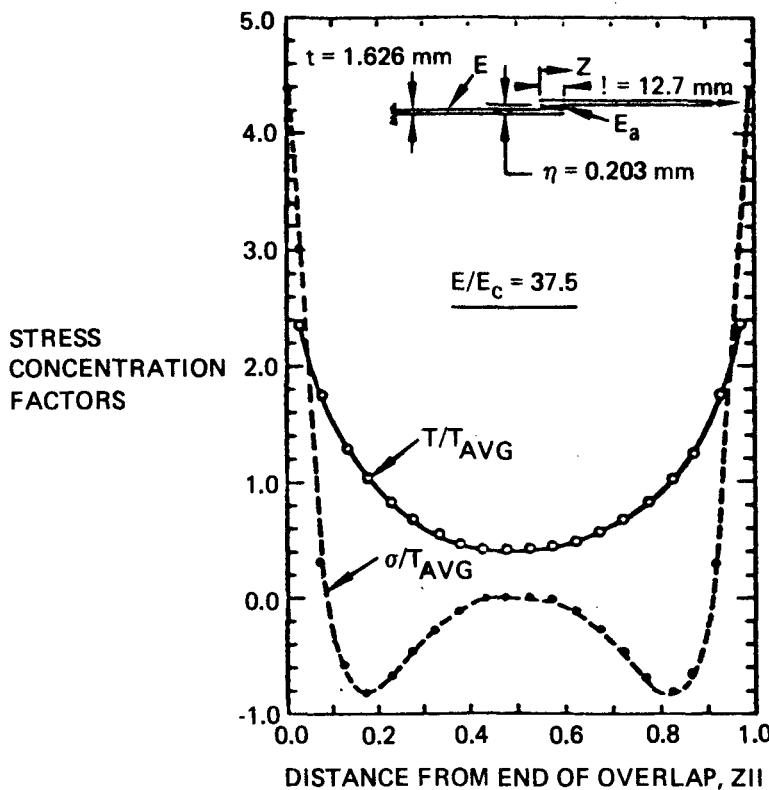
Figure 48. Results from Finite-Element Analysis Showing the Variation in the Stress Concentration with Position Along the Adhesive Bond Length

(b) Factor 2—Modulus of the Primer/Adhesive Combination

The stress gradients already described, longitudinally along the lap-shear length, are further complicated by the addition of several layers of adherents of different modulus. Additional testing reported by Guess et al. (ref 19) (fig. 49) revealed that both of these mode I and mode II stress gradients tend to decrease with increasing adherend-to-adhesive modulus, $E/E_{adhesive}$. This implies that lower modulus primer and/or adhesive or thicker lap adherends will result in reduced mode I and mode II gradients.

(c) Factor 3—Material Toughness

With the majority of materials, failure initiation occurs in the material weakest at a given stress level; however, crack propagation and subsequent failure generally occurs along the plane of least resistance, or toughness. Investigations into the mode I and mode II toughness of polymeric materials have been performed by Bascom et al. (ref 16). These investigations have shown that substantial mode I toughness gains are

81
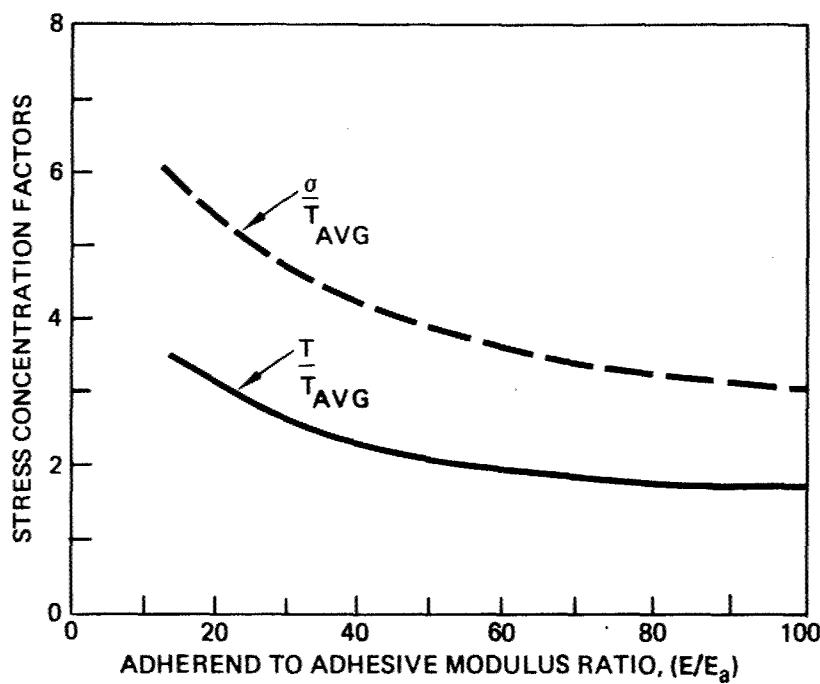
Figure 49. Results from Finite-Element Analysis Showing the Effect of E/E_a Ratio on Maximum Stress Concentration Factor in ASTM Test D 1002-72 Lap-Shear Specimen

available by elastomeric modification. However, Bascom et al. reported that these mode I toughnesses are not similarly carried over in mode I and mode II, mixed loading. In fact, the measured mixed-mode toughnesses reported were, in general, equal to the mode I toughness of the non-elastomer-modified resins.

The mode I toughness increases associated with elastomeric modifications are traditionally attributed to plastic energy zone size increases. This plastic zone size increase is believed to result from increased dilatational deformations of the matrix at the crack tip created by the triaxial stress state. However, as pointed out previously, this increased deformation, or toughness itself, does not imply increased ultimate strength, since this is a function of both crack initiation and propagation.

(d) Failure Types

The observed failure types—A, B, and C—can now be rationalized in terms of these factors.

82

Type A

Type A failures (fig. 29) occur with the elastomerically modified BR-227A primer. These failures occur on a single uniform plane within the primer 1000 to 3000A above the oxide surface. In addition, these failures were noted to occur predominantly on the epoxy side of the FM-61 duplex adhesive. This failure type is postulated to have resulted from several factors. The fact that this failure types occurs exclusively in BR-227A, regardless of oxide, indicates that it is predominantly a primer-controlled mechanism. Thus, the primer modulus and mode II toughness are rationalized as being the primary determinants of the failure plane.

In agreement with this rationalization, mechanical strain measurements, as well as fractographic information, suggest that the elastomerically modified BR-227A has a lower shear modulus than its unmodified counterpart, BR-227. Christensen (ref 8) presents the theory that the effective shear modulus of a composite consisting of glassy polymer containing a very compliant phase-separated rubber is:

$$\mu/\mu_G = 1 - (5/3) \left\{ 1 - (5/3)(\mu_R/\mu_G) \right\} c$$

where:
μ is the composite shear modulus
μ_G is the shear modulus of the glassy matrix polymer
μ_R is the shear modulus of the rubber additive
c is the volume fraction of the rubber additive

Reasonable values for the modulus ratio and c are 0.01 and 0.1, respectively. The composite modulus decreases 16% according to the above formula. This value is the "right order of magnitude" when compared to the experimental data. Furthermore, according to Bascom et al. (ref 16), the mode II toughness of BR-227A is approximately equal to or less than that of BR-227.

The resulting scenario postulates that the failure of BR-227A primed surfaces occurs primarily by mode II crack propagation in the BR-227A elastomer-modified primer. The exact locus within this primer is further postulated to occur nearest the interface of highest modulus mismatch. This would be near the oxide/primer interface. With the duplex FM-61 adhesive, these failures would be further postulated to occur on the

higher modulus adhesive side, adjacent to the oxide, where the least shear deformation alignment is allowed.

Type B

Type B failures, Figure 30, occurred with the non-elastomer-modified BR-227 primer when used with FM-61, a duplex, nitrile-phenolic/epoxy adhesive. These failures occurred on a single plane, generally just within the nitrile-phenolic side of the FM-61 adhesive.

The fact that this failure type occurs only with this primer/adhesive combination, regardless of oxide, indicates that it is predominantly a primer/adhesive-controlled failure. Both the absence of failure within BR-227 and its measured strain behaviors suggest that BR-227 has both a higher modulus and a higher mode II fracture toughness than the elastomer-modified BR-227A. The apparent weak link in this bonded joint is the nitrile-phenolic side of FM-61.

The heavily elastomer-modified appearance of the nitrile-phenolic layer suggests a similar behavior to BR-227A. This layer is assumed to have both a low modulus and a low mode II toughness. This conclusion is supportive of the assumption that the epoxy side is of a higher modulus, a result that is in general agreement with the BR-227A, epoxy-side-dominated failures.

The resulting scenario for a BR-227/FM-61 failure postulates that crack propagation occurs in the nitrile-phenolic part of FM-61, primarily by mode II loading. The exact locus within the nitrile-phenolic layer is further postulated to occur nearest the interface of highest modulus mismatch; in this case, the primer/adhesive interface.

Type C

Type C failures, Figure 31, occurred on all other oxide/primer/adhesive combinations. These failures generally occur on two planes, within the primer layer. These failures were not studied in as great detail as Types A and B.

The observed failures, as described in Section II.3.c, exhibited both uniformly slick and nonslick failures. This result, coupled with a lack of failure within the adhesive, itself suggests that a greatly improved modulus matching has been achieved with these

84

primer/adhesive combinations. The resulting failure planes appear to occur predominantly under either mode I or mode II loading, causing the subsequent failure of the less tough adherent, the primer. This means that the primer still acts as the weak link in the adhesive-bonded joints analyzed. This result indicates that new primer development that allows toughness increase without modulus decrease should result in superior lap-shear performance.

(5) Conclusions

Several distinct failure types have been recognized. These are specific to various primers and adhesives, as pointed out in Section II.3.c. Thus, the primers and adhesives, as well as their combinations, have proven to be the primary determinants of the failure locus. The exact locus has been postulated to be determined by three key factors:

1.   The overall lap-joint loading
2.   The modulus of the primer/adhesive combination
3.   The mode I and mode II toughness of the primer and adhesive system used

4. TASK IV—VALIDATION OF MECHANISMS OF BEHAVIOR DEFINED IN TASK III

a. Failure Mechanisms

Figure 50 shows the overall test plan for Task IV.
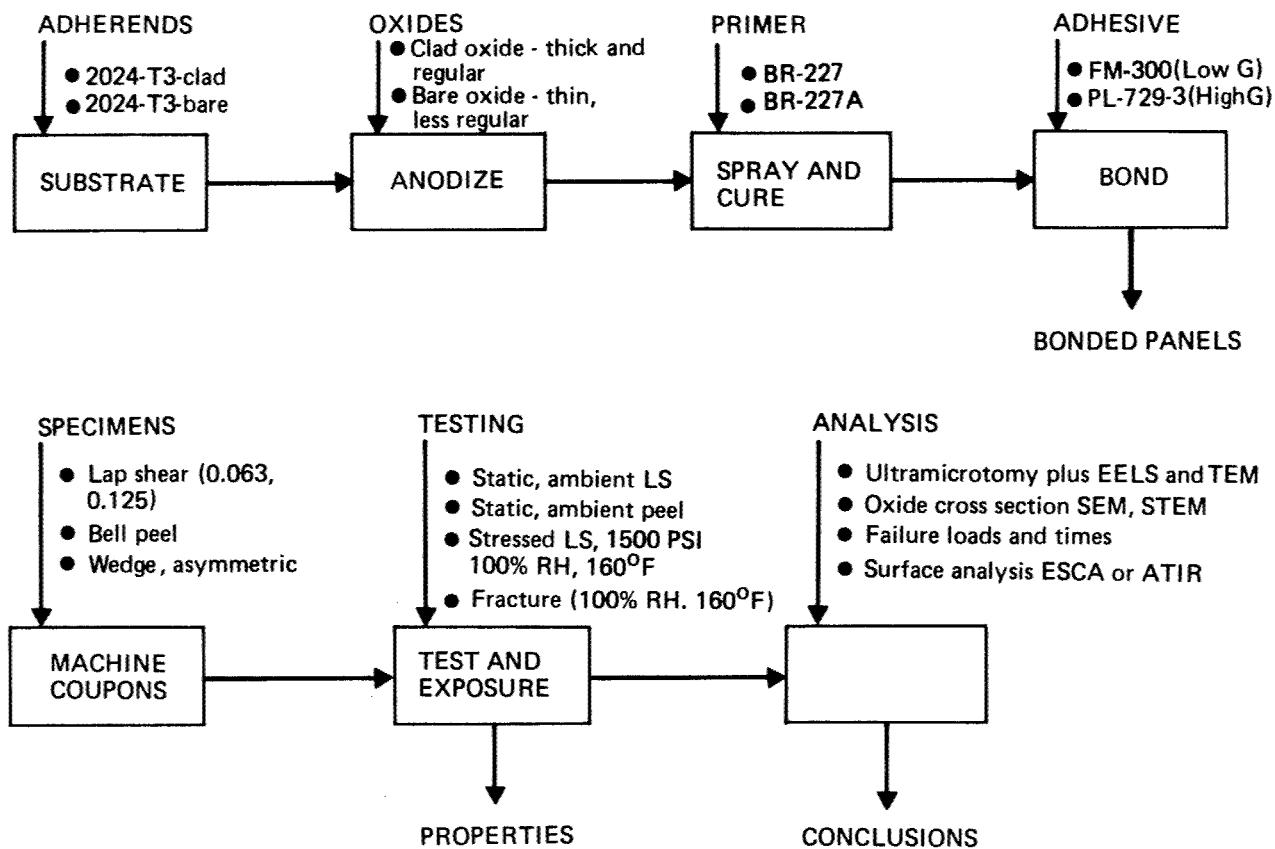
Figure 50. Task IV Test Plan

In Task III, we determined the following failure mechanisms:

1. Failure of BR-227A is cohesive in the primer layer. Primer modulus and mode II toughness are primary determinants of failure plane. Failure occurs near the interface possessing the greatest modulus mismatch, the primer/oxide interface.

2. Failure of BR-227 primed specimens occurs in the nitrile-phenolic side of the FM-61 adhesive or at the adhesive/primer interface on the nitrile-phenolic side of the FM-61 adhesive. This side of the duplex adhesive is rubber modified like BR-227A. Consequently, this layer is assumed to have a low modulus and a low mode II toughness like BR-227A.

3. A better modulus matchup of the other adhesive/primer systems results in greater lap-shear strength and stress durability.

The questions that then must be answered to verify these failure mechanisms are:

1. Will the failure mode of BR-227A change if this primer is bonded with a different adhesive?

2. Will the mechanical strength and stress durability of BR-227 improve if this primer is teamed with a better adhesive?

3. Will bonding of BR-227 and BR-227A with FM-300 and PL-729-3 adhesives (the adhesives used in the other adhesive systems) improve the performance of these primers?

The primer/adhesive systems that were tested in Task IV are as follows:

o   BR-227/FM-300

o   BR-227A/FM-300

o   BR-227/PL-729-3

o   BR-227A/PL-729-3

The adhesive systems were tested using the test configurations defined in Table 16. The strength and interfacial durability of the adhesive systems were measured at ambient and elevated temperature. The two "toughness" tests are essentially pure mode I tests that use unsymmetrical adherends that force the locus of failure toward the oxide/primer interface. This configuration promotes interfacial failure. Obviously, the Bell peel test is a measure of the peel strength of the systems. The unsymmetrical wedge test is a measure of the fracture toughness. This test configuration is recommended by Dr. W. B. Jones and W. L. Baun of AFWAL (ref 17).

Table 16. Test Configuration

Test	Adherends symmetric	Temperature	Mode	Crack	Strain rate
Bell Peel	No	75°F	I	No	Mod
Lap-Shear	Yes	75°F	Two I/II ratio	No	Mod
Wedge *	No	160°F	I	Yes	Low
Stress Lap-Shear *	Yes	160°F	One I/II ratio	No	Low

*100% Relative Humidity
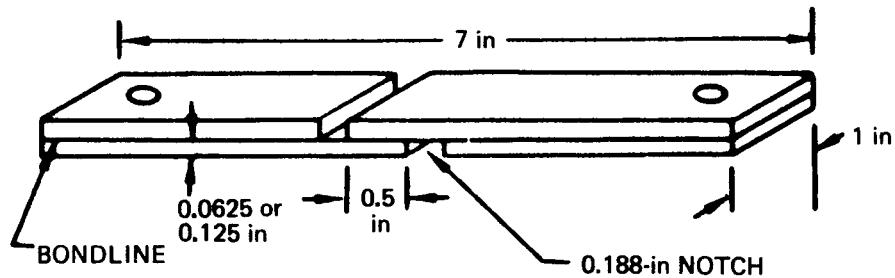
The lap-shear specimen used was the standard machined lap-shear specimen. The ambient testing was performed using 0.0625- and 0.125-inch adherends. Thin-adherend lap-shear specimens fail because of the high normal forces at the end of the lap (ref 18). For this reason, this specimen configuration is not a viable measure of an adhesive system's <u>shear</u> strength. Two reports (ref 19, 21) have recently come to our attention that recommend that thin lap-shear specimens not be used to measure shear strength. Also, this specimen should not be used to measure mode I strength or toughness. Mixed-mode tests usually should not be used because the tests are difficult to interpret. One should use pure mode tests to the extent possible, because these tests are better understood. In general, crack propagation mechanisms and the effects of boundary conditions on bonded assemblies are poorly understood. The sustained-stress lap-shear durability testing was performed using the 0.0625-inch adherends only so that these data could be compared to the previous sustained-stress lap-shear durability tests. Figure 51 illustrates the test specimen configurations.

b. Peel Test
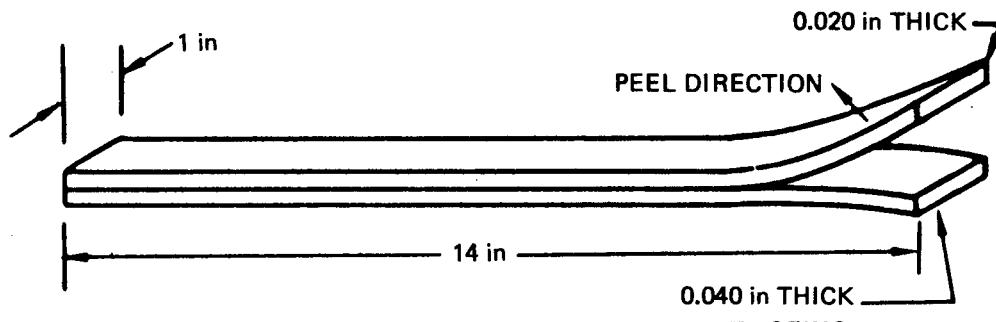
Table 17 lists the metal-to-metal peel data. Control specimens were bonded with a 250°F-curing adhesive system (BR-127 and FM-73) to verify the integrity of the PAA preparation. The average peel strength of the control specimens exceeded the specification requirement. Cohesive failures were observed in the adhesive. Peel specimens also were fabricated with BR-227 and BR-227A combined with FM-300 and PL-729-3 on optimized FPL etch. The adhesive systems (BR-227A with FM-300 and PL-729-3) on optimized FPL etch had a low peel strength. For all practical purposes, BR-227 combined with FM-300 and PL-729-3 on optimized FPL had no peel strength.

With two exceptions, the rest of the configurations tested had no peel strength. The two exceptions are BR-227A and PL-729-3 on 2024-T3 clad and bare. The peel strength of BR-227A/PL-729-3 and BR-227/PL-729-3 on PAA is as good as or better than the equivalent strength on FPL. The peel strength of BR-227A/FM-300 on 2024-T3 bare FPL may be greater than on 2024-T3 bare PAA. The most significant observation is the apparent equivalency of the peel strengths on both surface preparations.
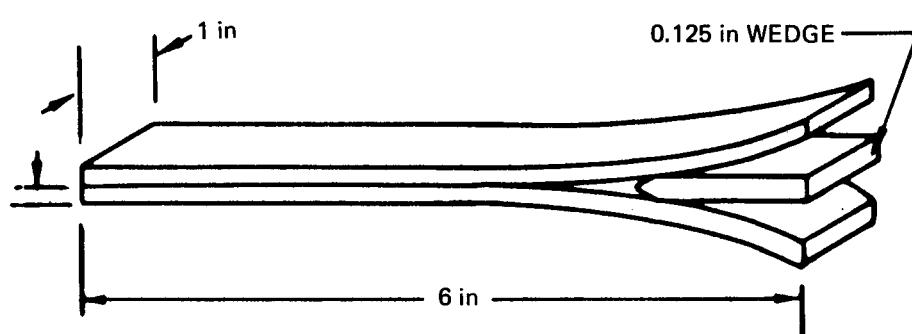
The evidence that only systems primed with BR-227A have any peel strength raises serious questions about one proposed primer failure mechanism. The unsymmetrical adherends force the failure surface into the primer/PAA interfacial region. This implies that the system BR-227A/PL-729-3 has greater adhesional strength on PAA

88

(A) MACHINED LAP SHEAR SPECIMEN

(B) PEEL SPECIMEN

(C) UNSYMMETRICAL WEDGE TEST SPECIMEN

Figure 51. Test Specimen Configurations

89

than does BR-227/PL-729-3. This contradicts the theory that the presence of the rubber additive creates a weak boundary layer.

Table 17. Room-Temperature Modified Bell Peel Test Data

Alloy/Oxide/Primer/Adhesive [1]	Peel strength (Pounds per inch width)
BR-127/FM-73-Bare PAA [2]	62.7 + 3.2
BR-227A/PL-729-3-Clad PAA	22
BR-227A/PL-729-3-Bare PAA	23
BR-227/PL-729-3-Clad PAA	6*
BR-227/PL-729-3-Bare PAA	5*
BR-227A/PL-729-3-Clad FPL	15
BR-227A/PL-729-3-Bare FPL	14
BR-227/PL-729-3-Clad FPL	8*
BR-227/PL-729-3-Bare FPL	4*
BR-227A/FM-300-Clad PAA	6*
BR-227A/FM-300-Bare PAA	10*
BR-227/FM-300-Clad PAA	4*
BR-227/FM-300-Bare PAA	6*
BR-227/FM-300-Bare FPL	4*
BR-227A/FM-300-Bare FPL	20

*Peel strength of Specimen is too low to bend .020" peel strip around roller

[1] The alloy is 2024-T3 aluminum

[2] Controls

c. Ambient Ultimate Lap-Shear Test

The room-temperature lap-shear test data for two adherend thicknesses are listed in Tables 18 and 19. The data reported are the mean value for five samples. The statistical test for the difference between means using Student's t distribution and a 1% critical value was employed to determine if different groups of lap-shear values are statistically significant.

All lap-shear strengths of specimens using FPL reported in Table 18 are superior to those on PAA and are statistically significant, except:

Adhesive System	Statistical Analysis Results
BR-227/FM-300 clad	Equivalent strength
BR-227/FM-300 bare	Equivalent strength
BR-227A/PL-729-3 clad	Superior strength on PAA

90

Table 18. Room-Temperature Lap-Shear Test Data (0.0625-inch Adherend)

Primer/Adhesive	PAA		FPL	
	Clad	Bare	Clad	Bare
BR-227/FM-300	3519	3535	3545	3880
BR-227/PL-729-3	3021	3418	4660	4520
BR-227A/FM-300	2486	2577	3253	2233
BR-227A/PL-729-3	2483	2457	2167	2776

Aluminum alloy is 2024-T3

Table 19. Room-Temperature Lap-Shear Test Data (0.125-inch Adherend)

Primer/Adhesive	PAA		FPL	
	Clad	Bare	Clad	Bare
BR-227/FM-300	4416	4656	4594	4726
BR-227/PL-729-3	4256	4856	3038	3508
BR-227A/FM-300	3156	3229	2216	3012
BR-227A/PL-729-3	3296	3172	2770	2388

Aluminum alloy is 2024-T3

The lap-shear strength on FPL was superior to equivalent values on PAA in five of eight cases. In all cases, BR-227 had higher lap-shear values than BR-227A on the same surface preparation.

All lap-shear strengths of specimens using PAA reported in Table 19 are superior to those on FPL and are statistically significant, except for BR-227/FM-300 clad and bare. The lap-shear strength is equivalent statistically for the systems BR-227/FM-300 FPL and BR-227/FM-300 PAA on the 2024-T3 clad aluminum. The adhesive system has superior shear strength, statistically, on 2024-T3 bare FPL in comparison to 2024-T3 bare PAA. In practice, the data are equivalent. On the same surface preparation, BR-227 had greater lap-shear values than BR-227A. In six out of eight cases, PAA was superior to FPL.

91

The primer BR-227A has reduced shear strength because the rubber additive reduces the modulus of the composite material (epoxy matrix and rubber additive). See Section II.3.

d. Unsymmetrical Wedge Test

The unsymmetrical wedge test data are presented in Table 20. The standard Boeing wedge test was used, except that the adherend thicknesses were 0.0625 and 0.125 inch. An unsymmetrical configuration was used to force the failure surface into the inter-facial region between the adhesive primer and the anodic oxide. This test configura-tion is recommended in reference 17. The testing environment was 160°F/condensing humidity.

All specimens listed in Table 20 had acceptable crack propagation rates, defined as less than 0.3-inch crack extension in 4 hours. The specimens primed with the unmodi-fied adhesive primer, BR-227, consistently had the best crack propagation rates.

Table 20. Unsymmetrical Wedge Test Data

Alloy	Surface prep	Primer	Adhesive	1 Hr*	4 Hr*	24 Hr*	1 Wk*	2 Wk*
2024-T3-bare	PAA	BR-227	FM-300	–	.028± .001	–	.096± .005	–
2024-T3-clad	PAA	BR-227	FM-300	–	.042± .016	–	.092± .014	–
2024-T3-bare	PAA	BR-227A	FM-300	.186± .063	.16± 0 ①	–	–	–
2024-T3-clad	PAA	BR-227A	FM-300	.064± .030	.090± .42 ②	–	–	–
2024-T3-bare	PAA	BR-227	PL-729-3	–	.020± 0 ①	–	.047± .015 ③	–
2024-T3-clad	PAA	BR-227	PL-729-3	–	.020± 0 ②	–	–	–
2024-T3-bare	PAA	BR-227A	PL-729-3	.074± .023	.126± .019	.158± .019	–	–
2024-T3-clad	PAA	BR-227A	PL-729-3	056± .015	.088± .013	.110± 0 ①	–	–

*Crack extension in inches

e. Thin-Adherend Stressed Lap-Shear Test

In Table 21, data are listed for the 0.0625-inch-thick symmetrical adherend machined stress lap-shear specimens. A sustained stress of 1500 lb was used because this is the maximum stress that the spring fixture would develop.

It is interesting to note that all specimens primed with BR-227A have extremely poor stress-durability values. These values are as low as or lower than equivalent specimens on FPL etch during the earlier stress lap-shear testing. Obviously, these values are very inferior to equivalent specimens (BR-227A/FM-61) on PAA.

Because of time constraints, the test was stopped after 1008 hours. The residual strength of all remaining specimens was determined. None of the specimens primed with BR-227 failed during the test. The mean, standard variation, and variance of the residual strength for the BR-227 primed specimens are listed in Table 21. Four specimens were tested.

Table 21. Stress Lap-Shear Test (0.0625-inch Symmetrical Adherends)

Alloy	Surface prep	Primer	Adhesive	Exposure (hr)	Residual strength	Standard deviation	Variance
2024-T3-clad	PAA	BR-227	PL-729-3	1008	3785	487	178025
2024-T3-bare	PAA	BR-227	PL-729-3	1008	4090	197	29250
2024-T3-clad	PAA	BR-227	FM-300	1008	4078	79	4669
2024-T3-bare	PAA	BR-227	FM-300	1008	4003	39	1169
2024-T3-clad	PAA	BR-227A	FM-300	222	–	–	–
2024-T3-bare	PAA	BR-227A	FM-300	246	–	–	–
2024-T3-clad	PAA	BR-227A	PL-729-3	30	–	–	–
2024-T3-bare	PAA	BR-227A	PL-729-3	74	–	–	–

The BR-227 primed specimens, in general, have the highest residual strengths of all those investigated. However, it must be remembered that the previous stress lap-shear test ran for over four times the duration of the current test, and it is very difficult to predict what the residual strength of these specimens would be at the longer test duration.

These residual lap-shear strengths are superior to those of the Series B lap-shear specimens primed with the same primer (BR-227). These strengths are excellent. Only the thick-adherend stress lap-shear specimens listed in Table 19 have higher shear strength. Consequently, the shear strength of the specimens has increased, possibly due to an aging effect (see table 18).

The mechanical properties—specifically, room-temperature and stress lap-shear strengths—of specimens primed with BR-227 were improved by combining this primer with FM-300 and PL-729-3 adhesives. Even the room-temperature lap-shear strength on 0.0625-inch-thick adherends improved. Also, the unsymmetrical wedge test data for BR-227 primer are superior to those for BR-227A. Consequently, the mechanical properties of systems primed with BR-227 have been improved.

The mechanical performance of bonded systems primed with BR-227A has not been improved. However, both room-temperature and stress lap-shear performance of BR-227 would be superior to that of BR-227A because of BR-227's higher modulus. The superior wedge performance of BR-227 is unexplained.

f. Failure Analysis

The room-temperature lap-shear data are not consistent. Using 0.0625-inch adherends, the measured shear strength on FPL is as good as or better than the shear strength on PAA for the same adhesive system. Using thicker adherends, the shear strength on PAA is greater than that on FPL for the same adhesive system. The thinaherend lap-shear specimen fails in peeling mode because of the significant normal stress gradients, while the thick-adherend specimen more nearly measures the shear strength.

Since many bonded assemblies transfer their load in shear, it is important that accurate estimates of the shear strength be obtained. Consequently, the primers are not incompatible with PAA as the earlier mechanical testing may have indicated.

The failure mode of BR-227A is Type A for both adhesives and surface preparations. Primer BR-227A fails in a Type A mode on the thick-adherend lap-shear specimen also. Figures 52 and 53 represent transverse SEM/STEM views of the fracture surfaces generated by BR-227A with FM-300 on 2024-T3 clad PAA and FPL oxides, respective-

ly. These photomicrographs are representative of the failure mode of BR–227A/ PL–729-3 on 2024-T3 clad PAA and FPL.
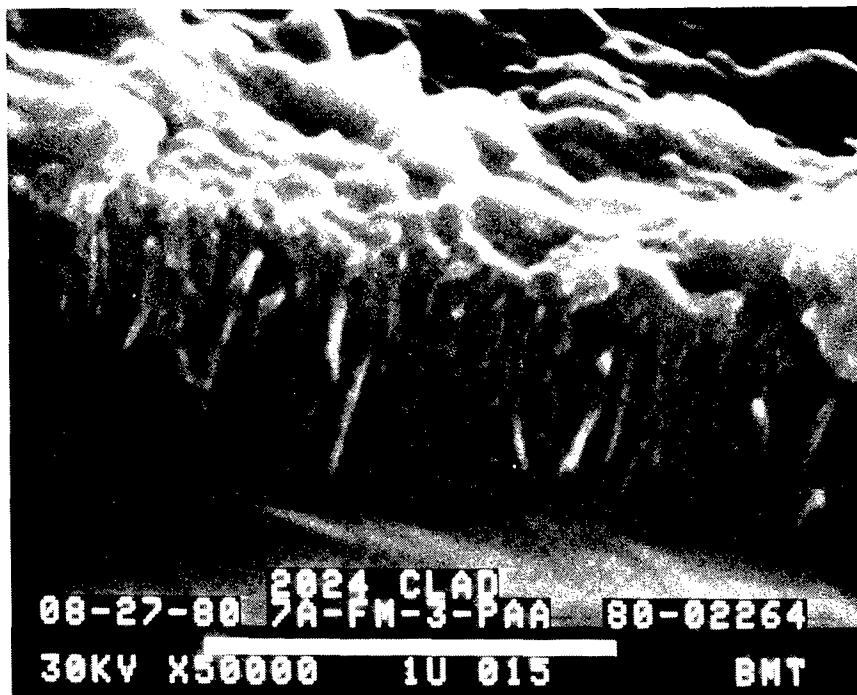
Figure 52. Transverse View of BR-227A/FM-300 on 2024-T3-Clad PAA

Figure 53. Transverse View of BR-227A/FM-300 on 2024-T3-Clad FPL

95

The failure mode of BR-227 is Type C (see Section II.3) in Task IV for both adhesives on both surface preparations. This also is true for both lap-shear adherend thicknesses and both aluminum alloys used. We were able to change the failure mode of BR-227 from Type B to Type C by using either of two adhesives whose failure mode in Task III is Type C. This confirms the mechanism defined in Task III, which states that the weak link for the system BR-227/FM-61 is the nitrile-phenolic side of the FM-61 adhesive.

Specimens bonded with BR-227/FM-300 and BR-227/PL-729-3 have visually detectable primer films over most of the surface of both adherends. Figure 54 depicts the relatively heavy primer coverage existing on the overall failure surface. This is the failure surface of BR-227/FM-300 on 2024-T3 clad FPL. There are some discrete regions of very thin residual primer, particularly on the PAA oxide analyzed (fig. 55). Representative samples also were analyzed with a Nicolet 7199 Fourier Transform Infrared Spectrometer equipped with an attenuated total reflection attachment (FTIR-ATR). The spectrum of a phosphoric acid anodized aluminum panel was subtracted from the spectrum of the failed specimens. The reslting spectrum demonstrated the presence of a residual primer layer on the adherend. Thus, it appears that the failures occur predominantly by crack propagation within the primer. However, this crack apparently is not localized to any specific locus and acts similarly to the PL-728/PL-729-3 primer/adhesive system.

Figure 54. Failure Surface of BR-227/FM-300 on 2024-T3-Clad FPL

96
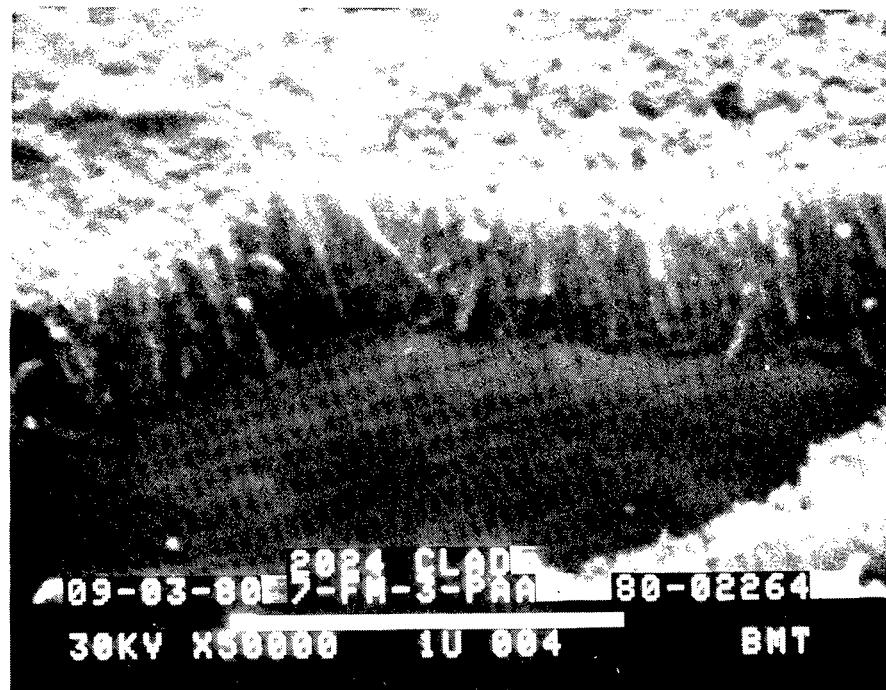
Figure 55. Transverse View of BR-227/FM-300 on 2024-T3-Clad PAA

The overall fracture morphology of BR-227 remains essentially the same as when it was combined with FM-61. The fracture surface morphology is generally featureless, revealing little evidence of plastic deformation. This result further verifies the brittleness, low ductility, and low strain of the BR-227 primer.

The failure surfaces of BR-227A/PL-729-3 and BR-227/PL-729-3 are, for all practical purposes, identical to those of BR-227A/FM-300 and BR-227/FM-300.

In conclusion, Task IV has verified the failure mechanisms determined in Task III.

5. TASK V—RANGE OF MATERIALS AND ENVIRONMENTAL PARAMETERS FOR ACCEPTABLE BONDED JOINT PERFORMANCE

The primary purpose of this task was to indicate how the performance of elevated-service-temperature bonded joints may be improved.

This task is divided into the following sections:

1. Surface preparation conclusions

2. Test conclusions

3. Primer formulation conclusions

4. Adhesive mechanical property conclusions

5. Failure analysis method conclusions

a. Surface Preparation Conclusions

Based on research on the PAA process at Boeing, the following points are recommended:

1. One's concept of oxide/primer compatibility depends on the design criteria used or the load that the assembly experiences. If the bonded assembly transfers its load in shear, PAA will provide better mechanical strength. If environmental durability is desired, PAA performs beter. If the bonded assembly experiences greater normal stresses, FPL etch provides better strength. Many assemblies are designed to transfer load in shear. Consequently, we believe that PAA is superior to FPL for most bonded applications.

2. The preferred anodization temperature has been raised from 72 to 77°F. Raising this temperature reduced the probability of an interfacial failure when 250°F-curing adhesive systems, anodized at the low end of the temperature range, were tested with the "wet peel" test. This test is a modified Bell peel test during which a detergent solution is placed in the crevice between the two metal adherends. This is a good, but severe, test of primer/oxide compatibility. An anodization temperature of 77°F would be consistent with current manufacturing practice.

3. The PAA process must be conducted within the acceptable parameter limits. A purple color on the metal surface is necessary, but not sufficient, for guaranteeing an acceptable surface for bonding.

b. Test Conclusions

The following tests are recommended for evaluating a new primer:

1. Lap-shear test—A thick-adherend machined lap-shear specimen should be used so that the adhesive system is evaluated primarily in shear. Accurate estimates of the strength are necessary because most bonded joints transfer load in shear. The effects of moisture and/or sustained stress can be evaluated using the same specimen.

2. Wedge test—The wedge specimen is a good, but essentially qualitative, method of measuring the fracture toughness of the system. An unsymmetrical wedge is a measure of mode I toughness.

3. Bell peel test—This test is a good peel test that uses unsymmetrical adherends. This test is preferable to the thin-adherend lap-shear test for testing peel strength.

4. Honeycomb peel—If the primer will be used to bond honeycomb core, then the honeycomb peel test should be employed.

c. Primer Formulation Conclusions

1. Primer strength and durability were determined during this investigation. The lap-shear test measured the ultimate shear strength of the adhesive-bonded joint. The wedge and stress lap-shear tests measured the environmental durability of the adhesive-bonded joint. Epoxy primers have high shear strength, which is advantageous to the former test. However, they are brittle, which is detrimental to the latter tests. Investigations at Boeing have identified five different types of epoxy materials with varying degrees of toughness. The five materials are:

   a. A brittle epoxy compound. An example of this is BR-227 epoxy primer.

   b. An epoxy compound modified with an incoherent rubber additive. Such an additive is not reactive. These additives form phase-separated rubber particles that have poor mechanical linkage with the matrix resin. An example is BR-227A.

   c. An epoxy compound modified with a coherent rubber additive. Such an additive is probably reactive. An example of a reactive rubber additive is carboxy-terminated butadiene-acrylonitrile (CTBN). These additives form phase-separated rubber particles that have good mechanical linkage with the matrix resin. An example is PL-728 epoxy primer.

   d. An epoxy compound toughened by modifying the matrix resin itself. In many instances, the manner in which this is accomplished is proprietary to the formulator. An example is PL-728.

   e. An epoxy compound modified with a coherent rubber additive and possessing matrix ductility. This type of compound can possess the greatest toughness. An obvious example is PL-728. The good environmental durability of this primer is explained by its toughness. The environmental durability of BR-227A is poor because of its limited toughness.

   Toughening an epoxy resin can result in a loss of shear strength. An example of this is BR-227A. This is probably the greatest single problem to be solved for

99

high-temperature adhesive primers. Reactive rubber additives and/or toughened matrix resins appear to be a means of formulating primers with good shear strength and environmental durability.

2. The primer must be chemically compatible with the adhesive with which it is to be used.

3. The mechanical properties of the primer must be compatible with the adhesive with which it is to be used.

d. Adhesive Mechanical Property Conclusions

1. The mechanical properties of the adhesive must be commensurate with those of the primer. Otherwise, the adhesive will fail instead of the primer. An example of this is the failure of BR-227/FM-61.

2. Because there are so many unknowns, more than one adhesive must be used to test any new primers being formulated.

e. Failure Analysis Method Conclusions

1. If this investigation demonstrated anything, it illustrated the importance of a thorough, systematic failure analysis.

2. The most definitive, but also most expensive, failure analysis technique for analyzing the primer/oxide interface is ultramicrotomy, followed by transmission electron microscopy.

3. It is very important that the failure mode and ductility of the failure surface be determined so that the mechanical test data can be properly interpreted.

SECTION III

RECOMMENDATIONS

The following are recommended:

1. There must be industry-wide agreement as to what constitutes the compatibility criterion between 350°F-curing adhesive primers and surface preparations for bonding. Currently, this agreement does not exist. The position taken in this report is that the shear strength, as measured by the thick-adherend lap-shear specimen, is the appropriate criterion. Many bonded assemblies are designed to transfer their load in shear. Other people contend that the shear strength, as measured by the thin-adherend lap-shear specimen, is appropriate.

2. The controversy concerning testing bonded joints with thin-adherend lap-shear specimens must be resolved. The position taken in this report is that the thin-adherend lap-shear specimen is not a suitable measure of bonded joint shear strength. It is a mixed-mode test that is difficult to interpret.

3. More information is needed to describe how the surface preparation affects the mechanical strength of bonded joints. The shear strength of the 350°F-curing adhesive systems that were tested is greater on PAA than on FPL. When the normal stress gradients present are increased, 350°F-curing adhesive systems have greater strength on FPL than on PAA.

4. This investigation has determined that if 350°F-curing adhesive primers are to possess good environmental durability, they must be tough. However, toughening the system should not result in significant loss of shear strength. Using coherent rubber additives (i.e., those that provide good mechanical linkage between the phase-separated rubber particles and the matrix resin) and/or ductile matrix resins appear to be two approaches to obtaining good strength and toughness. These approaches should be be further developed for 350°F-curing adhesive primers.

5. The PL-728/PL-729-3 system is recommended over the BR-227A/FM-61 or BR-227/FM-61 systems. Primer PL-728 has good matrix ductility.

6. Teaming BR-227 with a different adhesive would result in higher strength bonds. This may be productive for some applications. The toughness of the bonded joint would be limited by the low ductility of this primer.

7. The two model primers should be evaluated further as potential new "production" primers. These systems have good strength and durability.

REFERENCES

1. J. A. Marceau, "An SEM Analysis of Adhesive Primer Oriented Failures on Anodized Aluminum," 23rd National SAMPE Symposium and Exhibition, Los Angeles, CA, May 2-4, 1978.

2. Boeing Letter B-8800-429L dated January 7, 1977, from J. A. Marceau to H. S. Schwartz, AFWAL/MLBC.

3. J. A. Marceau and J. C. McMillan, "Exploratory Development on Durability of Adhesive Bonded Joints," Technical Report AFML-TR-76-173, October 1976.

4. P. G. Hoel, Introduction to Mathematical Statistics, John Wiley & Sons, New York, NY, 1954, pp. 211-228.

5. C. R. C. Standard Mathematical Tables, ed. C. D. Hodgman, Chemical Rubber Publishing Company, Cleveland, OH, 1959.

6. H. S. Schwartz, "Effect of Adherend Surface Treatment on Stressed Durability of Adhesive Bonded Aluminum Alloys," presented at Symposium on Durability of Adhesive Bonded Structures, U.S. Army Armament Research and Development Command, Dover, NJ, October 27-29, 1976; also published in SAMPE Journal, vol. 13, no. 2, March/April 1977.

7. J. A. Marceau and D. B. Arnold, "Technical Proposal—Relationship of Interfacial Compatibility to Durability of Adhesive-Bonded Joints," Boeing Document No. D180-24255-1, May 15, 1978.

8. R. M. Christensen, Mechanics of Composite Materials, John Wiley & Sons, New York, NY, 1979, pp. 292-294.

9. Douglas Aircraft Company, "Primary Adhesively Bonded Structure Technology (PABST)," Air Force Technical Report AFFDL-TR-76-141, December 1976.

10. Unpublished Boeing results, J. A. Marceau, 1970-1977.

11. S. Wernick and R. Pinner, "The Surface Treatment and Finishing of Aluminum and Its Alloys," vol. 1, Robert Draper Ltd., Teddington, 1972.

12. Boeing Process Specification BAC 5555, Rev. E, "Phosphoric Acid Anodizing of Aluminum for Structural Bonding."

13. Bell Helicopter Company Process Specification BPS FW 43452, Rev. G, "Surface Preparation of Materials for Adhesive Bonding."

14. Netherlands Aircraft Factories Fokker-VFW per British Mil Specification DEF 151.

15. Boeing Process Specification BAC 5514, Rev. P, "Common Bonding Requirements for Structural Adhesives."

16. W. D. Bascom, R. L. Jones, and C. O. Timmons, "Mixed Mode Fracture of Structural Adhesives," American Chemical Society, Division of Organic Coatings, Plastics Chemistry, preprint vol. 35, no. 1, 1975; meeting, Philadelphia, PA, April 7-11, 1975, pp. 501-511.

17. W. L. Baun, "Adhesive Bonding Experiments for Titanium 6 Aluminum 4 Vanadium (Ti-6Al-4V)—Part 1: Anodization Treatments," Technical Report AFML-TR-79-4172, Part 1, December 1979.

18. W. C. Wake, "Sticking Together to Last," Industrial Research & Development, vol. 21, no. 8, August 1979, pp. 94-98.

19. T. R. Guess, R. E. Allred, and F. P. Gerstle, Jr., "Comparison of Lap Shear Test Specimens," Journal of Testing and Evaluation, vol. 5, no. 2, March 1977, pp. 84-93.

20. E. A. Ledbury, A. G. Miller, P. D. Peters, E. E. Peterson, and B. W. Smith, "Microstructural Characterization of Adhesively Bonded Joints," 12th National SAMPE Technical Conference, Seattle, WA, October 7-9, 1980.

21. P. A. Cooper and J. W. Sawyer, "A Critical Examination of Stresses in an Elastic Single Lap Joint," NASA Technical Paper 1507, September 1979.

APPENDIX A

METHODS FOR CHARACTERIZING OXIDE
TOPOGRAPHY AND CHEMISTRY

INTRODUCTION

A variety of analytical techniques are used to analyze oxide structures, primer/oxide interactions, and failure modes. These techniques are:

1. Secondary electron imaging in:

    a. Scanning electron microscope (SEM)

    b. Scanning transmission electron microscope (STEM)

2. Transmitted electron imaging in:

    a. Transmission electron microscope (TEM)

    b. Scanning transmission electron microscope (STEM)

3. Surface analysis by:

    a. Auger electron spectroscopy (AES)

    b. Depth profiling by AES with sputter etching

    c. X-ray photoelectron spectroscopy (XPS)

These techniques are described in the following sections, together with a description of specimen preparation for each method.

SECONDARY ELECTRON IMAGING

This technique allows photomicrographs to be taken of surface features of a specimen at magnifications up to 200,000X. Secondary electron images can be taken in either an SEM or an STEM. The relative advantages of the two instruments are described. Basically, the STEM offers higher ultimate resolution capabilities than the SEM, but only at the cost of specimen handling limitations.

SPECIMEN PREPARATION

For showing the interaction zones between primer/oxide and primer/adhesive, a rapid screening technique was developed using the SEM. This involved a polish/etch process. Bonded specimens were cut at an oblique angle and polished metallographically to 0.25-μm finish. The polished specimen surfaces were etched with formic acid or Dynasolve 160 for 1 to 4 minutes, depending on the system. The surfaces were rinsed with tap water and air dried.

To view oxide structure or an oxide/primer interaction zone without the polish/etch technique, a suitable surface must be exposed. This is done by bending a specimen

107

until the oxide layer fractures, exposing a clean inner surface. Figure A-1 illustrates the process. A thin coating of a heavy metal is required on the surface of the specimen, and Boeing has made significant improvements in this area.

OXIDE LAYER, TYPICAL

BASE METAL

STRIP CUT FROM
PANEL - SIDE VIEW

END VIEW

RELIEF CUT OUT
TO ALLOW FRACTURING

CUT OFF FOR SEM OR
STEM SPECIMEN

BEND TO FRACTURE
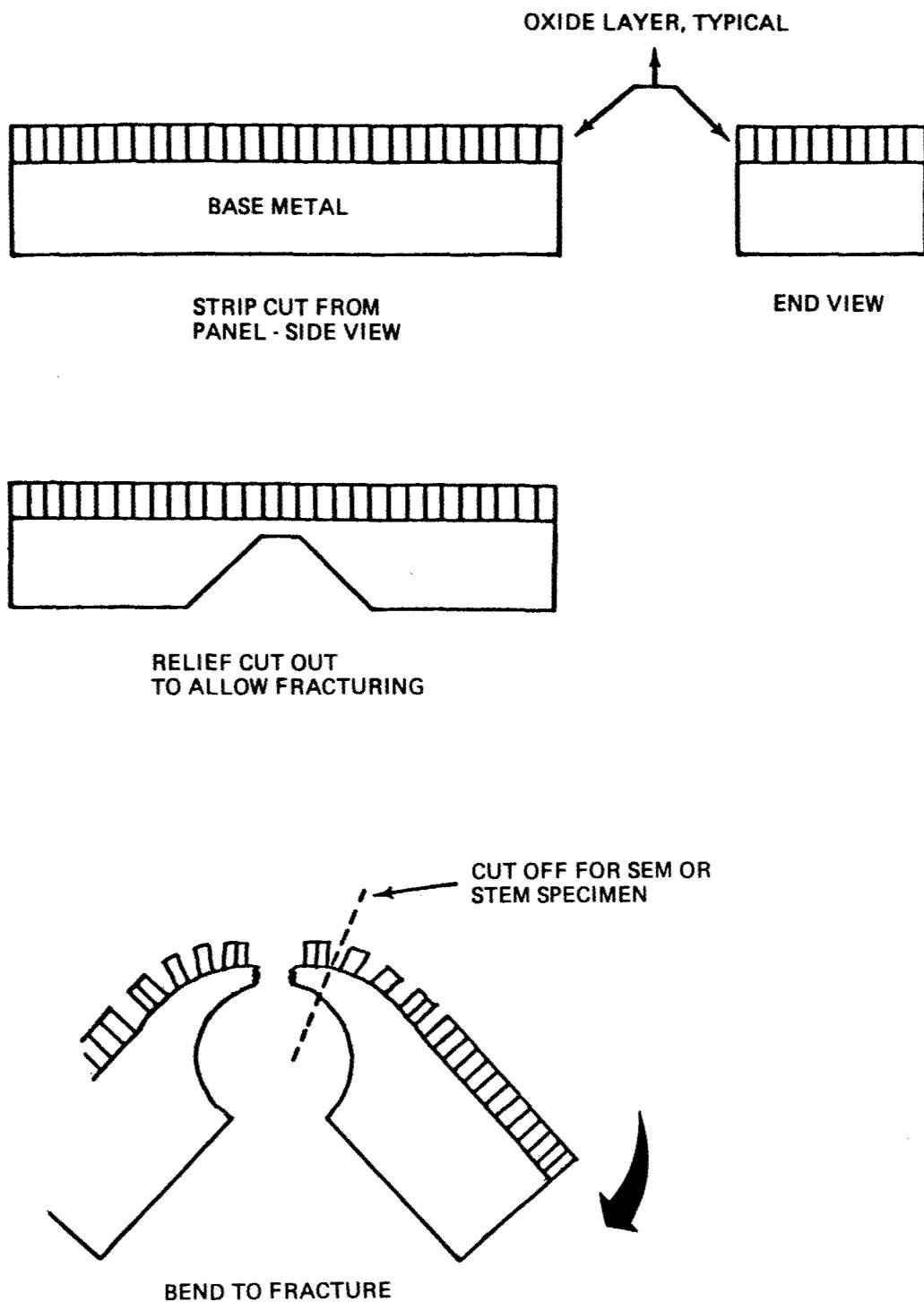
Figure A-1. Schematic of Specimen Preparation

Figure A-2 shows the PAA oxide on 7075-T6 in a photomicrograph taken in 1976. The structure shows a globular, rounded appearance not expected of the oxide structure. Figure A-3 shows a top view of the oxide structure indicating the same globular features as seen in Figure A-2. In both cases, the coating was a layer of vapor-deposited Au approximatley 70A thick.

(a)

(b)
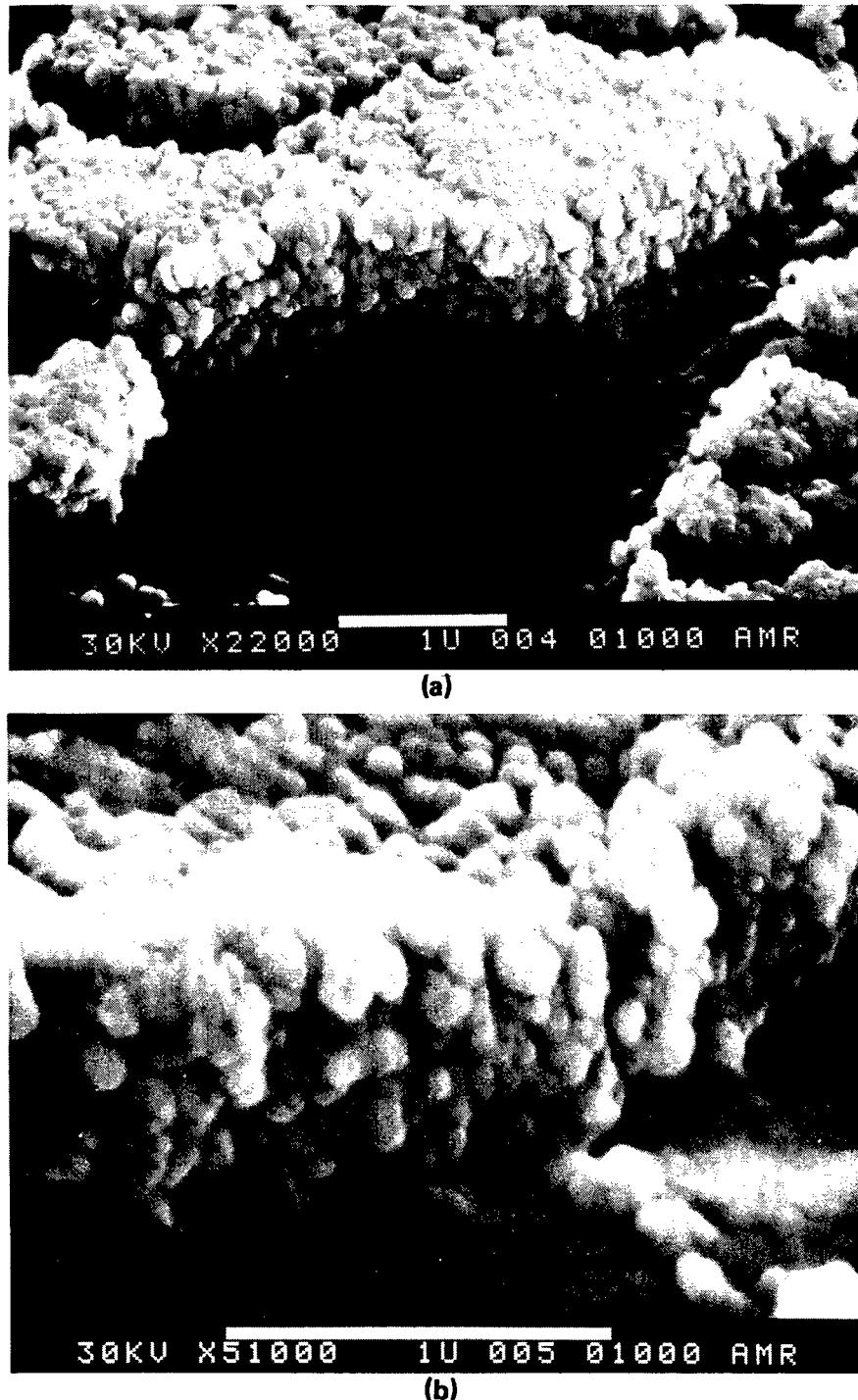
Figure A-2. SEM Photomicrographs of PAA Oxide on 7075-T6, Gold Coated, Fractured Oxide (a) x22,000 (b) x51,000
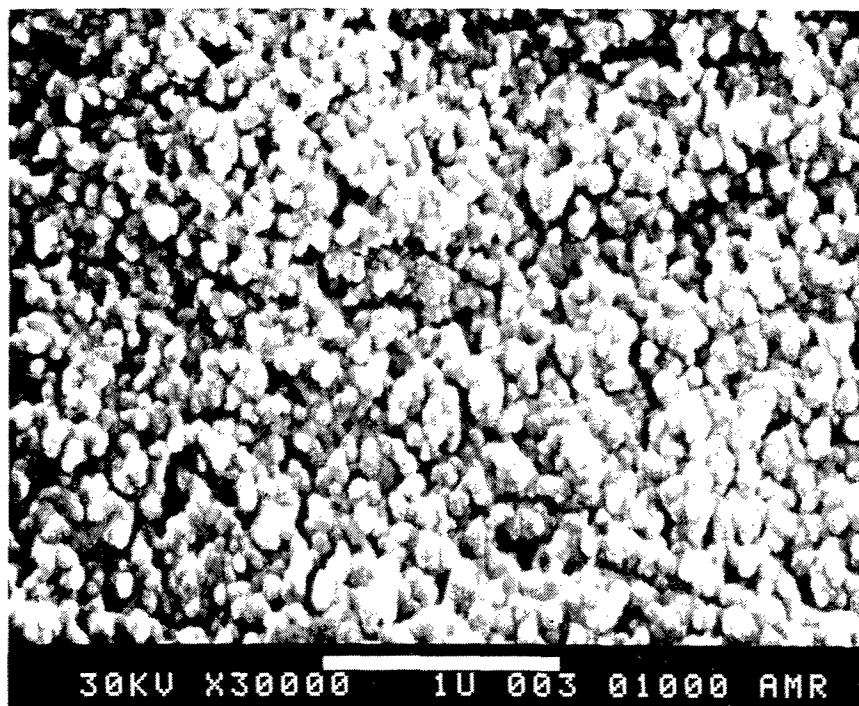
*Figure A-3. SEM Photomicrograph of PAA Oxide on 7075-T6,
Gold Coated, Top View of Oxide x30,000*

The observed structures are interpreted as being artifacts caused by crystal nucleation and growth of the Au. Each spheroidal structure may consist of individual grains of gold clumping together due to surface energy effects. The clumping totally obscured the oxide structure underneath. Thus, crystal nucleation and growth characteristics of Au films of this thickness obscure the native oxide structure.
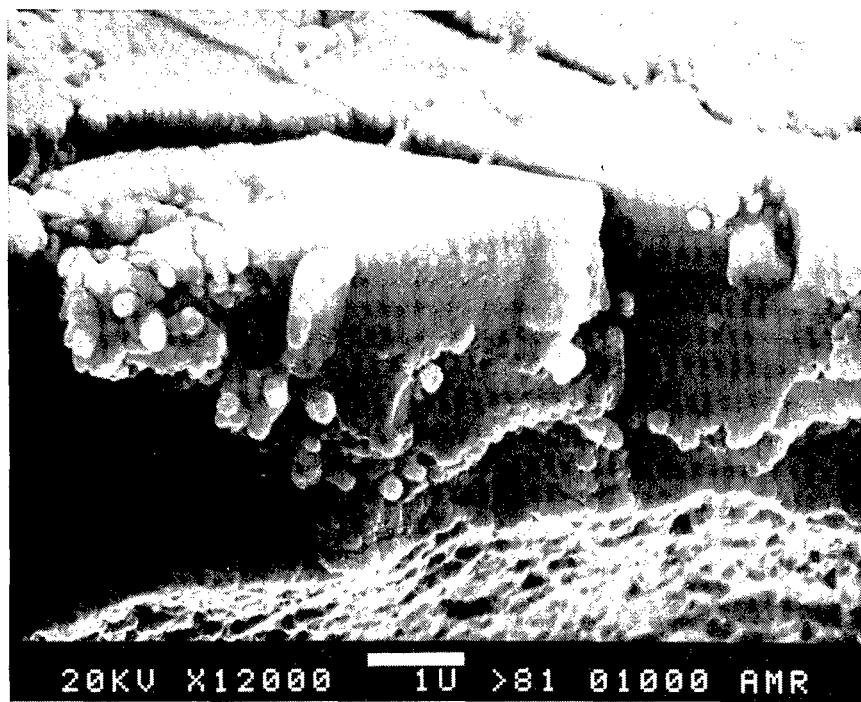
Figure A-4 shows the interaction zone between PL-728 primer and 7075-T6 PAA oxide. Again, the coating artifacts obscure the primer and oxide interactions, as well as the oxide structure.

These photomicrographs show no details of the oxide structure because of a problem in coating technology. At higher magnifications than shown, the photomicrographs begin to appear "fuzzy" and "grainy." These symptoms would indicate a limiting effect of the electron beam diameter, as well as a signal-to-noise (SNR) problem with the instruments at magnifications of 50,000.
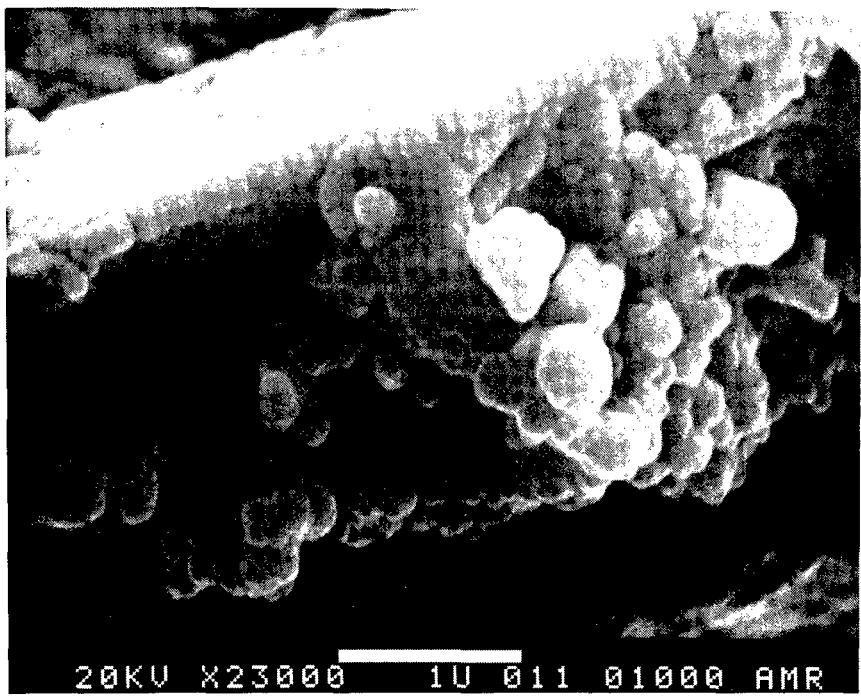
CURRENT CAPABILITIES

The recent improvements in Boeing SEM photomicrographs are due to:

1.   Better surface coating technology through the careful use of vapor-deposited Au/Pd alloys, rather than Au (the coating thickness is less than 50A)

110

(a)

(b)

Figure A-4. SEM Photomicrographs of PAA Oxide on 7075-T6, Covered with PL-728 Primer, Cold Coated, Fractured Specimen (a) x12,000 (b) x23,000

111

2. Improved electron source brightness through the use of a lanthanum hexaboride electron source in the Boeing SEM

3. An extremely large amount of cleaning and "tune-up" on the Boeing SEM to keep it at its ultimate resolution limits

SEM photomicrographs of PAA oxide on 2024-T3 clad are shown in Figures A-5, A-6, and A-7. The detail enhancement due to coating technology improvements is striking when compared to Figures A-2 and A-3. The oxide cell walls and branching are resolvable at higher magnifications than were obtainable earlier.
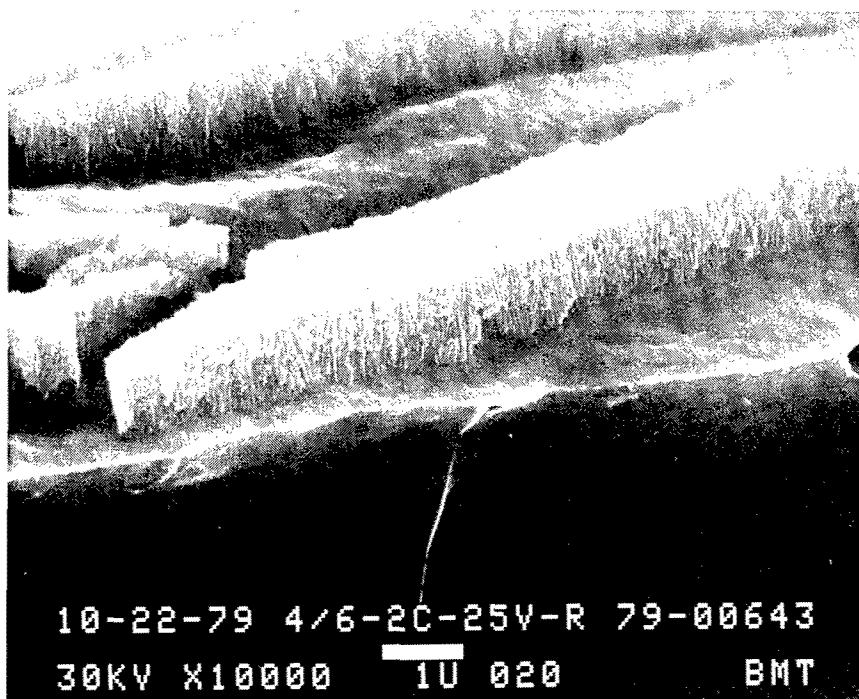
Figure A-5. SEM Photomicrograph of PAA Oxide on 2024-T3-Clad, Au/Pd Coated, Fractured Specimen x10,000

SEM/STEM CAPABILITIES

With the improvements in coating technology, the maximum resolution attainable was limited instrumentally by the SEM. To achieve better resolution, Boeing explored the use of an STEM.

The STEM secondary electron photomicrographs of 2024-T3 clad are shown as stereopairs in Figure A-8 (50,000 magnifications) and Figure A-9 (200,000 magnifications). At these magnifications, accurate calibration becomes difficult, but under the

112
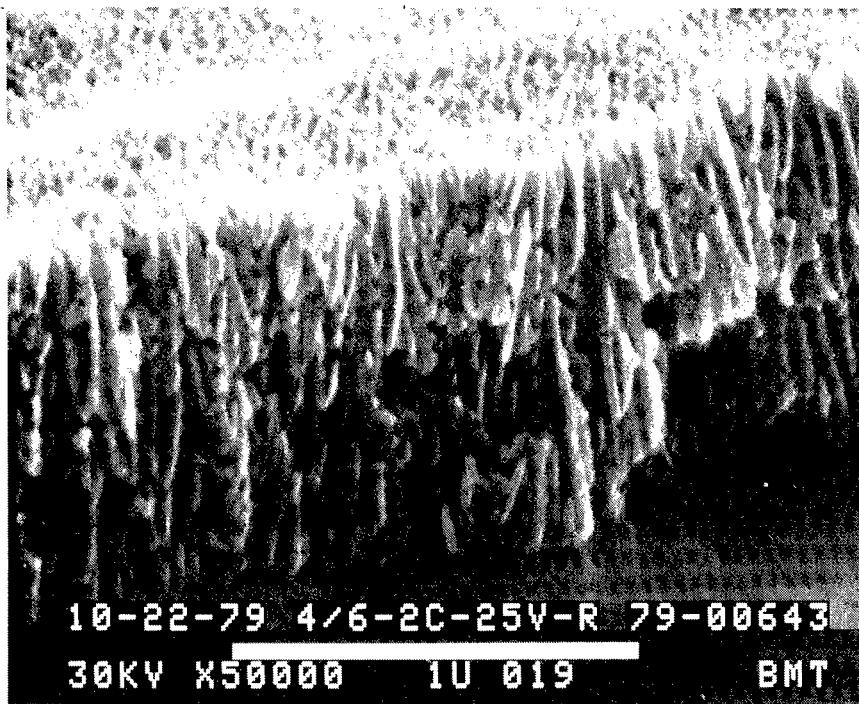
*Figure A-6. SEM Photomicrograph of PAA Oxide on 2024-T3-Clad,
Au/Pd Coated, Fractured Specimen x50,000*

*Figure A-7. SEM Photomicrograph of PAA Oxide on 2024-T3-Clad,
Au/Pd Coated, Fractured Specimen x100,000*

113

TOP OF OXIDE ——→

OXIDE ——

METAL ——
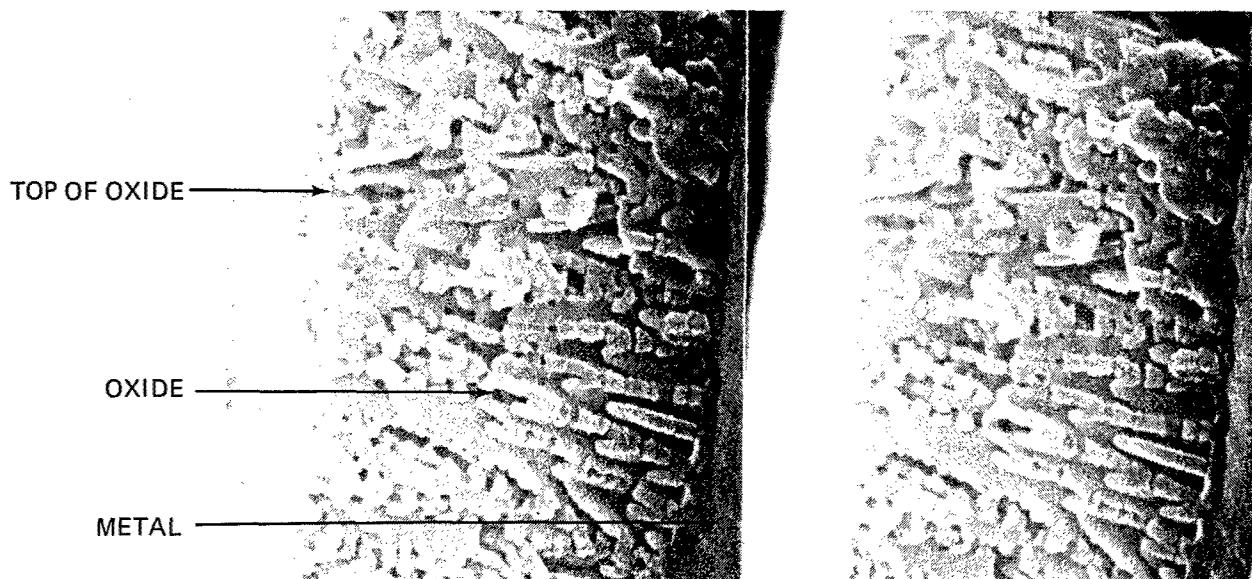
Figure A-8. STEM Stereo Pair of PAA Oxide on 2024-T3-Clad,
Au/Pd Coated, Fractured Specimen x50,000

POSSIBLE
COATING
STRUCTURES
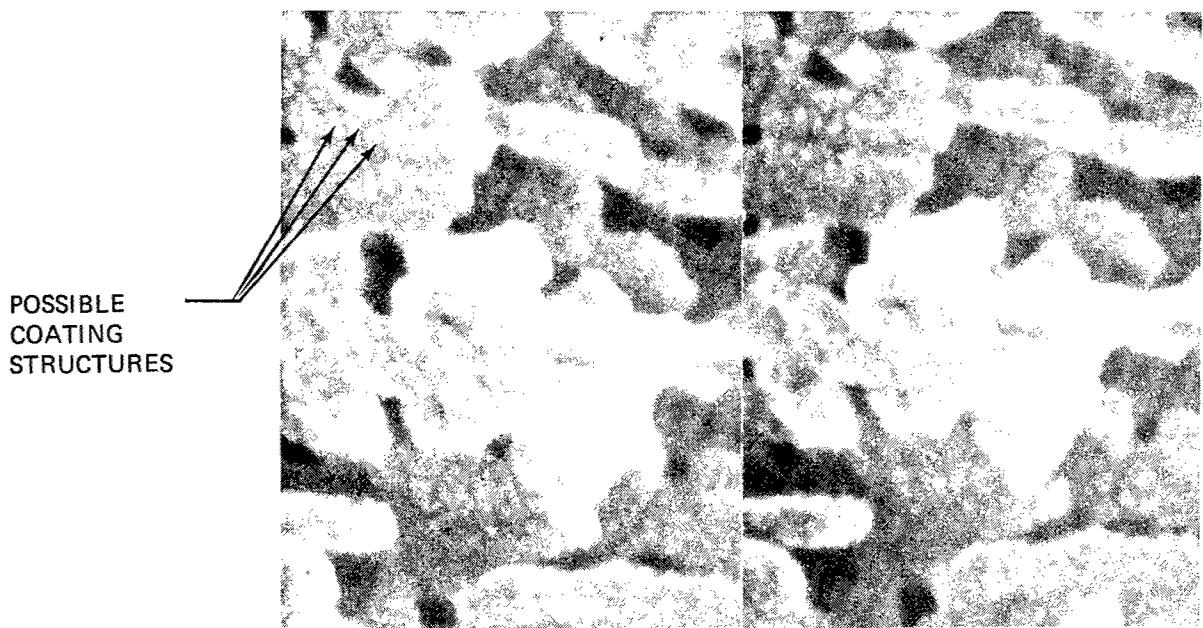
Figure A-9. STEM Stereo Pair of PAA Oxide on 2024-T3-Clad,
Au/Pd Coated, Fractured Specimen x200,000

114

assumption that the values approximate reality, 1 mm on a 200,000-magnification photomicrograph equals 50A, or nearly 38 close-packed oxygen ions.

The STEM photomicrograph in Figure A-8 shows better edge resolution than the corresponding Figure A-6 photomicrograph taken on the SEM. This is probably because of enhanced SNR and lower lens aberrations, which allow a more finely focused electron probe.

Figure A-9 shows the details of the oxide branches. The little nodules or bumps on the oxide surface are hypothesized to be the grain structure of the Au/Pd coating. Thus, the Au/Pd coating is usable up to 150,000 to 200,000 magnifications.

To prepare a specimen for the STEM, basically the same technique is used as for the SEM. However, difficulties are encountered because of the restricted space available for the specimen in the STEM. Whereas a specimen for the SEM can be as large as 30 mm square and 15 mm tall, for the STEM the specimen is limited to 6 mm in diameter and 3 mm tall. The restriction is imposed by the placement of the specimen in one of the lenses, which leads to the improved resolution of the STEM.

The structure of a PAA oxide on 2024-T3 bare is shown in Figures A-10 and A-11, which demonstrate the differences in oxide structure. These STEM photomicrographs show a finer, more intricate oxide cell structure than the 2024-T3 clad oxides. Many fine cell arms are observed to be present, in contrast to those observed in Figures A-8 and A-9. Again, the current methodology demonstrates enhanced detail resolution.
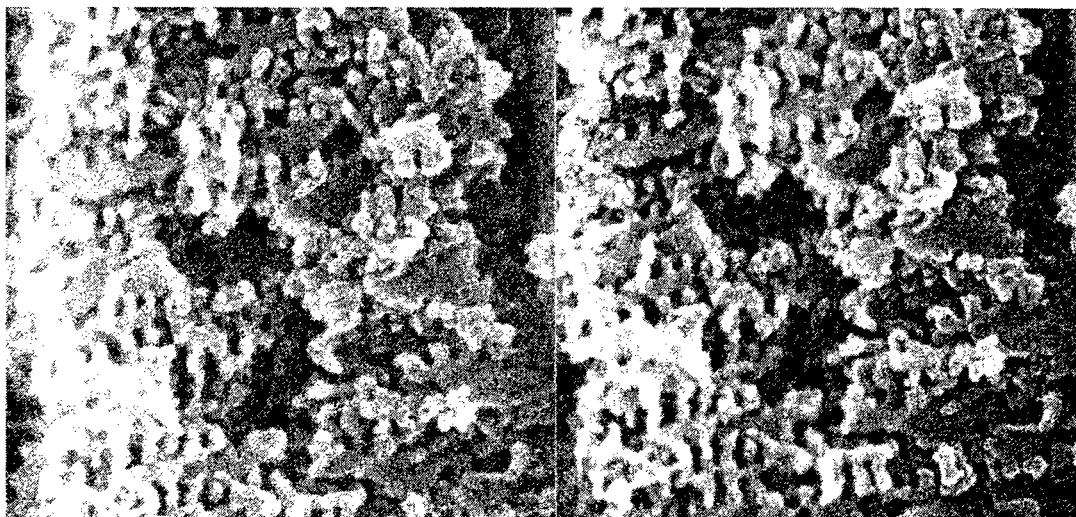
Figure A-10. STEM Stereo Pair of PAA Oxide on 2024-T3-Bare, Au/Pd Coated, Fractured Specimen x50,000

115
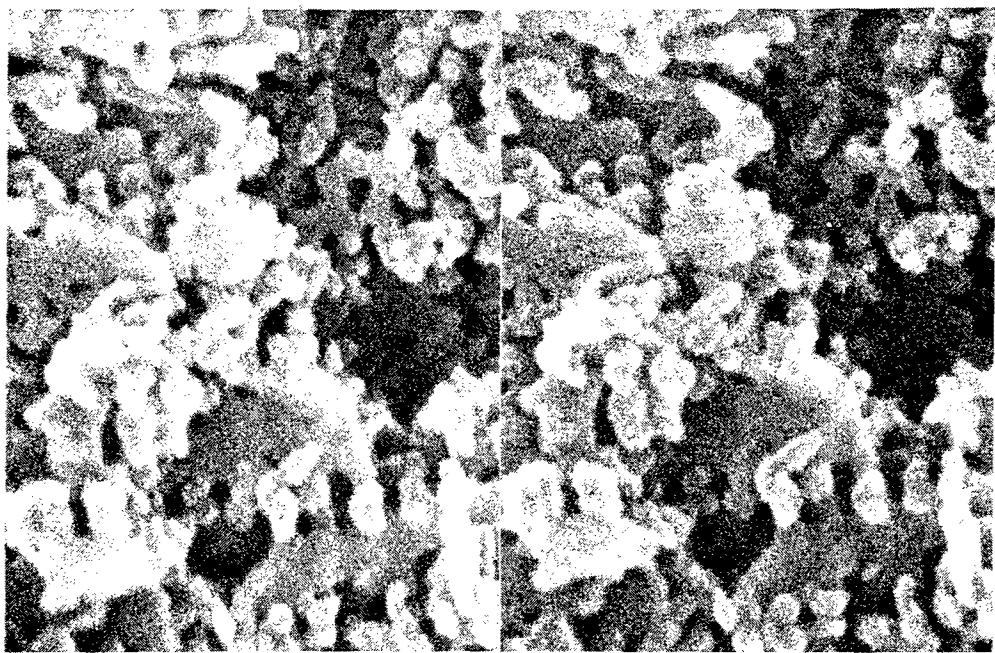
*Figure A-11. STEM Stereo Pair of PAA Oxide on 2024-T3-Bare,
Au/Pd Coated, Fractured Specimen x100,000*

TRANSMITTED ELECTRON IMAGING

For imaging by transmitted electron radiation, a thin specimen is required, typically less than 1000A. Such thin sections of material allow a different view than secondary electron surface imaging. A section of material can be cut through a metal/oxide/polymer bond, showing the oxide structure and interaction with the primer. The method can be used in two instruments: a transmission electron microscope (TEM) and an STEM.

SPECIMEN PREPARATION

To prepare thin sections for TEM requires the use of an ultramicrotome. The basic requirement of an ultramicrotome is a drive arm that holds the specimen and progresses steadily toward the knife that will cut the section (fig. A-12). A Sorvall MT2B microtome was used for all the work reported here. The microtome advance mechanism is mechanical, acting via a series of mechanical cogs. The degree of advance for each cycle is regulated to determine the thickness of section cut.

The speed at which a section is cut is very important to the cutting pattern obtained and has to be chosen according to the specimen material. Generally, the more brittle

116

the section, the slower the cutting speed required. With too high a cutting speed, a brittle material will shatter and a plastic material will suffer excessive compression.

The sectioning knife material must be diamond for cutting metals. Diamond knives give superior quality sections for polymers. The angle of the knife (α) is 55 deg. Clearance angle (β) also is important and, like knife angle α, is more critical for the more brittle materials. A range of angle values should be tried to determine the optimum for any system, but it is generally found that the smaller the clearance angle, the less damage is suffered by the specimen. The total angle through which a section will be bent during removal of a slice of material from the top of the specimen block is ($\alpha + \beta$), and this total angle must be optimized.

When sections are cut wet, the trough shown attached to the knife in Figure A-12 is filled with water to a level that causes it to wet the knife edge. As the section is cut, the cut edge will float onto the surface of the water, which will draw it away from the block, easing the cutting process and tending to smooth the section. Ideally, as second and subsequent sections are cut, they will be inclined to form themselves into a ribbon on the fluid surface.

An electron microscope grid (generally 3.05 mm in diameter) coated with a specimen supporting film of either formvar or carbon (formvar is simple, carbon more stable) is placed under the fluid surface and is raised to lift the sections onto the grid. The wet grid plus sections are placed in a desiccator to dry and the surface tension of the evaporting film of liquid tends to pull the sections down into close contact with the supporting film.

The size of the specimen is important, and blocks are normally trimmed down to give a cutting face no larger than 1 mm^2, preferably less. To cut a larger surface than required damages the knife edge unnecessarily, since every cutting stroke causes wear on the knife, and generally results in the production of an inferior section due to increased compression and drag on the knife.

Sections can be cut either transversely or laterally, as indicated in Figure A-13. Figure A-13a is a schematic diagram of an oxide layer on an aluminum surface, showing the oxide pores growing from the base oxide plate. A transverse section, cut normal to the metal surface, will show the oxide pores, as illustrated in Figure A-13b.
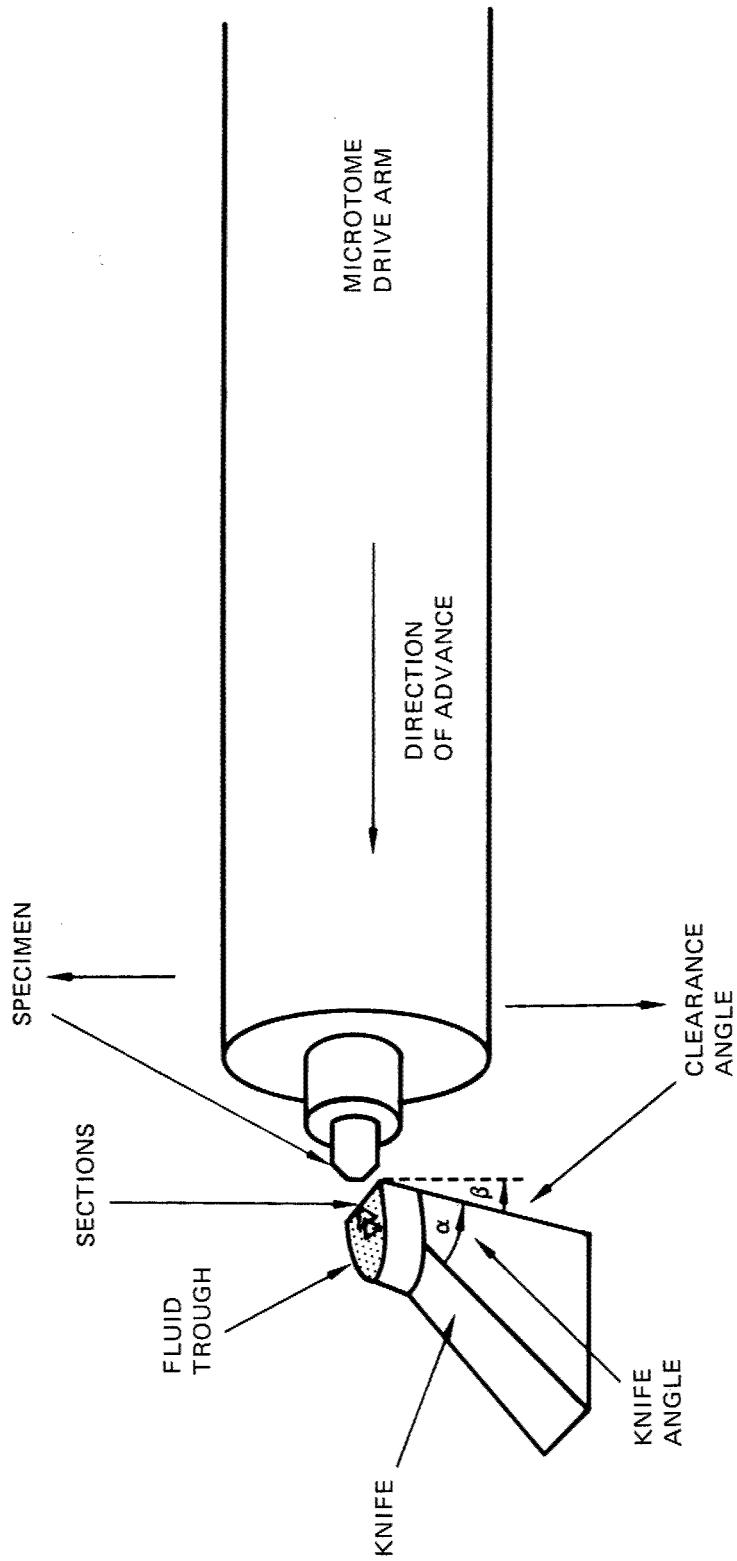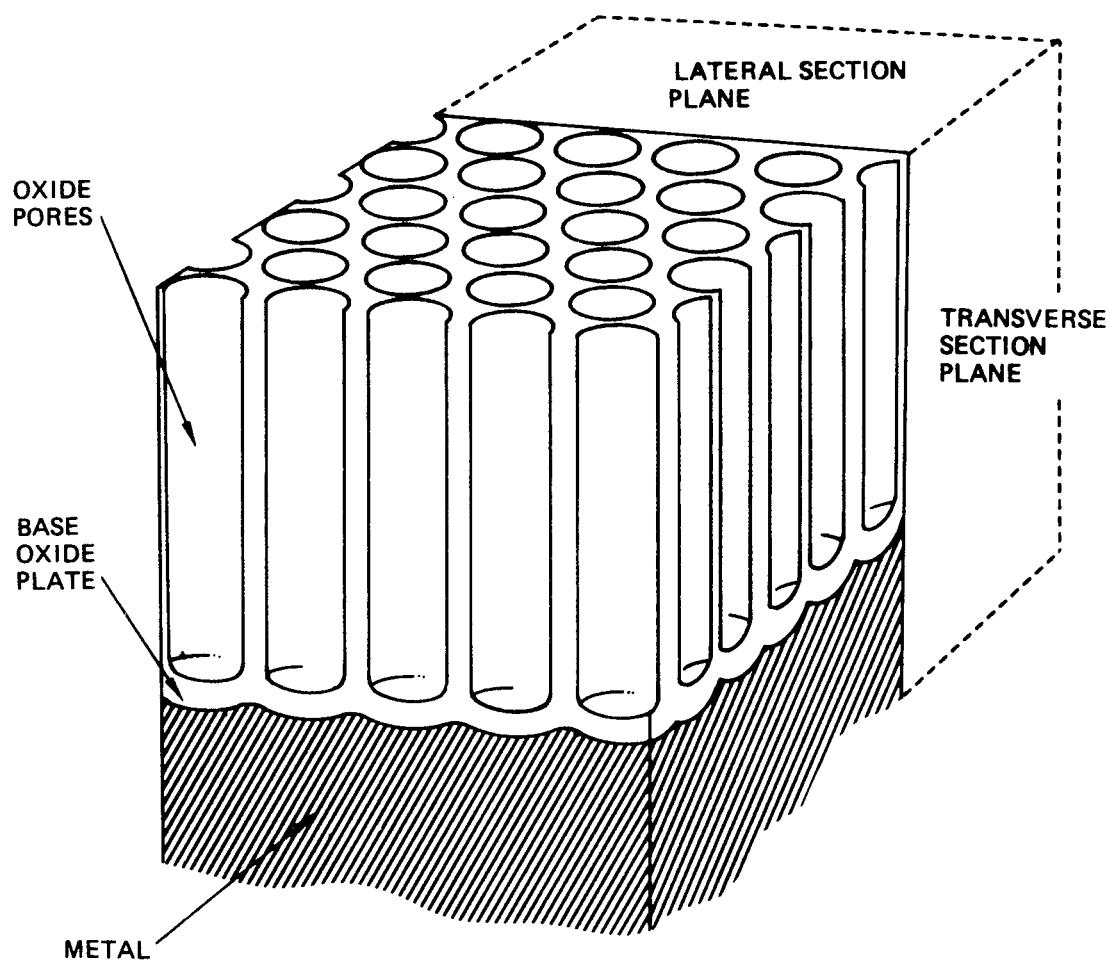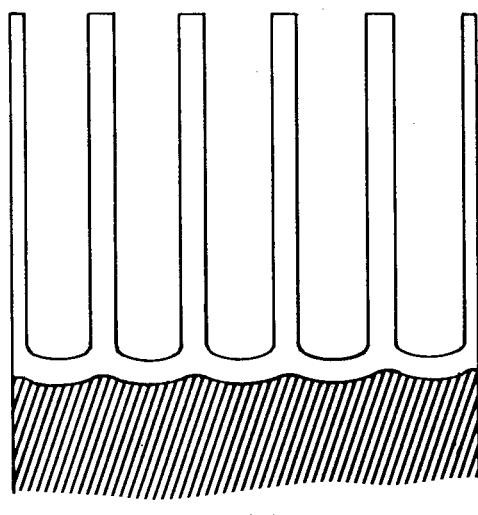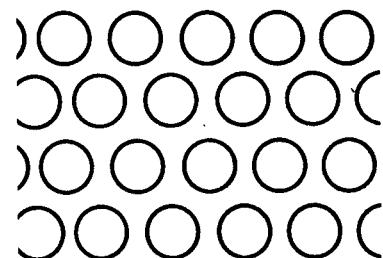
Figure A-12. Diagram of Microtome Showing Drive Arm and Knife

118

OXIDE PORES

BASE OXIDE PLATE

METAL

LATERAL SECTION PLANE

TRANSVERSE SECTION PLANE

(a)

(b)

(c)

(a) Specimen
(b) Transverse Section
(c) Lateral Section

Figure A-13. Diagram of Ultramicrotomy of Metal/Oxide/Polymer Bonds

119
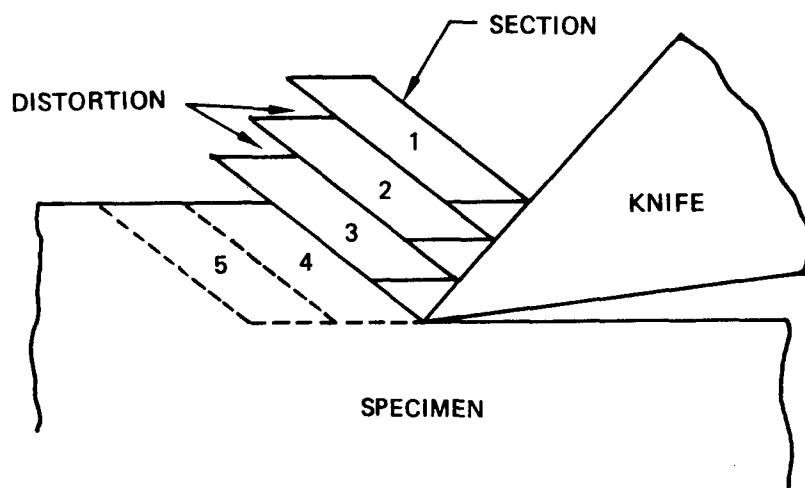
If a layer of polymer is on top of the oxides, the polymer layer will show, too. In this way, the penetration of primer into the oxide can be studied. Lateral sections, shown in Figure A-13c, are cut parallel to the metal surface. Lateral sections show the porous structures of the oxides. They can be cut with or without a polymer present, although the polymer stabilizes the oxide net and results in better quality sections.

For transverse sections, the specimen orientation is important, especially for multi-phase systems. For a system with two distinct boundaries (Al/oxide/primer) cutting normal to the boundary would give a high probability of separation of the phases at the boundary due to the sudden change in the resistance to cutting. Cutting in the direection of the boundary may obscure genuine detail by artifacts, which will be most evident parallel and perpendicular to the cutting direction (compression and knife marks). The optimum is probably between 30 and 45 degrees to the boundaries.
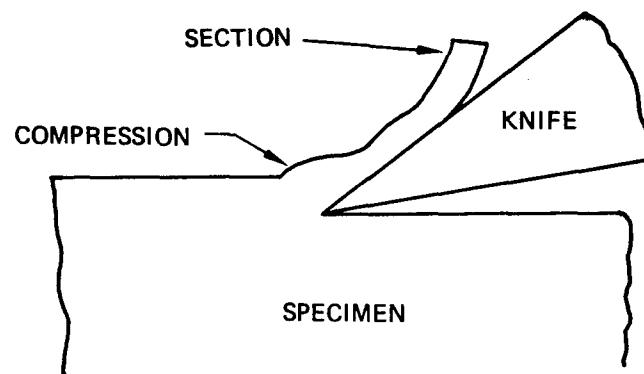
Thin sections can be cut for both analysis of ultrastructure and failure analysis. For failure analysis, it is necessary to define the failed edge of the sample. When a metal/oxide/polymer specimen is sectioned, the edge of the polymer is likely to tear, so that the section edge is not the specimen edge. To stabilize the edge and define its position, an evaporated layer of gold is applied to the failed edge before microtomy. The gold is more electron dense than the specimen components and clearly defines the edge of the specimen when viewed by transmitted radiation.

SECTIONING ARTIFACTS

It is important to describe the artifacts that may result from sectioning so that an artifact will not be interpreted as a physical entity. Compression is likely to be the most important artifact. To a certain degree, this is an inevitable result of the sectioning process itself, even when all cutting parameters are optimized. Figure A-14a shows a diagrammatic representation of the cutting process for a brittle material. Figure A-14b shows the same process for a plastic material. In either case, the thickness of the section will be greater than the thickness of the layer removed from the top of the specimen block. For plastic sections, there is a tendency for the sections to flatten out when floating on the fluid surface in the trough. For a more brittle material that has suffered slipping of adjacent planes relative to each other during sectioning, the resultant compression effect must be tolerated and allowed for when interpreting the photomicrographs of such a section. The compression artifacts

SECTION

DISTORTION

1

2

3

5   4

KNIFE

SPECIMEN

(a) BRITTLE MATERIAL

SECTION

COMPRESSION

KNIFE

SPECIMEN

(b) PLASTIC MATERIAL

Figure A-14. Diagram of Cutting Process

generally will be a regular phenomenon all across a section, evidenced as bands of increasing/decreasing thickness normal to the cutting direction. It is because of the different degrees of compression in materials of different cutting properties (more or less brittle materials) that inhomogeneities are likely to cause section artifacts. At the boundary of a hard inclusion in a matrix, there frequently will be a tear in the section that will cause an apparent shadowing effect, giving a region of less electron opacity on the same side of each of such inclusions.

Another type of section artifact that must be considered during interpretation of photomicrographs is that caused by an imperfection in the cutting edge of the knife. If the knife is not perfectly smooth, an irregular region will cause differences in thickness of the section at the irregularity, giving lines of more or less electron opacity. It is generally a simple matter to recognize such an artifact, because the marks will form a band all along the length of the section. In fact, such an artifact can be useful in determining the direction in which the section was cut.

Thin sections are cut for analysis in an electron microscope in a transmission mode, either as conventional TEM or STEM. Structures of different densities will have different electron-stopping powers that form the contrast in the image. Depending on the thickness of the section, an appropriate accelerating voltage on the microscope can be selected for optimum contrast between the structures of interest.

TRANSMISSION ELECTRON MICROSCOPE

For TEM analysis, a static electron beam illuminates the specimen, casting an image on a fluorescent screen or photographic plate. The contrast available is a result of the different degrees of electron absorption of the components and the thickness. Figure 9 shows a TEM image of BR-227 on 2024-T3 clad PAA.

SCANNING TRANSMISSION ELECTRON MICROSCOPE

In the transmission mode, the imaging of the STEM differs from that of the TEM. A finely focused beam of electrons scans the specimen, and a synchronous raster scans the display screen. The image formed on the screen is the summation of the signal at each point. It is possible to enhance the contrast electronically in the STEM to obtain pictures of greater contrast, such as shown in Figure A-15. This photomicrograph is of

BR-227 on 2024-T3 clad PAA, the same system as shown in Figure 9. Fine details of the oxide tips can be seen in the STEM image.

0.5 μm
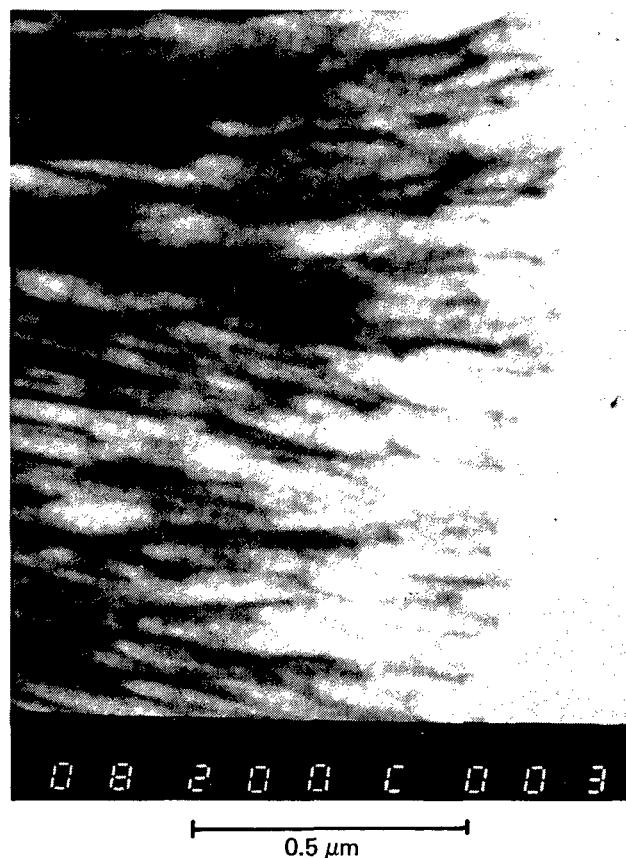
Figure A-15. STEM (Transmission) Photomicrograph of a Thin Section of 2024-T3-Clad PAA with BR-227 Primer

SURFACE ANALYSIS

The surface chemistry of the adherend oxide will influence the degree of chemical bonding between the polymer and oxide. Evaluation of the surface chemical composition of the oxides can be accomplished by two techniques: (1) Auger electron spectroscopy (AES), and (2) X-ray photoelectron spectroscopy (XPS), also known as electron spectroscopy for chemical analysis (ESCA). Both techniques are performed in the same instrument, a Perkin-Elmer Physical Electronics ESCA-SAM spectrometer, Model 550. Both AES and XPS provide a very sensitive way of observing the chemical state of the aluminum oxide at the surface and the extent of contamination at the surface.

XPS also is used to evaluate the disbonded surfaces of mechanical test specimens. The purpose is to see if there is a chemical segregating layer at the disbonded surfaces that contributed to a mechanically weak layer, as well as to determine if the disbond was adhesive or cohesive.

To check the chemical purity of the aluminum oxide throughout its thickness, AES sputter profiling is used. In this way, the presence of a chemically segregating layer within the oxide could be identified.

SPECIMEN PREPARATION AND ANALYSIS

The specimen must be cut to be no larger than 15 mm square and 10 mm deep. Care must be taken to avoid handling the surface during preparation, since touching the surface will introduce surface contaminants into the analysis.

X-RAY PHOTOELECTRON SPECTROSCOPY

XPS is based on the detection of photoelectron emission when a sample is irradiated by X-rays, in this case, magnesium K X-rays. Since XPS is an electron spectroscopy technique, its surface sensitivity derives from the short mean free path of electrons in a solid, which is approximately 0.5 to 5 nm for an oxide. The advantage of XPS is that it can analyze polymers as well as oxides, and so is used to evaluate the failure locus in mechanical specimens. XPS is very sensitive to the chemical bonding state of the elements present. It provides a powerful method to identify chemical species on the adherend surface or on the surface of failed mechanical specimens.

XPS peak heights were used to calculate the quantitative data included in this report. The data are normalized for elemental sensitivity and are reported as atom percent. The data are intended for relative comparison only.

AUGER ELECTRON SPECTROSCOPY

AES is based on the electronic process of de-excitation, which produces an energetic electron, rather than the competing process of X-ray emission. In AES, the material is excited by impinging a focused electron beam on the sample, creating an inner shell vacancy. The subsequent de-excitation by electron emission is the more probable

event for the low-atomic-number elements present in the aluminum samples. The focused electron beam allows some lateral definition, with a resolution of 5 µm. The surface sensitivity of AES is the result of the maximum escape depth of the electrons emitted from the surface, which is 0.5 to 5 nm. Each element present on the surface will emit a characteristic energy pattern of Auger electrons and so is the basis of identification. There are some overlap problems in identification that result when the element is present at very low levels and only the major Auger line can be detected. Specific problems with resolution in this study include the element pairs zinc and sodium (995 eV) and iron and fluorine (650 eV).

The AEA peak-to-peak heights are the basis for the quantitative data included in this report. The data are normalized for elemental sensitivity and reported as atom percent (i.e., number of atoms of element detected/total number of atoms detected). These data are included as a means of comparison between samples and are not absolute.

AES can be combined with argon ion beam sputtering to remove material from the surface. The computer monitors the Auger peak amplitudes as the material is removed, and plots of composition versus sputter time are obtained. This allows the composition of an area to be analyzed through the oxide to the metal substrate. By calibrating the sputtering rate to a known thickness of tantalum oxide, an approximate depth scale can be obtained.

APPENDIX B

OXIDE STRUCTURES AND CHEMISTRIES

INTRODUCTION

The microstructure of the oxide surface contributes to the strength of the adhesive bond by presenting more or less surface area for polymer/oxide interaction The degree to which the polymer can penetrate the oxide will influence the mechanical stability of the oxide/polymer bond. Electron microscopical techniques have been used to study oxide structures. Scanning electron microscopy (SEM) and scanning transmission electron microscopy (STEM) have been found to be complementary techniques for determining oxide ultrastructure. SEM techniques have shown PAA clad oxides to have a regular, open, columnar structure. PAA bare oxides are thinner and less ordered.

TEM techniques confirmed the information obtained from SEM techniques. Thin sections showed columnar structures and branching of the oxide pores. The presence of an oxide base plate lining the metal surface also is clearly indicated. Lateral sections of oxides for TEM analysis give a particularly clear view of oxide cross-sectional structure. FPL oxides were not extensively studied by electron microscopy because structure is not evident in these thin oxides.

The surface chemistry of the oxides will influence the degree of chemical bonding between the oxide and polymer. The presence of surface contaminants can both interfere with bonding and provide a mechanically weak surface layer. Both Auger electron spectroscopy (AES) and X-ray photoelectron spectroscopy (XPS) provide a very sensitive method for observing the chemical state of the aluminum oxide at the surface and the extent of surface contamination.

MATERIALS AND PROCEDURES

A variety of the analytical techniques described in Appendix A were applied to the study of the oxide ultrastructure. Techniques used were SEM, STEM, TEM, AES, and depth profile. The specimens studied by each technique are shown in Table B-1.

Results are shown for SEM and STEM (secondary) analyses on oxides with no primer present. TEM results are shown for unsupported oxides. Superior results are shown for TEM and STEM (transmission) studies when the oxide layer was stabilized for microtomy by a penetrating layer of primer.

The sequence of surface analysis was to perform an AES survey, sputter depth profile with multiplexing of the elements of interest; to take intermediate AES survey scans; and, after penetration to the base alloy, to take a postsputter AES survey.

The surface AES spectra were analyzed for the relative atomic percentage of the elements present using sensitivity factors to normalize each element's peak-to-peak amplitude. This method is semiquantitative.

Table B-1. Specimens Analyzed for Oxide Structure
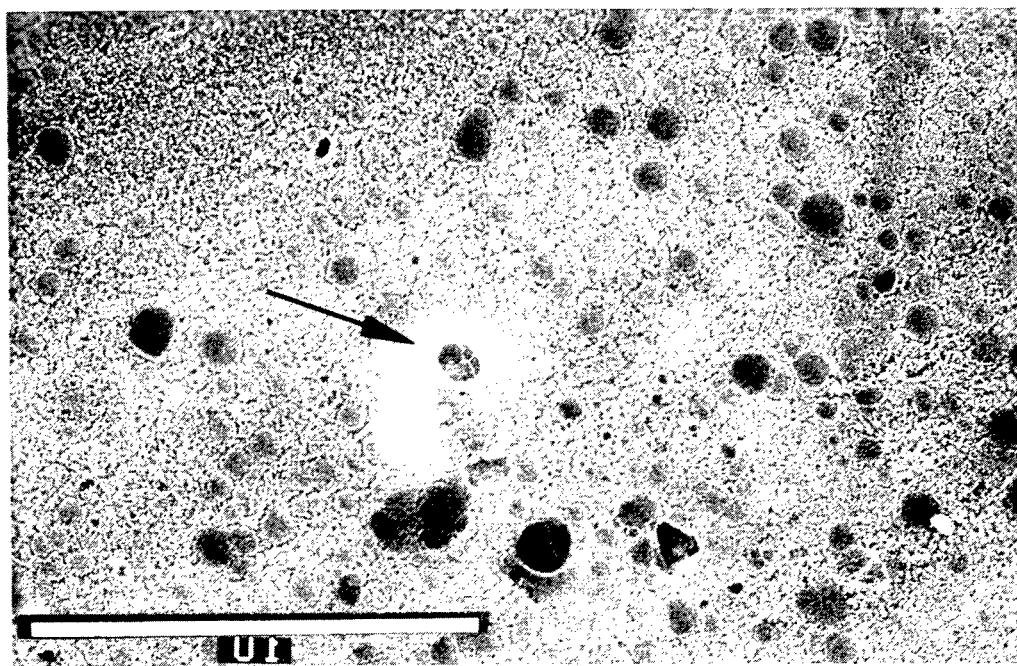
Surface preparation	Alloy	Analysis		
		SEM	TEM	Surface chemistry
PAA	2024-T3-clad	X	X	X
PAA	2024-T3-bare	X	X	X
PAA	2024-T81-bare	X		
PAA	7075-T6-bare	X		X
FPL	2024-T3-clad	X		
FPL	2024-T3-bare	X		X
FPL	7075-T6-bare			X

RESULTS
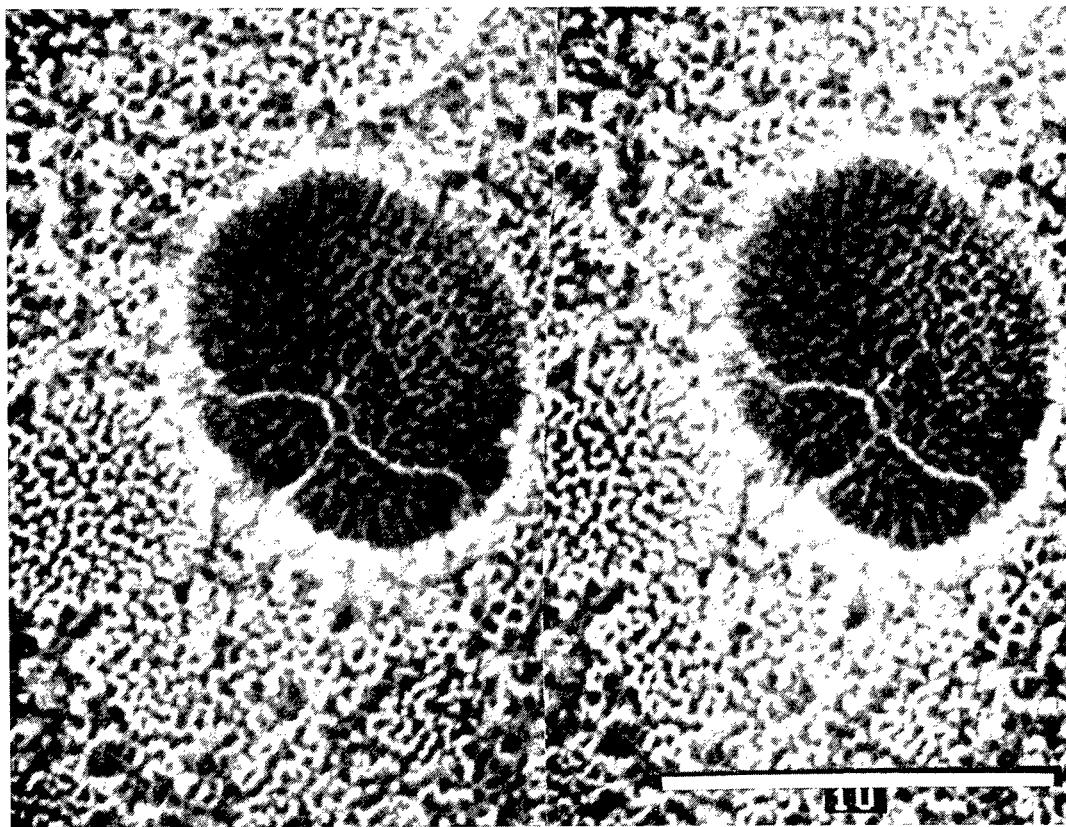
PAA OXIDE

PAA 2024-T3 Clad—SEM

A surface view of the PAA oxide structure formed under baseline conditions on 2024-T3 clad alloy is shown in Figure B-1. The oxide formed under baseline operating conditions was ultrasonically cleaned in alcohol for a few seconds prior to Au-Pd coating for the SEM. This cleaning procedure appears to have broken up the outer oxide surface in many places, revealing a geometric pore structure beneath the surface. For this reason, use of the cleaning process was discontinued. The stereo-pair photographs bring out this feature quite clearly. The large hole may have been formed by a small gas bubble adhering to the oxide surface early in the process and behaving as a resistor, thereby stopping the porous oxide growth at that point.
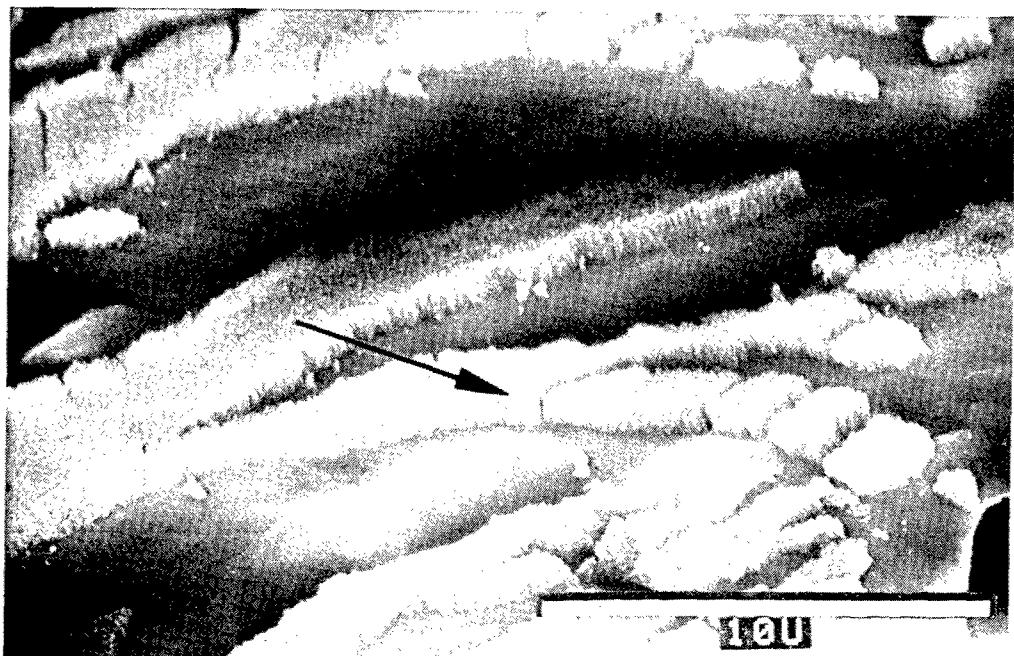
LOW MAGNIFICATION OF AREA OF STEREO PAIR
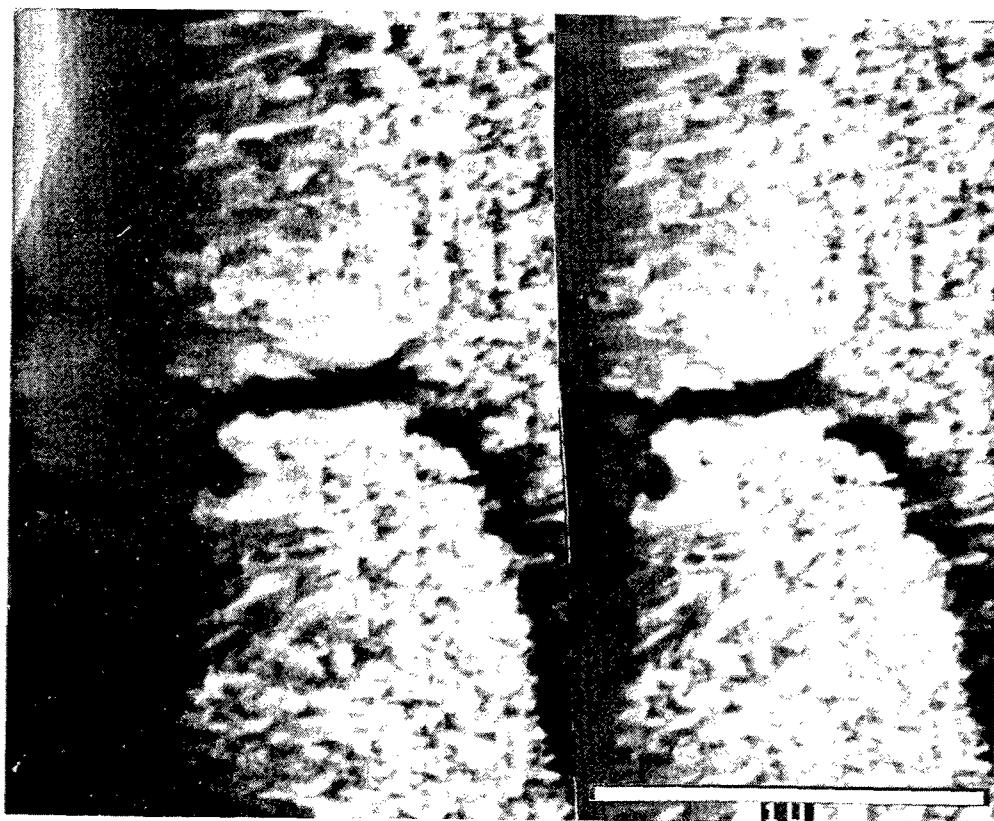
STEREO PAIR, VIEW LOOKING DOWN ON OXIDE SURFACE

Figure B-1. SEM Photomicrographs of PAA on 2024-T3-Clad

131
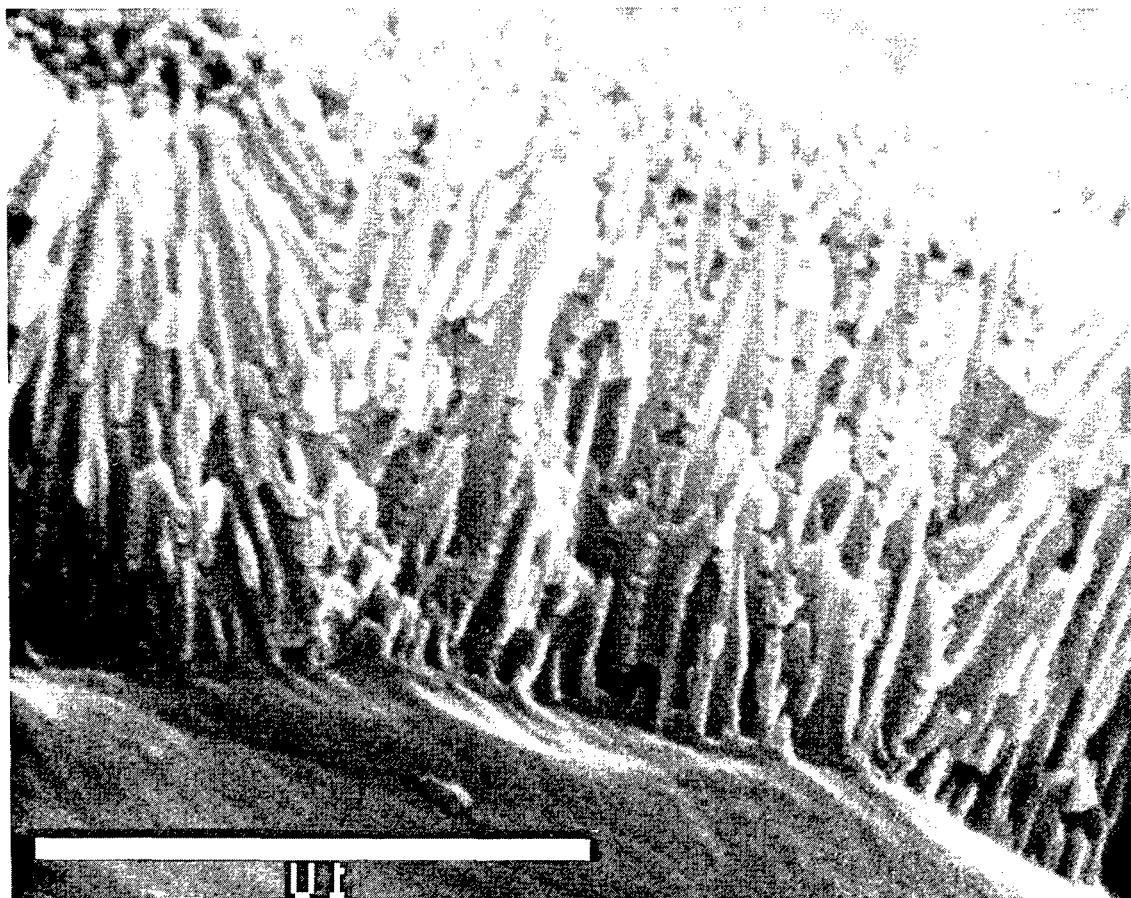
LOW MAGNIFICATION OF AREA OF STEREO PAIR
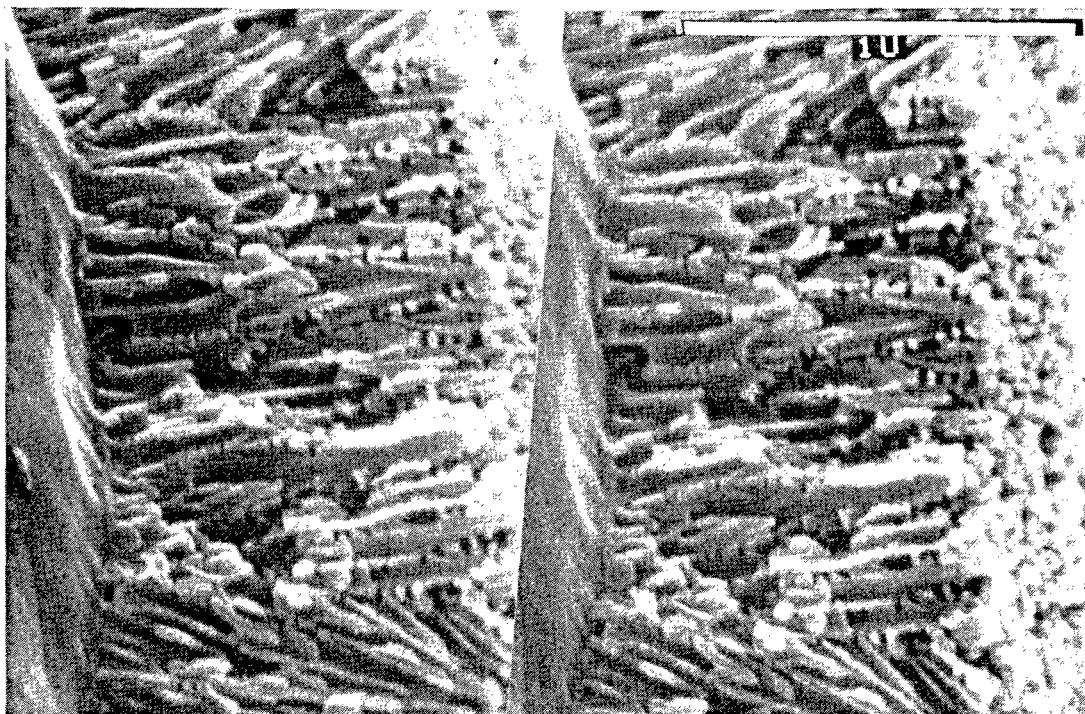
STEREO PAIR OF FRACTURED OXIDE

Figure B-2. SEM Photomicrographs of PAA on 2024-T3-Clad

HIGH RESOLUTION VIEW OF FRACTURED OXIDE

STEREO PAIR OF ABOVE PHOTOGRAPH

Figure B-3. STEM Photomicrographs of PAA on 2024-T3-Clad

The fractured cross-section of the above oxide is shown in Figure B-2. These photomicrographs reveal a very porous columnar oxide structure.

PAA 2024-T3 Clad—STEM (Secondary)

A high-resolution STEM secondary electron image of PAA 2024-T3 clad is shown in Figure B-3. The specimen was not ultrasonically cleaned. Comparison of Figure B-3 with Figure B-2 shows the improved resolution attainable with the STEM.
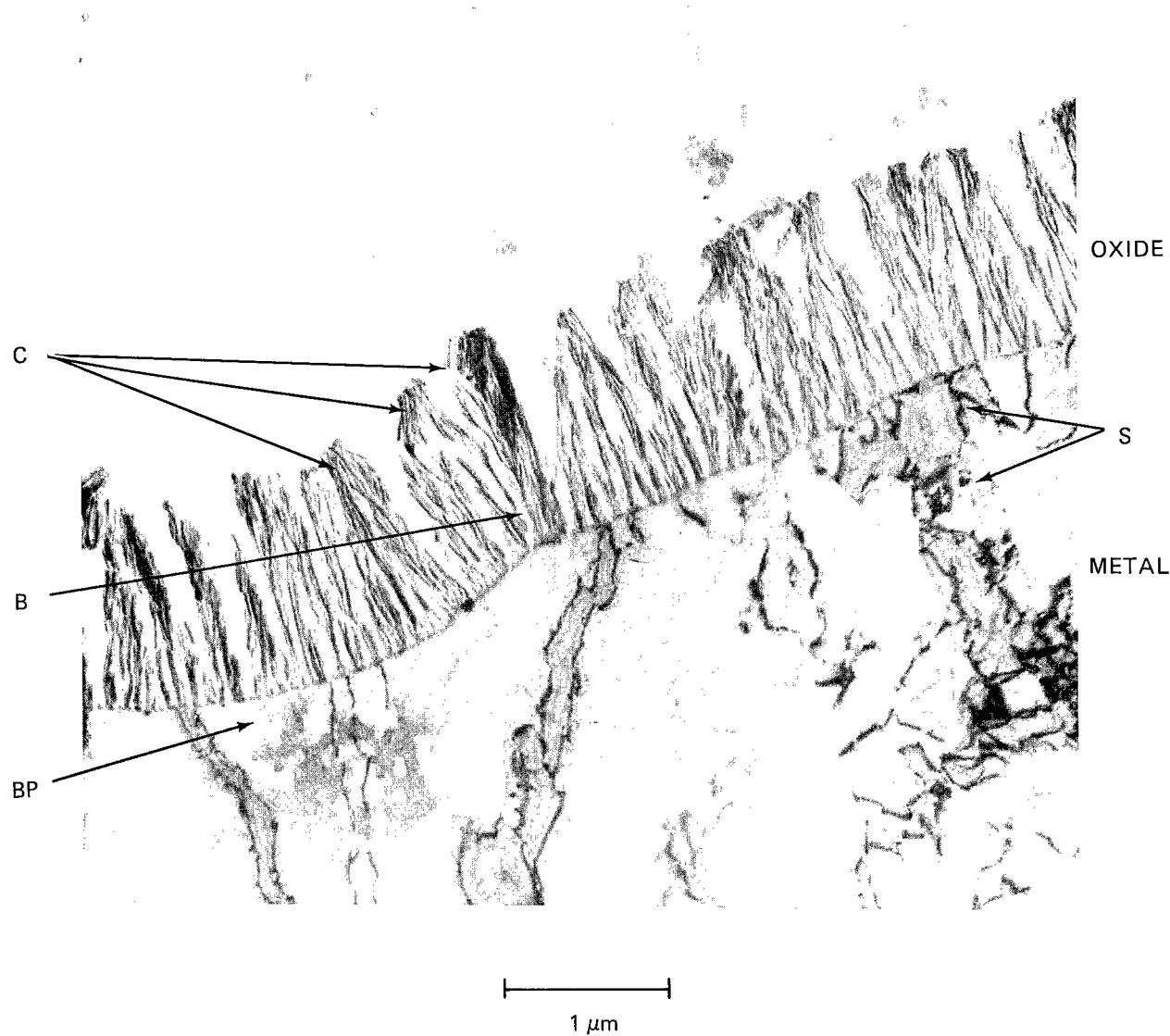
PAA 2024-T3 Clad—TEM (Transverse)

Figure B-4 shows a section of 2024-T3 clad PAA. The depth of the oxide layer is approximately $0.7\,\mu m$. The basal oxide plate (BP) attached to the metal is clearly visible. The oxide cell structure is regular, and the clumping (C) seen in this photomicrograph is caused by sectioning artifacts. A branching structure (B) of the oxide cells can be seen growing from a slight rise in the metal surface. Details also can be seen in the metal, such as slip planes (S).

All sections described so far have been of unsupported oxide. The clumping effect seen in transverse sections in Figure B-4 is typical of both sectioning and surface tension artifacts on unsupported oxide regions. Better ultrastructural details of oxides can be seen in sections stabilized by the presence of a primer that has penetrated the oxide layer.

PAA 2024-T3 Clad with BR-227 Primer—TEM (Transverse)

Figure B-5 shows a transverse section of 2024-T3 clad PAA with BR-227 primer. The penetration of the primer into the oxide layer stabilizes the oxide during the cutting process. The clumping artifacts seen in Figure B-4 do not occur with the polymer present. Figure B-5 shows the oxide structure clearly and also illustrates some cutting artifacts. C1 are compression artifacts in the polymer. C2 are compression artifacts in the metal. F are fractures occurring in the metal as a result of sectioning a brittle material.

OXIDE

S

METAL

C

B

BP

⊢————————⊣

1 μm

● BP represents the basal oxide plate.
● C   represents clumping due to sectioning artifacts.
● B   represents a branching structure of the oxide cells.
● S   represents slip planes in the aluminum.

Figure B-4. Transverse View of 2024-T3-Clad PAA

PAA 2024-T3 Clad—STEM (Transmission)

Figure B-6 shows a transverse section of 2024-T3 clad PAA supported by BR-227 primer. This is one of the same series of sections as shown in Figure B-5. The difference in contrast mechanisms between transmission electron images in the TEM and STEM can be seen clearly by a comparison of Figures B-5 and B-6.

0.5 μm

Figure B-5. TEM Photomicrograph of a Thin Section of 2024-T3-Clad PAA with BR-227 Primer
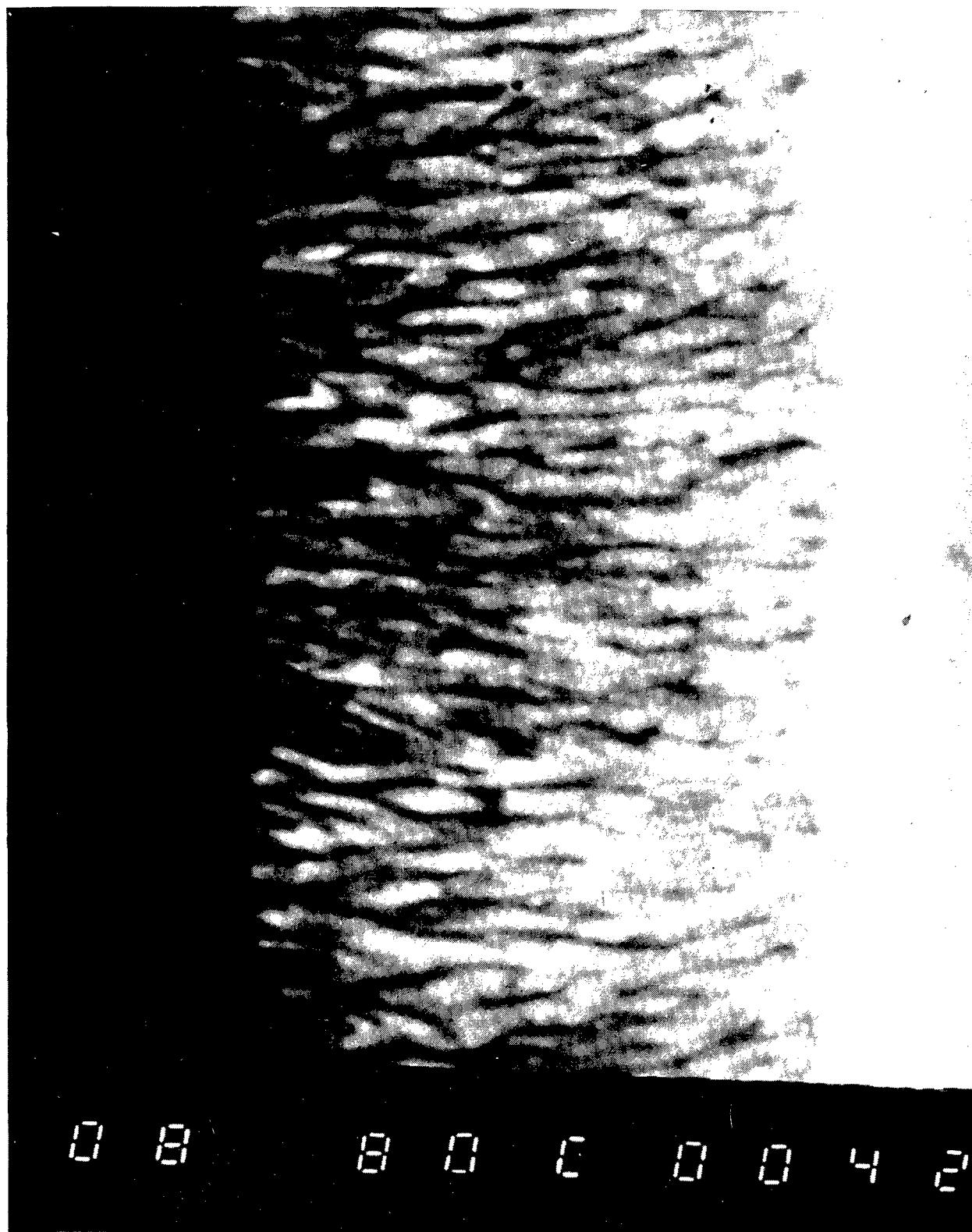
Figure B-6. STEM (Transmission) Photomicrograph of a Transverse Section of 2024-T3-Clad PAA

137

PAA 2024-T3 Clad—TEM (Lateral)

Figure B-7 shows a lateral section of 2024-T3 clad PAA. Lateral sections are much harder to cut than transverse sections. Only small regions (R) are found where the sections are normal to the direction of pore growth. From these regions, measurements can be made of the oxide pore diameter, which is approximately 50 nm. From these photomicrographs, there is clear evidence of gaps (G) left at the junctions between the pore walls.

PAA 2024-T3 Clad—Auger Survey and Depth Profile
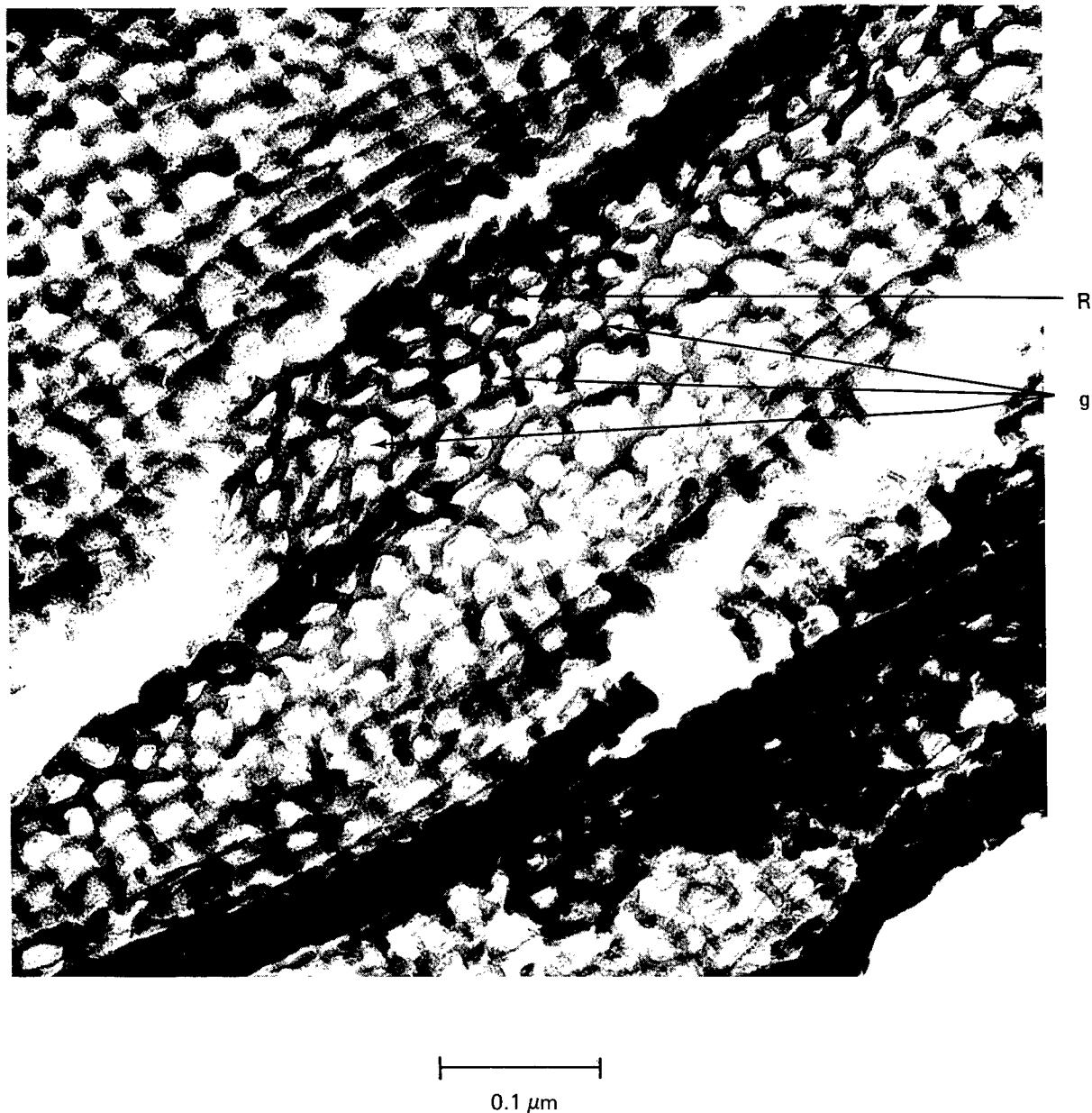
Figures B-8 and B-9 show that the clad alloy had high O, Al, and C at the topmost surface with lower levels of P (0.6%), F (0.5%), and S (0.5%). No Cu or Mg were detected at the surface of the oxide. Depth profiling of this oxide found that the C, P, F, and S were chiefly surface located and did not persist through the oxide. The surface elemental compositions expressed as atomic percent for the detected elements are shown in Table B-2 for all of the samples studied by surface analysis.

PAA 2024-T3 Bare—SEM

A surface and cross-sectional view of the PAA oxide structure on 2024-T3 bare alloy is shown in Figure B-10. The oxide does not exhibit the ordered, porous, columnar structure evident on the 2024-T3 clad alloy shown in Figure B-2. However, there is some suggestion of an overall columnar structure in the cross-sectional view. The top view of the oxide shown in Figure B-10 indicates the presence of a less organized porous structure. Figure B-11, moreover, shows a stereopair of photomicrographs looking down on the oxide surface, analogous to the bottom view shown in Figure B-10. The stereo pair shows more clearly the porous nature of the bare oxide structure, lacking the columnar regularity of the clad oxide shown in Figure B-2. The oxide is thinner on the bare alloy (about 250 nm) than on the cladding (500 nm) for the baseline PAA processing parameters.

PAA 2024-T3 Bare—TEM (Transverse Sections)

Figure B-12 shows a section of 2024-T3 bare PAA. This photomicrograph is at the same magnification as Figure B-4 and shows the oxide depth to be about a third of the oxide formed on clad metal. The structure of the oxide again is less well defined.

138

0.1 μm

- R represents a region where the section has been cut normal to the direction of pore growth.
- g represents gaps in the pore walls formed during growth of the oxide layer.

Figure B-7. Lateral Section of 2024-T3-Clad PAA

Table B-2. Surface Elemental Compositions Expressed as Atomic Percent for the Detected Elements

Samples	Elements											
	O	Al	P	Cu	Zn	Mg	Si	Ca	C	F	Cl	S
2024-T3-clad PAA	40.1	36.5	0.6	—	—	—	—	—	21.8	0.5	—	0.5
2024-T3-bare PAA	46.1	45.7	0.1	—	—	—	—	0.6	7.4	—	—	—
2024-T3-bare FPL	38.7	29.7	—	2.7	—	0.4	0.7	0.8	25.1	0.8	0.1	1.0
7075-T6-bare FPL	46.7	31.6	—	—	2.3	1.9	0.6	1.1	14.0	0.4	—	1.5
7075-T6-bare PAA	31.1	48.2	0.6	—	1.6	1.9	0.2	0.1	15.9	0.3	—	—

139
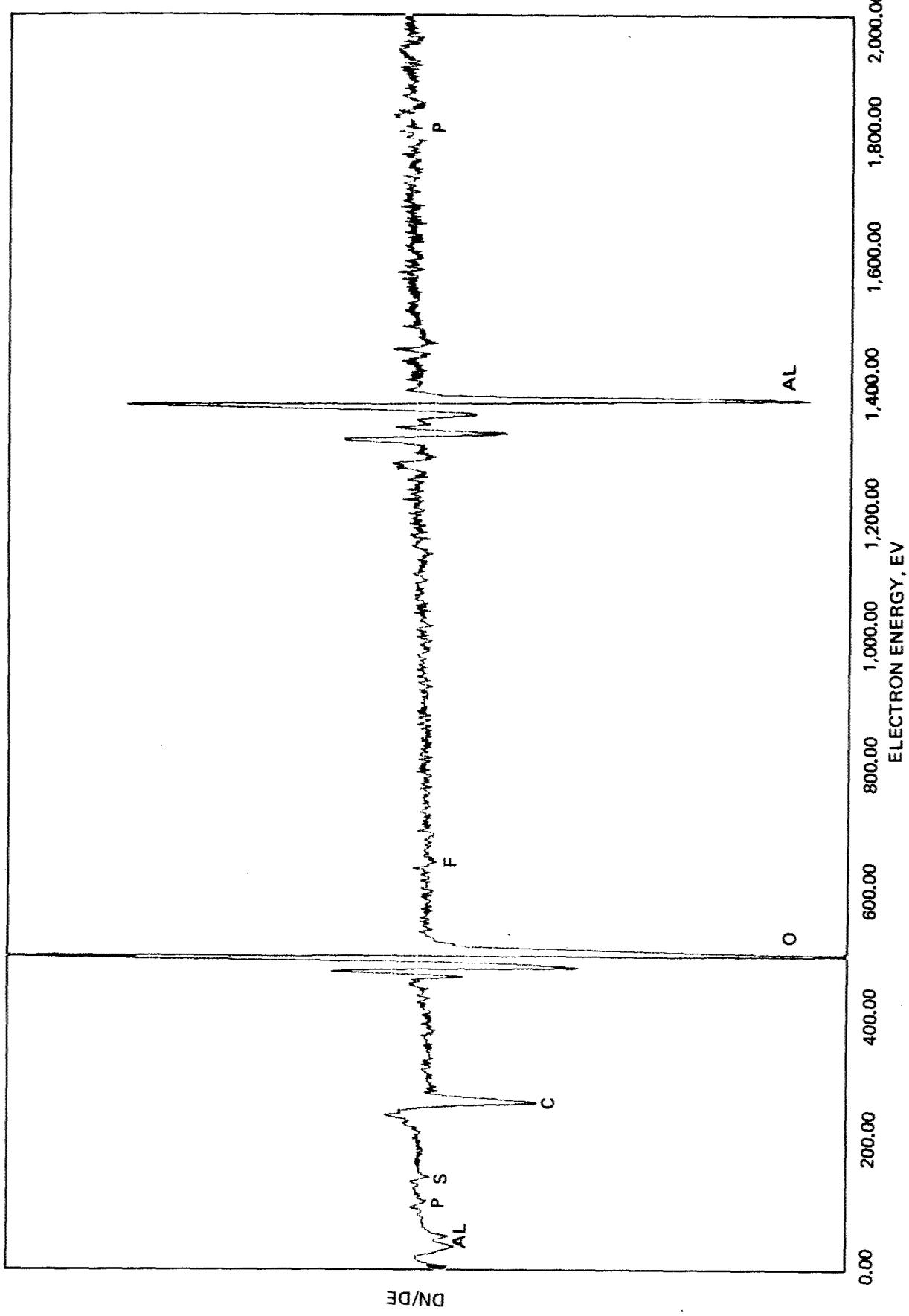
Figure B-8. Surface Composition of 2024-T3-Clad PAA

140
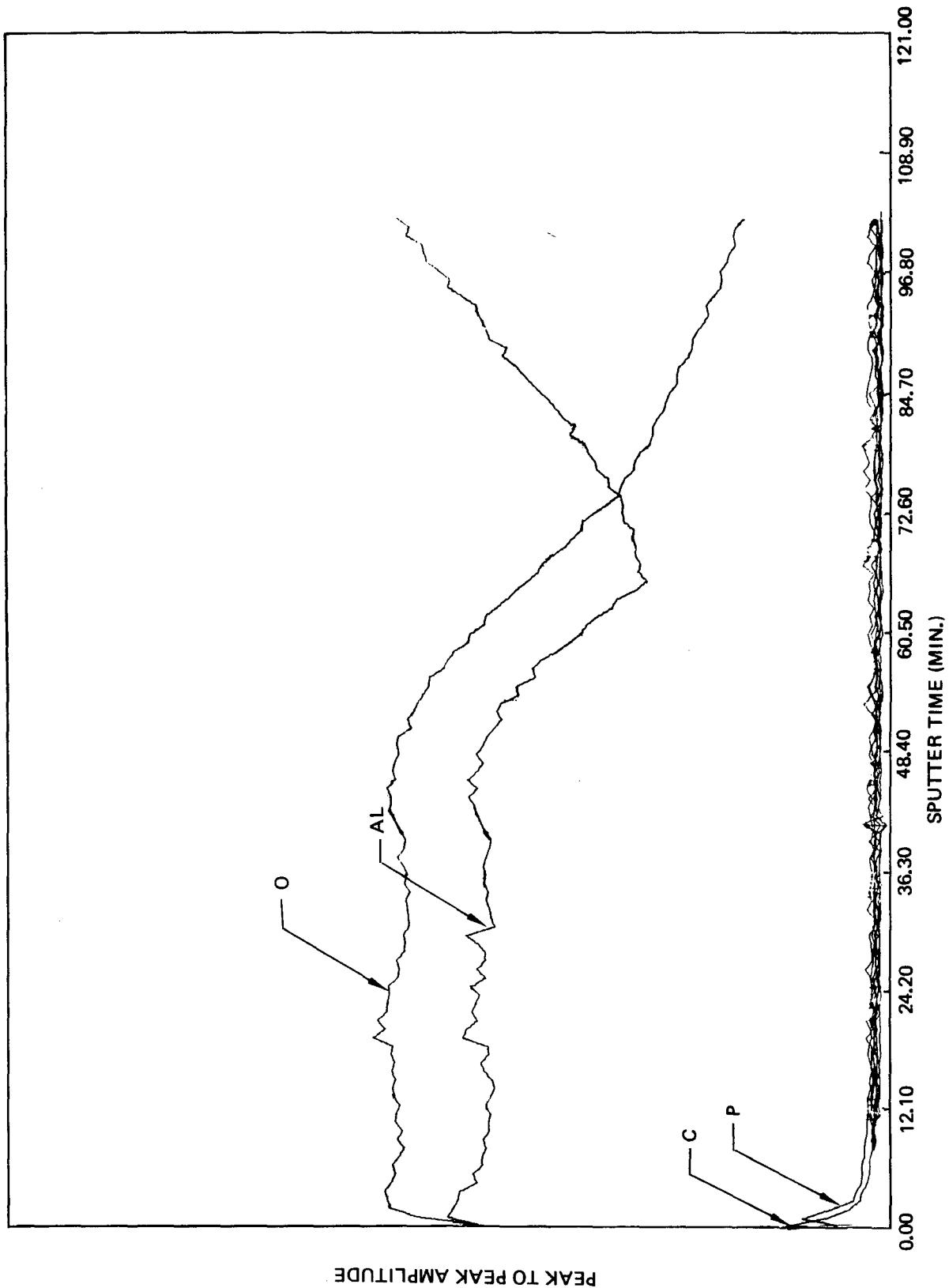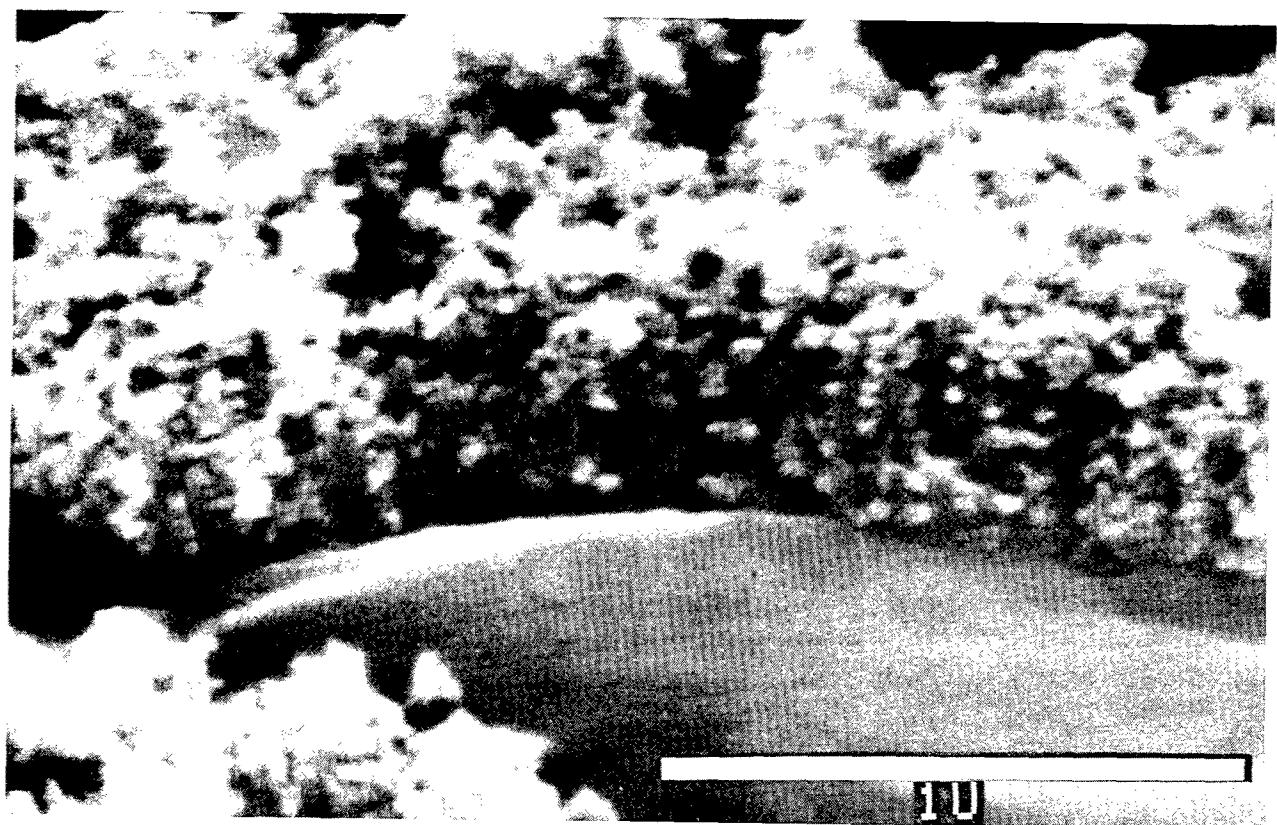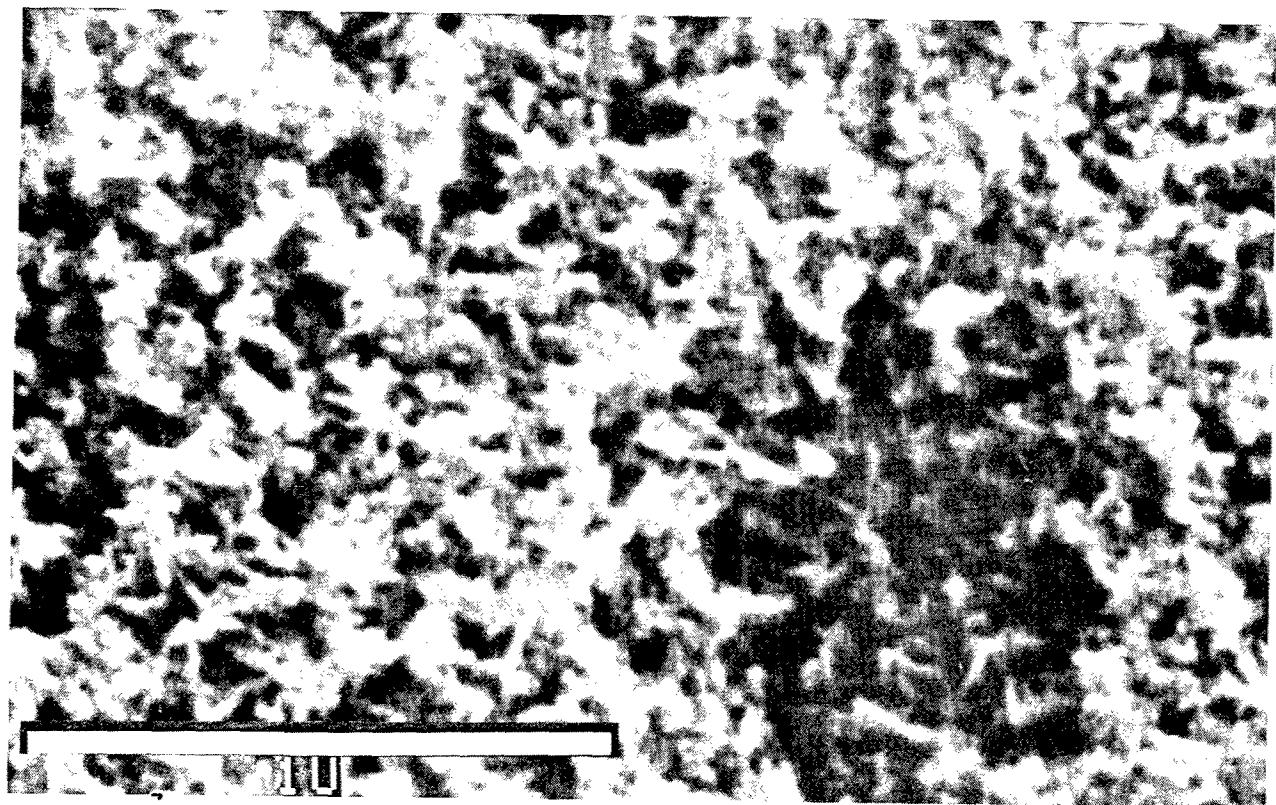
Figure B-9. Depth Profile of 2024-T3-Clad PAA

141
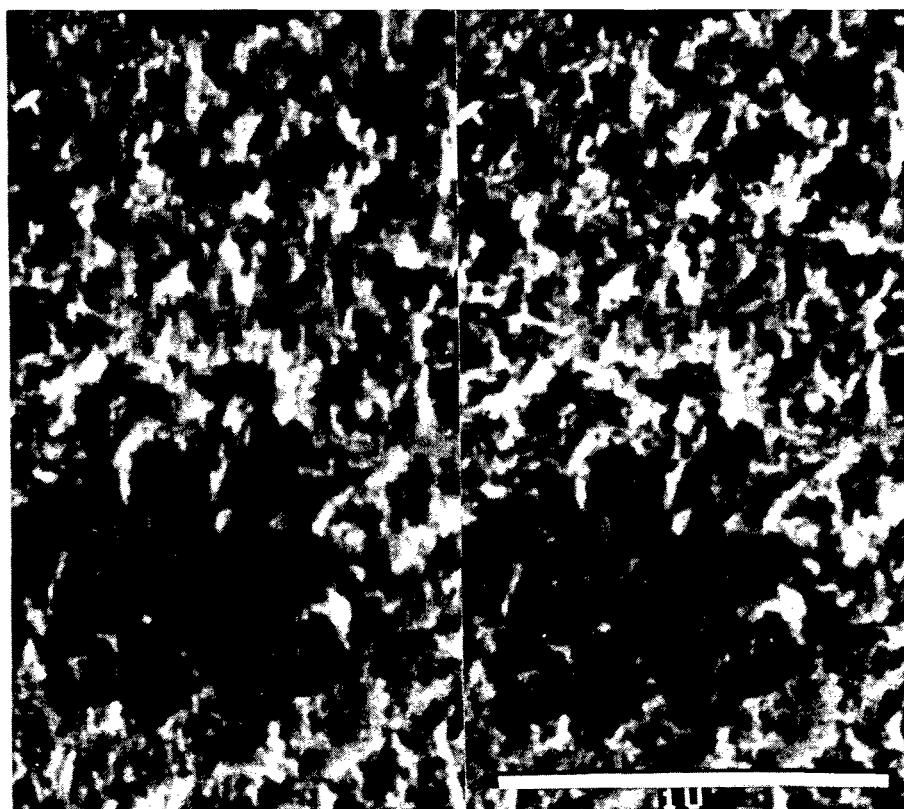
FRACTURED OXIDE

TOP VIEW LOOKING DOWN ON OXIDE SURFACE

Figure B-10. SEM Photomicrographs of PAA on 2024-T3-Bare

142

STEREO PAIR LOOKING DOWN ON OXIDE SURFACE

Figure B-11. SEM Photomicrograph of PAA on 2024-T3-Bare

OXIDE

METAL

1 μm
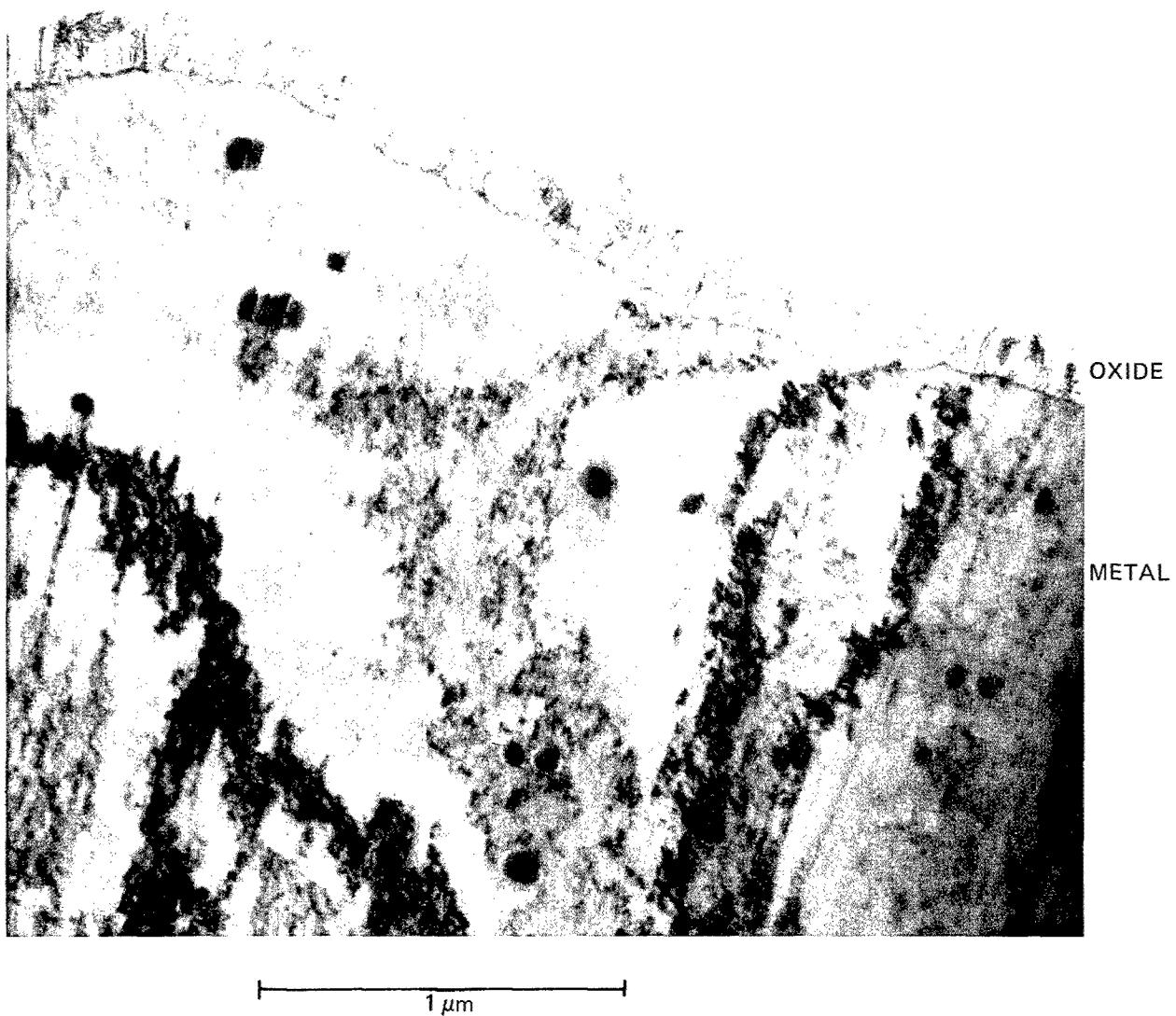
Figure B-12. Transverse View of 2024-T3-Bare PAA

144

PAA 2024-T3 Bare—TEM (Lateral Sections)

Figure B-13 shows a lateral section of 2024-T3 bare PAA. The bare metal is harder to section than the clad because (1) it is a less regular structure, and (2) the depth of the oxide layer on bare is approximately a third of that on clad. This makes the region very hard to locate in 500A-thick sections. Very few satisfactory regions were found; however, Figure B-13 shows that the oxide pore diameter is the same for both bare and clad metals. The structure also is the same, with pore walls giving gaps (G) at junctions. Figure B-13 shows well-defined pores for the bare metal oxide, whereas SEM techniques have shown an irregular structure for the same oxide (e.g., fig. B-10). This apparent discrepancy could be explained by the fact that very small regions have a more regular structure, and one of these was found in Figure B-13. Such regions were extremely difficult to locate in lateral sections of the oxide on bare metal.

PAA 2024-T3 Bare—Auger Survey and Depth Profile

Figures B-14 and B-15 show that the 2024-bare PAA oxide had high O and Al. The C level was lower than the clad-PAA oxide (21.8% versus 7.4%). P was detected at the 0.1% level compared with 0.6% P in the clad PAA oxide. This probably does not indicate a large change in P content. Ca was found as a trace element at 0.6% and no F and S were detected. No Cu or Mg typical of the base alloy were detected in the bare PAA oxide.

Depth profiling of this oxide found that all elements, except for oxygen and aluminum, were absent from the oxide. Cu rose to the alloy level as the metal was reached while sputter etching. A qualitative impression of the data would suggest that Cu may have increased in concentration just prior to reaching the metal-oxide interface.

PAA 2024-T81 Bare—SEM

A cross-section of the PAA oxide on 2024-T81 bare alloy is shown in Figure B-16. The oxide structure is similar to that in Figure B-11, although a porous columnar structure is even less evident.

STRUCTURE PROBE,INC.
141
BARE LATERAL
I1
180,000X

g

Figure B-13 Lateral Section of 2024-T3-Bare PAA
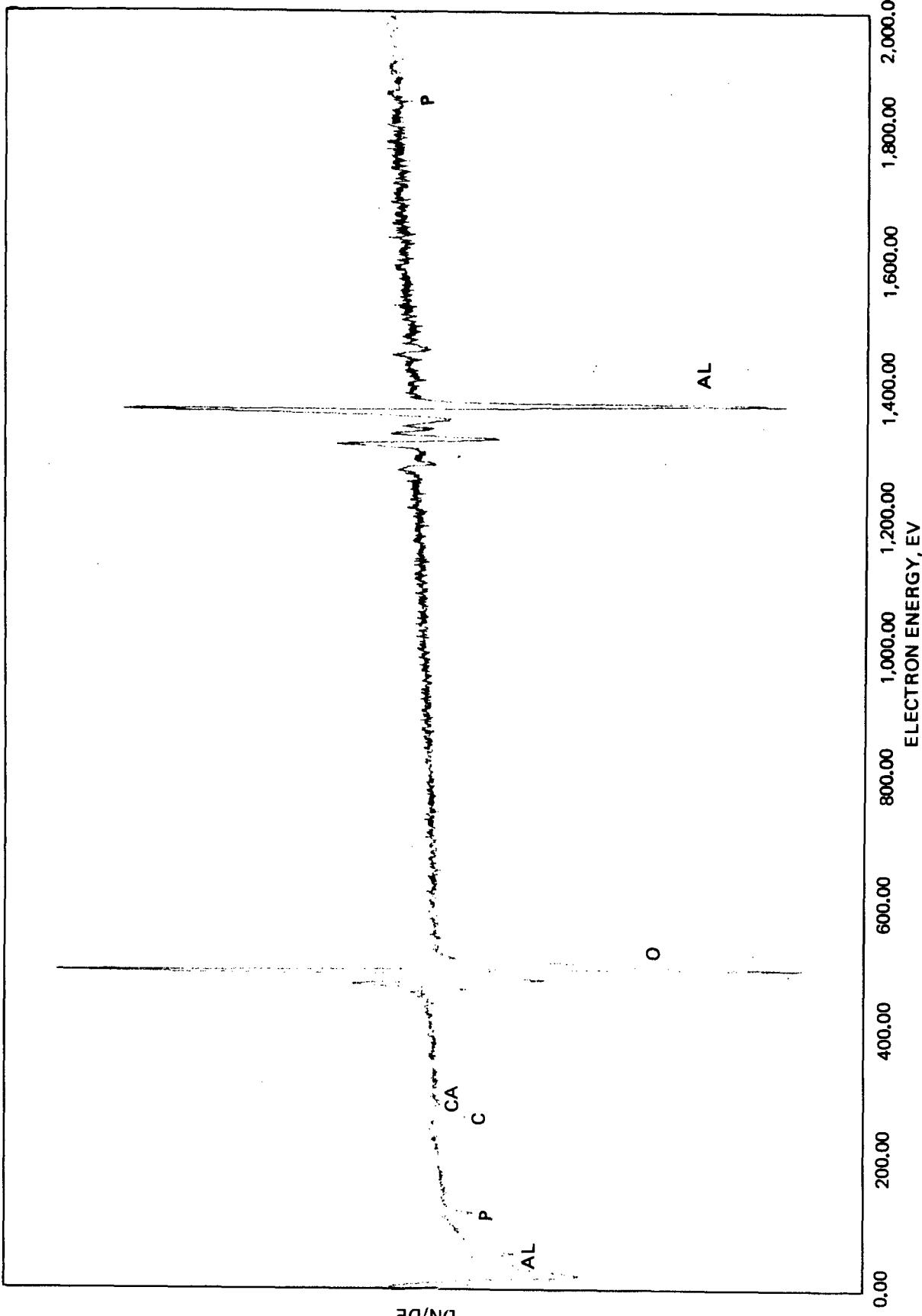
Figure B-14. Surface Composition of 2024-T3-Bare PAA

147
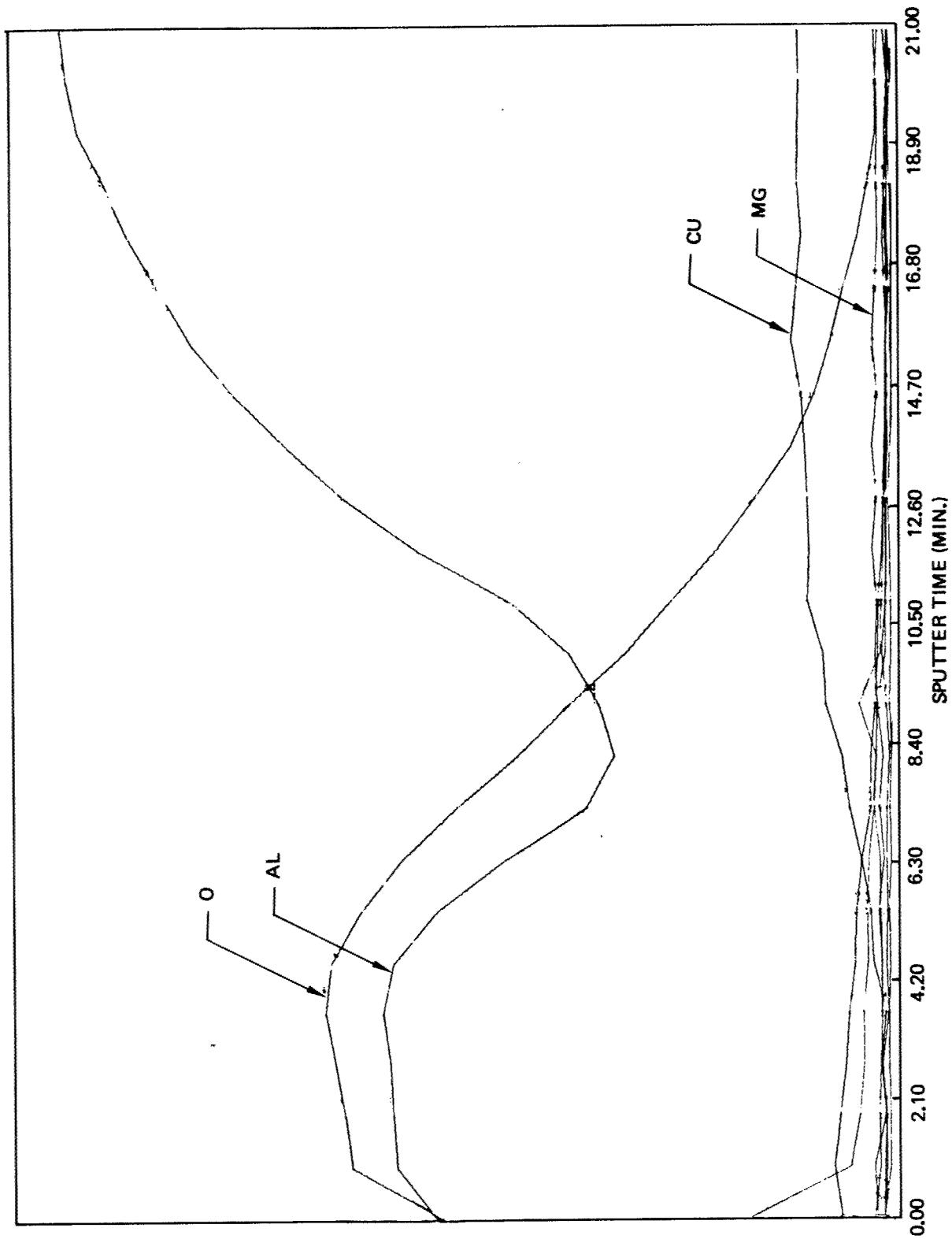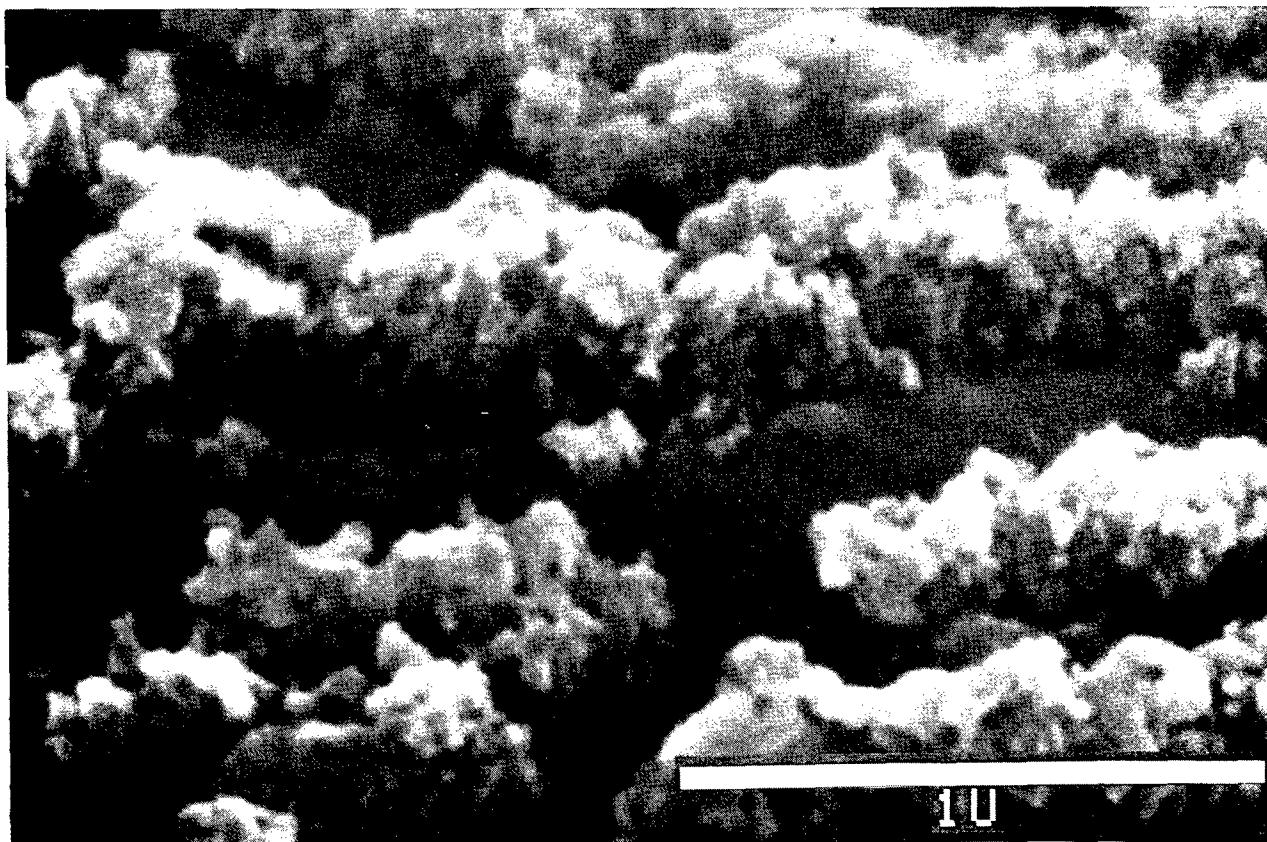
Figure B-15. Depth Profile of 2024-T3-Bare PAA

PEAK TO PEAK AMPLITUDE

SPUTTER TIME (MIN.)

148

FRACTURED OXIDE

Figure B-16.   SEM Photomicrograph of PAA on 2024-T81-Bare
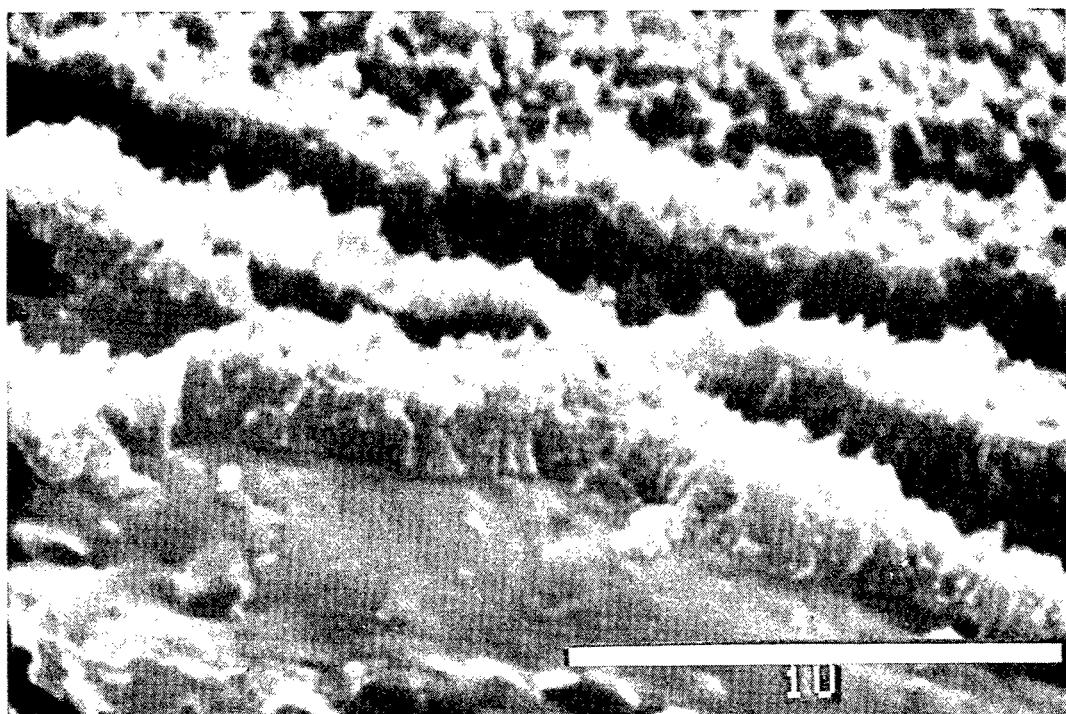
PAA 7075-T6 Bare—SEM

The fractured oxide structure of this alloy is shown in Figure B-17. The oxide appears similar to that of 2024-T3 bare and 2024-T81 bare, but perhaps slightly more ordered. The oxide thickness is approximately 200 nm, again similar to the other bare alloys.
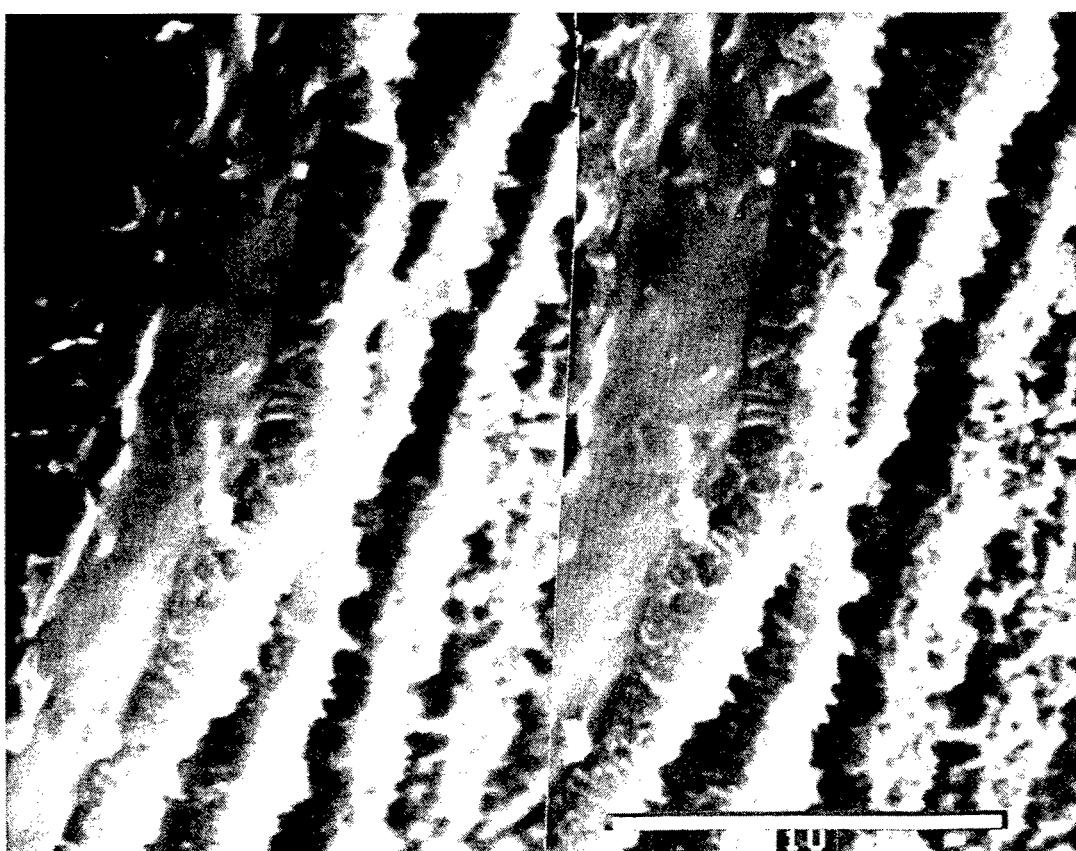
PAA 7075-T6 Bare—Auger Survey and Depth Profile

Figures B-18 and B-19 show that the 7075-bare PAA oxide displayed high levels of O, Al, and C at the surface. P (0.6%) was detected as for the other PAA oxide cases. Trace contaminant levels were detected of Ca (0.1%), Si (0.2%), and F (0.3%). The alloying elements of Zn (1.6%) and Mg (1.9%) were detected, but no Cu was observed.

Depth profiling of this oxide showed Al and O, with Cu rising to the alloy Cu level apparently prior to reaching the metal-oxide interface.

149

HIGH RESOLUTION VIEW OF FRACTURED OXIDE

STEREO PAIR OF ABOVE PHOTOGRAPH

Figure B-17. SEM Photomicrographs of PAA on 7075-T6-Bare

150
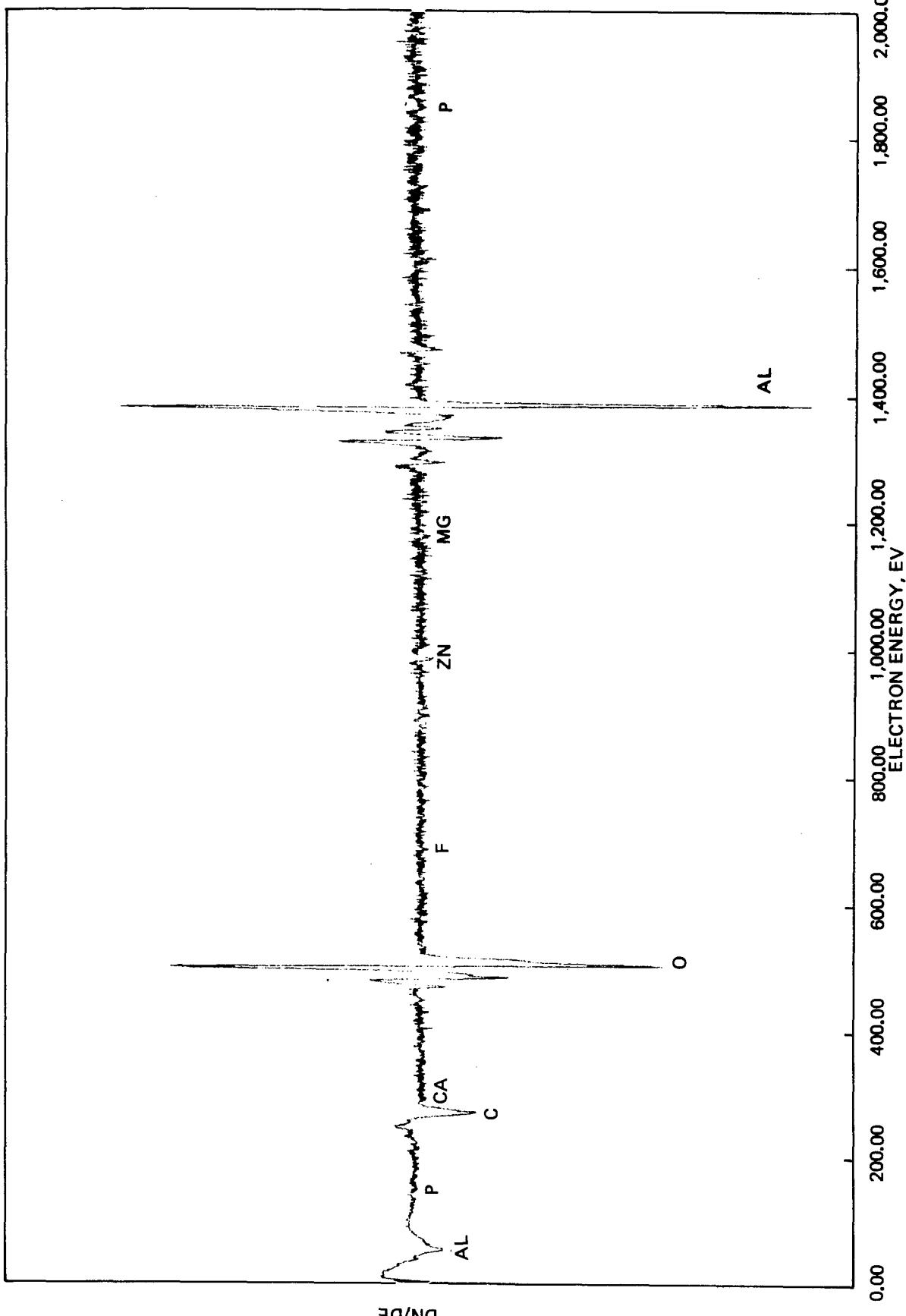
Figure B-18. Surface Composition of 7075-T6-Bare PAA

151
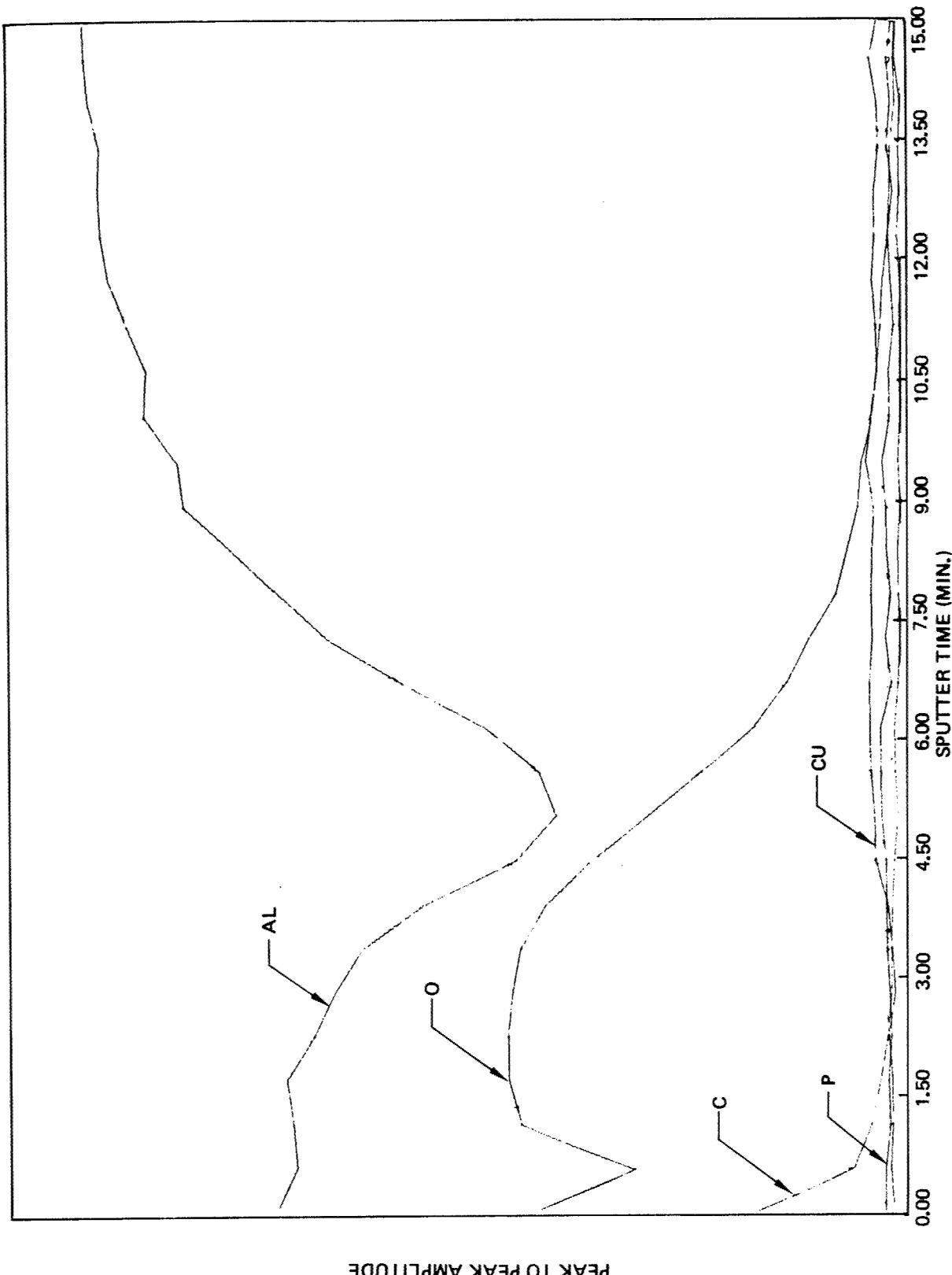
Figure B-19. Depth Profile of 7075-T6-Bare PAA

Summary of PAA Oxide Chemistry

Phosphorus--Two P peaks are analyzed by the AES spectra studied. A low energy peak at 120 eV has an escape depth of 0.3 to 0.4 nm while a high energy peak at 1859 eV has an escape depth of approximately 3 nm. The surface AES scan P data from these two peaks were normalized for sensitivity factors and then ratioed for comparison as shown in Table B-3. A ratio of P (low energy) to P (high energy) of values less than unity indicates an overlayer of material with a phosphorus-deficient composition, while a ratio with values greater than unity indicate an overlayer with a phosphorus-rich composition.

Table B-3. Summary of Oxide Surface Compositions

	Al/O	$\frac{P_{low} E}{P_{high} E}$	P(%)	CuMg[a]	ZnMg[b]	Bath elements (%)[c]	C(%)	S(%)
2024-clad PAA	1.1	1.2	0.6	0	0	1.0	21.8	ND
2024-T3-bare PAA	1.0	15.6	0.1	0	0	0.6	7.4	ND
2024-T3-bare FPL	1.3	ND*	ND	7.50	0	2.4	25.1	1.0
075-T6-bare PAA	0.6	0.9	0.6	0	0.84	0.6	15.9	1.5
7075-T6-bare FPL	1.5	ND	ND	0	1.20	2.1	14.0	ND

*Note: ND signifies that the element was not detected.

[a]The nominal atom ratios for 2024 alloy of CuMg = 1.14; for 7075, CuMg = 2.60.
[b]The nominal atom ratio for 7075 alloy for ZnMg = 0.83.
[c]The "bath elements" identification refers to all other elements referenced in the other columns (e.g., Si, Ca, F, Cl).

The computed ratio is unity for 2024-T3 clad PAA and 7075-T6 bare PAA, which indicates that the top 3 nm of these oxides have a relatively homogeneous phosphorus concentration. This region is relatively thin, as the depth profile data discussed earlier indicated that only the surface region contained appreciable phosphorus.

The PAA oxide of the 2024-T3-bare had a P (low energy) to P (high energy) ratio of 15.6, indicating an apparent P-rich zone at the top 0.3 to 0.4 nm. If the bare alloy showed this effect, the 7075-bare alloy would have been expected to show at least a trend in this direction. Because it did not, a phosphorus-rich zone is not thought to exist at the surface of 2024-T3 bare. This sample showed a lower percent carbon than any of the other samples, which may have influenced this measurement.

Alloy Elements—The chief alloying elements in 2024 are Cu and Mg, while the main alloying elements in 7075 are Zn, Cu, and Mg.

The 2024-clad PAA oxide, as expected, did not show the presence of Cu or Mg. However, the 2024-bare PAA oxide also did not show the presence of Cu or Mg from the base alloy. As noted earlier, the Cu may be present in the oxide near the oxide boundary region.

The 7075 bare PAA oxide did show Zn and Mg in the surface oxide at a ratio of 0.84, Table B-3. No Cu was detected for this system even though the alloy Cu/Mg ratio (atomic percent) is 2.6. The depth profile analysis did indicate a Cu concentration increase apparently in the oxide just prior to the metal-oxide interface.

Zinc does appear to be at the oxide surface, while Cu does not appear to migrate into the outer oxide layers. Magnesium, which is of a lower concentration than either Zn or Cu in the base alloy, has nearly the same surface concentration as the Zn (Zn/Mg = 0.84). This suggests that the PAA oxide formation mechanism on 7075-T6-bare allows Zn to come into the oxide, tends to suppress Cu migration into the oxide, and enhances Mg content of the surface oxide layers.

FPL OXIDES

FPL 2024-T3 Clad—SEM

A typical cross-section of a fractured FPL-formed oxide is shown in Figure B-20. The oxide appears to be approximately 30 nm thick. Porosity is difficult to determine because the oxide is so broken up and the presence of Au/Pd on the surface may obscure some of the fine structure.

FPL 2024-T3 Bare—STEM (Secondary)

An STEM photomicrograph of a fracture specimen of FPL 2024-T3 bare is shown in Figure B-21. The oxide layer is thin, approximatley 20 nm, and no evident structure can be seen by this analysis.

154

FRACTURED OXIDE

Figure B-20. SEM Photomicrograph of Optimized FPL on 2024-T3-Clad

FPL 2024-T3 Bare—Auger Survey and Depth Profile

Figures B-22 and B-23 show that the FPL oxide on the 2024-T3 bare alloy had high concentrations of oxygen, aluminum, and carbon. Trace levels were present of Ca (0.8%), F (0.8%), Si (0.7%), and Cl (0.1%). S (1.0%) may have come from the bath sulfuric acid. The alloying elements of Cu (2.7%) and Mg (0.4%) also were detected at the surface of this oxide.

Depth profiling of the FPL oxide showed a thinner oxide than the PAA oxides described above. The Cu concentration appears to increase as analysis proceeds into the oxide to a level higher than that observed in the alloy. Similar behavior was observed for Mg, but was less well-defined because of a lower concentration of Mg as well as a lower elemental sensitivity for this element compared to Cu. All of the other contaminants fell rapidly to nondetectable levels in the oxide as the sputter profiling continued.

155

0.1μm
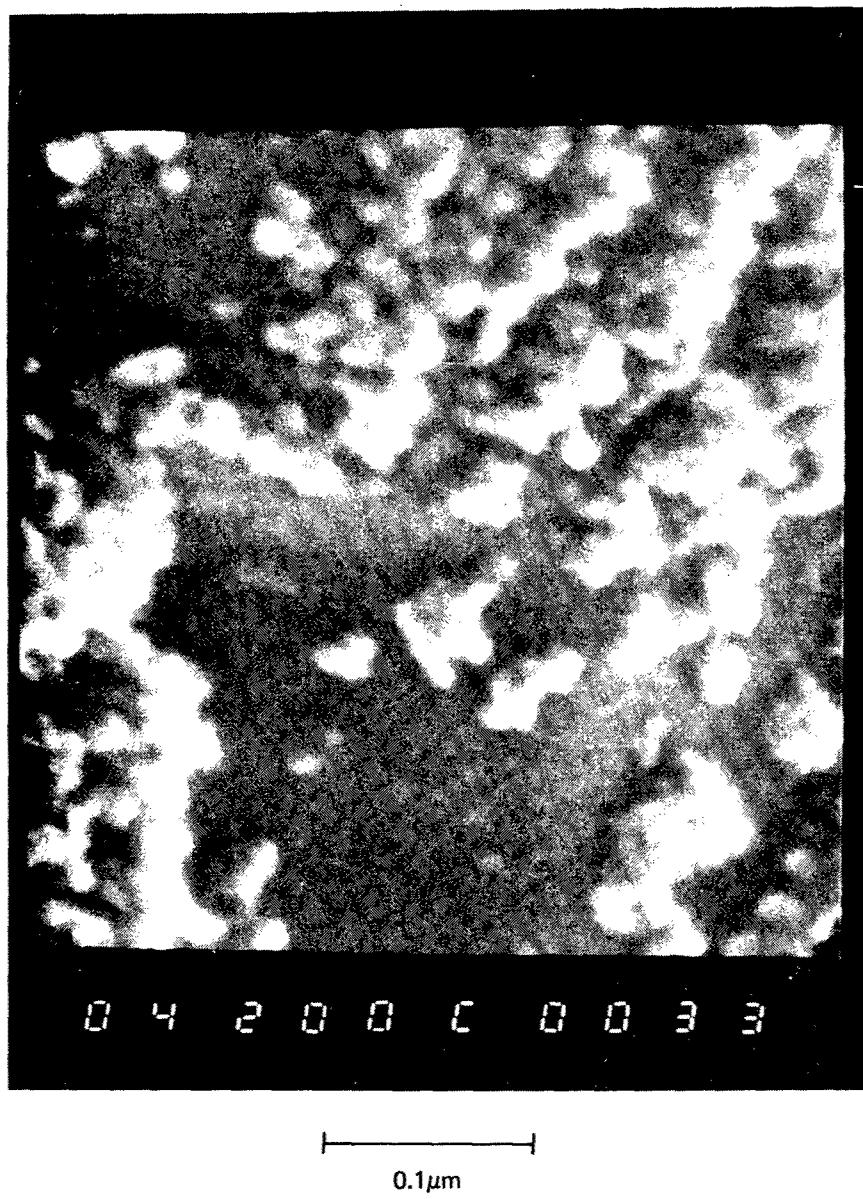
Figure B-21. STEM Secondary Electron Photomicrograph of 2024-T3-Bare FPL

FPL 7075-T6 Bare—Auger Survey and Depth Profile

Figures B-24 and B-25 show that the FPL oxide again had a thinner oxide than was observed for the PAA oxide. High levels of O, Al, and C were seen on the oxide surface. Trace levels were detected of Si (0.6%), Ca (1.1%), and F (0.4%). S (1.5%), probably from the bath, was observed. The alloy elements of Zn (2.3%) and Mg (1.9%) were found, but no Cu was detected. This is the same case as for the 7075-bare PAA oxide.
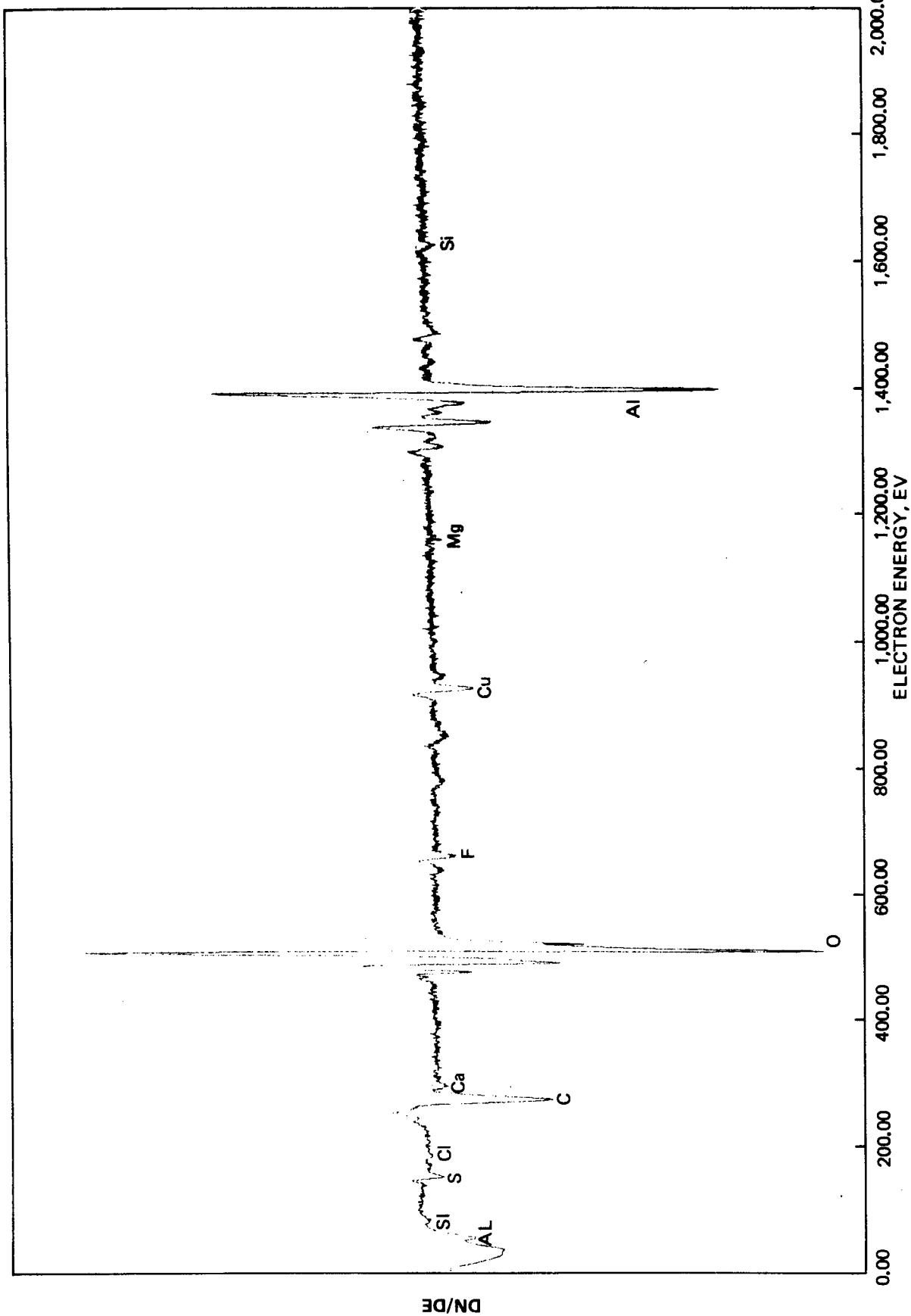
Figure B-22. Surface Composition of 2024-T3-Bare FPL
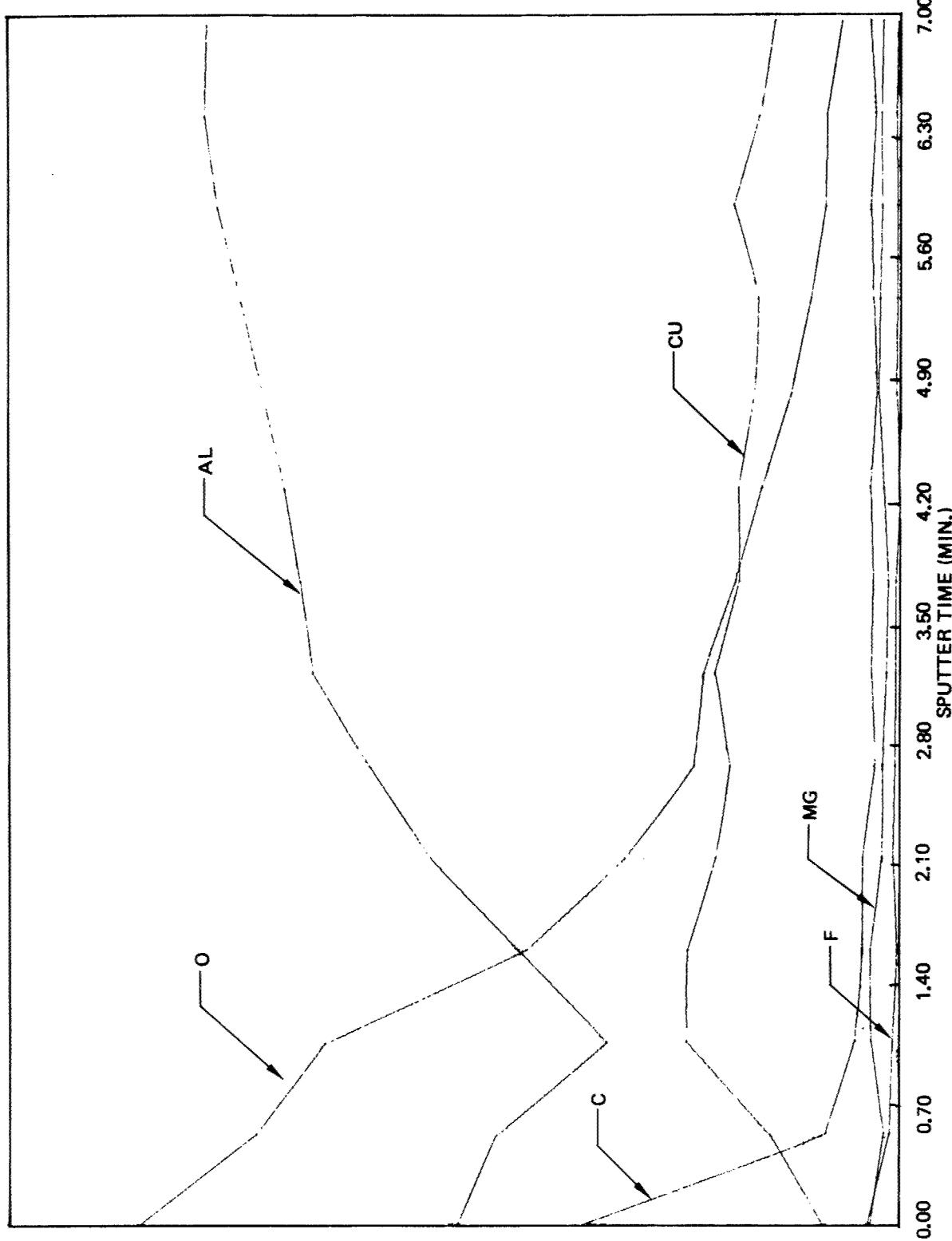
Figure B-23. Depth Profile of 2024-T3-Bare FPL
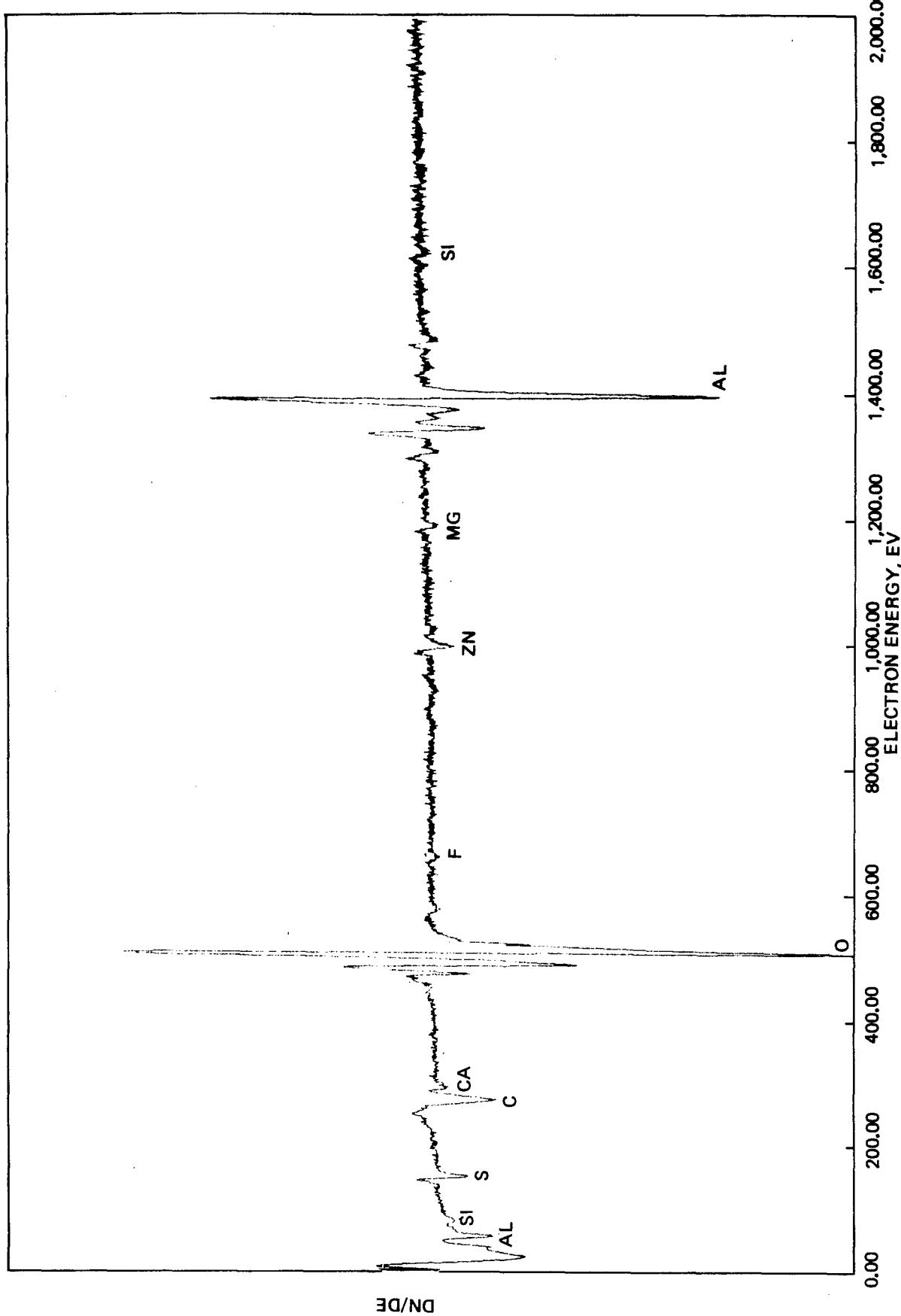
Figure B-24. Surface Composition of 7075-T6-Bare FPL
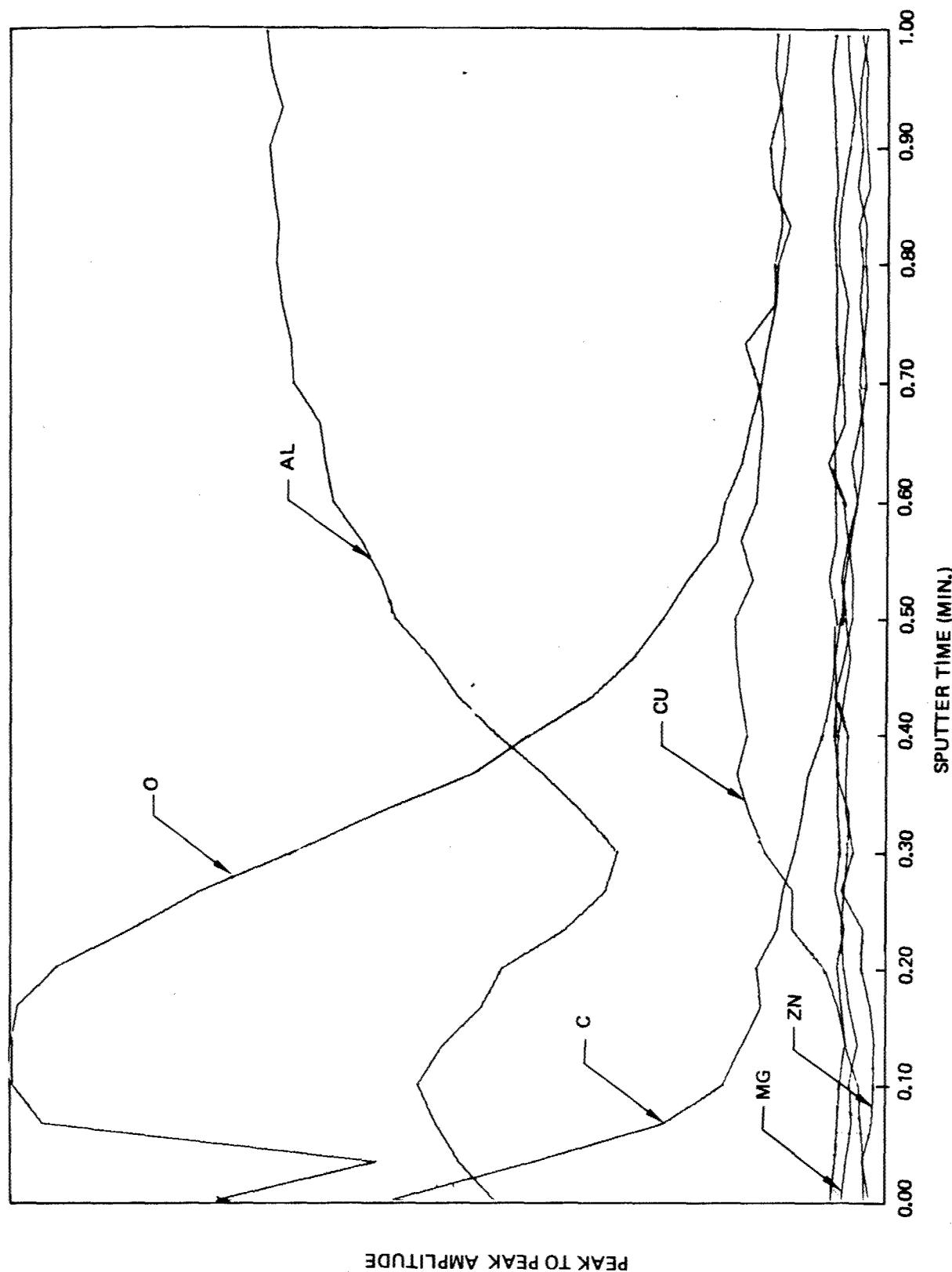
Figure B-25. Depth Profile of 7075-T6-Bare FPL

Depth profiles of this oxide found that the Zn level rose in the oxide to the alloy value prior to the oxide-metal interface. The Cu level rose to a value apparently greater than the base alloy and fell to the base alloy level in the metal. Magnesium may have the same behavior as Cu, but the data are not conclusive.

Summary of FPL Oxide Chemistry

Alloy Elements in FPL Oxides—The 2024-bare FPL oxide displayed a high Cu/Mg ratio. As indicated earlier, these elements have an appreciable concentration in the oxide, rising to values apparently as high as or even higher than that observed in the alloy.

The 7075 bare FPL oxide displayed a Zn/Mg ratio of 1.20 in the surface oxide, which compares favorably with the value of 0.84 observed in the PAA oxide of this alloy. Again, no Cu was observed at the surface. Copper, having a higher concentration in the alloy than Mg, did not migrate out to the surface of the oxide. This behavior is similar to that observed for the 7075-T6-bare PAA oxide.

APPENDIX C

CHEMICAL CHARACTERIZATION OF ADHESIVE PRIMERS

INTRODUCTION

The six primers were chemically fingerprinted by infrared spectroscopy (IR) and high-pressure liquid chromatography (LC) methods. Gel permeation chromatography (GPC) analyses of the six primers were also performed using Waters Associates -styragel GPC column. Due to the poor resolution of the GPC chromatogram, detailed peak comparison was not performed. The following primers were analyzed:

Primer 1   BR-227   Batch L-41L66
Primer 2   BR-227A   Batch L-41L67
Primer 3   BXR-MSR   Batch L-41L69
Primer 4   BXR-MSNR   Batch L-41L70
Primer 5   BR-238   Batch B-13F-49
Primer 6   BXR-238   B-13F-50

INFRARED METHOD

The primer solution was shaken and one drop of solution was applied to a 1-inch-diameter NaCl IR window. The IR sample was then dried in a 120°F vacuum oven for 20 minutes. An IR spectrum was obtained and interesting absorption peaks were normalized to the peak at 1150 cm^{-1}.

The presence of butadiene and acrylonitrile rubbers in primers 2, 3, and 5 is clearly indicated by IR absorption peaks at 2240 cm^{-1} (C = N) and 970 cm^{-1} (C = C).

REVERSE-PHASE LIQUID CHROMATOGRAPHY METHOD

LC results showed the distinct differences among batches. Due to the nature of the LC technique, sample solutions were filtered through a 0.5-μm filter that retained the larger particles and only the filtrate was characterized. The high-resolution capability of the LC technique has made the LC analysis an optimized technique for resin fingerprinting.

LC analysis was performed using the following conditions for primers 1-6:

Column: μ-Bondapak/C_{18}
Solvent: 50%-95% CH_3CN/H_2O in 15 min.

Flow: 2 ml/minute

Detection: UV 254 nm

A sample solution was prepared (0.6%) by dissolving the dried (40 minutes, 120°F vacuum oven) primer in tetrahydrofuran, and the solution was filtered using a paper pulp packed syringe and 0.5-μm millipore filter. Summaries of the analyses are shown in Table C-1.

Table C-1. Sample Absorbance Ratios

Sample	P_2/P_1		P_3/P_2		P_4/P_2	
BR-227 Batch L-41L66 Primer 1	1.4156 1.4265	1.4210	0.2900 0.3564	0.3232	1.2811 1.2838	1.2824
BR-227A Batch L-41L69 Primer 2	0.6618 0.6931	0.6774	0.5556 0.5357	0.5456	1.2889 1.2930	1.2910

Sample	P_2/P_1		P_3/P_2		P_4/P_1	
BXR-MSR Batch L-41L69 Primer 3	1.2820 1.2210	1.2515	1.2200 1.2069	1.2134	0.7026 0.7895	0.7466
BXR-MSNR Batch L-41L70 Primer 4	0.7642 0.7485	0.7564	1.2034 1.2500	1.2267	0.6218 0.6900	0.6559

Sample	P_1/P_4		P_2/P_4		P_3/P_4	
BR-238 Batch B-13F-49 Primer 5	0.1426 0.1443	0.1434	0.1465 0.1423	0.1444	0.1109 0.1113	0.1111
BR-238 Batch B-13F-50 Primer 6			0.1483 0.1512	0.1498		

There are potentially four major peaks present on the chromatograms of each pair of primers listed in Table C-1. Each peak represents the elution of a major component, the identify of which is currently unknown.

Because of variability of sample size, flow rate, etc., a standard technique is to report ratios or the peaks present when comparing pairs of chromatograms. The first two numbers of each column are the values for separate analyses. The second number is the average of the two.

A comparison of chromatograms indicates that primers 1-4 have similar chemical ingredients. Chromatograms of primers 1 and 2 are considerably different, especially in the P_2/P_1 ratio (1.421 for primer 1, 0.677 for primer 2). Absorbance ratio P_2/P_1 is higher in primer 3 (1.252) than in primer 4 (0.756). A comparison of chromatograms for primers 5 and 6 indicated that P_1 and P_3 were present in primer 5 and absent in primer 6. Identification of peaks was not performed.

GEL PERMEATION CHROMATOGRAPHY METHOD

Chemical characterization of the adhesive primers using GPC at Boeing was not initially successful. We have improved our GPC analysis technique. Using eight polystyrene molecular weight standards, we established a calibration cure. The molecular weights of the eight standards are: 2000; 3000; 15,000; 35,000; 110,000; 200,000; 470,000; and 2,700,000. We employed a bank of μ-styragel columns whose size exclusion limit is 10^5, 10^4, 10^3, 500, and 100 A.

A sample of BXR-MSR was analyzed with the following procedures:
- Sensitivity setting: 0.05 AUF (a detector response of 0.05 absorbance units will be plotted full scale)
- Solvent: Methylene chloride (as extracting solvent and mobile phase)
- Flow rate: 3 ml/min
- Sample preparation: The sample was filtered to remove strontium chromate particles and rubber.
- Detector: Set at 254 nm (UV)

The primer was resolved into seven components whose molecular weights ranged from 1 to 9000.

Since the molecular weights of all constituents of the primer were below 10,000, we switched to a bank of μ-styragel columns with the following size exclusion limits: 2 x 500A and 3 x 100A. We obtained better peak separation by not employing the columns required for separation of higher molecular weight components. The following six primers were analyzed:
- BXR-238
- BR-238
- BXR-MSR

- BXR-MSNR
- BR-227
- BR-227A

The major molecular weight fractions detected for each primer are listed in Table C-2.

BR-227A has a greater percentage of high molecular weight fractions than does BR-227. This may be due to incomplete filtering of the higher molecular weight rubbers. The percentage of lower molecular weight components is similar.

Table C-2. Molecular Weight Distribution of Primers

BR-227		BR-227A	
Percent	Molecular weight	Percent	Molecular weight
15.4	10,400	1.5	36,000
14.5	2,590	8.3	8,870
15.4	639	14.7	2,190
14.5	158	12.5	540
12.3	39	14.1	133
10.0	10	11.7	33
18.8	2	9.7	8
		16.3	2

BXR-MSNR		BXR-MSR	
Percent	Molecular weight	Percent	Molecular weight
11.9	8,870	2.77	36,000
19.4	2,190	12.4	8,870
17.7	540	19.7	2,190
13.5	133	17.9	540
10.3	33	12.7	133
8.0	8	9.0	9
12.5	2	7.4	8
		11.9	2

BR-238		BXR-238	
Percent	Molecular weight		
5.7	146,000	No low to medium molecular weight fractions were detected	
1.1	36,000		
0.8	2,190		
0.4	540		
2.6	8		
5.2	2		

BXR-MSNR and BXR-MSR are compared next. Again, the rubber-modified primer (BXR-MSR) has a greater percentage of higher molecular weight fractions for the same reason. The percentages of lower molecular weight fractions also are similar.

The last two entries in the table clearly indicate that we were not successful in separating the components of BR-238 and BXR-238. We speculate that the filtration process somehow removed the major constituents of the two primers.

APPENDIX D

FINAL REPORT ON WORK PERFORMED
AT WASHINGTON STATE UNIVERSITY

FINAL REPORT

on

Work Performed at Washington State University
under P.C. #G-A13049-7668

A Subcontract of Air Force Sponsored Research

entitled

Relationship of Interfacial Compatibility
to Durability of Adhesive Bonded joints

Emission Phenomena During Deformation of
Materials and During Anodizing

by

J. Thomas Dickinson
Physics Department
Washington State University
Pullman, WA 99164

FOREWORD

This final report was prepared by Washington State University, Pullman, Washington, under P.C. #G-A13049-7668.

ABSTRACT

This report presents a summary of work performed from March 1979 to June 1980. The report covers a number of experiments concerning emission phenomena accompanying deformation of materials and also during anodization of aluminum. This includes electron and positive ion emission, as well as acoustic emission from anodized alulminum during plastic deformation; electron and positive ion emission during fracture of a number of materials (e.g., ionic covalent and hydrogen-bonded materials), including composites; and, briefly, the chemiluminescence that occurs during H_3PO_4 anodization of aluminum.

SUMMARY

This report discusses work performed at Washington State University from March 1979 to June 1980. The principal objective was to explore the emission of particles from materials during deformation. Our major goals have been to provide experimental evidence of the use of this emission to characterize anodized oxide films, to provide insight into the mechanisms of this emission, and to explore the nature of such emission from different types of materials. In this reporting period, we have concentrated on:

1. The characterization of anodized oxide films by exoemission and acoustic emission

2. A comparison of acoustic emission with electron and ion emission from anodized oxide films

3. The acoustic emission accompanying tensile deformation of adhesively bonded aluminum

4. The electron and positive ion emission during fracture of ionic, covalent, and hydrogen-bonded materials

5. The chemiluminescence emitted during H_3PO_4 anodization of aluminum

Results from items 4 and 5 are still in a preliminary stage, but will be reported on briefly because of their possible significance to the technology of adhesive bonding and composites.

The following is a summary of the results:

1. The electron emission (EE) from Boeing baseline H_3PO_4 anodized 2024 clad and bare aluminum was studied as a function of anodization bath temperatures. The EE was found to be sensitive to changes in this variable. Bath temperature also affected the acoustic emission (AE) observed while straining the aluminum. The combination of EE and AE serves as a probe of the anodized coating.

2. Comparison of AE caused by cracking of the anodized oxide layer with the accompanying EE shows that EE is intimately related to crack propagation in the oxide. The AE and EE count rate versus strain are closely related, most electron bursts are in near coincidence with an AE burst (therefore, with crack initiation), and most EE occurs within a few microseconds of crack propagation. There appear to be two components of EE, one occurring at crack-tip propagation and the other following propagation with a decay time of a few microseconds.

We also have evidence of a component of EE unrelated to EE that is attributed to chemi-emission.

3. Comparison of the positive ion emission (PIE) with both AE and EE shows that it also is caused by cracking of the oxide. PIE shares one feature of the EE time distribution, suggesting a common mechanism for PIE and part of the observed EE. '

4. There is a distribution in the number of electrons and positive ions detected per burst. This is a distribution of the form $\exp(-(n-1)/\eta)$, where η is 0.96 and $n = 1$, 2, . . . (the number of electrons observed per burst). Both PIE and EE have the same distribution.

5. There is a correlation between the number of electrons emitted in a burst and the size of the accompanying AE burst. This correlation suggests that the number of electrons emitted is dependent on the strain energy released upon crack elongation.

6. A wide range of other materials has been fractured, including metals with natural oxide coatings, ionic materials such as sapphire and quartz, glass, polymers, and pure carbon. All have been observed to emit electrons. Those that have been tested for PIE also have been seen to emit ions.

7. During the fracture of fibers of glass and carbon, very short bursts of EE and PIE are observed. The fracture of pure epoxy samples also produces short-lived EE and PIE. However, when composites are fractured, extremely intense, long-lived EE and PIE are observed. PIE is seen whenever pullout and/or deformation occurs.

8. During tensile deformation of porous anodized aluminum, little AE from oxide fracture is detected. When such an oxide is coated with epoxy primer or primer and adhesive, changes in AE are observed. In some cases, AE is suppressed; in others, increased.

9. Photon emission is observed during H_3PO_4 anodization of aluminum. This emission is easily detected and could provide a convenient way to monitor anodization in a commercial situation.

INTRODUCTION

Exoelectron emission is generally caused by release of highly localized energy at the surface of a solid in a relative short time period. Many competing processes can dissipate this energy, particle emission being one of the least likely and photon production being the most likely. The emission that we observe in these experiments can be directly correlated with the propagation of cracks in the oxide coating. The manner in which an oxide coating responds to uniform straining of the aluminum substrate and the resulting emission of particles is strongly dependent on the mechanical and chemical nature of the oxide coating. These physical and mechanical properties can play an important role in the adhesive bonding characteristics and/or corrosion resistance of the films. An overall test of an oxide layer sensitive to a number of oxide properties is difficult to find. With this thought in mind, we began examining tribostimulated exoemission from anodized oxide films.

In this report, recent data on a series of samples prepared by The Boeing Company are summarized and conclusions given concerning the use of exoemission as a means of detecting differences in oxide layers. The relationship between acoustic emission (AE) and electron emission (EE), as well as details of the fracture of oxide coating and EE, are examined. Recent results of positive ion emission (PIE) are presented. Another emission phenomenon, the chemiluminescence that occurs during anodization of aluminum of H_3PO_4 is briefly examined. Finally, recent studies of fracture of other materials, including composites, are reported.

CHARACTERIZATION OF ANODIZED OXIDE FILMS BY EXOEMISSION AND ACOUSTIC EMISSION

As previously reported (ref D-1, D-2, D-3), EE from anodized oxide layers on a number of substrates has been examined. Recently, the detection of AE from such samples was added. As will be shown later, the majority of AE observed from soft aluminum substrates is from oxide cracking, and the EE correlates strongly with this AE.

On alloy substrates, there is a larger component of AE from the substrate itself. Also, the Boeing "baseline" oxide on both bare and clad 2024 aluminum alloy does not seem to crack very much during plastic deformation of the aluminum, as determined by optical microscopy of the samples during elongation. The cracks are very sparsely

distributed and tend to be relatively short, with no particular orientation relative to the strain axis. This leads to somewhat weak EE and AE caused by oxide cracking.

PROCEDURE AND COMMENTS

The sample sets provided for this study were anodized by The Boeing Company according to Boeing baseline specifications (H_3PO_4 anodization), except that the temperature of the anodization bath was varied. The temperatures were 62, 72 (baseline), and 82°F for both clad and bare 2024 aluminum alloy. Detectable EE was found for each set of samples provided, and a substantial change was found in the AE observed as we changed from one set of samples to another.

These particular samples differed from supposedly identical samples produced previously at Boeing (ref D-1) and our laboratory (ref D-2) in the following ways:

1. The total EE from the deformed samples was smaller by a factor of 10 on 2024 bare.

2. The cracks on the bare samples were not as long and numerous as on previous samples, in agreement with item 1.

3. The variation over a set of samples was greater for these samples than in the past.

4. The dependence of total EE on anodization temperature for 2024 clad came out differently than an equivalent series anodized in our laboratory (ref D-2).

These differences may well be due to small procedural changes or, perhaps, treatment after anodization. We tried to keep our handling of the samples as rigidly controlled as possible. For future comparison, the procedure is outlined as follows:

Following receipt of the samples from Boeing, they were stored in a desiccator to keep them free of excess moisture. Just before mounting in the vacuum system, the samples were rinsed thoroughly in clean acetone. The sample was placed in the straining apparatus (ref D-3) and an AE transducer attached near one end of the sample. The system was pumped down to 2×10^{-6} torr, then strained uniaxially to 18% strain. The electron detector is a channeltron electron multiplier positioned 1 cm away from the sample and biased +300V relative to the ground sample.

The electron discriminators, amplifiers, count-rate meters, and chart recorders were maintained at constant levels for each run. The major source of vibration between samples within a set (as well as between sets of identical samples) was changes in the oxides. When samples are produced and handled identically in our laboratory, there is agreement in the basic features and total EE to within 8% deviation. Identical samples have the same crack densities after straining and should have close to identical physical and chemical structures. Since these are the factors that determine EE behavior, it is concluded that significant differences (8%) in the observed EE are due to differences in the oxides. This could be caused by a number of factors, including:

1. Differences in the anodization procedure (see ref D-2) before, during, or directly after anodization
2. Contamination of the anodization bath
3. Differences in the surface of the oxide; e.g., contamination or damage due to handling
4. An aging effect (see ref D-2)

Factors 1, 3, and 4 have been shown to strongly influence EE. It is suspected that contamination in the anodization bath also could alter EE through chemical alteration of the anodic film.

RESULTS

Despite the slight inconsistencies in comparison with previous results, we can nevertheless compare the six sets of samples provided and point out the substantial changes that occur between them. To present the data, we first tabulate total EE and AE for each of these sample sets, then present typical count-rate curves for each set. Table D-1 presents the averages for each set. Each set contains 5 to 10 samples, and the uncertainty represents one standard deviation.

All samples yielded detectable exoemission above the background count rate, although the baseline 2024 bare sample emission rate was very low. Nevertheless, deviations from baseline anodization are detectable in both clad and bare alloys.

The AE from these samples is very interesting. With the exception of the 62°F 2024 bare samples, AE is substantially reduced from that of the unanodized samples.

Table D-1. Summary of EE and AE Results on Clad and Bare Al 2024

	Anodization temperature	EE	AE
Al 2024-Clad	62F	2220± 600	11,600 ± 4,000
	72F	520± 100	4,600± 3,000
	82F	220± 80	2,500± 1,000
	No oxide	4 (Background counts)	22,300± 2,000
Al 2024-Bare	62F	255± 10	25,000± 11,000
	72F	50± 10	12,400± 3,000
	82F	135± 20	12,700± 3,000
	No oxide	4 (Background counts)	20,700± 7,000

Several investigators (ref D-4, D-5, D-6) have shown a completely different trend—an increase in AE with the presence of oxide. In fact, Dunegan and Tatro (ref D-6) report that for 6061 aluminum alloy, the total number of AE bursts increases with the fifth power of the oxide thickness (they do not specify their type of oxide). In our earlier work (ref D-1), it was shown that exoemission on clad and bare 2024 aluminum alloy also was strongly dependent on oxide thickness. The following section will show that one of the parameters of the anodized oxide layer on Al 1350 that determines both the AE and EE totals is the number of crack increments that occur during straining.

To make all of these results consistent, we believe that in the case of Al 6061, AE from oxide cracking was being observed. In the case of our porous oxides on Al 2024, we believe that the oxide is <u>inhibiting</u> AE from the Al 2024 substrate. A possible cause of this reduction in AE due to the presence of the oxide is the prevention of slip-step formation at the substrate surface. This is frequently associated with AE production in aluminum.

Thus, it appears that for the porous oxides provided, very little AE is detected due to oxide cracking. However, the cracking that does occur leads to EE. Both the AE and EE show changes with the anodization bath temperatures. The two types of emission, used together, might provide an even stronger indicator of the oxide coating.

184

Figure D-1 presents typical data (count rate versus strain) for the EE from Al 2024 clad samples anodized at the three different temperatures. The major differences seen are, of course, the shapes and intensities of the emissions. The basic shapes were quite reproducible. The periodic structure that occurs at all temperatures, but is most evident in the 72°F curves, is caused by an effect that is observed on Al 2024 but not on anodized pure Al or the purer alloys. It is a consequence of localized straining along the length of the gage. The electron detector views only about 1 cm of the sample (determined by decreasing the length of the anodization region). If the sample ceases to elongate for a short time within this 1-cm interval, the oxide cracking would cease and the accompanying emission also would cease. When the surface of a sample is viewed under a microscope during uniform elongation, one can easily see that, locally, the strain starts and stops somewhat sporadically. A student, Dave Snyder, is currently examining mechanisms of plastic deformation in aluminum alloys to explain this effect. A simple way to avoid this "fine structure" would be to use an electron multiplier with a larger anode (e.g., a channeltron with a cone) and stronger electric fields to increase the collection efficiency from the entire length of the sample.

Figure D-2 shows a similar set of data for Al 2024 bare. Although the emission is quite weak, it is well above background (the number of counts due to background is 2 to 5 counts for the duration of the test). We also see that the basic shape of the emission curve is different from that of the clad samples; i.e., a rise in emission intensity as the sample elgonates. This basic shape is in good agreement with our previous work (ref D-1, D-2). Finally, we note that the intensity indeed depends on anodization bath temperature.
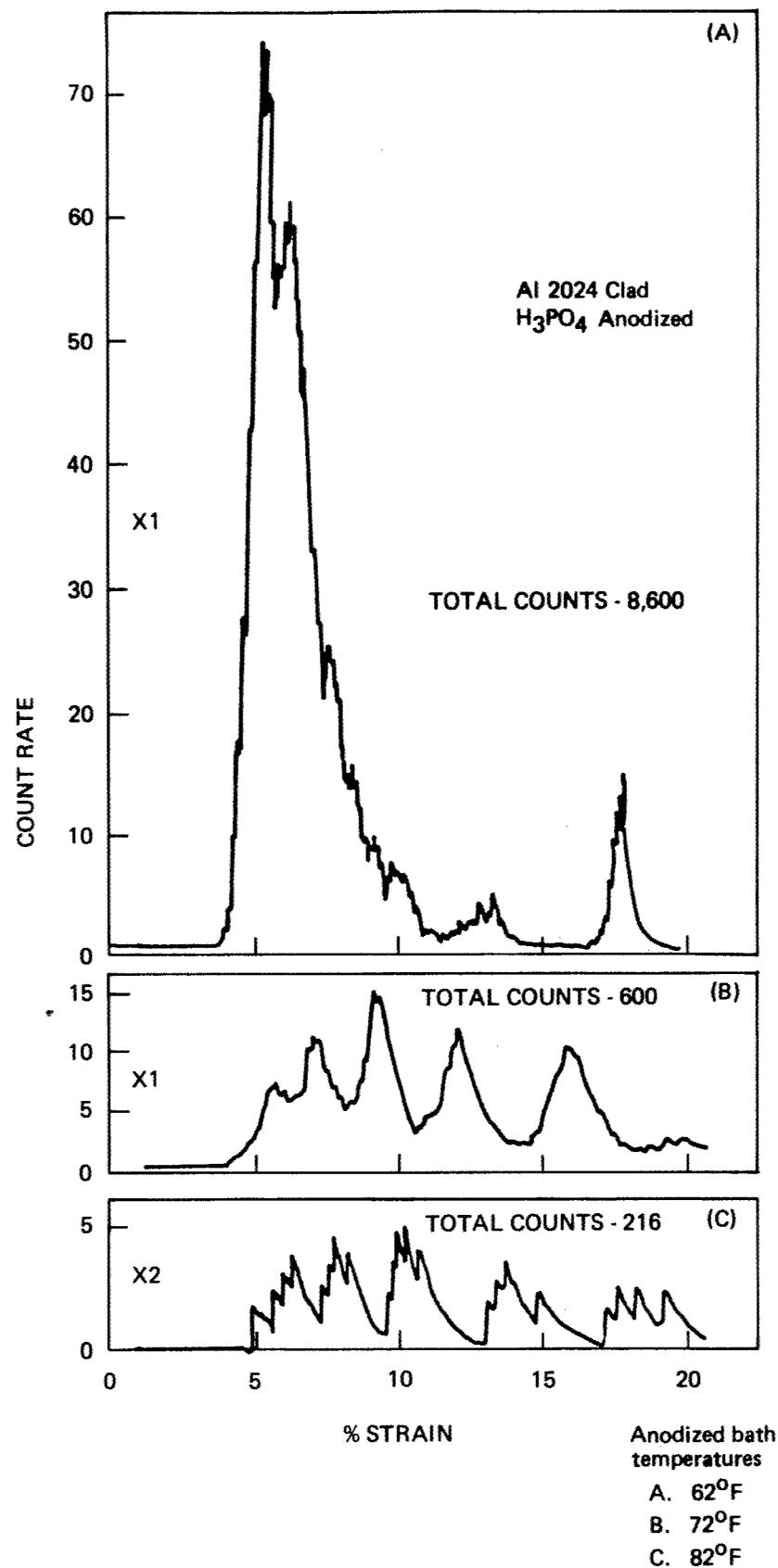
Figure D-1. *Typical Electron Emission Curves (Count Rate vs Strain)*
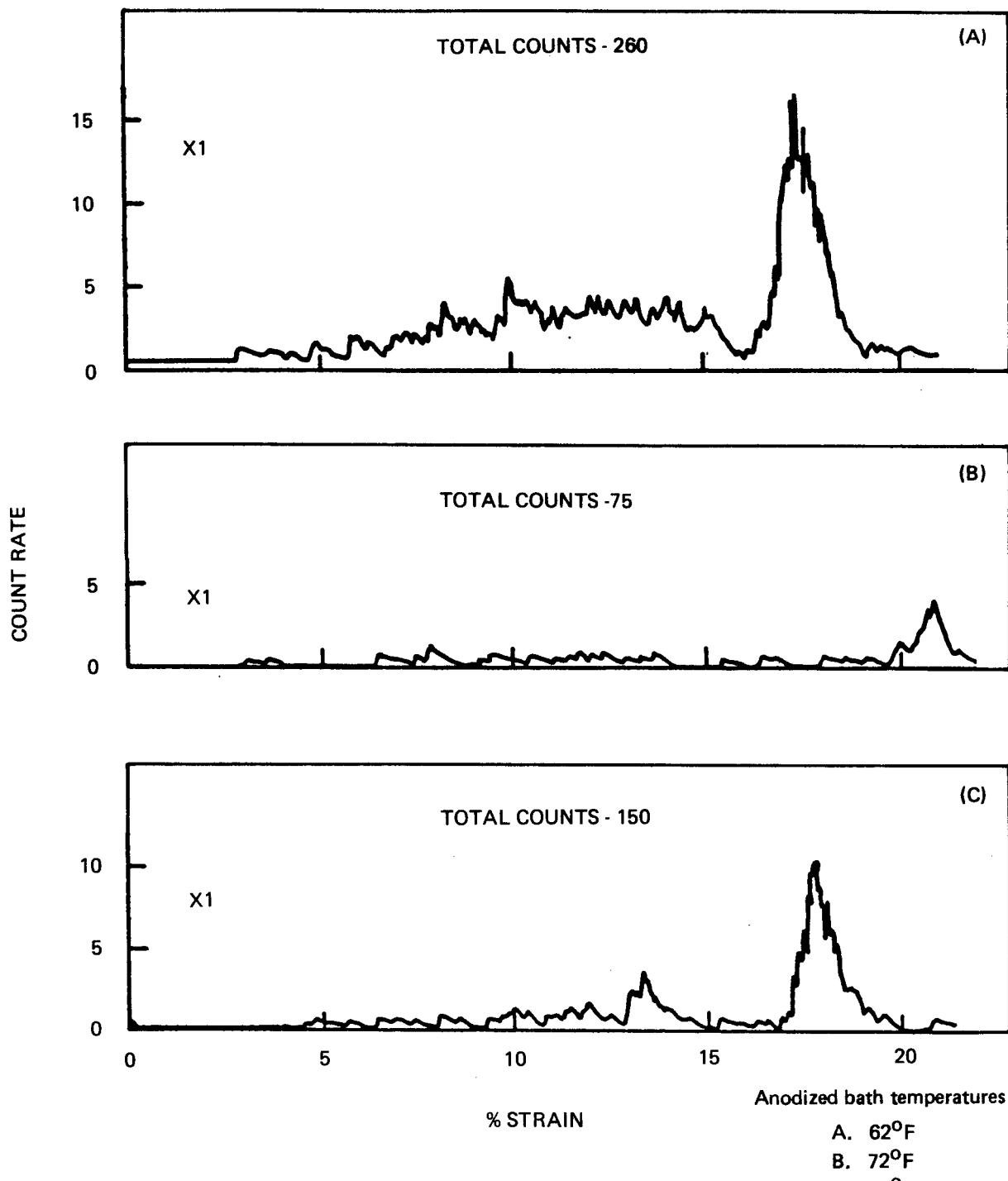
Figure D-2. Typical Electron Emission Curves (Count Rate vs Strain)

CONCLUSIONS

As we have shown previously (ref D-1, D-2), as well as in this report, tribostimulated exoemission is a sensitive probe of the physical and chemical properties of an anodized oxide coating. The results obtained here and earlier are consistent with optical and scanning electron microscopy and the hypothesis that oxide disruption (e.g., cracking) is a prerequisite for emission. The oxides studied here differ in their pore structure and thickness, both of which can greatly influence the manner in which the films respond to tensile deformation. An example is that when the oxide becomes thick and the pores more columnar, increased exoemission is observed (ref D-2). Similarly, for a given thickness, as the oxide becomes more porous and "fluffy," exoemission decreases (ref D-2). Both of these results are due to the fact that the nature and number of cracks in the oxide are strongly dependent on these oxide characteristics.

Although the AE results also show sensitivity to the oxide on Al 2024 clad, it appears to be such that the oxide tends to inhibit AE. This is somewhat more difficult to use as a probe of oxide character. Nevertheless, in conjunction with EE, AE might be very useful in providing unambiguous characterization of oxide films. In the next section, we will explore the correlation of AE and EE where almost all of the AE is coming from oxide cracking.

ACOUSTIC EMISSION AND ELECTRON EMISSION
DURING DEFORMATION OF ANODIZED ALUMINUM

Anodic oxide coatings are widely used in industry today. For example, two important uses of anodic oxide films on aluminum are as protective coatings and as preparation for adhesive bonding. There is considerable interest in characterizing oxide films and surfaces and in understanding the mechanical properties of oxide layers under stress.

We have been investigating the emission of different types of particles from anodized aluminum during uniaxial tensile deformation. The types of emission observed include electrons (ref D-1, D-2, D-3), positive and negative ions (ref D-1), photons (ref D-1), and neutral molecules (ref D-4). The EE observed often is referred to as tribo-stimulated exoelectron emission because the deformation of the material leads to the emission. In general, the observed EE is closely associated with the production and growth of cracks in the oxide coating, although the mechanism is not at all clear. In this report, we present new experimental data relating EE and cracking of the oxide layer, leading to a better understanding of this phenomenon. An important new addition to our measurements is the detection of AE from the samples during their deformation in vacuum. We have evidence that the AE we observe actually accompanies the propagation of a crack in the oxide film. A major goal of this work has been to examine the correlation of EE and AE.

EXPERIMENT

The experimental details for observing tribostimulated exoemission from anodized aluminum samples may be found in references D-1 through D-3 and D-15. The experiments we now describe were performed at a pressure of 10^{-4} Pa in a liquid-nitrogen-trapped, diffusion-pumped vacuum system. This system could be recycled in 30 minutes, which allowed rapid data collection. The major features of the EE are unchanged when performed under UHV conditions (10^{-8} Pa) (ref D-2). The electrons emitted during tensile deformation of the anodized samples were detected with a channeltron electron multiplier with an estimated quantum efficiency of 50 to 80% (ref D-16). The entrance to the electron multiplier was at a potential of +270V relative to the sample (at ground) to enhance the collection efficiency.

The specimens were made from annealed Al 1350 sheet (99.5% pure), 1.14 mm in thickness, machined in a dogbone shape with a gage of 5 x 25 mm. The samples were cleaned in a $CrO_3-H_2SO_4$ solution and anodized in a 0.05 M ammonium tartrate solution at room temperature for 30 minutes at 230 V. This produces a very dense barrier-type oxide with a thickness of 300 nm (ref D-1). A commercial masking material was used to limit anodization to a small 30-mm^2 patch on one side near the center of the gage. The masking material was peeled off after anodization. When inserted into the pulling apparatus in the vacuum system, the oxide film faced the channeltron, approximately 1 cm away.

An acoustic transducer was attached to the center of the specimen on the side opposite the oxide film. The transducer was attached by a rubber band, and a film of Apiezon N vacuum grease provided acoustic coupling to the specimen. Two AE transducers were used in this work: an AC 175L and an AC 1500L, both available from Acoustic Emission Technology Corporation. A broad-band amplifier with 160-dB gain was used with appropriate filters to boost the signal-to-noise ratio. The signals associated with the AE during deformation were in the form of discontinuous bursts observed as ring-down pulses. For the AC 175L, the frequency of ringing was 170 kHz and typically 500 s in duration. The AC 1500L ringing occurred at 2 MHz for approximately 100 µs. In most of our experiments, a pulse discriminator was set slightly above the noise level to detect the start of the acoustic signal and to produce an easily handled, single pulse in near coincidence with this event. Extreme care was taken to measure one AE pulse per burst and to ensure that the discriminator output was as nearly as possible in coincidence with the beginning of the AE burst. With the AC 1500L transducer, we estimate that the discriminator output pulse is 1.8 ± 0.5 µs after the onset of the AE event, taking into account both the time required for the stress wave to reach the transducer crystal and amplifier rise times.

RESULTS

AE and Oxide Cracking

To determine the role of the anodized layer in the production of AE, we tested several unanodized Al 1350 samples. With the exception of a small peak that occurs in the elastic portion of the stress-strain curve (also observed with anodized samples), the AE bursts observed were negligible in number. The anodized samples, on the other hand,

produced a total of 10,000 to 20,000 detectable AE bursts when strained to 10%. This led us to the hypothesis that the AE bursts are due to cracking of the oxide coating. Further supporting evidence was obtained by directly observing the initiation and incremental growth of cracks in the oxide in air under an optical microscope (100X) while simultaneously listening to the demodulated AE bursts over a loudspeaker. A significant number of the two events appeared to coincide. We are attempting to quantify these results by simultaneous video and audio recording.

In addition, the average length of both new cracks and the increments of crack growth was observed under the microscope to be about 0.1 mm. A measurement of total crack length in the oxidized area leads to an estimate of roughly 12,000 increments of crack growth during the experiment (10% strain). This is consistent with the total AE counts we observed, again indicating that the oxide cracking is the source of the AE.

Finally, the characteristic AE curve (AE count rate versus strain) for samples strained in air differs strikingly from that of samples strained in vacuum. For samples strained in air, the onset of AE and peak positions are shifted to a strain about 1% lower than in vacuum and the total AE is about 40% of the AE detected in vacuum. These differences are attributed to the changes in the mechanical properties of the oxide in air versus vacuum. (A prime suspect is H_2O vapor absorption (ref D-2, D-17).) For anodized samples strained in air, optical microscopy shows that the rate of crack growth as a function of strain correlates very well with the AE characteristic curve. Again, this supports the hypothesis that the observed AE bursts result from oxide cracking.

Characteristic Emission Curves for Anodized Al 1350 Strained in Vacuum

The characteristic AE and EE curves taken simultaneously with two count-rate meters are shown in Figure D-3 for a dense oxide on Al 1350. The close correlation between the two types of emission thus supports our early hypothesis that the EE is caused by cracking of the oxide layer (ref D-3, D-15).

Recording AE and EE simultaneously at a lower strain rate ensured that the absolute rates of detected emission were determined accurately. This provided an accurate ratio of EE to AE as a function of strain. Typical AE, EE, and EE/AE curves are shown in Figure D-4. The ratio is near unity and indeed depends on strain. During the initial rise of the major peak (near 2% strain), the cracking of the oxide appears to be
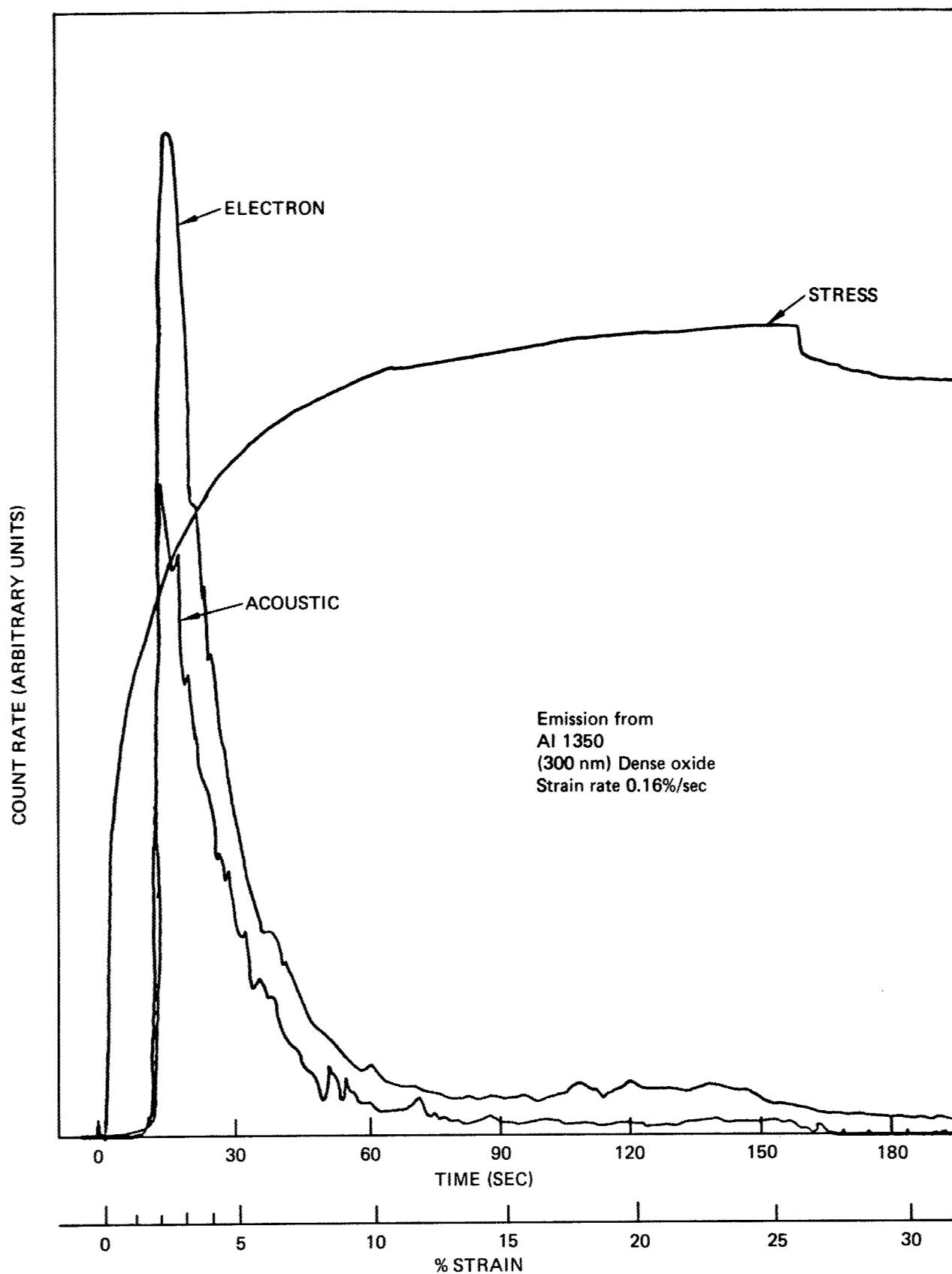
Figure D-3. *Acoustic Emission, Exoelectron Emission, and Stress, All vs Strain*
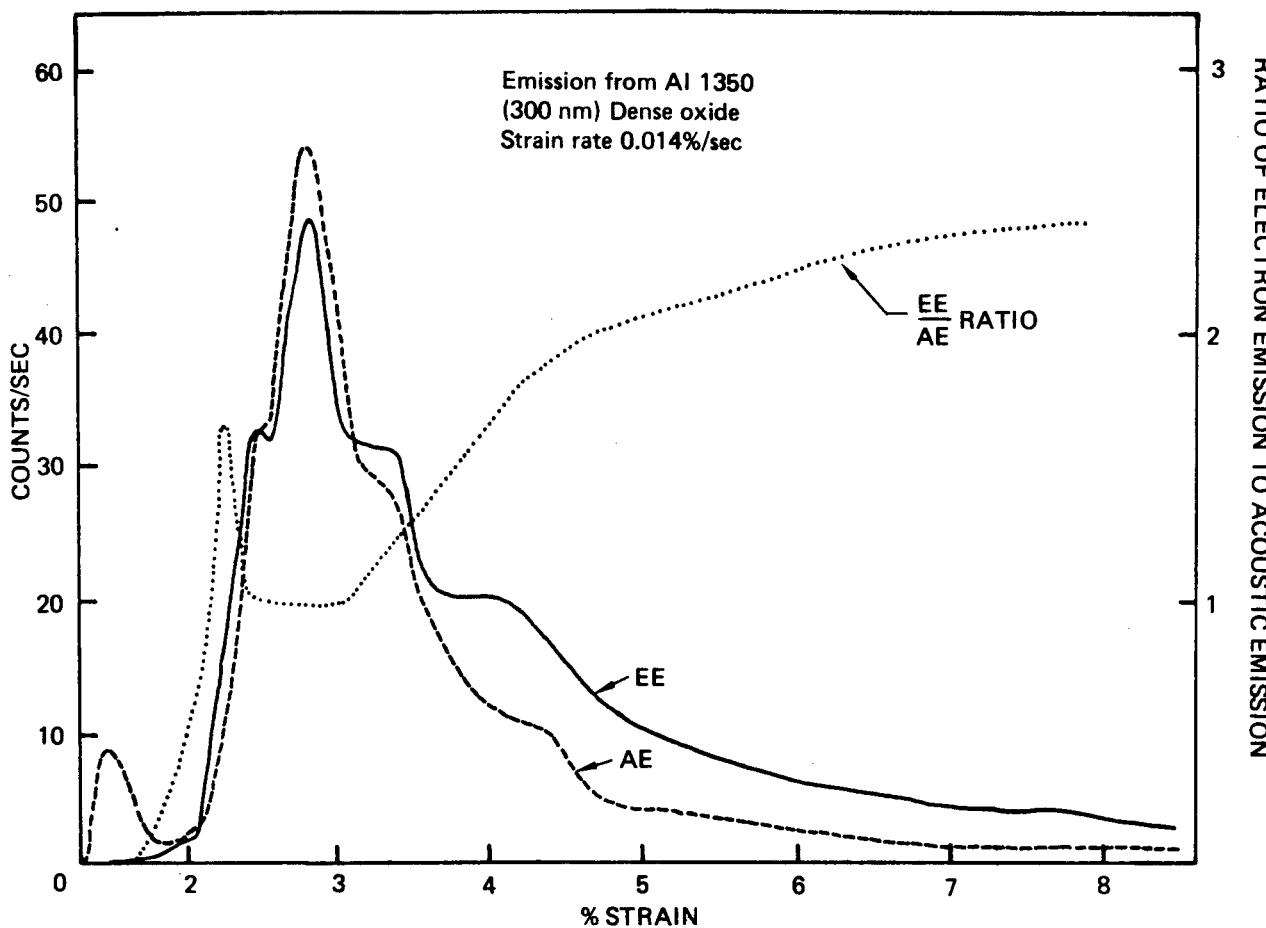
Figure D-4. EE and AE Rates and Their Ratio (EE/AE) as a Function of Strain for a Sample of Anodized Al 1350

noticeably more "efficient" in producing electrons. Optical microscopy shows that these are the initial cracks formed in the oxide, whereas the cracking occurring later is primarily crack extension. In the central portion of the emission curves, the ratio is near unity and constant. Finally, the ratio climbs as the AE curve is seen to drop off faster than the EE curve. We believe that this increase is due to chemi-emission, as we will discuss shortly.
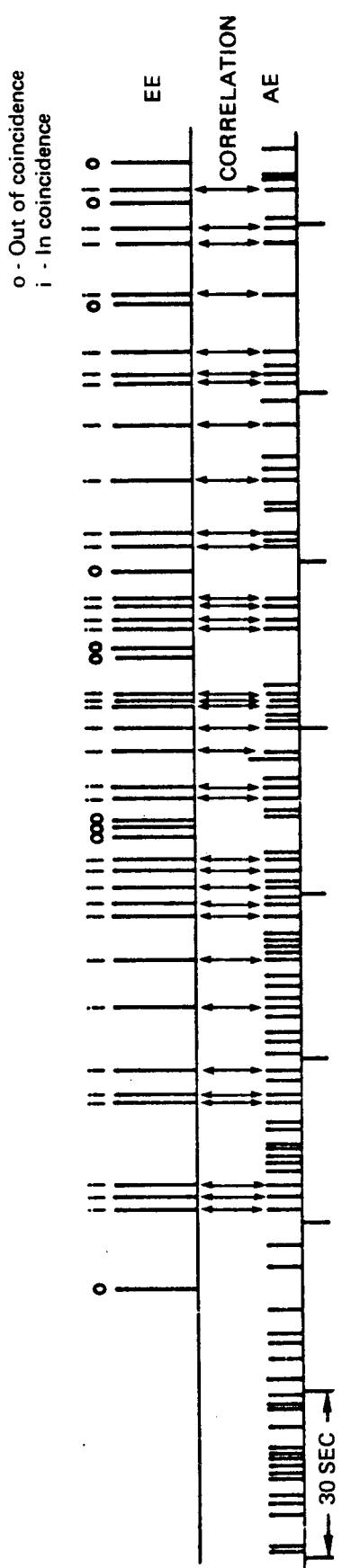
Correlation of AE and EE—Slow Time Scale

Another basic question is the time relation between AE and EE. If one pulls the sample very slowly, the bursts of AE and EE can be displayed as single events by means of suitable pulse shaping and the use of two synchronized strip-chart recorders. A Two Graduate Student Coincidence Detector (TGSCD) was used to detect EE and AE events in and out of coincidence. We estimate that our particular TGSCD could detect coincidences between the two types of bursts to within about 0.1 s. The results are as follows:

1. Near the peak of the emission, most of the electron bursts are in coincidence with AE bursts. Those EE bursts out of coincidence with AE bursts can, for the most part, be accounted for by background (2 to 3 counts per minute). This implies that EE occurs within roughly 0.1 s of the propagation of the crack in the oxide (see fig. D-5a).

2. Near the peak of emission, the majority of AE bursts occur without an accompanying electron. However, the ratio of EE to AE in this region remains near unity, which implies that many electron bursts consist of more than one electron. We calculate an average of three electrons per burst. This is substantiated by display of the electron pulses on an oscilloscope. Usually, single pulses are observed, but often two, three, or more occur within a few microseconds.

3. If the above "coincidence" experiment is performed after the elongation of the sample has been stopped (see fig. D-5b), one finds that the AE quickly drops to zero, but a small, very slowly decreasing EE component continues. It is this random component that we attribute to chemi-emission (ref D-18) due to the reaction of gaseous species with the fresh Al surface exposed by cracking of the oxide. The source of the gas could be the oxide itself (ref D-15) or it could be the 10^{-4} Pa background gas.

Time Correlation between AE and EE—Microsecond Time Scale

A multichannel scaler with time-of-flight (TOF) capability was used to determine the distribution of electrons in time relative to an acoustic burst. Because the acoustic waves took a finite time to propagate from crack to transducer, it was necessary to delay the electron pulses to display their entire time distribution. Figure D-6a shows the resulting distribution on a time-scale of 1-μs/channel. The $t = 0$ mark is uncertain to about ± 0.5 μs ($\pm 1/2$ channel). Oscilloscope traces of the AE bursts show that, frequently, the amplitude of the signals takes several cycles to reach a maximum. The structure seen on the left-hand side of the peak is due to triggering the TOF unit on an oscillation other than the first in the AE ringing burst. If one raises the discriminator level a few percent, the features before $t = 0$ grow considerably, becoming larger than the $t = 0$ peak. Figure D-6b is another time distribution obtained at $1/4$ μs/channel. The "spike" at $t = 0$ takes on a finite width and decay time. The time constants for the electron emission decay following the peak are about $3/4 \pm 1$ μs and a slower decay of 5 ± 1 μs. Any decay faster than $3/4$ μs probably would not be observable due to the finite rise-times and jitter in the pulse electronics. Thus, the observed time distribution is consistent with a process or processes that decay in $\leq 3/4$ μs and in 5 ± 1 μs.
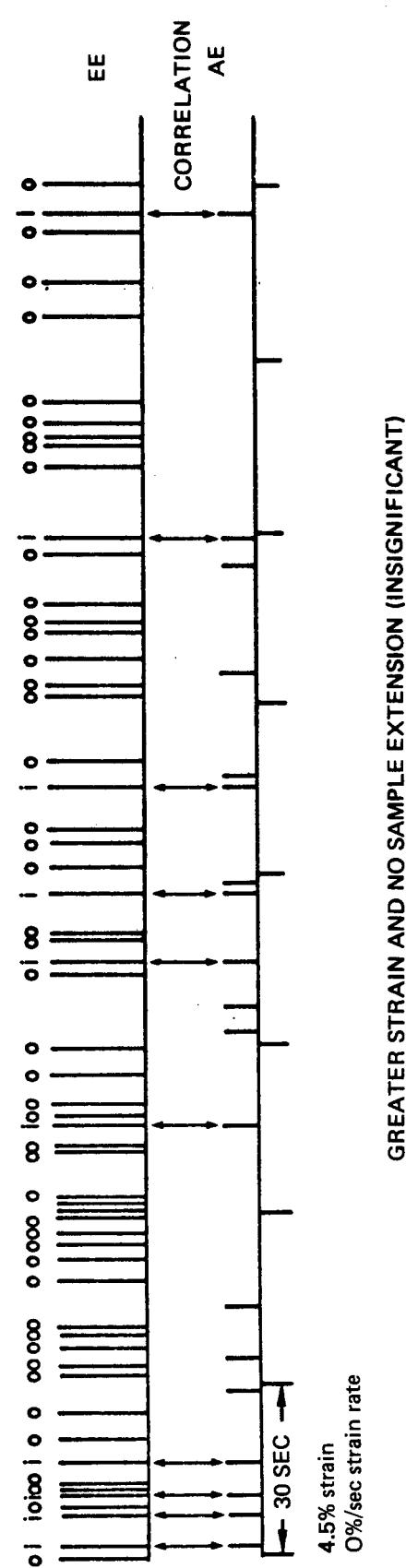
Figure D-5. Time Correlation of Electron Bursts and Acoustic Emmission

As mentioned earlier, some EE signals come in bursts of more than one electron. By triggering the TOF unit with the <u>first</u> electron in the burst, we could obtain the time distribution of the remaining electrons in the burst (with the exception of those within 1 μs of the first electron). We found an exponentially decaying function with a time constant of 4 ± 1 μs. Thus, the slower decay observed in Figures D-6a and D-6b could be due to the decay in the multiple electron bursts.

EE time distributions relative to AE taken at 8 μs/channel show decay components of even longer time constants; about 30 and 200 μs.

DISCUSSION

The AE bursts that we detected for these samples are clearly associated with the cracking of the anodic oxide coating and closely accompany actual propagation of the crack tip. The observed EE correlates strongly with the AE. This correlation is revealed on both a long time scale (figs. D-3 and D-4) and a short time scale (figs. D-6a and D-6b).

Within our uncertainty in the position of t = 0, the peak of the EE relative to AE occurs in coincidence. The decay from the peak exhibits a number of time constants and suggests that a number of mechanisms may be involved. Also, we have established that the highest rate of electron emission occurs very near the onset of crack propagation. For brittle materials, cracks propagate at near the speed of sound (ref C-8), implying that 0.1-mm-long cracks grow in times on the order of 0.1 μs. Thus, the electrons emitted in the narrow peak near t = 0 are leaving the sample in times less than a few tenths of a microsecond following crack propagation, and it is very likely that they <u>actually accompany crack propagation.</u> On the other hand, the slower decaying components, which involve a substantial fraction of the emission, occur after the crack tip has come to rest.

Clearly, these results provide strong evidence that tribostimulated exoemission accompanies and follows the propagation of cracks in the oxide film on the time scale of submicroseconds and microseconds. These two time scales prove decisively that there are at least two, possibly more, mechanisms involved. When one considers decay times for the various mechanisms considered for EE, one can differentiate between those that would decay faster than 3/4 μs and those that would decay more slowly. For the thin oxide coatings on aluminum, temperature spikes, electric fields due to

196
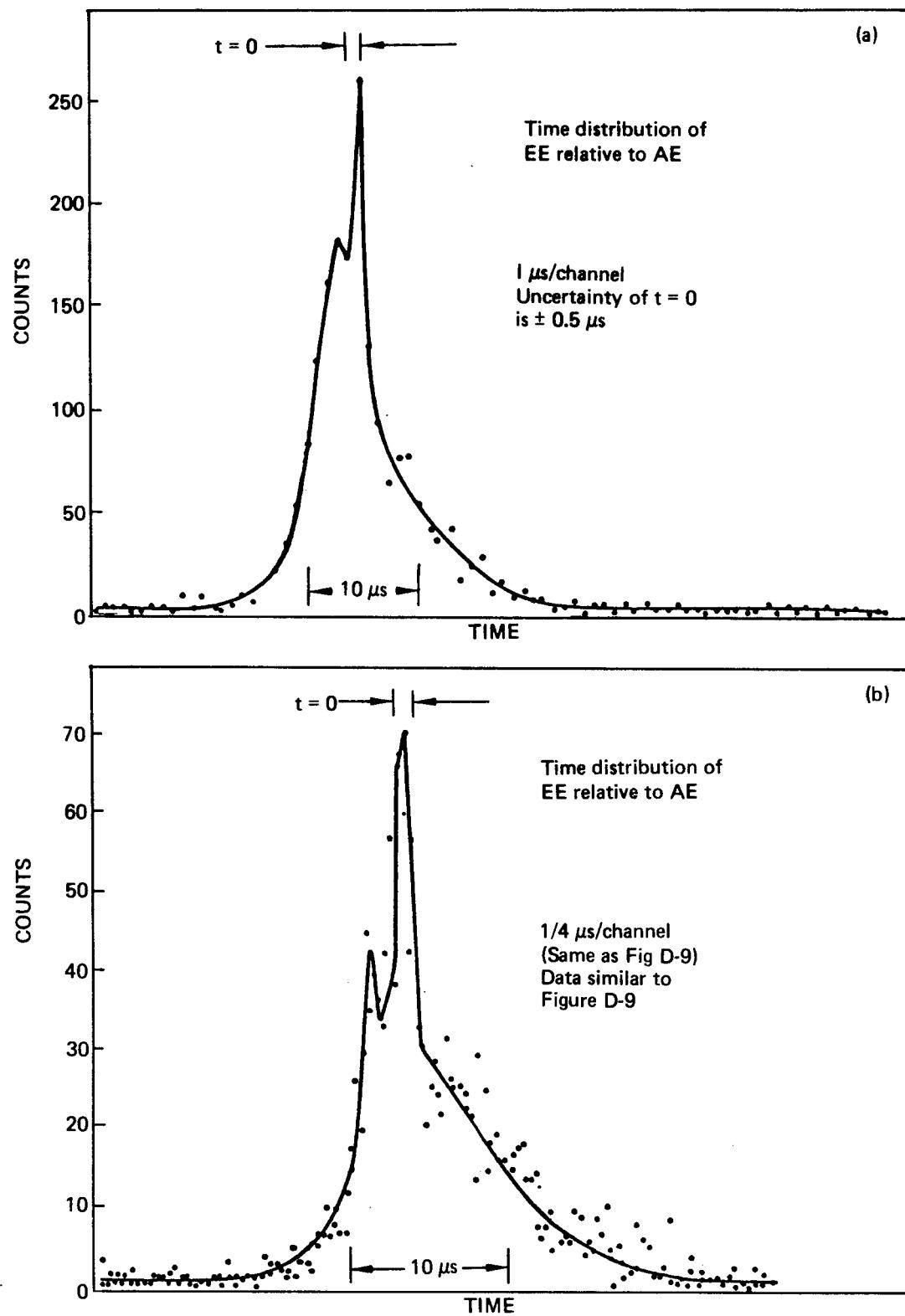
Figure D-6. Distribution of EE in Time Relative to AE

charge separation, the atomic and molecular de-excitations all would decay at times faster than $3/4\,\mu$s. Processes involving defect interactions, bulk diffusion, and chemi-emission occur on slower time scales. Improved measurements of the time dependence of both the fast and slower components of EE relative to AE should provide a basis for testing theoretical models of EE produced from oxide coating fracture. In conclusion, we mention that positive ions also are emitted during elongation and show a component accompanying fracture and a component that decays in $1.5\,\mu$s. Although the component accompanying fracture could involve the same mechanism producing the electrons, the "slower" ion component appears to have a distinctly different mechanism.

FURTHER WORK ON EMISSION PHENOMENA DURING
DEFORMATION OF ANODIZED ALUMINUM

In this section, we report on additional studies of emission from dense anodized Al 1350 that support the premise that crack propagation in the oxide film is necessary for particle emission to occur. However, the probability of detecting AE and the numbers of charged particles produced per crack increment are not necessarily constant with strain. We present evidence, for example, that shows a rapidly declining probability of AE burst detection as the oxide thickness is decreased due to a decrease in the energy released in the acoustic burst. We also observe a strain dependence in the energy content of the AE bursts. In addition, we find a correlation between the number of electrons released in an EE burst and the energy content of the accompanying AE burst. This results in a substantially larger number of electrons released per crack event for thicker oxides than for thin oxide coatings. We also present results on positive ion emission (PIE).

EXPERIMENT

The experimental details for observing tribostimulated exoemission from anodized aluminum samples may be found in references D-1 through D-3. The experiments we now describe were performed at a pressure of 10^{-4} Pa in a diffusion-pumped vacuum system. A liquid nitrogen cold trap was used to help lower the partial pressure of condensible background gases. The charged particles emitted during tensile deformation of the anodized samples were detected with a channeltron electron multiplier with an estimated quantum efficiency of 50 to 80% for electrons and nearly 100% for positive ions (ref D-16).

The specimens were made from annealed Al 1350 sheet (99.5% pure), 0.5 mm in thickness, machined in a dogbone shape with a gage of 5 x 25 mm. The samples were cleaned in a CrO_3-H_2SO_4 solution and anodized in a 0.05 M ammonium tartrate solution at room temperature for 30 minutes at a voltage to produce the desired thickness of oxide. This produces a very dense barrier-type oxide with a thickness from 100 to 400 nm (ref D-17). A commercial masking material was used to limit anodization to a small 30-mm^2 patch on one side near the center of the gage. The masking material was peeled off after anodization. When inserted into the pulling apparatus in the vacuum system, the oxide film faced the channeltron, approximately 1 cm away.

An acoustic transducer was attached to the center of the specimen on the side opposite the oxide film. The transducer was attached by spring clamps, and a film of Dow Corning silicone grease provided acoustic coupling to the specimen. The AE transducer used in this work was an AC 175L from Acoustic Emission Technology Corporation. A broad-band amplifier with 160-dB gain was used with appropriate filters to boost the signal-to-noise ratio. The signals associated with the AE during deformation were in the form of discontinuous bursts observed as ring-down pulses. For the AC 175L, the frequency of ringing was 175 kHz and typically 500 μs in duration. In most of our experiments, a pulse discriminator was set slightly above the noise level to detect the start of the acoustic signal and to produce an easily handled, single pulse in near coincidence with this event. In most of the experiments, care was taken to measure one AE pulse per burst and to ensure that the discriminator output was as nearly as possible in coincidence with the beginning of the AE burst.

In a limited number of cases, we examined the relative energy content of the detected AE bursts. In particular, we were interested in the dependence of the AE energy distribution on strain and oxide thickness. Rough energy distributions were determined by counting the number of cycles that the AE waves remained above threshold during ring-down. Using the analysis described by Harris et al. (ref D-18), we obtained an energy distribution relative to this threshold. Although this technique is not accurate, it does provide a rough measure of the energy content for comparison of the energy released under different conditions (e.g., oxide thickness or percent strain).

RESULTS

Oxide Coating Fracture

As previously mentioned, on 300-nm dense anodized Al 1350 samples, we observed crack initiation and incremental crack growth under a microscope while simultaneously listening to the demodulated AE bursts over a loudspeaker, and found that a significant number of the two events appeared to coincide. In further studies of correlation between AE and oxide fracture, we used a television camera attached to the microscope and a video tape recorder to monitor crack growth versus strain on a 1-mm^2 patch of oxide, while simultaneously measuring the AE count rate. From the recorded video data, we were able to measure crack density versus strain (fig. D-7). The derivative of this curve is the rate of crack growth. In Figure D-7, the peak at 1%
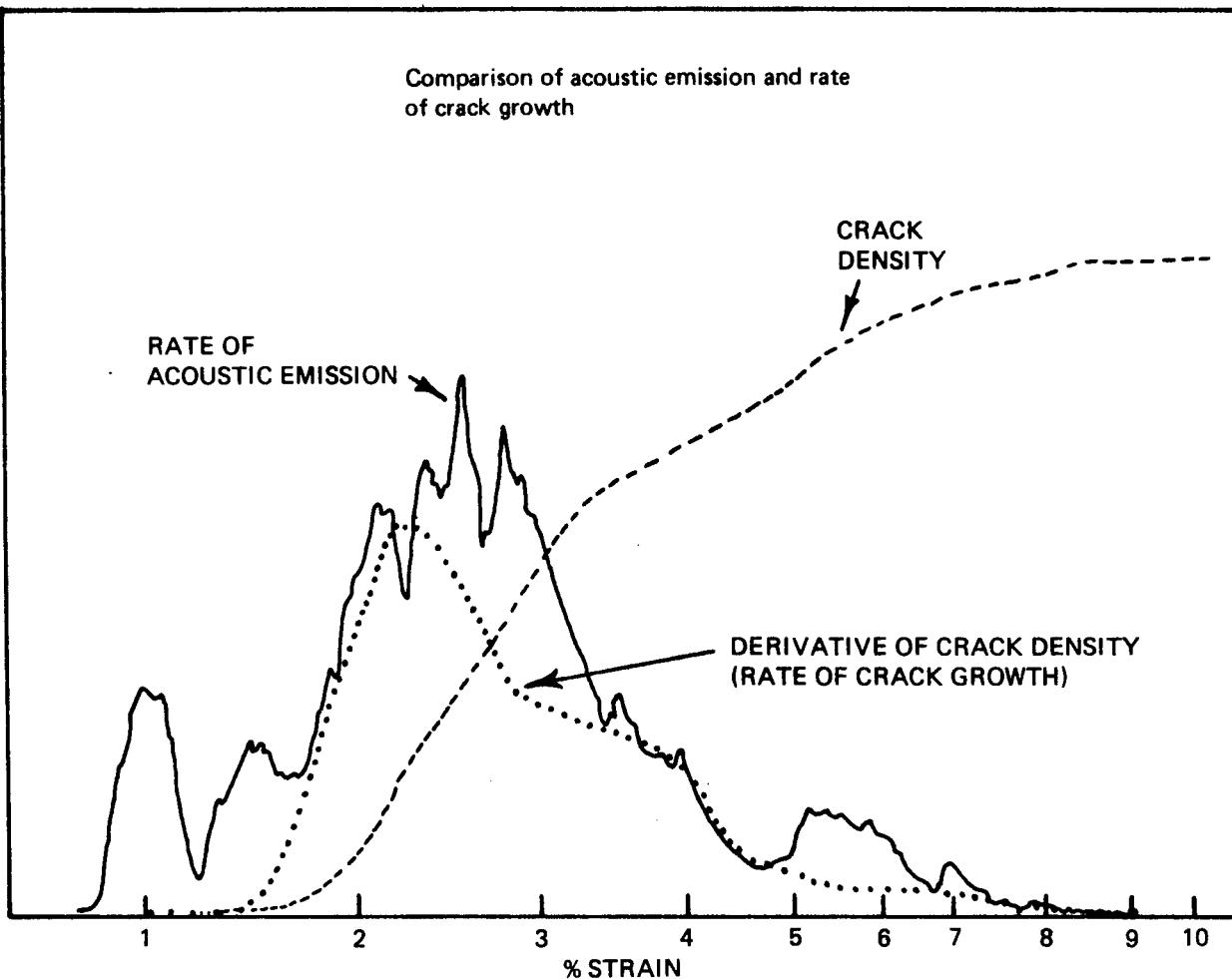
Figure D-7. AE Count Rate and Rate of Crack Growth vs Strain

is a substrate AE peak. The shape of the AE count rate is somewhat irregular due to the small area of oxide. Nevertheless, we see that the rate of crack growth and the AE count rate follow each other closely, considering the fact that we could not see the entire patch of oxide. Therefore, we conclude that the observed AE is indeed due to oxide cracking and that AE bursts initiate during crack propagation.

Optical microscopy also indicated that for oxide thicknesses from 100 to 400 nm, the average initial crack length (crack opening) increases slightly from 0.05 to 0.12 mm. However, the average crack extension is constant—about 0.06 nm in length and independent of strain. (These values were measured in air and, as mentioned in the previous section, there could be differences in oxide behavior under vacuum.) The EE and AE were measured until 7% strain; measurement of crack density at 7% strain allows the actual number of crack increments to be calculated. Figure D-8 shows that the number of crack events that occur decreases with oxide thickness; from 100 to 400 nm, a 40% <u>decrease</u> is observed!

201
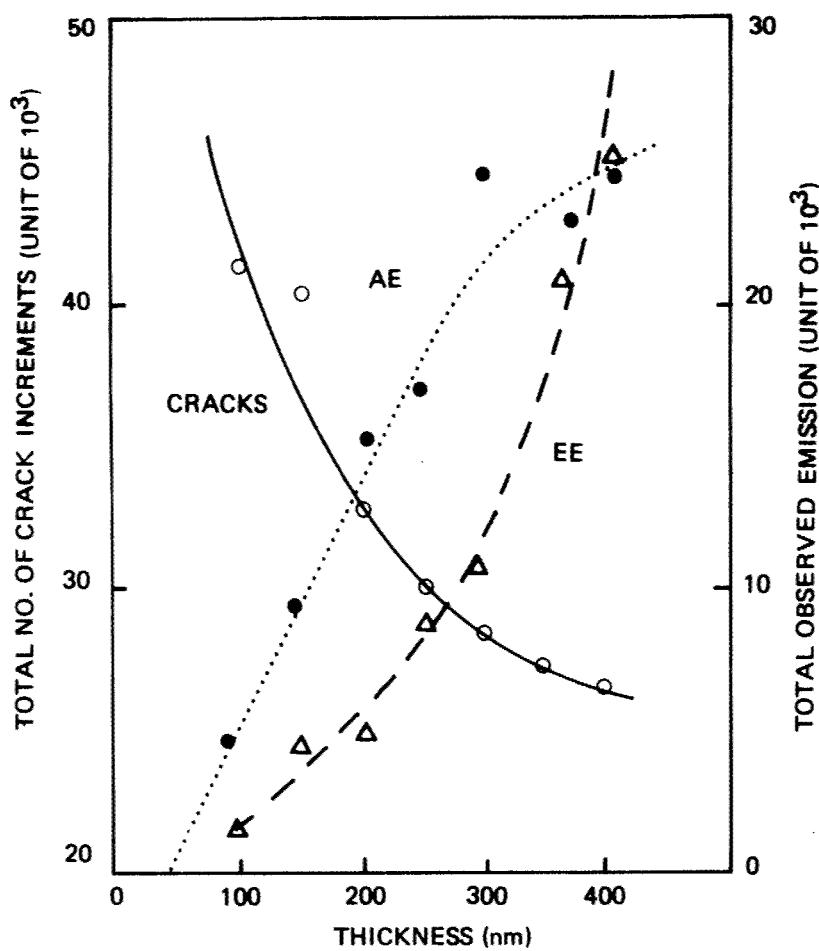
Figure D-8. The Dependence on Oxide Thickness of Total EE, Total AE, and Total Number of Cracks (Based on Crack Density Measurements)

Dependence of Total Emission on Oxide Thickness

The total number of events detected for both EE and AE versus oxide thickness also is shown in Figure D-8; both increase sharply with thickness. The clear implication of Figure D-8 is that the probabilities of detecting both AE and EE per crack increase dramatically with oxide thickness. For example, the number of electrons per crack increment increases from 0.03 for a 100-nm oxide to 0.93 for a 400-nm oxide, representing a factor of 30 increase. These results suggest that the EE process has a strong dependence on the energy released per crack increment. PIE shows a similar increase in emission with oxide thickness.

Energy Release and Electrons per Crack

Obviously, every crack increment does not produce detectable electrons. For a 300-nm oxide, 23% of the cracking events are accompanied by one or more electrons. Most frequently, only one electron is emitted, but often several are released within a few microseconds after crack propagation. The same is true for positive ions. The number of electrons released per EE burst shows an exponentially decaying probability, as shown in Figure D-9. The number distribution for PIE also is shown in Figure D-9. The function for this distribution is given by: $f(n) = \exp{-(n - 1)/\eta}$, where $f(n)$ is the fraction of bursts consisting of n electrons or ions. For a 300-nm oxide, $\eta = 0.96$, which indicates that multiple particle bursts of large n occur only rarely. These results also support the concept of an energy-dependent emission probability, because one expects an exponential distribution in the energy released from the oxide coating fracture.
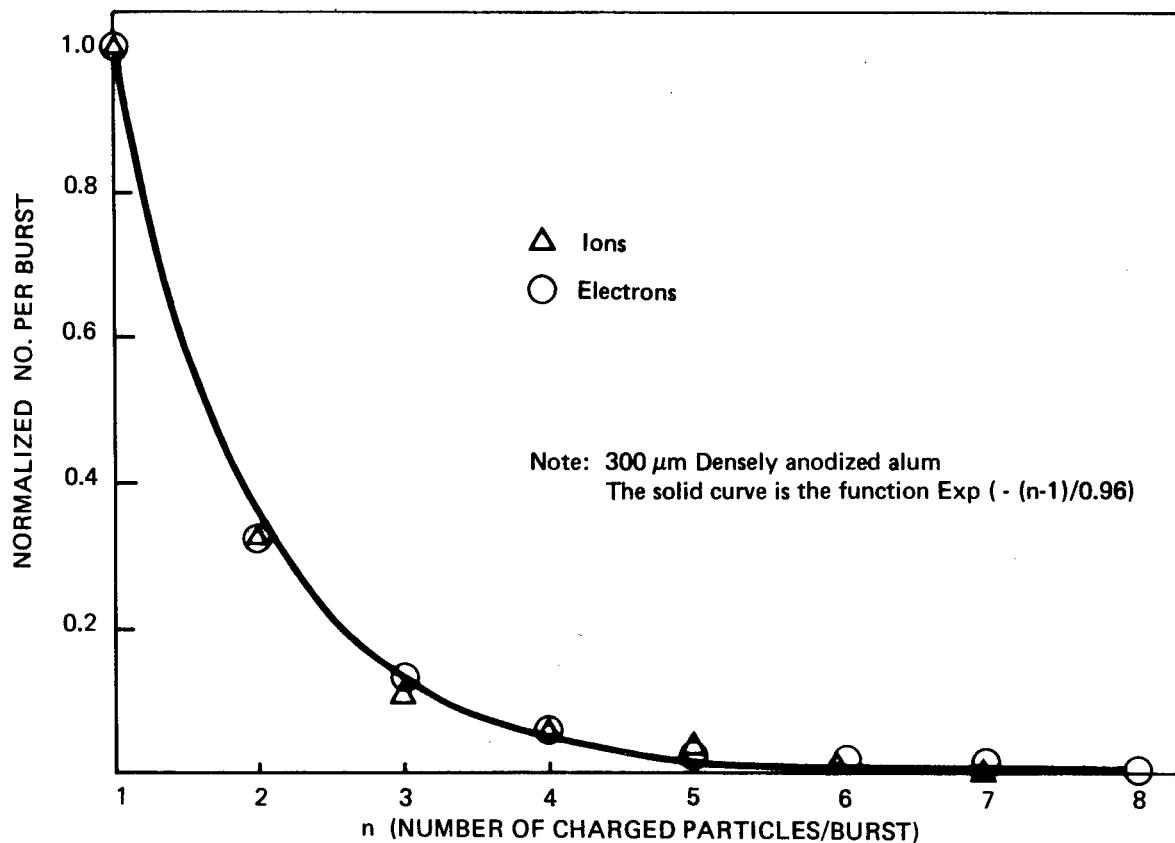
Figure D-9. The Distribution of the Number of Electrons and Number of Ions Emitted Per Burst

203

To determine whether this is the case, we examined the ring-down counting results, which did yield a nearly exponential energy distribution. Furthermore, the acoustic energy distributions changed with oxide thickness and, for a given sample, changed with strain. For example, the average energy of the acoustic signals tends to increase in the region of 1 to 1.25% strain, reach a maximum at about 1.5% strain, and then decrease with further strain. For both thick and thin oxides, several orders of magnitude spread in energy is observed. For thin oxides, the AE energy distribution falls rapidly to zero slightly above threshold. The average value of the AE energies compared to threshold are given for two oxide thicknesses at different strains:

300-nm oxide at 1.5% strain, average AE energy 5.5 x threshold energy

300-nm oxide at 6% strain, average AE energy 1.5 x threshold energy

100-nm oxide at 3% strain, average AE energy 1.13 x threshold energy

100-nm oxide at 10% strain, average AE energy 1.07 x threshold energy

Thus, these results suggest that thicker oxides do release more energy per crack, which leads to a higher probability of AE burst detection and more EE and PIE.

As further evidence that more electrons should be emitted for cracks that release more energy, we correlated the number of electrons in the EE bursts with the size of the corresponding AE burst (number of rings above threshold). The plot for such a correlation (640 pairs of data) shows a clear positive correlation (fig. D-10). A linear least-squares fit to the data indicates that, on the average, one electron is associated with a crack producing an AE burst having 1.3 times the threshold energy. A 10-electron burst is, on the average, associated with a crack producing an AE with 3.2 times threshold energy. Although we are still analyzing these data, the results are sufficient to say that larger acoustic bursts (and, therefore, cracking events with larger energy release) tend to be accompanied by more electron emission.

Comparison of PIE and EE Time Distributions

Measurements of the time distributions of EE relative to crack propagation presented in the previous section suggest that several mechanisms may be involved in the release of the charged particles. In additional experiments, we found relatively intense PIE during deformation of the dense anodized Al 1350. On a slow time scale, it appeared to have the same characteristic rate of emission versus strain curve as the EE and AE. Thus, we conclude that PIE also is due to oxide cracking.
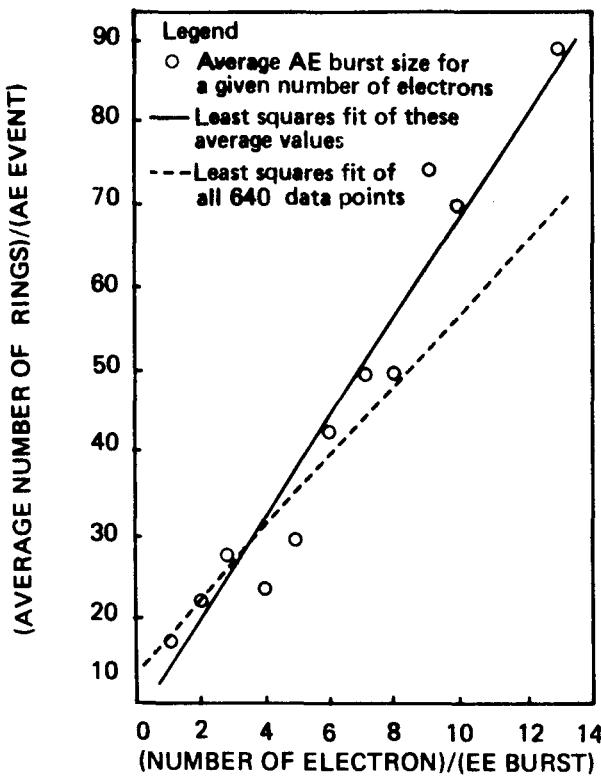
Figure D-10. Correlation of Size of AE Burst and Number of Electrons in the Burst

For comparison of PIE and EE time distributions relative to the AE bursts, the TOF multichannel analyzer was used. For samples prepared under similar conditions, we obtained the data shown in Figures D-11 and D-12. The plots are on a $\log_e$-linear scale. Curve (b) in Figure D-11 was taken on a much faster time scale (0.05-μs time resolution) using a fast oscilloscope and a video tape recorder. The latter method yields a decay constant of 0.13 μs plus an additional decay of about 4 μs. The slower decay constants (around 30 and 200 μs) still occur, but are not observed on these faster time scales. The fastest component represents close to 90% of all the emission. It also is being emitted on a time scale very close to the motion of the crack tip.

The same experiments were performed with the PIE. The resulting time distributions of PIE relative to AE are shown in Figure D-12. Only one decay constant is observed, with a value of 0.9 $\pm$ 0.15 μs. No very fast and no longer lasting components are observed. This suggests that PIE has a completely different mechanism from the EE that we observe. Also, no PIE component appears to be occurring only during crack propagation. It is strictly the product of a relaxation mechanism following fracture.

205
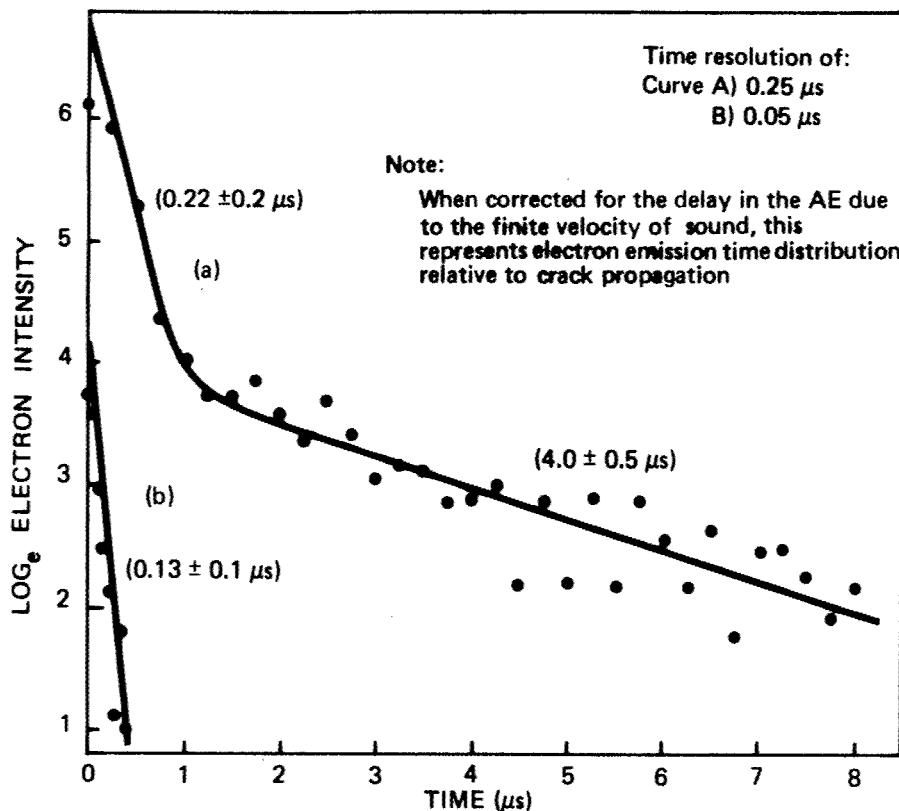
Figure D-11. Distributions in Time of the Electrons Relative to the AE Signal

CONCLUSIONS

In this section, we have presented evidence that supports the following conclusions concerning emission phenomena during tensile deformation of anodized aluminum:

1. EE and PIE are intimately related to crack propagation in the oxide coating.

2. The number of crack increments occurring in the oxide from 0 to 7% strain decreases with oxide thickness, whereas the detectable AE, EE, and PIE increase. This implies that EE, PIE, and the observable AE depend on the energy released per crack increment.

3. The number of bursts of charged particles follows a function of the form $f(n) = \exp[-(n-1)/\eta]$ for both electrons and positive ions. One-particle bursts are by far the most probable.

4. The acoustic energy released during crack propagation has a distribution that changes significantly with oxide thickness and, for a given thickness, with strain.

5. There is a positive correlation between the number of electrons per EE burst and the energy of the accompanying AE burst.

206
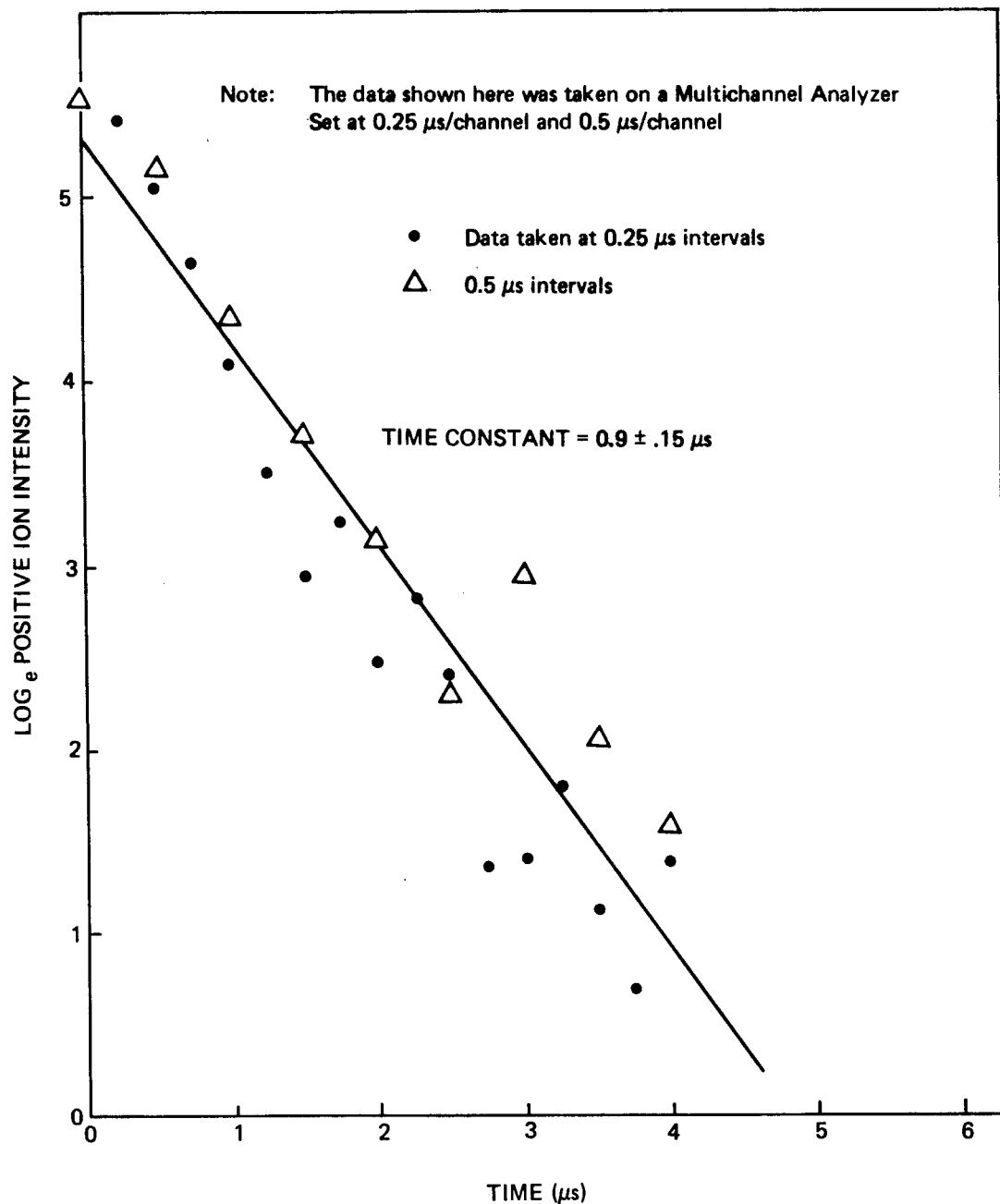
Figure D-12. The Positive Ions Emission Time Distribution Relative to Crack Propagation

6. The EE exhibits a feature in its time distribution relative to oxide coating fracture that is close to the propagation time of a crack. Most EE occurs within 0.1μ s of cracking.

7. The PIE has a decay constant equal to 0.9μ s, which does not appear to be shared with the EE. Thus, a separate mechanism for PIE is most likely. Further work needs to be done in relating these observations to known defects and atomic processes that can occur in metal oxides. The information we have provided should be valuable for relating the fracto-emission to fundamental processes. In addition, it provides useful facts for the application of fracto-emission to the study of dynamic crack propagation.

SUMMARY OF AE STUDIES ON POLYMER-COATED ANODIZED ALUMINUM

The AE work previously discussed proved interesting because two effects were observed:

1. For dense coatings on pure aluminum, AE could be used to detect fracture of the oxide itself. Essentially no AE was detected from the aluminum substrate.

2. For porous oxides on aluminum alloy samples, the oxides tended to suppress AE from the substrate, presumably due to the prevention of dislocation motion near the interface.

To further explore the utility of AE, we investigated the AE accompanying tensile deformation of anodized aluminum coated with polymer materials used in adhesive bonding of aluminum. The substrates were Al 1350 to minimize AE from the aluminum itself. All samples were anodized by the Boeing H_3PO_4 process (PAA), except that a 20V forming potential was used instead of 10V. The samples were strained at 1.2% per minute. The samples consisted of the following:

1. PAA only
2. PAA + BXR-MSR primer
3. PAA + BXR-MSNR primer
4. PAA + BXR-MSR + FM-300 bonded specimens
5. PAA + BXR-MSNR + FM-300 bonded specimens

The AE versus strain curves for these coatings are shown in Figure D-13, with total counts presented for each curve. For comparison, the AE from an unanodized sample is about 1000 counts. Almost all of these occur in a fracture below 1% strain.
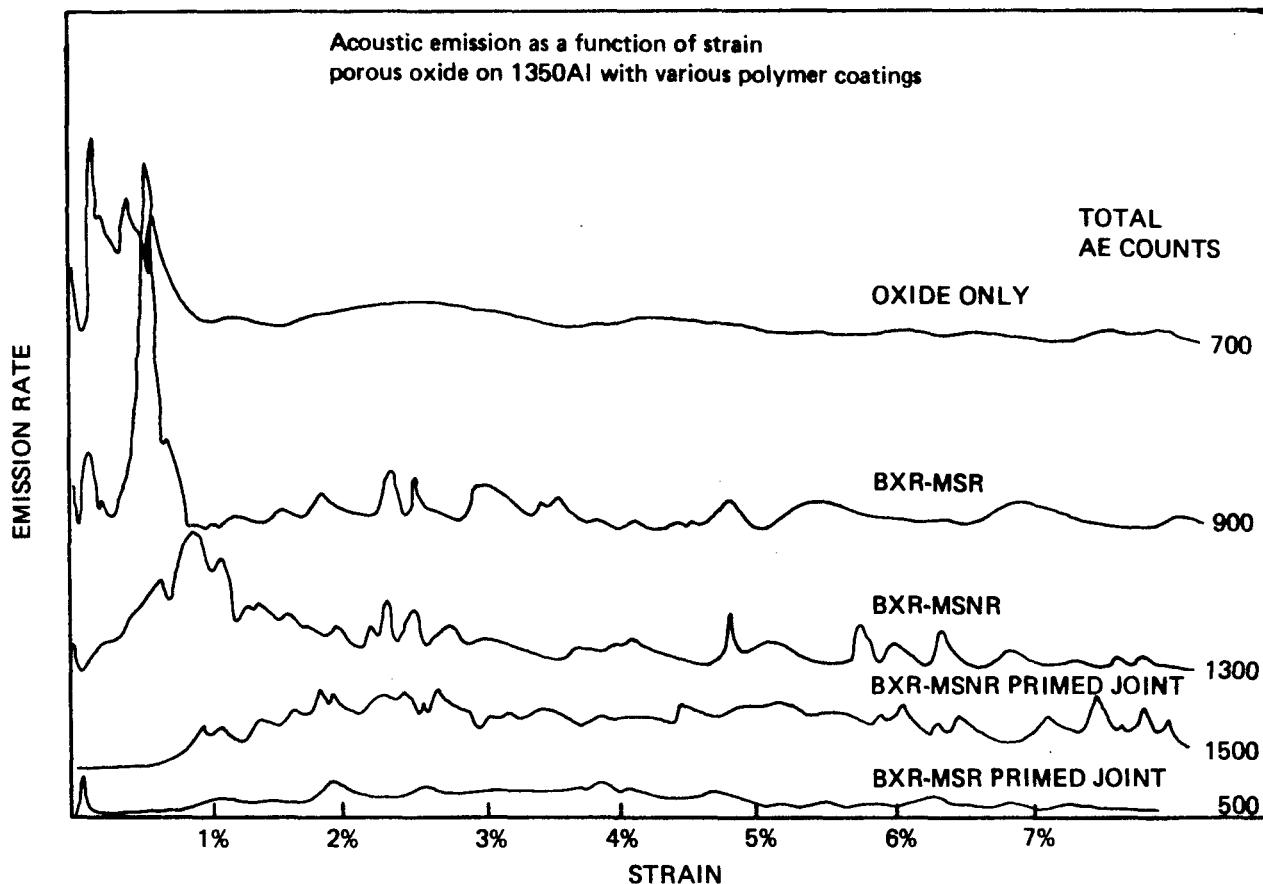
Figure D-13. Acoustic Emission Curves for H_3PO_4 Anodized Aluminum (1350) with
Various Polymer Coatings used in Adhesive Bonding of Aluminum

The first characteristic to note is that the porous oxide tends to suppress the AE from the substrate. Second, the BXR-MSR primed and bonded samples do likewise. There does not appear to be any signficant AE from oxide cracking. Third, the samples involving layers of BXR-MSNR epoxy appear to have slightly higher AE than the others. Although optical microscopy shows no evidence of fracture of the epoxy layer, it is probable that the increase in AE is caused by damage in the epoxy or at an interface (i.e., delamination). Finally, the shape of the AE count rate versus strain curve shows considerable change for the different kinds of coatings.

In summary, small changes occurred in the AE emitted from polymer-coated, anodized aluminum. In the case of primed samples, there is some evidence that damage such as delamination was detected.

FRACTO-EMISSION DATA FROM OTHER MATERIALS

Because charged particles are efficiently detected with a channeltron electron multiplier (CEM), the decision was made to explore crack propagation in a number of materials. Investigation of possible emission mechanisms and evaluation of the applicability of particle emission to problems of material fracture were the basis of the endeavor. Material fracture is of considerable interest for a number of reasons. From the point of view of fracture mechanics, one frequently is interested in mechanisms causing fracture, the dependence of crack growth on external parameters, modeling unstable crack extension, and finding crack-arrest mechanisms. Studies have been conducted on all types of materials including metals, ceramics, glasses, and polymers. A closely related interest is the energy release phenomena accompanying fracture. Particle emission may prove useful in these areas.

Particle emission during mechanical deformation of materials often is referred to as fracto-, mechano-, or tribostimulated emission (in the case of photons, it often is called triboluminescence). We are primarily interested here in emission associated with the release of strain energy caused by the rupture of bonds in a material during crack growth. Therefore, we shall refer to such emission, including photons, as fracto-emission (FE). Although it needs to be clearly established, we have preliminary evidence that FE characteristics, such as the types of particles emitted, their intensities, and their time dependence, depend strongly on the velocity of crack propagation. Certainly, we expect the rate of energy release in the vicinity of the crack tip to strongly influence the creation of the initial states responsible for FE and, therefore, the FE characteristics.

EMISSION PHENOMENA ACCOMPANYING CRACK PROPAGATION

During crack propagation through materials, a high concentration of energy is deposited into a small volume due to the sudden release of elastic strain energy. For a short time (on the order of microseconds), this can result in the following:
1. Production of highly localized heat
2. Creation of excitations and defects in the material
3. Production of dangling bonds and trapped electrons on or near the freshly created crack wall surface
4. Emission of excited and reactive species (ions and neutrals) into the gas phase

5. Separation of charges on the crack walls with accompanying intense electric fields for many insulating materials

6. Production of acoustic waves

In principle, all of the above consequences of crack growth could contribute to FE from the material. For large band gap insulators, it is doubtful that the peak localized temperatures reached are sufficient to elevate the valence bond electrons thermionically into the vacuum. However, the temperature maxima reached might be quite adequate to excite and release electrons from the surface traps. Likewise, thermal stimulation of the defects produced during fracture can lead to a number of de-excitations and recombinations that produce electron, ion, and neutral particle emission, as well as photons (ref D-15, D-19).

The interaction of excited and reactive species at a surface can readily produce electrons, free ions, and photons via Auger de-excitation (ref D-20), stimulated desorption (ref D-21, D-22), chemi-emission (ref D-23), and chemiluminescence (ref D-24), particularly on a highly reactive surface such as the freshly created crack wall. The significant differences between a clean crystal surface and a freshly created cleavage surface on silica and quartz have been investigated by Hochstrasser and Antonni (ref D-25). They demonstrated the high density of dangling bonds, as well as the increase in chemical reactivity that occurs upon fracture. Thus, it is reasonable to assume that freshly fractured surfaces of all materials would have considerable reactivity. In the case of polymers, for example, electron spin resonance investigations found that fractured polymers have high concentrations exhibited by highly crystalline oriented fibers (ref C-26). It was suggested that crosslinkage enhances the type of fracture (presumably molecular fracture) that produces free radicals.

Clearly, fractured surfaces are potentially very reactive and could be expected to produce emission. For example, a reactive species, perhaps from the fractured material itself or from the background gases, can react with a site of high reactivity on the surface with sufficient energy release (Kasemo, ref D-23, D-24, suggests via an excited, adsorbate-induced hole state) during de-excitation to yield electrons or photons.

The separation of charges that occurs during fracture of ionic crystals (ref D-27) is known to produce electric field intensities that can exceed 15,000V/cm. Such fields

can contribute to electron emission by providing accelerating fields; e.g., electron energies up to 120 keV have been observed coming from alkali halides (ref D-28). Ion emission of a few hundred eV has been observed from granite specimens (ref D-29). During thermally stimulated exoemission, several other substances have exhibited electron emission with energies in the range of 5 eV to 10 keV (ref D-30, D-31).

Other phenomena associated with the high temperatures produced at the crack tip involve thermal decomposition, diffusion of impurities, and desorption of decomposition and diffusion species into the gas phase. This investigation determined that neutral emission from thin anodized coatings on aluminum is very intense and intimately related to oxide cracking (ref D-15). The species observed (e.g., O_2, H_2O, and CO_2) and intensities were dependent on the type of anodizing electrolyte used (H_3PO_4 and ammonium tartrate) and the oxide thickness. There was strong evidence that thermal decomposition and diffusion were involved in the release of the gases. Fox and Soria-Ruiz (ref D-32) detected gases released during fracture from a number of inorganic materials. They observed intense bursts of products caused by both endothermic and exothermic reactions. Urakaev et al. (ref D-33) saw volatile products and evidence of highly excited ions and radicals from mechanical fracture of inorganic crystals. Regel et al. (ref D-34) saw intense neutral emission during fracture of PMMA, observing several mass peaks. Andrews (ref D-26) points out that the observed material evolving from the fractured polymers may be low-molecular-weight species already present in the specimen released by stress-assisted diffusion rather than thermally activated decomposition.

Finally, the stress wave created as the crack tip moves through the material could, in principle, produce FE. Asay (ref D-35) has examined shock-induced vaporization and has seen significant amounts of mass ejected from surfaces accelerated by strong shock waves. Hayes (ref D-36) has seen electrical effects on shocked materials, suggesting that charged particles might be leaving the surface. Although the shock intensity is significantly higher in these studies than is created by fast crack growth, the stress wave might contribute to part of the observed emission during fracture.

EXPERIMENT

The survey of emission phenomena was carried out by producing catastrophic failure on samples of two geometries:

1.   A rectangular parallelpiped broken in a three-point bending mode. The surface under tension faced the CEM.

2.   Tensile specimens, often notched in the center

Typical dimensions were such that the fractured surface had a cross section from 5 to 20 mm^2. In addition, we fractured a number of bare fibers of materials such as E-glass, S-glass, and oriented carbon. Epoxy-fiber bundles of these materials also were fractured, each bundle containing a few thousand fibers. For all materials studied, we looked for electrons and, in some cases, positive ions. This was accomplished simply by changing the potential of the front end of the CEM relative to the sample. The distance from the fracture line to the detector was 5 mm.

Emission rates were measured in two time regimes using a multichannel scaler. One time scale was 0.8 s/channel (512 channels maximum). The instant of fracture was determined on a synchronized stripchart recorder displaying the applied stress. Much faster time scales were used to determine faster decay phenomena down to a resolution of 0.05 μs.

RESULTS

Table D-2 summarizes the data taken so far for electron emission. All samples were fractured at room temperature. In each case, a sharp emission maximum accompanied failure, followed by an emission delay. In some materials, the decay was with time constants on the order of microseconds or milliseconds. In others, a very long-lived emission continued for minutes.

Several comments can be made at this point:

1.   The chance of detecting electrons probably is enhanced when a fiber is broken in comparison with the tensile fracture of the same material in bulk. The change of electron collection probably is improved for the fiber geometry because there is less chance of the sample being in the way.

2.   The more energetic fracture gives rise to the more copious FE. If more elastic energy is stored before fracture, then more energy will be released via particle emission. An example is the comparison of E-glass and S-glass fibers, where an order of magnitude greater emission was observed for the material with the larger tensile strength.

Table D-2. Electron Emission from Various Materials

Materials	Approx decay times of fracto-emission	Electrons detected/ cm^2 of crack wall
Sapphire	1 sec, minutes	1,500
Alumina	2 sec, minutes	15,000
Al_2O_3 anodized layer	1 - 20 μsec	3×10^5
Bn	1 sec, minutes	$\sim 10^6$
Quartz		$\sim 10^6$
Crystalline sugar	2 sec, minutes	$\sim 2 \times 10^6$
Fused silica	Several msec	2,000
Soda lime glass	Several msec	$\sim 1,000$
Kelvar 49 fibers	$\ll 1$ sec	$\sim 10^8$
Graphite fibers	10 - 100 μsec	$\sim 10^8$
E glass fibers	10 μsec	$\sim 10^8$
S glass fibers	10 - 50 μsec	$\sim 10^8$
Epoxy (DER 332)	25 - 50 μsec	$\sim 10^3$
Lucite	< 2 msec	$\sim 10^2$
Polystyrene	< 20 msec	$\sim 10^2$

Table D-3. Positive Ion Emission from Various Materials

Material	Approx decay times of FE emission	Ions detected/ cm^2 of crack wall
Fibers		
Kevlar 49	<0.1 s	$\sim 10^8$
Carbon	10 μs	$\sim 10^8$
E-glass	10 μs	$\sim 10^7$
S-glass	11 μs	$\sim 10^8$
Plastics		
Epoxy (DER 332)	25 μs	$\sim 10^3$
Lucite	<2 msec	few
Polystyrene	35 μs	500

3. Materials listed in Table D-3 have been examined for PIE. Every material examined so far has produced free positive ions with fracture.

This survey of FE indicates that it is indeed a widespread phenomenon.

An extremely interesting observation was made concerning epoxy-fiber systems. We note in Table D-2 that fibers and pure epoxy produce FE having a relatively simple decay curve, with time constants in the range of 10 to 100 μs. However, we discovered that when interfacial failure occurred, the FE produced was several orders of magnitude more intense and decayed with a time constant of several seconds, even minutes. Figure D-14 shows typical FE curves for fibers, epoxy, and one of the composite bundles. The epoxy in all cases is Dow DER 332. The EE curves for the composites show a feature coincident with rupture. On a faster time scale, this peak is found to consist of short spikes of emission due to fracture of fibers and matrix material. During and following delamination, the dominant long-lived emission occurs. Similar results were found on all composite bundles for both electrons and positive ions.

As a test of this phenomenon, E-glass/epoxy bundles were split lengthwise, causing extensive delamination, this being determined by optical microscopy. This splitting by delamination produced the same long time-constant emission observed in fracture of the fiber bundles.

Similar results were found in studies of epoxy-to-lucite bonds. When epoxy or lucite was fractured alone, microsecond delays occurred in the emission. However, if the epoxy-lucite interface was made to fail, the intense, long-lived emission occurred.

CONCLUSIONS

In this section, we have shown that fracto-emission occurs from a variety of materials. It is possible that this emission will be useful for studying phenomena accompanying fracture on a microscopic scale. Also, we have reported the discovery of a unique difference between fracture of fibers and epoxy and fracture of composites. We attribute this difference to the delamination or interfacial failure that occurs. Perhaps the bonds that are broken during interfacial failure are particularly efficient for particle emission. We plan to pursue this effect in our future research programs.
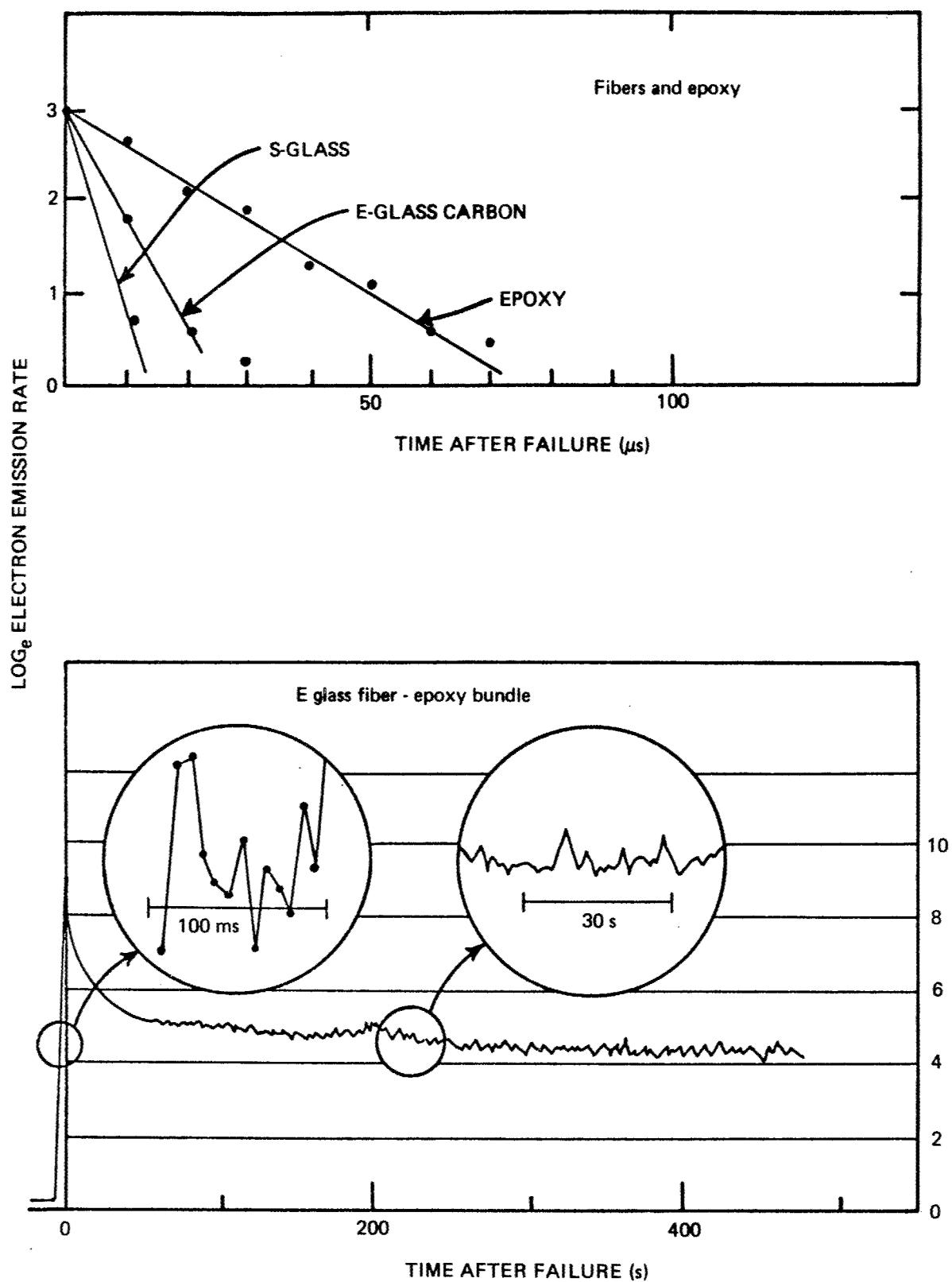
Figure D-14. Typical Log_e vs Time Plots of Electron Emission from Fibers, Epoxy, and E-Glass Fiber-Epoxy Bundles

CHEMILUMINESCENCE DURING H$_3$PO$_4$ ANODIZATION OF BARE AL 2024

When oxygen reacts with a clean metal surface, two forms of particle emission sometimes have been observed: electrons and photons. The first is called chemi-emission and the second is called chemiluminescence. Exposure of Al to O$_2$ has yielded both chemi-emission (ref D-37) and chemiluminescence (ref D-38). The observed luminescence seems to be in the visible spectrum and has a probability of around 10^{-5} photons per O$_2$ molecule reacting.

We hypothesized that such luminescence might be detectable from an aluminum sample during anodization in an H$_3$PO$_4$ solution under conditions like those used in the preparation of aluminum for adhesive bonding. Thus, a preliminary experiment using a photomultiplier (PM) tube sensitive to visible light only was performed. The PM used was rather noisy, but proved adequate. For this experiment, the dark current was 5 x 10^{-9} amp when the PM voltage was 1 kV. Normally, this PM would be run at much higher voltage, 2.5 kV, and therefore higher gain. A Keithley Electrometer was used to measure the PM output. The PM was pointed at an Al 2024 bare sample of about 4 cm^2 (10 cm away from the PM tube) in a 1000-ml beaker containing a 10% H$_3$PO$_4$ solution. The cathode also was aluminum.

There was no difficulty in detecting photons that accompanied anodization. In fact, initially at 10V forming volage, the detector saturated. The photon emission versus time was a complicated function that depended on how long the sample stayed in the solution prior to turning on the voltage and the current. The intensity also was strongly dependent on the applied voltage, being roughly proportional. The power supply used would not go below 3.5V, but at this voltage, substantial photon fluxes still were detected.

A sample of Al 1350, a relatively pure Al alloy, also was tried. It also was a good photon emitter. The intensity versus time was completely different from the Al 2024 sample.

A literature search showed that a wide number of effects such as the above have been observed (ref D-39). However, we have not as yet found a study of luminescence during H$_3$PO$_4$ anodization.

Such emission could provide a very easy way to monitor anodization in a commercial situation. There appears to be sufficient intensity that spectroscopy could be performed, which might allow the usefulness of a monitoring technique to be greatly expanded. If time permits, we will pursue this effect further.

REFERENCES

D-1. J. T. Dickinson, P. F. Braunlich, L. Larson, and A. Marceau, Appl. of Surf. Sci. 1, 515 (1978).

D-2. D. L. Doering, T. Oda, J. T. Dickinson, and P. F Braunlich, Appl. of Surf. Sci. 3 196 (1979).

D-3. B. Z. Rosenblum, P. F. Braunlich, and L. Himmel, J. Apply. Phys. 48, 5262 (1977).

D-4. R. G. Liptai and R. G. Tatro, "Proceedings of the Fourth Annual Symposium on Nondestructive Testing of Aircraft and Missile Components," 284-346, Southwest Research Institute, San Antonio, Texas, 1963.

D-5. R. G. Liptai, "An Investigation of the Acoustic Emission Phenomenon," PhD dissertation, Michigan State University, East Lansing, Michigan, 1963.

D-6. H. L. Dunegan and D. A. Tatro, "Acoustic Emission Effects during Mechanical Deformation," 243-312, Techniques of Metals Research, vol. 5, Interscience Publishers, John Wiley and Sons (New York, 1971).

D-7. B. Z. Rosenblum, J. P. Carrico, P. Braunlich, and L. Himmel, J. Phys. E. Sci. Instr. 10 (1977).

D-8. L. R. Danielson, M. J. Dresser, E. E. Donaldson, Jr., and L. Himmel, Surf. Sci. 71, 599 (1978).

D-9. D. R. Arnott and J. A. Ramsey, Surf. Sci. 28, 1 (1971).

D-10. J. W. Diggle, T. C. Downie, and C. W. Goulding, Chem. Rev. 69, 365 (1969).

D-11. J. E. Lewis and R. C. Plumb, J. Electrochem. Soc. 105, 496 (1958).

D-12. R. B. Mason, J. Electrochem. Soc. 102, 671 (1955).

D-13. R. E. Herfort, "Fundamental Investigation of Anodic Oxide Films on Aluminum Alloys as a Surface Preparation for Adhesive Bonding," U.S. Air Force Technical Report AFML-TR-76-142.

D-14. C. S. Taylor, C. M. Tucker, and J. D. Edwards, Trans. Electrochem. Soc. 88, 325 (1945).

D-15. L. A. Larson, J. T. Dickinson, P. F. Braunlich, and D. B. Snyder, J. Vac. Sci. Tech. 16, 590 (1979).

D-16. E. A. Kurz, American Laboratory, March 1979, p. 67.

D-17. S. Tajima in Advances in Corrosion Science and Technology, Volume 1, ed. M. G. Fontana and R. W. Staehle (Plenum Press, New York, 1970), p. 229.

D-18.   D. O. Harris, A. S. Tetelman, and F. A. I. Darwish in Acoustic Emission, ASTM STP 505 (American Society for Testing and Materials, Philadelphia, 1972), pp. 238-249.

D-19.   K. Becker, CRC Critical Reviews in Solid State Sciences 3, 39 (1972).

D-20.   H. Hagstrum in Experimental Methods in Catalytic Research, Volume III, ed. R. B. Anderson and P. T. Dawson (Academic Press, New York, 1976), pp. 42-81.

D-21.   Y. P. Sitonite, F. S. Zimin, and T. V. Krylova, Russian J. of Physics and Chemistry 44, 1023 (1970).

D-22.   M. L. Knotek and P. J. Feibelman, Phys. Rev. Letters 40, 964 (1978).

D-23.   J. Harris, B. Kasemo, and E. Tornqvist, Chem. Phys. Letters 52, 538 (1977).

D-24.   B. Kasemo, E. Tornquist, J. K. N. Orskov, and B. I. Lundquist, Surf. Sci. 89, 554 (1979).

D-25.   G. Hochstrasser and J. F. Antonni, Surf. Sci. 32, 644 (1972).

D-26.   E. H. Andrews, "Cracking and Crazing in Polymeric Glasses," in The Physics of Glassy Polymers, ed. R. N. Haward (John Wiley & Sons, New York, 1973), pp. 448-451.

D-27.   M. I. Kornfeld, J. Phys. D.: Appl. Phys. 11, 1295 (1978).

D-28.   J. Wollbrandt, J. E. Linke, and K. Meyer, Phys. Stat. Sol.(A) 27, K53 (1975).

D-29.   S. A. Hoenig, "The Application of Electrostatic Techniques to the Analysis of Pre-Fracture Phenomena in Ceramic Materials, NSF Report, Contract ENG75-13639, August 1975.

D-30.   B. Rosenblum, P. Braunlich, and J. P. Carrico, Appl. Phys. Letters 25, 17 (1974).

D-31.   H. Glaefeke, "Exoemission," in Thermally Stimulated Relaxation in Solids, ed. P. Braunlich (Springer-Verlag, Berlin, 1979).

D-32.   P. G. Fox and J. Soria-Ruiz, Proc. Roy. Soc. Lond. A317, 79 (1970).

D-33.   F. K. Urakaev, V. V. Boldyrev, O. F. Pozdynyakov, and V. R. Regel, Kinetika i Kataliz 18, 350 (1977).

D-34.   V. R. Regel, T. M. Muinov, and O. F. Pozdynyakov in Physical Basis of Yield and Fracture (Institute of Physics, London, 1966), p. 194.

D-35.   J. R. Asay, "A Model for Estimating the Effects of Surface Roughness on Mass Ejection from Shocked Materials," Sandia Laboratories Report SAND78-1256 (1978).

D-36.   B. Hayes, private communication.

D-37.   J. A. Ramsey, Surf. Sci. 8, 313 (1967).

D-38.   J. Harris, B, Kasemo, and E. Tronquist, Chem. Phys. Letters 52, 538 (1977).

D-39.   S. Ikonopisov, Electrochimica Acta 20, 783 (1975).